DOT/FAA/TC-13/25, P3

Federal Aviation Administration
William J. Hughes Technical Center
Aviation Research Division
Atlantic City International Airport
New Jersey 08405

Development of a New Metal Material Model in LS-DYNA®

Part 3: Plastic Deformation and Ductile Fracture of 2024 Aluminum Under Various Loading Conditions

April 2014

Final Report

This document is available to the U.S. public through the National Technical Information Services (NTIS), Springfield, Virginia 22161.

This document is also available from the Federal Aviation Administration William J. Hughes Technical Center at actlibrary.tc.faa.gov.

U.S. Department of Transportation
Federal Aviation Administration

NOTICE

This document is disseminated under the sponsorship of the U.S. Department of Transportation in the interest of information exchange. The U.S. Government assumes no liability for the contents or use thereof. The U.S. Government does not endorse products or manufacturers. Trade or manufacturers' names appear herein solely because they are considered essential to the objective of this report. The findings and conclusions in this report are those of the author(s) and do not necessarily represent the views of the funding agency. This document does not constitute FAA policy. Consult the FAA sponsoring organization listed on the Technical Documentation page as to its use.

This report is available at the Federal Aviation Administration William J. Hughes Technical Center's Full-Text Technical Reports page: actlibrary.tc.faa.gov in Adobe Acrobat portable document format (PDF).

Technical Report Documentation Page

1. Report No.	2. Government Accession No.	3. Recipient's Catalog No.
DOT/FAA/TC-13/25, P3		

4. Title and Subtitle	5. Report Date
DEVELOPMENT OF A NEW METAL MATERIAL MODEL IN LS-DYNA® PART 3: PLASTIC DEFORMATION AND DUCTILE FRACTURE OF 2024 ALUMINUM UNDER VARIOUS LOADING CONDITIONS	April 2014
	6. Performing Organization Code
7. Author(s)	8. Performing Organization Report No.
Jeremy Daniel Seidt	
9. Performing Organization Name and Address	10. Work Unit No. (TRAIS)
The Ohio State University Department of Mechanical Engineering Scott Laboratory 201 W 19th Ave. Columbus, OH 43214	
	11. Contract or Grant No. 2006G004
12. Sponsoring Agency Name and Address	13. Type of Report and Period Covered
U.S. Department of Transportation Federal Aviation Administration New England Region—Aircraft Certification Service Engine and Propeller Directorate 12 New England Executive Park Bunington, MA 01803	Final Report
	14. Sponsoring Agency Code ANE-110

15. Supplementary Notes

The Federal Aviation Administration William J. Hughes Technical Center Aviation Research Division Technical Monitors were Donald Altobelli and William Emmerling.

16. Abstract

A team consisting of The Ohio State University (OSU), The George Washington University, the National Aeronautics and Space Administration Glenn Research Center, and the Federal Aviation Administration Aircraft Catastrophic Failure Prevention Research Program collaborated to develop a new material model in LS-DYNA® for 2024 aluminum. This report is part 3 of a three-part report that describes the experimental material characterization work conducted at OSU. The plastic deformation and ductile fracture behavior of 12.7-mm-, 6.35-mm-, and 3.175-mm-thick 2024 aluminum plates and sheets were investigated. Tension, compression, and shear experiments were conducted at strain rates ranging from 10^{-4} s^{-1} to 11,000 s^{-1} and temperatures ranging from -50° to 450°C. Results show the material flow stress was insensitive to strain rate in tension, compression, and shear between 10^{-4} s^{-1} and 5000 s^{-1}. In compression, increased stresses are observed at strain rates between 5000 s^{-1} and 11,000 s^{-1}. Flow stress decreases monotonically with increasing temperature. The strain-hardening behavior of the material also changed dramatically between 150° and 300°C. The 12.7-mm-thick 2024-T351 plate was anisotropic with respect to plastic deformation. Tensile and compressive stresses determined from specimens oriented ±45° to the plate's rolled direction were significantly lower than those determined from specimens oriented in the rolled and transverse directions. The dependence of fracture on the state of stress was studied through mechanical experiments on specimens with various geometries subjected to multiple load conditions. Tension tests of plane stress (thin), axisymmetric, and plane strain (thick) specimens were conducted for this purpose. Combined tension—torsion, pure shear and compression—torsion tests and punch experiments were also conducted. Tension test results showed that peak axial load increases and fracture displacement decreases with decreasing stress triaxiality. Load versus displacement and torque versus rotation curves were given for axial-torsional tests. Load versus displacement curves were given for static and dynamic punch tests. The specimen failure mode evolution of specimens subjected to dynamic punch loading is also discussed. These data are used in a coupled experimental-numerical technique to develop a fracture locus for 2024-T351 aluminum in part 2 of this report.

17. Key Words	18. Distribution Statement
Plastic deformation, Fracture, Strain rate sensitivity, Temperature sensitivity, Stress state dependence, Split Hopkinson bar, Digital image correlation	This document is available to the U.S. public through the National Technical Information Service (NTIS), Springfield, Virginia 22161.

19. Security Classif. (of this report)	20. Security Classif. (of this page)	21. No. of Pages	22. Price
Unclassified	Unclassified	223	

Form DOT F 1700.7 (8-72) Reproduction of completed page authorized

ACKNOWLEDGEMENTS

This research was funded by the Federal Aviation Administration. The authors are grateful to Don Altobelli, Bill Emmerling, and Chip Queitzsch, who oversaw a remarkable team of researchers for this project. Thanks to Mike Pereira, Kelly Carney, Duane Revilock, Chuck Ruggeri, and Brad Lerch of the National Aeronautics and Space Administration Glenn Research Center. Thanks also to Steve Kan, Paul Dubois, Jeanne He, Murat Buyuk of George Washington University, Tim Schmidt of Trillion Quality Systems, and Alistair Tofts of Correlated Solutions.

TABLE OF CONTENTS

EXECUTIVE SUMMARY xiv

1. INTRODUCTION 1

1.1 Purpose 2
1.2 Background 4

1.2.1 Plastic Deformation of 2024 Aluminum 5
1.2.2 Ductile Fracture of 2024 Aluminum 6
1.2.3 Punch Experiments 7

2. METHODOLOGY AND EXPERIMENTAL PROGRAM 8

2.1 Plastic Deformation of 2024 Aluminum 8
2.2 Ductile Fracture of 2024-T351 Aluminum 14

3. EXPERIMENTAL TECHNIQUES 24

3.1 Low-Strain Rate Experiments 24

3.1.1 Low-Rate Tension Experiments 29
3.1.2 Low-Rate Compression Experiments 35
3.1.3 Low-Rate Torsion and Combined Loading Experiments 37
3.1.4 Low-Rate Punch Experiments 43
3.1.5 Elevated- and Low-Temperature Experiments 45

3.2 High-Strain Rate Experiments 47

3.2.1 Compression SHB Experiments 48
3.2.2 Dynamic Punch Experiments 52
3.2.3 Tension SHB Experiments 56
3.2.4 Torsion SHB Experiments 61

3.3 Digital Image Correlation 66
3.4 Data Management and Transfer 69

4. EXPERIMENTAL CHARACTERIZATION OF THE PLASTIC DEFORMATION OF 2024 ALUMINUM IN TENSION, COMPRESSION, AND SHEAR 69

4.1 Experimental Data From 12.7-mm-Thick 2024-T351 Plate 69

4.2 Experimental Data From 6.35-mm-Thick 2024-T351 Plate 77

4.3 Experimental Data From 3.175-mm-Thick 2024-T3 Sheet 78

4.4 Data Comparison: 12.7- and 6.35-mm-Thick 2024-T351 Plate and 3.175-mm-Thick 2024-T3 Sheet 80

5. DUCTILE FRACTURE OF 2024-T351 ALUMINUM 80

5.1 Tension Experiments 80
5.2 Combined Loading Experiments 83
5.3 Punch Experiments and Results 91

6. SUMMARY AND CONCLUSIONS 94

6.1 Plastic Deformation of 2024 Aluminum 94
6.2 Ductile Fracture of 2024-T351 Aluminum 95

7. REFERENCES 96

APPENDICES

A—Aluminum Certified Test Reports

B—Specimen Fabrication Method Test Series

C—Test Naming Convention

D—Drawings of Test Specimens and Fixtures Used in the Ductile Fracture Test Series

E—Fracture Test Series Dic Extensometer Positions and Strain Contours Prior to Fracture

F—Data Transfer Procedure Document

G—Repeatability of the Experimental Data From the Plastic Deformation Test Series

LIST OF FIGURES

Figure		Page
1	The Uncontained Engine Debris Threat: Damage to a DC-9 Aircraft From Uncontained Engine Debris and a Subsequent Fire, Damage to an Aircraft From an Uncontained Turbine Blade, Recovered Debris From a Fan Disk Failure Event, and an Uncontained Fan Blade Experiment	1
2	Tension Test Specimen Dimensions, Specimen Clamped in Inconel 718 Attachment Fixture, and Epsilon 3442 Extensometer Attached to Specimen	9
3	Spool-Shaped Torsion Specimen	9
4	Tension, Compression, and Torsion Specimens Fabricated From 12.7-mm-Thick 2024-T351 Aluminum Plate	12
5	Tension and Compression Specimens Fabricated From a 6.35-mm-Thick 2024-T351 Plate and a 3.175-mm-Thick 2024-T3 Sheet	14
6	Combined Axial and Torsional Loading of a Thin-Walled Tube Specimen	20
7	Various Tension, Combined Loading, and Punch Test Specimens Fabricated From a 12.7-mm-Thick 2024-T351 Aluminum Plate	23
8	Stress Triaxiality and Lode Parameter vs. Axial-Stress-to-Shear Stress Ratio for Combined Axial and Torsional Loading of a Thin-Walled Spool Specimen	25
9	Instron 1321 Bi-Axial Servohydraulic Load Frame: Equipped With the Lebow Cell and Hydraulic Wedge Grips, and Equipped With the Interface Cell and Inconel 718 Push Rods	28
10	Low-Strain Rate Compression Experimental Setup Specimen Placed Between Inconel 615 Platens and Pushrod and Platen Setup With Secondary LVDT Fixture	28
11	Torsion Specimen and Adaptors and Specimen-Adaptor Assembly, Instrumentation, and Grip Fixtures	29
12	Sample Data From a Servohydraulic Tension Experiment: Engineering Stress and Engineering Strain History Data and Engineering and True Stress Strain Curves	30
13	Plane Stress Notched Specimen Tension Experiment: Specimen Instrumented With a Bi-Axial Strain Gage Rosette, and Experimental Data	32
14	Maximum Principal and Minimum Principal Strains on the Surface of a Notched, Plane Stress Tension Specimen	32

15 Experimental Setup for Axisymmetric and Plane Strain Tensile Tests 33

16 Three-Dimensional Surface Features of Notched Axisymmetric Tension Specimen and Notched Plane Strain Tension Specimen 34

17 Tension Specimen Surface Strains Just Prior to Fracture: Maximum and Minimum Principal Strains of Notched Axisymmetric Specimen, Maximum and Minimum Principal Strains of Notched Plane Strain Specimen 34

18 Sample Data From a Tension Test on Notched Axisymmetric Specimen: Force and Strain History Data and Force vs. Displacement Data 35

19 Sample Data From a Servohydraulic Compression Experiment: Engineering Stress and Engineering Strain History Data and Engineering and True Stress Strain Curves 37

20 Sample Data From a Servohydraulic Torsion Experiment: Shear Stress and Shear Strain History Data and Shear and Effective Stress Strain Curves 39

21 Surface Strains on a Combined Loading Specimen: Maximum Principal Strain and Minimum Principal Strain 40

22 Experimental Data From a Combined Loading Experiment: Axial Force vs. Displacement, Torque vs. Rotation, and Strain vs. Time 42

23 Low-Rate Punch Test Experimental Setup 43

24 Low-Rate Punch Test Data: History Data and Load vs. Displacement Data 44

25 Instron 1321 Load Frame Equipped for Elevated-Temperature Testing and Low-Temperature Testing 45

26 Elevated- or Low-Temperature Experiments Instrumented With Thermocouples Tension, Compression, and Torsion 47

27 Compression SHB: Schematic Representation of a Typical Compression SHB Apparatus and Compression SHB Used in This Research 50

28 Sample Data From a Compression SHB Experiment on 2024-T351 Aluminum: Wave Data, Reduced History Data, and Stress Strain Data 51

29 Experimental Setup for Dynamic Punch Test on a Compression SHB Apparatus: Configured for Unrestricted Displacement and Configured for Restricted Displacement 53

30 High-Speed DIC Camera System 54

31 Experimental Results From an Unrestricted Punch Test: SHB Wave Data; Reduced History Data, Including Transmitted Force, Relative Velocity, and Relative Displacement; and One- and Two-Wave Force vs. Displacement Data 55

32 Sketch of a Direct-Tension SHB Apparatus 57

33 A Direct-Tension SHB Apparatus and a Stored-Torque Torsion SHB Apparatus 58

34 Specimen Attachment for a Tension SHB Experiment: Top View of a Specimen Instrumented With a Strain Gage, Side View of the Specimen, and Post-Test Photograph 59

35 Specimen Data From a Tension SHB Experiment on 2024-T351 Aluminum: Wave Data, Reduced History Data, and Stress-Strain Data 60

36 Sketch of a Stored-Torque SHB Apparatus 63

37 Spool-Shaped, Thin-Walled Tube Specimen for Torsion SHB Experiments: Drawing, Specimen Epoxied Between Incident and Transmitter Bars, and Post-Test Photograph 64

38 Specimen Data From a Torsion SHB Experiment on 2024-T351 Aluminum: Wave Data, Reduced History Data, and Stress Strain Data 65

39 Sketch Showing Two Cameras Are Necessary to Resolve 3D Features: One Camera and Two Cameras 67

40 Transformations Between Coordinate Systems for a Single Camera Model and a Stereo Rig Camera System 68

41 Stress vs. Strain Curves From Tension, Compression, and Torsion Tests Conducted Over a Wide Range of Strain Rates on a 12.7-mm-Thick 2024-T351 Aluminum Plate 70

42 Effective Stress vs. Strain Rate From Tension, Compression, and Torsion Tests on a 12.7-mm-Thick 2024-T351 Aluminum Plate: Effective Stress Values Extracted at Equivalent Strains of 0.075 and Effective Stress Values Extracted at Equivalent Strains of 0.15 72

43 Stress vs. Strain Curves From Tension, Compression, and Torsion Tests Conducted Over a Wide Range of Temperatures on 12.7-mm-Thick 2024-T351 Plate 73

44 Stress vs. Temperature From Tension, Compression, and Torsion Tests on a 12.7-mm-Thick 2024-T351 Plate: Effective Stress Values Extracted at Equivalent Strains of 0.075 and Effective Stress Values Extracted at Equivalent Strains of 0.15 74

45 True Stress vs. True Strain Curves From Tension and Compression Tests Conducted on Specimens Fabricated in Several Orientations Within the 12.7-mm-Thick 2024-T351 Plate 75

46 Comparison of Effective Stress vs. Equivalent Strain Curves From Tension, Compression, and Torsion Experiments 76

47 Tension/Compression Effective Stress Ratio and Torsion/Compression Effective Stress Ratio at Two Equivalent Strains 77

48 Stress vs. Strain Curves From Tension and Compression Tests Conducted at Two Strain Rates on a 6.35-mm-Thick 2024-T351 Aluminum Plate 78

49 Stress vs. Strain Curves From Tension and Compression Tests Conducted at Two Strain Rates on a 3.175-mm-Thick 2024-T3 Aluminum Sheet 79

50 Stress-Strain Comparison of the Three 2024 Aluminum Stocks: Tension and Compression 80

51 Load vs. Displacement Curves From the Plane Stress Tension Test Series 82

52 Load vs. Displacement Curves From the Axisymmetric Tension Test Series 82

53 Load vs. Displacement Curves From the Plane Strain Tension Test Series 83

54 Experimental Data From Tension-Torsion Tests With $\frac{\sigma_x}{\tau_{xy}} = 2.59$ Axial Load vs. Displacement and Torque vs. Rotation 85

55 Experimental Data From Tension-Torsion Tests With $\frac{\sigma_x}{\tau_{xy}} = 1.15$ Axial Load vs. Displacement and Torque vs. Rotation 86

56 Torque vs. Rotation Data From Torsion Tests $\frac{\sigma_x}{\tau_{xy}} = 0.0$ 87

57 Experimental Data From Compression-Torsion Tests With $\frac{\sigma_x}{\tau_{xy}} = -0.92$ Axial Load vs. Displacement and Torque vs. Rotation 88

58 The 3D DIC Data From Test No. M1-CL-LR1-P3-SR3-T1-N3: Initial Tracking Point Positions on *y*-Coordinate Contour and Tracking Point Positions Immediately Prior to Fracture on Maximum Principal Strain Contour 89

59 The 3D DIC Data From Test No. M1-CL-LR4-P3-SR3-T1-N5: Initial Tracking Point Positions on *y*-Coordinate Contour and Tracking Point Positions Immediately Prior to Fracture on Maximum Principal Strain Contour 90

60 Load vs. Displacement Curves From Static and Dynamic Punch Tests on Thin 2024-T351 Aluminum Disks Using a Punch With a 2.39-mm Nose Radius 91

61 Load vs. Displacement Curves From Static and Dynamic Punch Tests on Thin 2024-T351 Aluminum Disks Using a Punch With a 4.75-mm Nose Radius 92

62 Load vs. Displacement Curves From Static and Dynamic Punch Tests on Thin 2024-T351 Aluminum Disks Using a Blunt Punch 92

63 Failure Mode Evolution of a 2024-T351 Disk Under Load From a 2.39-mm-Radius Punch After 1.6-mm Relative Displacement, 2.4-mm Relative Displacement, and Unrestricted Displacement 93

64 Failure Mode Evolution of a 2024-T351 Disk Under Load From a 4.75-mm-Radius Punch After 2.4-mm Relative Displacement, 3.9-mm Relative Displacement, and Unrestricted Displacement 94

LIST OF TABLES

Table		Page
1	Reported Chemical Compositions of the Aluminum Plate and Sheet Products	3
2	Plastic Deformation Experimental Program for a 12.7-mm-Thick 2024-T351 Plate	11
3	Plastic Deformation Experimental Program for a 3.175-mm-Thick 2024-T3 Sheet and a 6.35-mm-Thick 2024-T351 Plate	13
4	Ductile Fracture Experimental Program: Tensile Tests Conducted on Plane Stress Test Specimens	15
5	Ductile Fracture Experimental Program: Tensile Tests Conducted on Axisymmetric Specimens	17
6	Ductile Fracture Experimental Program: Tensile Tests Conducted on Plane Strain Specimens	19
7	Ductile Fracture Experimental Program: Pure Shear (Torsion) and Combined Loading (Tension/Torsion, Compression/Torsion) Experiments	22
8	Ductile Fracture Experimental Program: Punch Tests	24
9	The DIC Extensometer Gage Lengths Used for All Tension Specimen Geometries	26

LIST OF ABBREVIATIONS AND ACRONYMS

2D	Two-dimensional
3D	Three-dimensional
DIC	Digital image correlation
DMML	Dynamic Mechanics of Materials Laboratory (OSU)
EDM	Electrical discharge machining
FCC	Face centered cubic
FPS	Frames per second
GWU	The George Washington University
IR	Infrared
LS-DYNA®	Livermore Software Explicit Finite Element Code
LVDT	Linear variable differential transformer
NASA	National Aeronautics and Space Administration
NASA-GRC	National Aeronautics and Space Administration Glenn Research Center
NCAC	National Crash Analysis Center
OSU	The Ohio State University
RVDT	Rotary variable differential transformer
SHB	Split Hopkinson bar
SSD	Sum of the squared differences

EXECUTIVE SUMMARY

A team consisting of The Ohio State University (OSU), The George Washington University (GWU), the National Aeronautics and Space Administration Glenn Research Center (NASA-GRC), and the Federal Aviation Administration (FAA) Aircraft Catastrophic Failure Prevention Research Program collaborated to develop a new material model in Livermore Software Explicit Finite Element Code (LS-DYNA®) for 2024 aluminum. This model was based on tabulated data from several material tests performed by OSU. This research was conducted under an FAA grant and sponsored by the Aircraft Catastrophic Failure Prevention Program. The research was directed toward improving the numerical modeling of turbine engine blade-out containment tests required for certification of aircraft engines.

This is part 3 of a three-part report, organized as follows:

- Part 1—FAA, NASA, and Industry Collaboration Background
- Part 2—Development of a Tabulated Thermo-Viscoplastic Material Model With Regularized Failure for Dynamic Ductile Prediction of Structures Under Impact Loading
- Part 3—Plastic Deformation and Ductile Fracture of 2024 Aluminum Under Various Loading Conditions

This report documents the material characterization tests performed at OSU to support the development of the new material model and the technical details of this effort.

The plastic deformation and ductile fracture behavior of 12.7-, 6.35-, and 3.175-mm-thick 2024 aluminum plates and sheets were investigated. Tension, compression, and shear experiments were conducted at strain rates ranging from 10^{-4} s^{-1} to 11,000 s^{-1} and temperatures ranging from -50° to 450°C. Results showed the material flow stress was insensitive to strain rate in tension, compression, and shear between 10^{-4} s^{-1} and 5000 s^{-1}. In compression, increased stresses were observed at strain rates between 5000 s^{-1} and 11,000 s^{-1}. Flow stress decreased monotonically with increasing temperature. The strain-hardening behavior of the material also changed dramatically between 150° and 300°C. The 12.7-mm-thick 2024-T351 plate was anisotropic with respect to plastic deformation. Tensile and compressive stresses determined from specimens oriented ±45° to the plate's rolled direction were significantly lower than those determined from specimens oriented in the rolled and transverse directions.

The dependence of fracture on the state of stress was studied through mechanical experiments on specimens with various geometries subjected to multiple load conditions. Tension tests of plane stress (thin), axisymmetric, and plane strain (thick) specimens were conducted for this purpose. Combined tension—torsion, pure shear, and compression—torsion, and punch tests were also conducted. Tension test results showed peak axial load increased and fracture displacement decreased with decreasing stress triaxiality. Load versus displacement and torque versus rotation curves are given for axial-torsional tests. Load versus displacement curves were given for static and dynamic punch tests. The specimen failure mode evolution of specimens subjected to

dynamic punch loading is also discussed. These data were used in a coupled experimental-numerical technique to develop a fracture locus for 2024-T351 aluminum in part 2 of this three-part report.

1. INTRODUCTION.

The Federal Aviation Administration (FAA) Aircraft Catastrophic Failure Prevention Program is interested in the behavior of 2024-T351 aluminum because it is a common component in aircraft structures. As shown in figure 1, uncontained engine debris can pose a significant threat to the safety of passengers and crew onboard commercial transport aircraft; figure 1(a) shows damage to a DC-9 aircraft after uncontained engine debris caused a fire [1]; and figure 1(b) shows the damage to an aircraft from an uncontained turbine disk [2]. Recovered debris from a failed fan disk is shown in figure 1(c) [2]. A full-scale, uncontained fan disk experiment is shown in figure 1(d) [1].

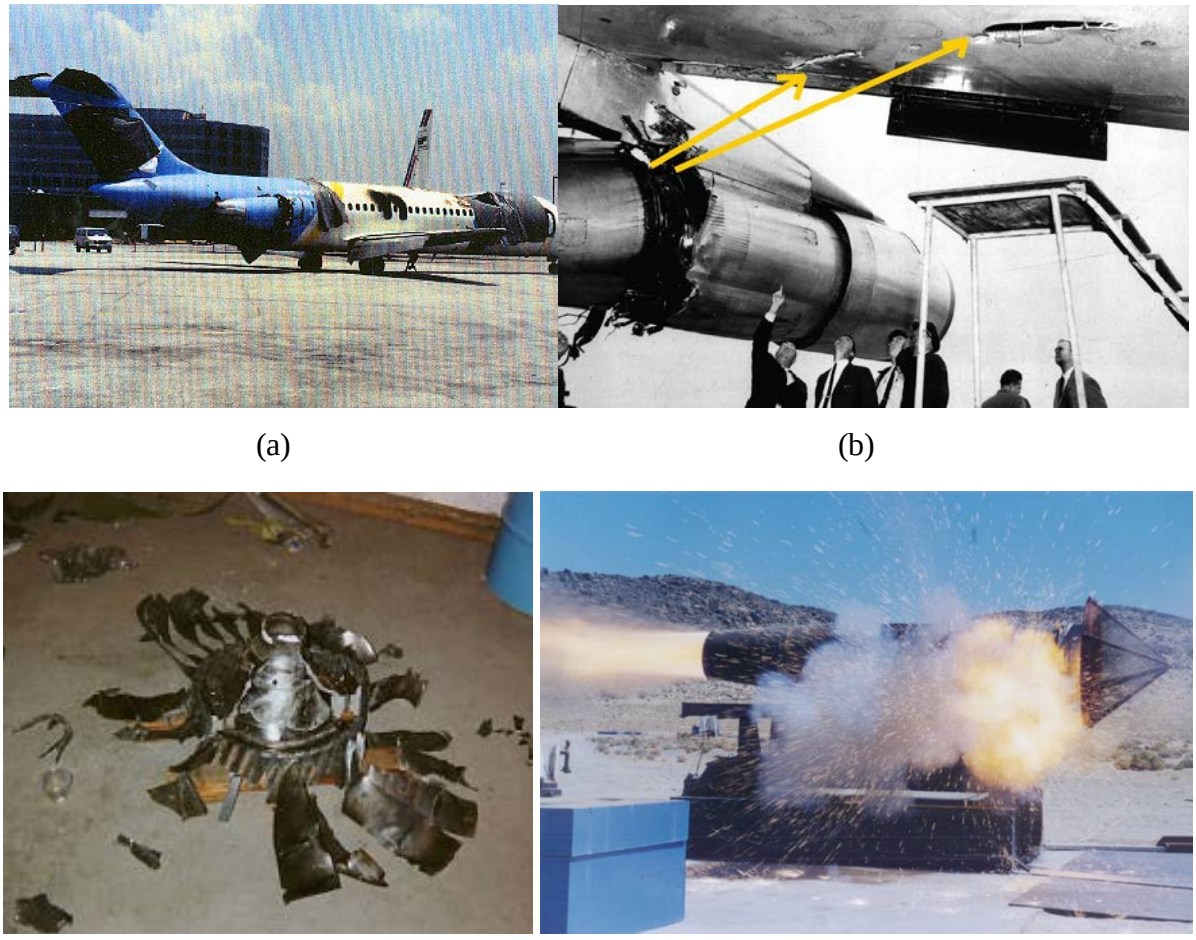

(a) (b)

(c) (d)

Figure 1. The Uncontained Engine Debris Threat: (a) Damage to a DC-9 Aircraft From Uncontained Engine Debris and a Subsequent Fire [1], (b) Damage to an Aircraft From an Uncontained Turbine Blade [2], (c) Recovered Debris From a Fan Disk Failure Event [2], and (d) an Uncontained Fan Blade Experiment [1]

Title 14 Code of Federal Regulations 25.903(d)(1) addresses the safety hazards related to an engine rotor failure and states that design precautions must be implemented to minimize and

mitigate these hazards [2]. Frankenberger [2] shows that these precautions can be implemented in the following ways:

- Minimizing the frequency of uncontained disk events
- Decreasing the hazard to safe flight by minimizing the quantity and energy of the fragments as well as taking precautions that cause fragment trajectories that are less harmful to the aircraft structure
- Mitigating the hazard to safe flight through structure designs that can safely hold uncontained disk debris

Each aircraft engine in operation must be certified for use because of the significant threat this problem poses. The certification process involves full-scale experiments on real aircraft engines, such as the experiment shown in figure 1(d). These experiments are difficult to conduct and extremely expensive. This, coupled with the maturity of the field of computational mechanics, provides motivation to supplement experimental data with numerical simulations.

The results of uncontained engine debris failures can be catastrophic in loss of human life. Therefore, the supplemental simulations used to design hazard mitigation must be accurate. The scenario is one of impact and penetration as engine debris fragments are ejected at high velocities tangent to the disk. The engine debris threat, shown in figure 1(c), is diverse in geometry and impact velocity. Accurate simulations of these events must be able to capture the failure modes of the impacted targets. These failure modes include petaling, plugging, ductile hole growth, brittle fracture, and spall fragmentation. To capture these phenomena, material models that accurately describe the plastic deformation, as well as the damage accumulation and fracture behavior of the target, are necessary. Therefore, the availability of experimental data at the strain rates, temperatures, and stress states present in the application is critical.

1.1 PURPOSE.

The research objective was to devise and execute an experimental program to develop constitutive and ductile fracture models for 2024 aluminum. The vast majority of the experiments were conducted on specimens made from a single 12.7-mm-thick 2024-T351 plate; however, limited tension and compression tests were also conducted on both 6.35-mm-thick 2024-T351 aluminum plate and a 3.175-mm-thick 2024-T3 sheet since these materials were used as targets in a separate ballistic impact study. The 12.7- and 6.35-mm-thick plates were produced by Kaiser Aluminum, and the 3.175-mm-thick sheet was produced by AMAG rolling GmbH. The reported chemical compositions for the three aluminum materials are shown in table 1. Certified test reports for these materials are shown in appendix A. The data compiled from this experimental program is the most comprehensive collection of mechanical property data from a single stock of 2024 aluminum. Material models developed from these data under a separate grant to The George Washington University (GWU) will be used in numerical simulations supporting the FAA Uncontained Engine Debris Mitigation Program.

Table 1. Reported Chemical Compositions of the Aluminum Plate and Sheet Products

Stock		Chemistry										
Alloy/Treatment	Thickness (mm)	Si	Fe	Cu	Mn	Mg	Cr	Zn	Ti	V	Zr	Ni
2024-T351	12.700	0.08	0.22	4.47	0.59	1.37	0.01	0.18	0.02	0.01	0.01	0.00
2024-T351	6.350	0.10	0.24	4.43	0.59	1.38	0.03	0.12	0.02	0.01	0.00	0.00
2024-T3	3.175	0.06	0.13	4.60	0.64	1.50	<0.01	0.09	0.03	0.00	0.00	<0.01

The first phase of the experimental program was devised to determine the strain rate and temperature dependence on the plastic deformation behavior of the material. Tension, compression, and shear (torsion) experiments at strain rates ranging from 1.0×10^{-4} s^{-1} to 1.0×10^{4} s^{-1} and temperatures ranging from -50° to 450°C were conducted. Directional strength characteristics within the plate were also studied with tension and compression tests on specimens oriented in several different directions relative to the plate's rolling axis.

The second phase of the experimental program studied the ductile fracture behavior of the material. The program was designed specifically to study the effect of the stress state on the equivalent plastic fracture strain of the material. The goal was to generate a fracture locus for 12.7-mm-thick 2024-T351 aluminum from several different mechanical experiments. These experiments included tension tests on specimens with several different geometries, pure shear tests (torsion), and combined loading (tension-torsion or compression-torsion) tests. Three-dimensional (3D) digital image correlation (DIC) [3] was used to measure the full-field displacements and to calculate strains in many of these experiments. This measurement technique has a substantial advantage over traditional measurement techniques, such as the use of strain gages and extensometers, since deformation gradients and strains in localizations (e.g., necking and shear bands) can be resolved. These full-field surface strains can be directly compared to results from numerical simulations, making detailed critiques of the constitutive and fracture models more practical. For experiments with complex specimen geometries, a coupled experimental-numerical technique was used to determine the state of stress at the fracture initiation site. The technique consists of comparing results from a parallel numerical simulation to the experimental data. Simulation results were used to provide equivalent plastic fracture strain and stress state histories at the fracture initiation site. The details of the numerical simulations and the methods used to compare their results to the experimental data are found under separate cover (Development of a New Metal Material Model in LS-DYNA, Part 2: Development of a Tabulated Termo-Viscoplastic Material Model With Regularized Failure for Dynamic Ductile Failure Prediction of Structures Under Impact Loading [4]).

Punch experiments were also conducted in the ductile fracture experimental program. Static and dynamic punch tests were conducted using a servohydraulic load frame or a compression Kolsky or split Hopkinson bar (SHB) apparatus. Punches with varying geometry (nose radius) were used to alter the stress state in the specimen. In certain dynamic tests, a stop ring was used to limit the punch displacement relative to the specimen to study the evolution of the specimen impact failure mode.

1.2 BACKGROUND.

As the field of computational mechanics has matured, many numerical codes have been developed that can accurately predict the mechanical response of complex physical phenomena. One such code is Livermore Software Explicit Finite Element Code (LS-DYNA) [5], a finite element program that is commonly used to simulate dynamic nonlinear structural deformation. LS-DYNA has allowed analysts and researchers to gain valuable insight into their applications. Simulation results, however, are heavily dependent on the material models used. These material models are usually application-specific. Simple, static applications that incur small strains can be modeled adequately with a simple linear elasticity model. If the application is complex and includes plastic deformation at high strain rates and elevated temperatures as well as fracture, more complex material models must be used to have any confidence in the numerical result.

The Johnson-Cook plasticity and fracture models [6 and 7] are phenomenological material models commonly used to simulate impact and penetration. The constitutive model defines the effective material flow stress as:

$$\bar{\sigma} = \left[A + B(\bar{\varepsilon}^p)^n \right] \left[1 + C \ln\left(\frac{\dot{\bar{\varepsilon}}}{\dot{\varepsilon}_0} \right) \right] \left[1 - \left(\frac{T - T_r}{T_m - T_r} \right)^m \right] \tag{1}$$

where, $\bar{\varepsilon}^p$ is the equivalent plastic strain, $\dot{\varepsilon}_0$ is the reference strain rate (typically 1.0 s^{-1}), T is the material temperature, T_r is the reference temperature (typically room temperature), T_m is the melt temperature, and A, B, n, C, and m are model parameters. These parameters are typically determined from tension, compression, or shear mechanical experiments over a wide range of strain rates and temperatures.

The fracture model defines a damage parameter for each element in a given simulation. This parameter ranges from zero for pristine material to unity for fractured material. The parameter is defined as:

$$D = \sum \frac{\Delta \bar{\varepsilon}^p}{\bar{\varepsilon}_f^p} \tag{2}$$

or the sum of the ratio of equivalent plastic strain increment ($\Delta \bar{\varepsilon}^p$) to the equivalent fracture strain ($\bar{\varepsilon}_f^p$) for each numerical integration cycle. The Johnson-Cook model defines the equivalent plastic fracture strain as:

$$\bar{\varepsilon}_f^p = \left[D_1 + D_2 e^{-D_3 \sigma^*} \right] \left[1 + D_4 \ln\left(\frac{\dot{\bar{\varepsilon}}}{\dot{\varepsilon}_0} \right) \right] \left[1 + D_5 \left(\frac{T - T_r}{T_m - T_r} \right) \right] \tag{3}$$

where σ^* is a stress state parameter known as the triaxiality, and D_1, D_2, D_3, D_4, and D_5 are model parameters. These parameters are typically determined from mechanical experiments on notched and smooth axisymmetric specimens at several strain rates and temperatures.

The goal of this project was to develop a new, more versatile, material model for LS-DYNA that captures the physical behavior for which the Johnson-Cook model was designed. These phenomena include strain rate and temperature-sensitive plastic deformation (equation 1) and stress state, strain rate, and thermal sensitive fracture (equation 3). The new model is tabulated and contains actual experimental data. The new model is not limited by the interactions of the bracketed expressions in equation 1. For example, most materials have very different strain-hardening behavior at room and elevated temperatures. Strain hardening in the Johnson-Cook model is always defined by the *A*, *B*, and *n* parameters. The model simply scales the curve as the temperature is increased. In this case, the flow stress is accurate only at one value of equivalent plastic strain. The tabulated model can discriminate between strain-hardening effects at two different temperatures because it is comprised of actual experimental data.

However, the drawback of a tabulated model is that it requires a large database of experimental data. This report details the results from the experimental program devised to populate this model.

1.2.1 Plastic Deformation of 2024 Aluminum.

Several researchers have studied the strain rate sensitivity of 2024 aluminum, including Li et al. [8], Hodowany et al. [9], Johnson et al. [10], and Lesuer [11]. They studied the material response under compression, torsion, and tension at room temperature. All except Lesuer reported negligible to minor strain rate sensitivity at strain rates ranging from 10^{-3} s^{-1} to 4.0×10^{3} s^{-1}. Lesuer, on the other hand, compiled Johnson's low-rate and dynamic torsion data with his own dynamic compression and tension data. The resulting data set showed a 12.7% increase in stress from 10^{-3} s^{-1} to 8.0×10^{3} s^{-1}.

Elevated temperature data from tensile experiments on 2024-T3 aluminum presented by Zhao and Lampman [12] demonstrate that as temperature increases, the ductility increases and the strength decreases. These phenomena arise because of dynamic recovery and recrystallization, which occur at high temperatures and reduce the room temperature restrictions on grain mobility, resulting in deformation at significantly lower stresses.

Anisotropic strength behavior in 2024-T3 aluminum has been reported by many authors. Barlat et al. [13] reported strongly anisotropic behavior in a 0.30-mm-thick 2024-T3 sheet. Tension specimens were fabricated in seven different directions relative to the rolled direction of the sheet (0°, 15°, 30°, 45°, 60°, 75°, and 90°). These data show that the strength of the sheet decreased by as much as 15% at angles larger than 45° to the rolled direction. Gilmour et al. published two papers on the anisotropic plastic behavior of 1.27-mm-thick 2024-T3 aluminum [14 and 15]. In the first paper [14], experimental data were presented from tensile tests on specimens cut from the sheet in seven orientations, equivalent to those used by Barlat et al. The data showed similar strength reductions in the 45° and 90° orientations to those reported by Barlat et al. The second paper [15] focused on the in-plane shear behavior of a 1.27-mm-thick 2024-T3 aluminum sheet. Shear stress versus shear strain data from samples in the seven orientations and tested in a custom-designed shear fixture were presented. The data demonstrated that the in-plane shear strength was weaker in the 0° orientation than in the 45°

direction. Gilmour et al. reported yield stresses in shear that were roughly half the magnitude of the yield stress in uniaxial tension.

1.2.2 Ductile Fracture of 2024 Aluminum.

Most damage evolution and fracture models implemented for ductile metals are based on theories of microscopic void nucleation, growth, and eventual coalescence. Rice and Tracey [16] developed a model to analyze the growth of a single spherical void in a rigid plastic body. The authors found that the dilatational amplification factor of the void increased exponentially with the far-field mean stress, or $\sigma_m = \frac{1}{3}\sigma_{kk}$. Thus, volume increase of the void was enabled by the presence of large far-field mean stresses. Hancock and Mackenzie [17] made the assumption that the equivalent plastic fracture strain of a material was inversely proportional to the void volume growth rate. Therefore, the equivalent plastic fracture strain must decrease exponentially with decreasing stress triaxiality or:

$$\sigma^* = \frac{-\sigma_m}{\bar{\sigma}} = \frac{p}{\bar{\sigma}} \tag{4}$$

where p is the pressure, and the effective stress is defined as:

$$\bar{\sigma} = \left(\frac{3}{2} S_{ij} S_{ij}\right)^{\frac{1}{2}} \tag{5}$$

where, $S_{ij} = \sigma_{ij} - \sigma_m \delta_{ij}$ is the deviatoric stress tensor. Hancock and Mackenzie [17] and Mackenzie, Hancock, and Brown [18] described an experimental technique in which the dependence of equivalent plastic fracture strain on stress triaxiality was determined using tensile tests on notched axisymmetric specimens and Bridgeman's analysis of the stress state at the necking localization of an axisymmetric specimen [19].

Many authors have used the findings of McClintock, Rice, Tracey, Hancock, and Mackenzie. For example, the widely used damage evolution and fracture model proposed by Johnson and Cook [7] defines the equivalent plastic fracture strain as an exponential function of the stress triaxiality (see equation 3). The classic method to determine this relationship was to conduct a series of tensile tests on axisymmetric notched bars with varying radii. Bau and Wierzbicki [20 and 21], however, have used various specimen geometries and loading methods to explore a wider range of stress states.

Using results from Bau and Wierzbicki [20 and 21], Barsoum and Faleskog [22] concluded that the stress triaxiality parameter alone was insufficient to describe material fracture behavior over the entire range of potential stress states. Therefore, they studied the effect of the Lode parameter, another indicator of stress state, defined as:

$$\mu = -\frac{2\sigma_2 - \sigma_1 - \sigma_3}{\sigma_1 - \sigma_3} \tag{6}$$

where $\sigma_1 \geq \sigma_2 \geq \sigma_3$ are the principal stresses. Carney et al. [23] recently proposed a new parameter, product triaxiality, based on the third stress invariant, which is expressed as:

$$\sigma_p^* = \frac{\sigma_1 \sigma_2 \sigma_3}{\overline{\sigma}_3} = \frac{I_3}{\overline{\sigma}_3} \tag{7}$$

This work typically seeks a relationship between the equivalent plastic fracture strain and the stress state, or:

$$\overline{\varepsilon}_f^p = f\left(\sigma^*\right) \tag{8}$$

in the case of stress triaxiality dependence only. Using the conclusions of Barsoum and Faleskog [22] and Carney et al. [23], the definition of the relationship can be extended to:

$$\overline{\varepsilon}_f^p = f\left(\sigma^*, \mu\right) \tag{9}$$

in the case of Lode parameter dependence or, alternatively:

$$\overline{\varepsilon}_f^p = f\left(\sigma^*, \sigma_p^*\right) \tag{10}$$

in the case of product triaxiality dependence.

1.2.3 Punch Experiments.

The punch experiment is useful for studying impact events because the experiment is similar to the application. In a dynamic punch test, the specimen deforms plastically at high strain rates and is subject to stress states that are similar to those present in an impacted target. Data from these experiments, such as force versus displacement curves, can be used to calibrate continuum damage evolution and fracture models. These data can also be used as an eventual means of validation for newly developed constitutive and fracture models.

Lee et al. [24] and Grytten et al. [25] used servohydraulic actuators to perform low strain rate punch experiments for the purposes of studying ductile fracture. Walters [26] studied the fracture of advanced high-strength steels at intermediate strain rates (up to 500 s^{-1}) using a drop weight test rig. Grytten et al. [27] also studied dynamic perforation of aluminum plates using a tethered, instrumented, pneumatically-driven projectile.

The SHB apparatus was also used for dynamic punch experiments by several authors [28, 29, and 30]. Zurek [28] used a custom-designed compression SHB fixture to conduct dynamic punch tests on pearlitic 4340 steel. The focus of the work was to examine adiabatic shear band

instabilities in the material. Roessig and Mason [29] used a modified compression SHB apparatus to study adiabatic shear bands in plate specimens fabricated from 1018 steel, 6061-T6 aluminum, and Ti-6Al-4V. The authors used an apparatus that consisted of only the striker and incident bars that typically comprise a SHB apparatus. A clamped plate specimen was contacted by one end of the incident bar. A two-wave analysis was used to construct load versus displacement records for the experiments. The authors also conducted parallel numerical simulations of the experiments in a separate study [31]. Daboussi and Nemes [30] used the technique to study dynamic ductile fracture. The authors used dynamic punch experiments on a compression SHB apparatus to generate Johnson-Cook constitutive and fracture model parameters for 6061-T6 aluminum, Ti-6Al-4V, and Nitronic 33. Only blunt punch geometries were used in the SHB experimental work described above, so the stress states achievable in the specimens were limited.

Certain experimental techniques can be used to control the displacement of the punch into the specimen, allowing impact failure mode evolution to be studied. On impact, ductile metals typically fail in plugging, petaling, ductile hole growth, or some combination of these modes. Meyers et al. [32] used a stop ring to limit the amount of shear strain imparted to a hat-shaped SHB specimen to study shear bands in preshocked copper. This technique can be implemented with the dynamic punch tests and recovered specimens can be examined at different stages in the failure process.

2. METHODOLOGY AND EXPERIMENTAL PROGRAM.

The experimental program devised to study both the plastic deformation and ductile fracture behaviors of 2024 aluminum is presented in this section. The plastic deformation experimental program consists of tension, compression, and torsion (pure shear) tests. The ductile fracture experimental program consists of several test series, including tensile tests on plane stress, axisymmetric and plane strain specimens, combined loading (axial-torsional) tests, and punch tests.

2.1 PLASTIC DEFORMATION OF 2024 ALUMINUM.

The plastic deformation of 12.7- and 6.35-mm-thick 2024-T351 aluminum plates and a 3.175-mm-thick 2024-T3 sheet was investigated. The goals were to determine (1) if the effective stress–equivalent strain response of the material varies in tension, compression, and shear loading, (2) the strain rate sensitivity of the stress-strain behavior, (3) the temperature sensitivity of stress-strain behavior, (4) the anisotropic strength behavior present in the plate due to crystallographic texture from processing, and (5) the difference in the tension and compression response between the three material stocks.

Tension, compression, and torsion specimens were fabricated from the three 2024 aluminum products (see table 1). Tension specimens are flat dogbone specimens (see figure 2). Compression specimens are cylinders with a length-to-diameter ratio of one. Torsion specimens are spools with a thin-walled tube gage section, see figure 3. All specimen geometries were consistent throughout the plastic deformation test program to eliminate geometric effects skewing the overall interpretation of the data.

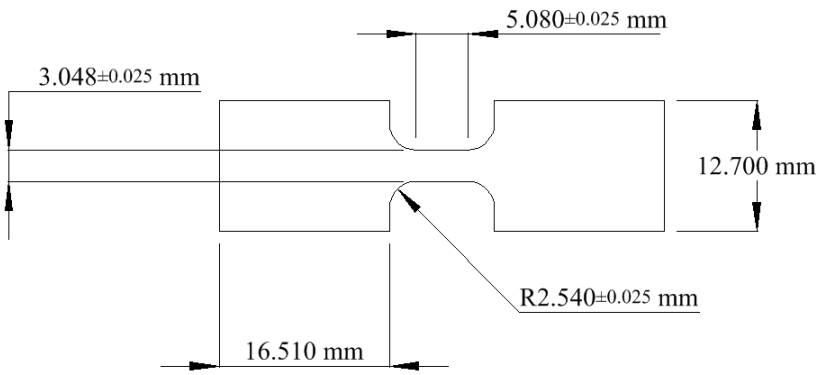

(a)

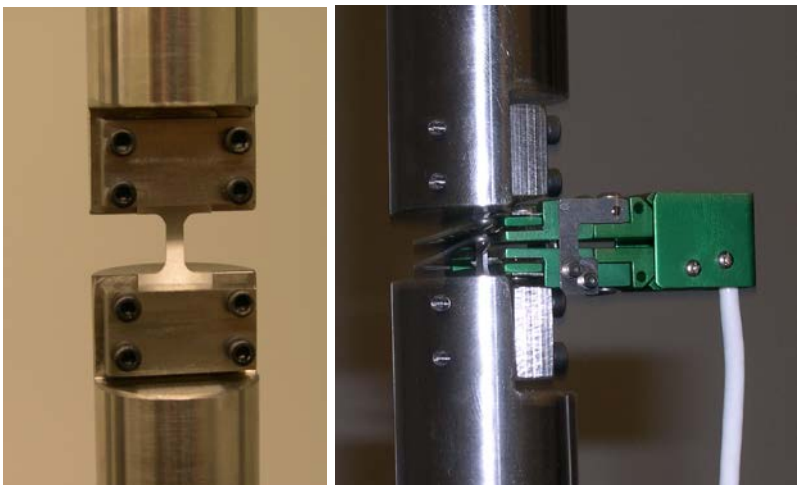

(b) (c)

Figure 2. (a) Tension Test Specimen Dimensions (0.762-mm-Thick), (b) Specimen Clamped in Inconel 718 Attachment Fixture, and (c) Epsilon 3442 Extensometer Attached to Specimen

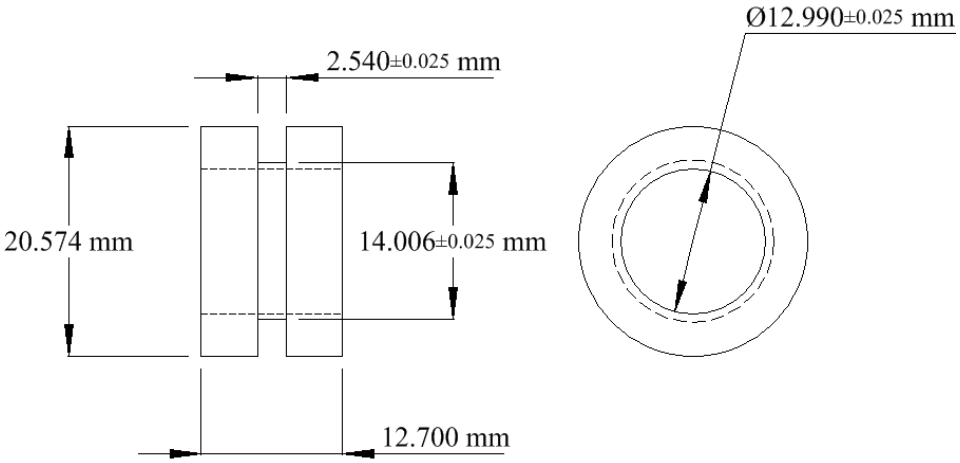

Figure 3. Spool-Shaped Torsion Specimen

The plastic deformation experimental program for 12.7-mm-thick 2024-T351 aluminum is shown in table 2. The program was designed to determine the plastic deformation behavior of the material at various strain rates and temperatures as well as in several orientations. Tests at and below equivalent strain rates of 1.0 s^{-1} were conducted using the axial (for tension and compression tests) or rotational (for torsion tests) degree of freedom of an Instron biaxial servohydraulic load frame, while a direct-tension [33], compression [34], and a stored-torque torsion SHB [35] were used to conduct experiments above 1.0 s^{-1}. Figure 4 illustrates how the various test specimens are fabricated from the 12.70-mm-thick plate.

Table 2. Plastic Deformation Experimental Program for a 12.7-mm-Thick 2024-T351 Plate

Test No.	Test Mode	Apparatus	Equivalent Strain Rate (1/s)	Temperature (°C)	Specimen Orientation
1	Tension	Servohydraulic Load Frame	1.00E-04	RT	0°
2			1.00E-02		
3			1.00E-00		
4		Tension SHB	5.00E-02		
5			1.80E-03		
6		Servohydraulic Load Frame	1.00E-00	-50	
7				150	
8				300	
9				450	
10				RT	45°
11					90°
12					-45°
13	Compression	Servohydraulic Load Frame	1.00E-04	RT	0°
14			1.00E-02		
15			1.00E-00		
16		Compression SHB	1.50E-03		
17			5.00E-03		
18			8.00E-03		
19			1.00E-04		
20			1.10E-04		
21		Servohydraulic Load Frame	1.00E-00	-50	
22				150	
23				300	
24				450	
25				RT	45°
26					90°
27					-45°
28					Through Thickness
29	Torsion	Servohydraulic Load Frame	1.00E-04	RT	Through Thickness
30			1.00E-02		
31			1.00E-00		
32		Torsion SHB	5.00E-02		
33			2.80E-03		
34		Servohydraulic Load Frame	1.00E-00	-50	
35				150	
36				300	
37				450	

RT = room temperature

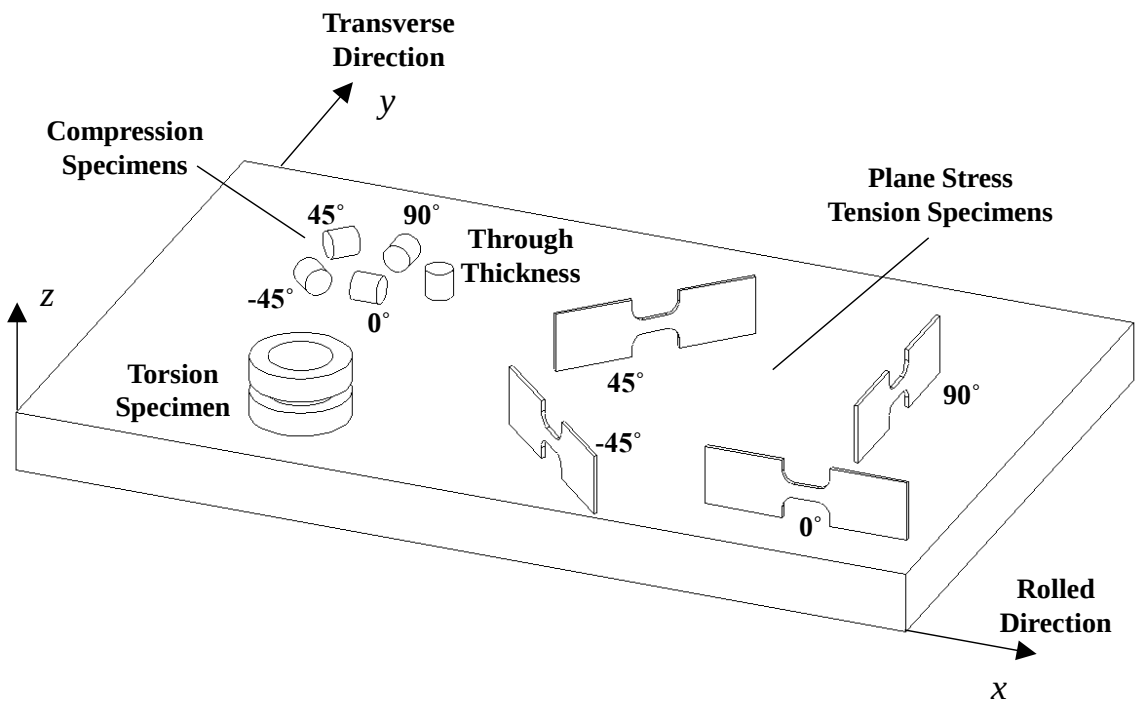

Figure 4. Tension, Compression, and Torsion Specimens Fabricated From 12.7-mm-Thick 2024-T351 Aluminum Plate

Tension tests were conducted on specimens fabricated in the rolled direction (0°) of the 12.7-mm-thick plate at room temperature and nominal strain rates of 1.0×10^{-4} s^{-1}, 1.0×10^{-2} s^{-1}, 1.0 s^{-1}, 5.0×10^{2} s^{-1}, and 1.8×10^{3} s^{-1}. Tension experiments were also conducted on specimens aligned in the plate-rolled direction at a strain rate of 1.0 s^{-1} at -50°C, 150°C, 300°C, and 450°C. Tension tests were conducted on specimens aligned in three additional plate directions (±45° and 90°) at room temperature and a nominal strain rate of 1.0 s^{-1}.

Compression tests were conducted on specimens fabricated in the rolled direction (0°) of the 12.7-mm-thick plate at room temperature and nominal strain rates of 1.0×10^{-4} s^{-1}, 1.0×10^{-2} s^{-1}, 1.0 s^{-1}, 1.5×10^{3} s^{-1}, and 5.0×10^{3} s^{-1}. Compression experiments were also conducted on specimens aligned in the rolled direction at a strain rate of 1.0 s^{-1} at -50°C, 150°C, 300°C, and 450°C. Compression tests were conducted on specimens aligned in four additional directions (±45°, 90°, and through-the-plate thickness).

Torsion tests were conducted at room temperature and equivalent strain rates of 1.0×10^{-4} s^{-1}, 1.0×10^{-2} s^{-1}, 1.0 s^{-1}, 5.0×10^{2} s^{-1}, and 2.8×10^{3} s^{-1}. Torsion experiments were also conducted at a strain rate of 1.0 s^{-1} at -50°C, 150°C, 300°C, and 450°C. All torsion specimens were fabricated so the axis of symmetry was parallel to the thickness direction of the 12.7-mm-thick plate (see figure 4). Each test listed in table 2 was conducted at least three times to assess the repeatability of the measurements.

A subset of the tests used to characterize the 12.7-mm-thick plate was conducted on specimens fabricated from a 6.35-mm-thick plate and a 3.175-mm-thick sheet (see table 3). Figure 5 shows how tension and compression specimens were machined from both the 6.35-mm-thick plate and the 3.175-mm-thick sheet. Tension and compression specimens were fabricated so they were aligned with the rolled direction of the plate or sheet. Note that the tension specimen width direction was aligned with the transverse direction of the plate/sheet while the width direction of the 12.7-mm-thick specimens was oriented in the plate's thickness direction. Tension and compression tests were conducted at two strain rates: tension tests at 1.0 s^{-1} and 5.0×10^2 s^{-1} and compression tests at 1.0 s^{-1} and 1.5×10^3 s^{-1}.

Table 3. Plastic Deformation Experimental Program for a 3.175-mm-Thick 2024-T3 Sheet and a 6.35-mm-Thick 2024-T351 Plate

Test No.	Test Mode	Apparatus	Equivalent Strain Rate (1/s)	Temperature (°C)	Specimen Orientation
1	Tension	Servohydraulic Load Frame	1.00E+00	RT	0°
2		Tension SHB	5.00E+02		
3	Compression	Servohydraulic Load Frame	1.00E+00	RT	0°
4		Compression SHB	1.50E+03		

All specimens were fabricated using traditional machining techniques to a surface finish of 32 or better. Specimen edges were left unbroken. These specimen fabrication guidelines were based on the results of a separate test series designed to determine the effect of specimen fabrication technique on the results of mechanical tests on small tension speciments, typically used for SHB tests. The details of this test series are presented in appendix B.

The naming convention for all tests is outlined in appendix C.

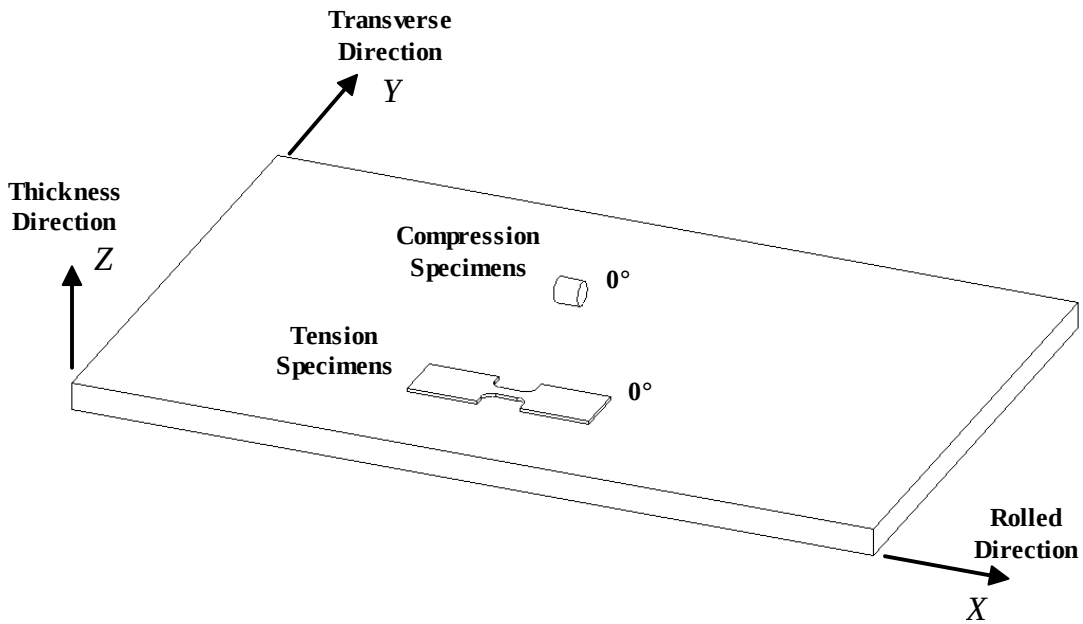

Figure 5. Tension and Compression Specimens Fabricated From a 6.35-mm-Thick 2024-T351 Plate and a 3.175-mm-Thick 2024-T3 Sheet

2.2. DUCTILE FRACTURE OF 2024-T351 ALUMINUM.

The ductile fracture behavior of a 12.7-mm-thick 2024-T351 aluminum plate was investigated. The goal of this work was to construct a new fracture locus in stress space using both experimental data and parallel numerical simulations of specimens subjected to a wide range of stress states. The dependence of equivalent plastic fracture strain on stress triaxiality and other stress state parameters, such as the Lode parameter and product triaxiality, was also explored.

The ductile fracture behavior was investigated using three separate tensile test series and a combined loading (axial-torsional) test series. The first tensile test series was conducted on thin, flat, smooth, and notched specimens (plane stress). These experiments are summarized in table 4. Specimen dimensions are provided in the table along with estimates for stress triaxiality (σ^*), Lode parameter (μ), and product triaxiality (σ_p^*). When loaded, the thin, flat tensile specimens are in a state of plane stress ($\sigma_3 = 0.0$). Consequently, the product triaxiality term is zero for all thin specimens.

Table 4. Ductile Fracture Experimental Program: Tensile Tests Conducted on Plane Stress Test Specimens

Specimen #	Specimen Dimensions	σ^* Triaxiality	μ Lode Parameter	σ_p^* Product Triaxiality
1 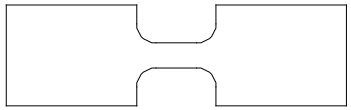	Thin smooth specimen (plane stress) Gage Length: 5.080 mm Gage Width: 3.048 mm Thickness: 0.762 mm	-0.333	1.000	0.000
2 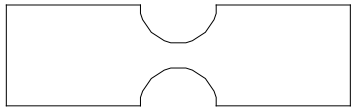	Thin notched specimen (plane stress) Notch Radius: 4.763 mm Minimum Notch Width: 3.048 mm Thickness: 0.762 mm	-0.431	0.660	0.000
3 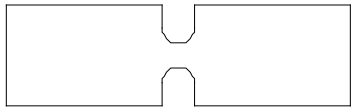	Thin notched specimen (plane stress) Notch Radius: 1.984 mm Minimum Notch Width: 3.048 mm Thickness: 0.762 mm	-0.490	0.415	0.000
4 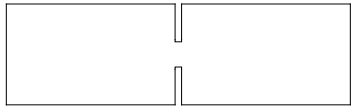	Thin notched specimen (plane stress) Notch Radius: 0.396 mm Minimum Notch Width: 3.048 mm Thickness: 0.762 mm	-0.577	0.000	0.000

The second tensile test series was conducted on axisymmetric, smooth, and notched specimens. The specimens are shown with dimensions and estimated stress state parameter values in table 5. This test series is the method typically used for calibrating ductile fracture models as presented by Hancock and Mackenzie [17]. Several researchers have used experiments like these to calibrate ductile fracture models [7, 18, and 20]. When loaded in tension, these specimens undergo a stress state in which two principal stresses are equal ($\sigma_2 = \sigma_3$). This means that the Lode parameter value is 1.0 for all specimens listed in table 5.

Table 5. Ductile Fracture Experimental Program: Tensile Tests Conducted on Axisymmetric Specimens

Specimen #	Specimen Dimensions	σ^* Triaxiality	μ Lode Parameter	σ_p^* Product Triaxiality
5 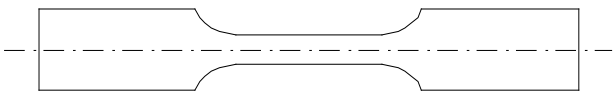	Axisymmetric smooth specimen Gage Length: 24.130 mm Gage Diameter: 4.763 mm	-0.333	1.000	0.000
6 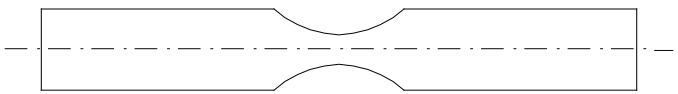	Axisymmetric notched specimen Gage Length: 14.503 mm Minimum Gage Diameter: 4.763 mm	-0.524	1.000	0.048
7 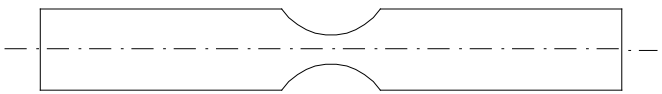	Axisymmetric notched specimen Gage Length: 9.144 mm Minimum Gage Diameter: 4.763 mm	-0.607	1.000	0.097
8 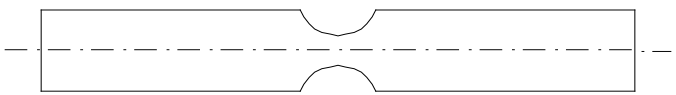	Axisymmetric notched specimen Gage Length: 6.096 mm Minimum Gage Diameter: 4.763 mm	-0.675	1.000	0.164
9 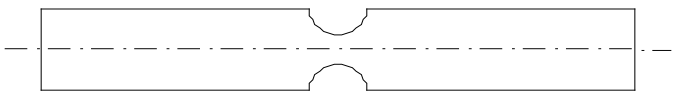	Axisymmetric notched specimen Gage Length: 4.470 mm Minimum Gage Diameter: 4.763 mm	-0.763	1.000	0.265
10 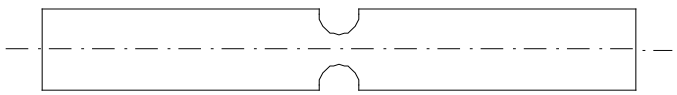	Axisymmetric notched specimen Gage Length: 3.048 mm Minimum Gage Diameter: 4.763 mm	-0.855	1.000	0.438

Experiments on thick, smooth, and notched specimens comprised the third tensile test series. Specimen geometries and anticipated stress state parameter values are shown in table 6. These specimens are sufficiently thick (25.4 mm) to approach a state of plane strain in the center of the specimen.

The specimens listed in tables 4, 5, and 6 were designed to have similar stress triaxiality parameters, yet different Lode and product triaxiality parameters. For example, the sharp notch plane stress specimen (number 4 in table 4) has similar stress triaxiality to two axisymmetric specimens (numbers 6 and 7 in table 5) and two plane strain specimens (numbers 11 and 12 in table 6). However, the Lode and product triaxiality parameters for these experiments are different. If the stress triaxiality parameter alone is sufficient to describe the fracture locus, the equivalent plastic fracture strains for each of these experiments should be similar. In contrast, variance between the fracture strains for these experiments is an indication that additional stress state parameters are necessary to increase the fidelity of the fracture locus.

Table 6. Ductile Fracture Experimental Program: Tensile Tests Conducted on Plane Strain Specimens

Specimen #	Specimen Dimensions	σ^* Triaxiality	μ Lode Parameter	σ_p^* Product Triaxiality
11 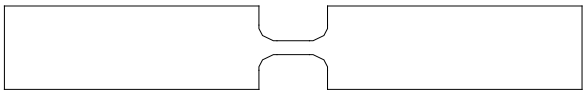	Thick smooth specimen (plane strain) Gage Length: 5.080 mm Gage Width: 2.032 mm Thickness: 25.400 mm	-0.577	0.000	0.000
12 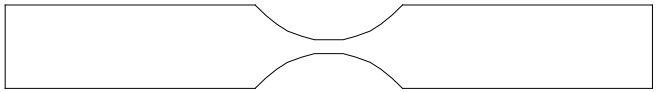	Thick smooth specimen (plane strain) Notch Radius: 13.970 mm Minimum Notch Width: 2.032 mm Thickness: 25.400 mm	-0.606	0.000	0.038
13 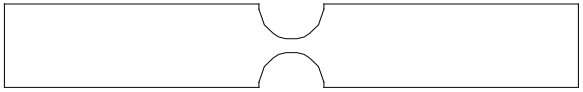	Thick smooth specimen (plane strain) Notch Radius: 4.763 mm Minimum Notch Width: 2.032 mm Thickness: 25.400 mm	-0.730	0.000	0.155

Combined axial-torsional experiments on thin-walled tube specimens provide a useful method of generating fracture strain data at a wide variety of stress states. Consider the thin-walled tube specimen subjected to axial load (*P*) and torque (*T*) in figure 6; the axial load can be either tensile or compressive. The gage section of the specimen is subjected to the following state of stress:

$$\sigma = \begin{pmatrix} \sigma_x & \tau_{xy} & 0 \\ \tau_{xy} & 0 & 0 \\ 0 & 0 & 0 \end{pmatrix} \tag{11}$$

The principal stresses are:

$$\sigma_1 = \frac{\sigma_x}{2} + \sqrt{\left(\frac{\sigma_x}{2}\right)^2 + \tau_{xy}{}^2} \quad , \sigma^2 = 0 \quad , \sigma_3 = \frac{\sigma_x}{2} - \sqrt{\left(\frac{\sigma_x}{2}\right)^2 + \tau_{xy}{}^2} \tag{12}$$

The stress triaxiality for this load condition is:

$$\sigma^* = \frac{-\sigma_m}{\bar{\sigma}} = -\frac{\sigma_x}{3\left(\sigma_x{}^2 + 3\tau_{xy}{}^2\right)^{\frac{1}{2}}} \tag{13}$$

and the Lode parameter can be found by substituting equation 12 into the definition of the Lode parameter (equation 6):

$$\mu = \frac{\sigma_x}{2\sqrt{\left(\frac{\sigma_x}{2}\right)^2 + \tau_{xy}{}^2}} \tag{14}$$

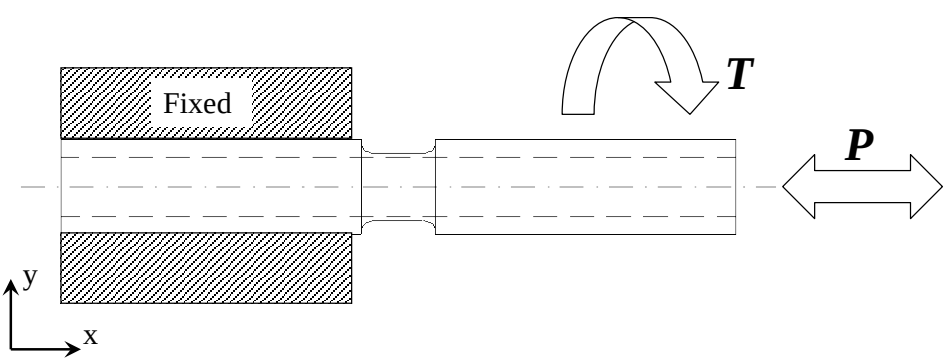

Figure 6. Combined Axial and Torsional Loading of a Thin-Walled Tube Specimen

The stress triaxiality and Lode parameters are plotted versus the axial stress/shear stress ratio in figure 7. When $\frac{\sigma_x}{\tau_{xy}} > 0.0$, the axial stress component is tensile. Conversely, when $\frac{\sigma_x}{\tau_{xy}} < 0.0$, the

axial stress component is compressive. When $\frac{\sigma_x}{\tau_{xy}} = 0.0$, the specimen is subjected to pure shear loading. Figure 7 indicates that this relatively simple experiment can be used to investigate a wide range of potential stress states. Stress triaxialities within the range of 0.333 (pure compression) to -0.333 (pure tension) are achievable. Likewise, the entire possible range of Lode parameters (-1.0 to 1.0) can be attained. There are, however, some practical restrictions on the stress states that can be achieved. Because the thin-walled tube gage sections tend to buckle for $\frac{\sigma_x}{\tau_{xy}} << 0.0$, it is more difficult to conduct these experiments in the compression. When buckling occurs, a more complex stress state than the one described in equation 11 exists in the specimen gage and the previous analysis no longer applies. Shortening the specimen gage and increasing the wall thickness of the tube specimen can delay buckling; however, achieving stress states described at the far left of the scale of the plot in figure 8 is unrealistic. Even with this limitation, the experiment is an extremely useful tool to characterize the fracture strain dependence on the state of stress.

This experiment had two main advantages over other experiments typically used to characterize ductile fracture behavior. First, the axial stress/shear stress ratio could be maintained at a nearly constant level by using load and torque control on a biaxial servohydraulic load frame. This means that the stress state was nearly constant for the duration of the experiment and damage in the material accumulated at a constant rate. The geometry of tension specimens, such as those shown in tables 4, 5, and 6, evolved significantly from the initiation of loading to fracture. Therefore, the stress state also evolved significantly during this time. The second advantage was that the stress state was easily determined from the experimental force and torque records, using equations 13 and 14.

Combined axial torsional and pure shear experiments on thin-walled tube specimens are summarized in table 7. Specimen numbers 14 and 15 were tested under combined tensile and torsional loading, specimen number 16 was tested in pure shear (torsion), and specimen number 17 was tested under combined compression and torsional loading. The specimen used for the compression–torsion experiment (specimen number 17) had a different geometry than the others. The gage length was shortened and the wall thickness was increased to ensure the specimen did not buckle. The ratio of axial stress to the shear stress in the specimen was held constant at 2.587 and 1.148 for specimen numbers 14 and 15, respectively. In the compressive experiment (specimen number 17), an axial stress/shear stress ratio of -0.920 was targeted.

Table 7. Ductile Fracture Experimental Program: Pure Shear (Torsion) and Combined Loading (Tension/Torsion, Compression/Torsion) Experiments

Specimen #	Specimen Dimensions	$\frac{\sigma_x}{\tau_{xy}}$	σ^* Triaxiality	μ Lode Parameter	σ_p^* Product Triaxiality
14 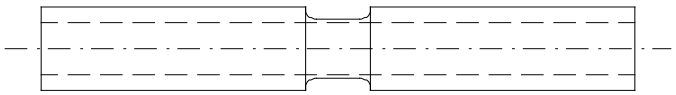	Combined Tension/Torsion specimen Gage Length: 6.35 mm Inside Diameter: 7.925 mm Outside Diameter: 9.144 mm	2.587	-0.281	0.805	0.000
15 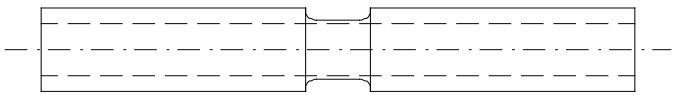	Combined Tension/Torsion specimen Gage Length: 6.35 mm Inside Diameter: 7.925 mm Outside Diameter: 9.144 mm	1.148	-0.188	0.509	0.000
16 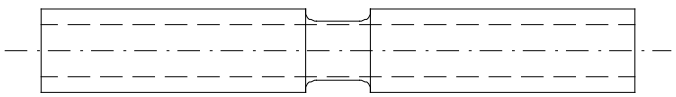	Pure Shear specimen Gage Length: 6.35 mm Inside Diameter: 7.925 mm Outside Diameter: 9.144 mm	0.000	0.000	0.000	0.000
17 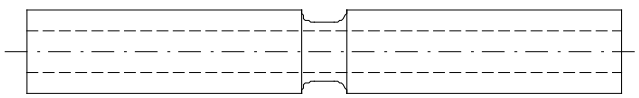	Combined Tension/Torsion specimen Gage Length: 3.175 mm Inside Diameter: 6.35 mm Outside Diameter: 9.144 mm	-0.920	0.147	-0.390	0.000

All tension and combined loading specimens were fabricated so the direction of loading was parallel to the rolled direction of the plate (see figure 7).

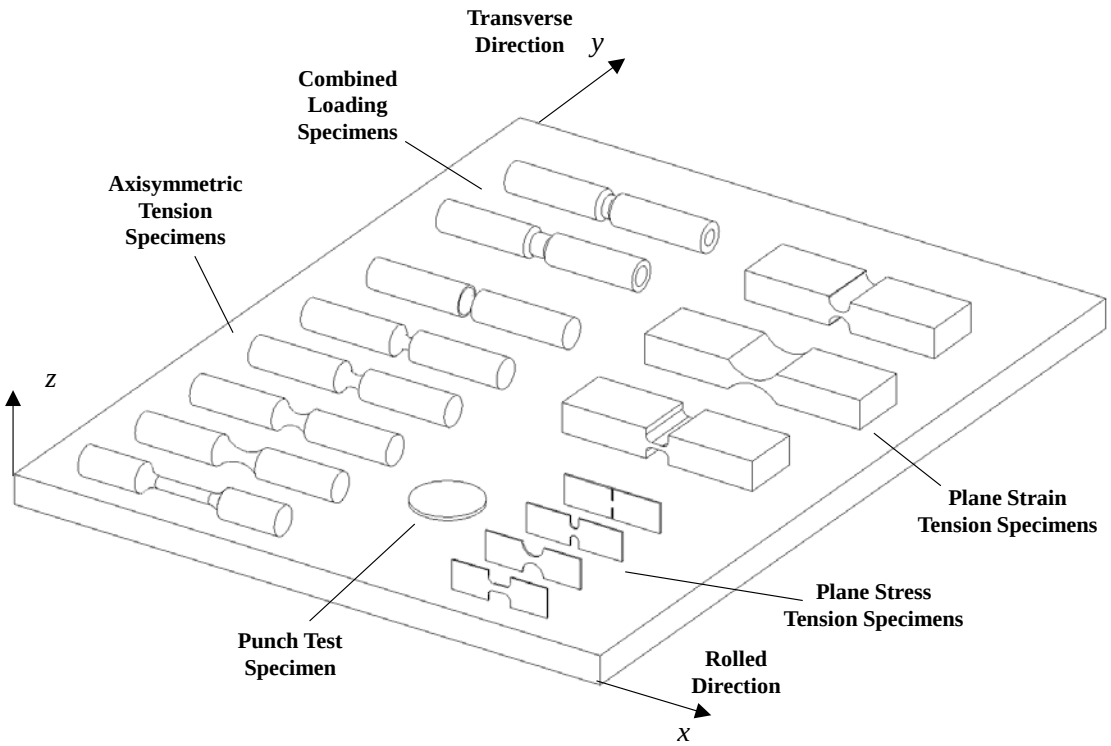

Figure 7. Various Tension, Combined Loading, and Punch Test Specimens Fabricated From a 12.7-mm-Thick 2024-T351 Aluminum Plate

The punch test program is shown in table 8. These experiments were conducted primarily to validate the fracture locus determined from the tension and combined loading tests. Three punch geometries, with tip radii of 2.39 mm, 4.75 mm, and perfectly blunt, were used to alter the stress state in the disk specimen. Samples loaded with these three-punch geometries were denoted specimen numbers 18, 19, and 20. The specimens were 1.473-mm-thick, 14.73-mm-diameter disks constrained outside of a 5.842-mm radius from its center using epoxy and adaptor fixtures. Specimens were fabricated in the orientation shown in figure 7. Static and dynamic tests were conducted with identical specimens and fixtures to ensure no scaling problems. Static tests were conducted on a load frame with a punch velocity of 2.34E-4 m/s. Dynamic tests were conducted on a compression SHB at relative punch velocities of 16.75 to 22.10 m/s.

Table 8. Ductile Fracture Experimental Program: Punch Tests

Specimen #	Specimen/Punch Dimensions	Punch Velocity (m/s)
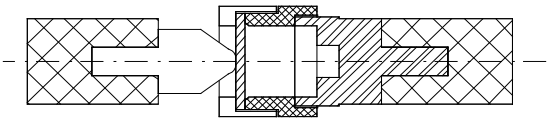 18	Sharp Punch, Radius: 2.39 mm Specimen Thickness: 1.473 mm	2.34E-04
		22.10
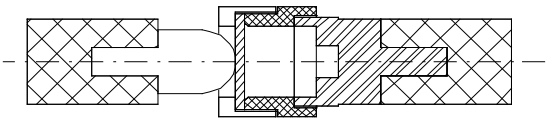 19	Intermediate Punch, Radius: 4.75 mm Specimen Thickness: 1.473 mm	2.34E-04
		20.20
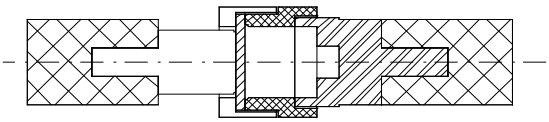 20	Blunt Punch, Radius: ∞ Specimen Thickness: 1.473 mm	2.34E-04
		16.75

The dynamic failure mode of the disk specimen was further studied by conducting additional tests with the 2.39-mm- and 4.75-mm-radius punches. Test fixtures were designed to restrict the penetration of the punch into the specimen to a predetermined displacement. Points of interest identified on the unrestricted displacement force versus displacement curve were used to determine the restricted relative displacements. For example, drops in force could be associated with strain localizations, crack formations, or crack propagation. The specimen was then recovered and inspected to document failure mode evolution. Only the unrestricted displacement experiment was conducted with the blunt punch.

Drawings of the specimens and test fixtures used in ductile fracture test series are shown in appendix D. Section 3 discusses additional details on the experiments used to explore the ductile fracture behavior of 2024-T351 aluminum.

The naming convention for all tests is outlined in appendix C.

3. EXPERIMENTAL TECHNIQUES.

This section discusses the techniques used to conduct the experiments outlined in the plastic deformation and ductile fracture test series. The section is separated into techniques used for low-strain-rate and high-strain-rate experiments. A brief discussion of the 3D DIC technique for experimental mechanics and descriptions of the measurement systems used in this work are also presented.

3.1 LOW-STRAIN-RATE EXPERIMENTS.

Low-strain-rate experiments were conducted using the Instron 1321 biaxial servohydraulic load frame shown in figure 9. The machine's actuator can move axially with stroke limits of ±63 mm and rotate with angle limits of ±45°. Multiple experiments can be conducted with this load frame

because of these two degrees of freedom. These experiments include uniaxial tension and compression, pure shear (torsion), and combinations of both tension shear and compression shear. The load frame can be equipped with two load cells, depending on the amount of load/torque expected in the experiment. The Lebow 6467-107 load cell has a maximum load capacity of 89 kN and a torque capacity of 1110 N-m and is used for experiments that require large loads or torques. An Interface 1216CEW-2K load cell is used for experiments requiring loads less than 8.9 kN and torques less than 111 N-m. The machine is controlled with an MTS® FlexTest® SE controller equipped with multipurpose testware, a suite of software that allows the user to independently control both the axial and torsional channels of the load frame. The FlexTest SE is also used for digital data acquisition through MTS 493.25 Digital Universal Conditioners with maximum sample rates of 100 KHz and 22-24 bit resolution.

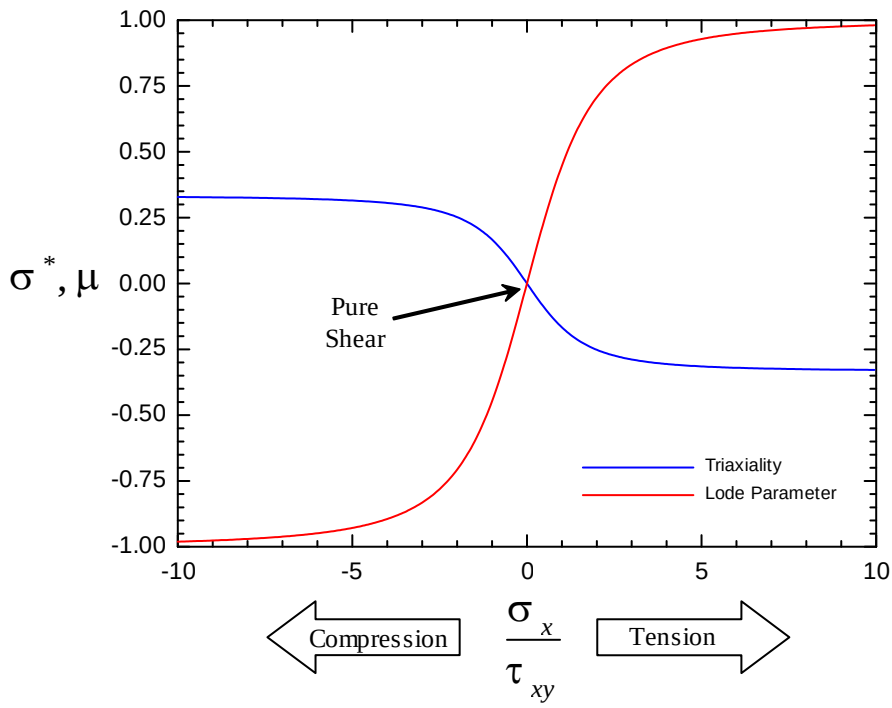

Figure 8. Stress Triaxiality and Lode Parameter vs. Axial-Stress-to-Shear Stress Ratio for Combined Axial and Torsional Loading of a Thin-Walled Spool Specimen

Multiple grips are used for specimen attachment and loading, depending on the test conducted. MTS 647.02B-22 axial-torsional hydraulic wedge grips (see figure 9(a)) were used to conduct the low-rate experiments outlined in the ductile fracture test series. A summary of the conditions in these experiments are shown in tables 4 through 7. Flat and V-notch wedges were available to grip flat (for tests listed in tables 4 and 6) and round (for tests listed in tables 8 and 9) specimens, respectively. Inconel 718 push/pull rods (see figure 7(b)), were used to conduct the low-rate tension and compression experiments outlined in table 2. Separate adaptors were used with the push/pull rods for compression and tension experiments. The tension adaptors were fabricated from Inconel 718 and are shown in figure 2(b and c). The compression adaptors were comprised of Inconel 615 and are shown in figures 9(b) and 10. Custom MAR-246 torsion fixtures (see figure 11(e)) were used for the low-strain-rate torsion experiments in table 2.

Table 9. The DIC Extensometer Gage Lengths Used for All Tension Specimen Geometries

Test #	Geometry	Specimen Dimensions	DIC Extensometer Gage Length (mm)
Thin (Plane Stress)			
1	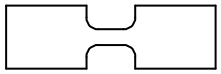	Thin smooth specimen (plane stress) Gage Length: 5.080 mm Gage Width: 3.048 mm Thickness: 0.762 mm	12.7
2	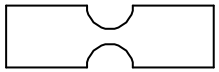	Thin notched specimen (plane stress) Notch Radius: 4.763 mm Minimum Notch Width: 3.048 mm Thickness: 0.762 mm	11.3
3	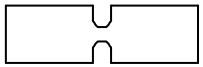	Thin notched specimen (plane stress) Notch Radius: 1.984 mm Minimum Notch Width: 3.048 mm Thickness: 0.762 mm	6.6
4	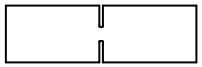	Thin notched specimen (plane stress) Notch Radius: 0.396 mm Minimum Notch Width: 3.048 mm Thickness: 0.762 mm	3.8
Axisymmetric			
5	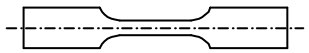	Axisymmetric smooth specimen Gage Length: 24.130 mm Gage Diameter: 4.763 mm	22.3
6		Axisymmetric notched specimen Gage Length: 14.503 mm Minimum Gage Diameter: 4.763 mm	17.9
7		Axisymmetric notched specimen Gage Length: 9.144 mm Minimum Gage Diameter: 4.763 mm	13.5
8		Axisymmetric notched specimen Gage Length: 6.096 mm Minimum Gage Diameter: 4.763 mm	10.2
9		Axisymmetric notched specimen Gage Length: 4.470 mm Minimum Gage Diameter: 4.763 mm	7.7

Table 9. The DIC Extensometer Gage Lengths Used for All Tension Specimen Geometries (continued)

Test #	Geometry	Specimen Dimensions	DIC Extensometer Gage Length (mm)
10	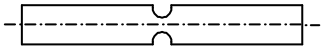	Axisymmetric notched specimen Gage Length: 3.048 mm Minimum Gage Diameter: 4.763 mm	5.0
Wide (Plane Strain)			
11	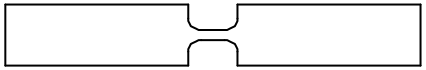	Thick smooth specimen (plane strain) Gage Length: 5.080 mm Gage Width: 2.032 mm Thickness: 25.400 mm	7.9
12		Thick smooth specimen (plane strain) Notch Radius: 13.970 mm Minimum Notch Width: 2.032 mm Thickness: 25.400 mm	19.5
13	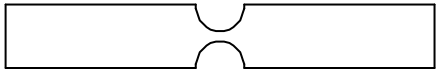	Thick smooth specimen (plane strain) Notch Radius: 4.763 mm Minimum Notch Width: 2.032 mm Thickness: 25.400 mm	8.0

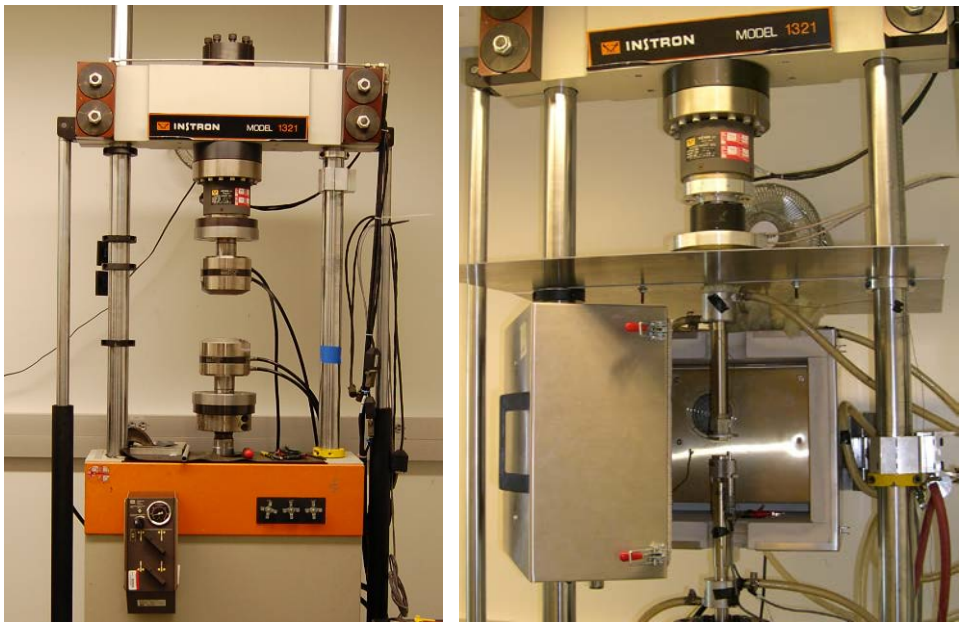

(a) (b)

Figure 9. Instron 1321 Bi-Axial Servohydraulic Load Frame: (a) Equipped With the Lebow Cell and Hydraulic Wedge Grips and (b) Equipped With the Interface Cell and Inconel 718 Push Rods

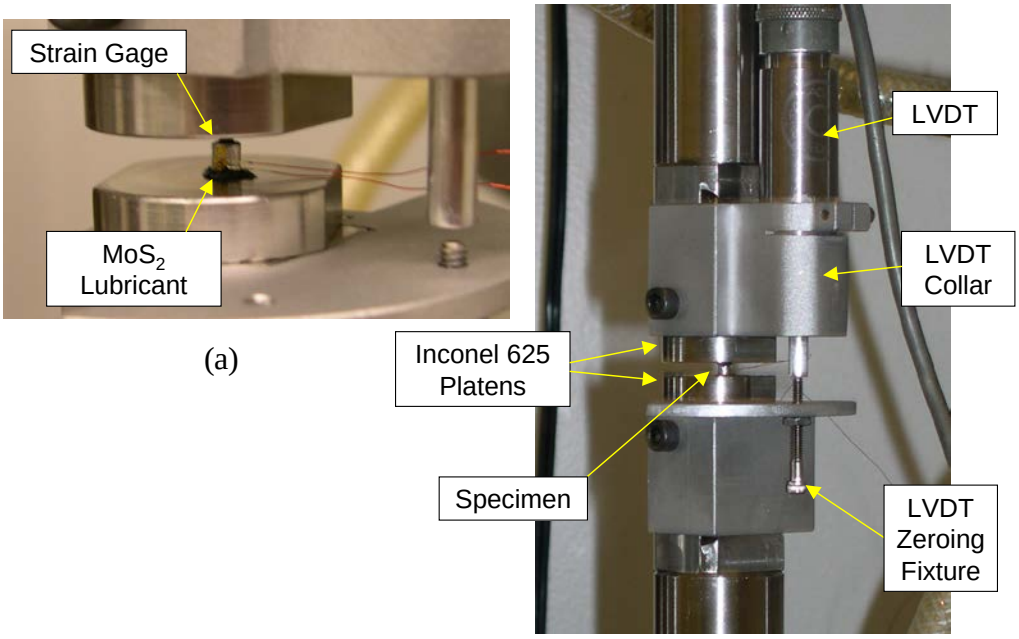

(a) (b)

Figure 10. Low-Strain Rate Compression Experimental Setup (a) Specimen Placed Between Inconel 615 Platens and (b) Pushrod and Platen Setup With Secondary LVDT Fixture

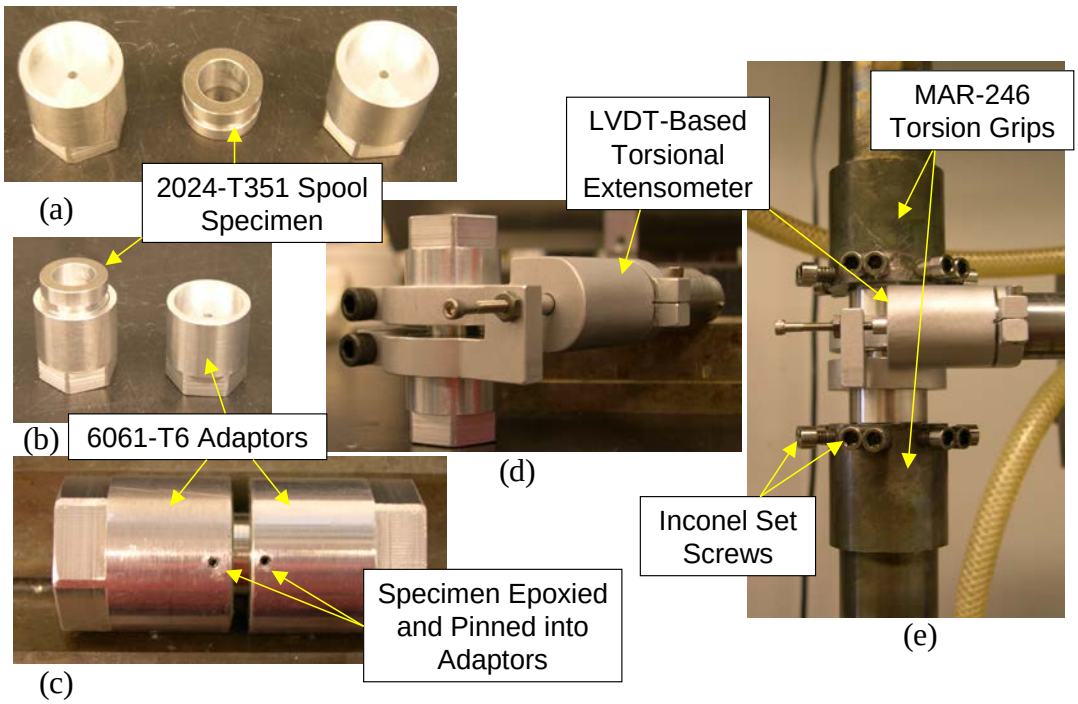

Figure 11. Torsion Specimen and Adaptors (a) and (b), Specimen-Adaptor Assembly (c), Instrumentation (d), and Grip Fixtures (e)

3.1.1 Low-Rate Tension Experiments.

Low-strain-rate tension tests were conducted on several test specimen geometries for the various purposes, as outlined in section 2. These include:

- The smooth, flat, thin specimens used to study the plastic deformation behavior of 2024 aluminum, as shown in tables 2 and 3. These specimens were used to study the rate and temperature dependencies of plastic deformation.

- The plane stress specimens tested to study the ductile fracture behavior of the material, as shown in table 4.

- The axisymmetric specimens used to study ductile fracture, as shown in table 5.

- The plane strain specimens used to study ductile fracture, as shown in table 6.

The specimen geometry used to study the plastic deformation behavior is shown in figure 2(a). Inconel 718 grip fixtures, shown in figure 2(b and c), were used to attach the specimens to the load frame. An Epsilon 3442 miniature axial extensometer with a 4.0-mm initial gage length was used for all tensile plastic deformation experiments at temperatures equal to and below 150°C (see figure 2(c)). The experiments were conducted by imposing a constant downward axial actuator velocity, resulting in a constant strain rate. The following are the actuator velocities for the three low-strain-rate experiments:

- Strain rate: 1.0E-04 s^{-1}, actuator velocity: 5.08E-04 mm/s
- Strain rate: 1.0E-02 s^{-1}, actuator velocity: 5.08E-02 mm/s
- Strain rate: 1.0 s^{-1}, actuator velocity: 5.08 mm/s

Axial load was measured with the interface load cell and the extension of the specimen gage was measured with the extensometer. Sample data from a servohydraulic tension experiment are shown in figure 12. The histories of engineering stress and strain are shown in figure 12(a). The black trace is engineering stress and corresponds to the vertical axis on the left. Strain traces are represented by the gray traces and correspond to the vertical axis on the right. Two strain traces are shown, one calculated from the extensometer record (solid trace) and one from the linear variable differential transformer (LVDT) record on the Instron frame (dashed trace). The extensometer trace is more accurate because machine compliance and pull rods are eliminated. A nominal strain rate of 0.893 s^{-1} was calculated from the extensometer record. Engineering (black trace) and true (gray trace) stress strain curves are shown in figure 12(b).

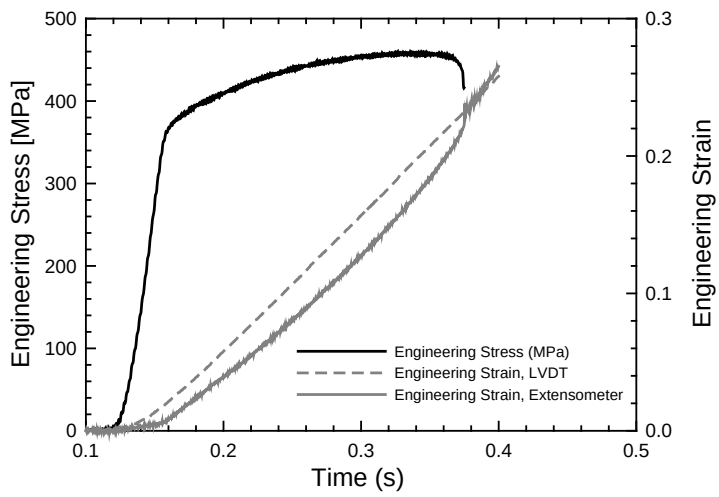

(a)

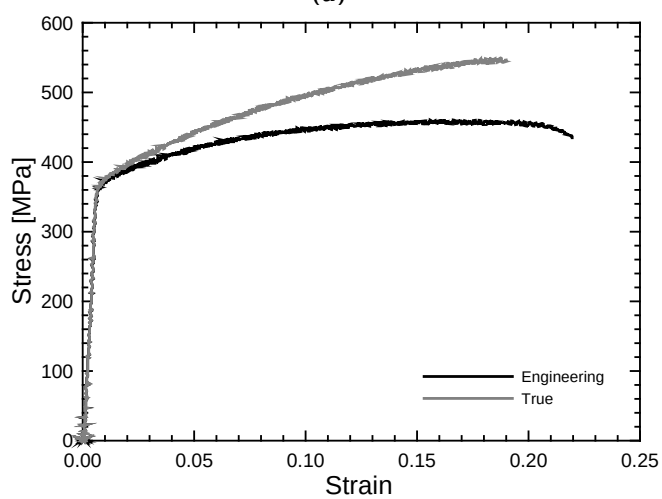

(b)

Figure 12. Sample Data From a Servohydraulic Tension Experiment: (a) Engineering Stress and Engineering Strain History Data and (b) Engineering and True Stress Strain Curves

True stress and true strain are calculated using:

$$\varepsilon = 1n\left(1+\varepsilon_E\right) \tag{14}$$

$$\sigma = \sigma_E\left(1+\varepsilon_E\right) \tag{15}$$

where ε and σ are true strain and stress, respectively, and ε_E and σ_E are engineering strain and stress. These formulas assume volume constancy and that the deformation takes place uniformly within the specimen. These assumptions are no longer valid at the onset of the necking localization; therefore, care must be taken when interpreting the true stress versus true strain response at large strains.

Additional measurements were made for the plane stress ductile fracture tension test series. The test series is summarized and nominal specimen dimensions are shown in table 4. Selected experiments were instrumented with Vishay Micro-Measurements CEA-06-032WT-120 biaxial strain gage rosettes. The rosettes were bonded to the specimen at the center of the minimum cross-sectional area. A plane stress specimen with a 0.396-mm notch radius was instrumented with the rosette, as shown in figure 13(a). On the opposite side of the specimen, surface displacements and strains were measured using a commercially available 3D DIC system. Maximum and minimum principal strains on a specimen with a 0.396-mm notch radius are shown in figure 14 (a and b, respectively). History data for the 0.396-mm notch radius specimen are shown in figure 13(b). The black trace represents the load sustained by the specimen while the solid and dashed gray traces are the longitudinal and transverse surface strains at the center of the notch, measured with the rosette. The markers indicate the maximum and minimum principal strains at the same location on the opposite surface of the specimen measured using DIC. Figure 10(b) clearly shows that the two measurement techniques agree well. The DIC and rosette strain measurements agree for the other plane stress specimen geometries as well. Fracture onset is identified by a drop in the force history. The data shown in figures 13(b) and 14 were used to generate a fracture locus data point for 2024-T351 aluminum. More detail regarding the use of these data for fracture locus construction is found in part 2 of this report [4].

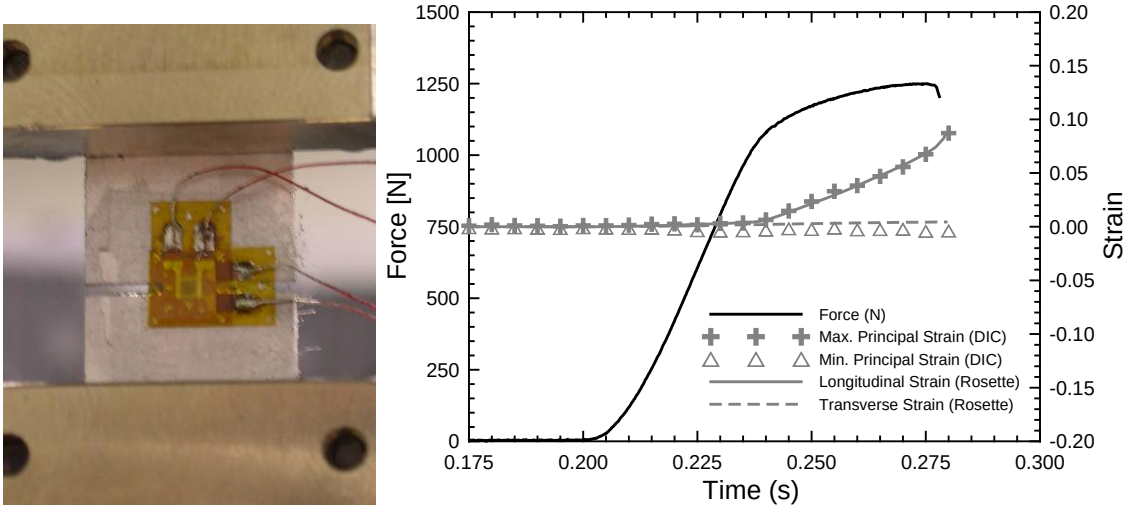

(a) (b)

Figure 13. Plane Stress Notched Specimen Tension Experiment: (a) Specimen Instrumented With a Bi-Axial Strain Gage Rosette and (b) Experimental Data

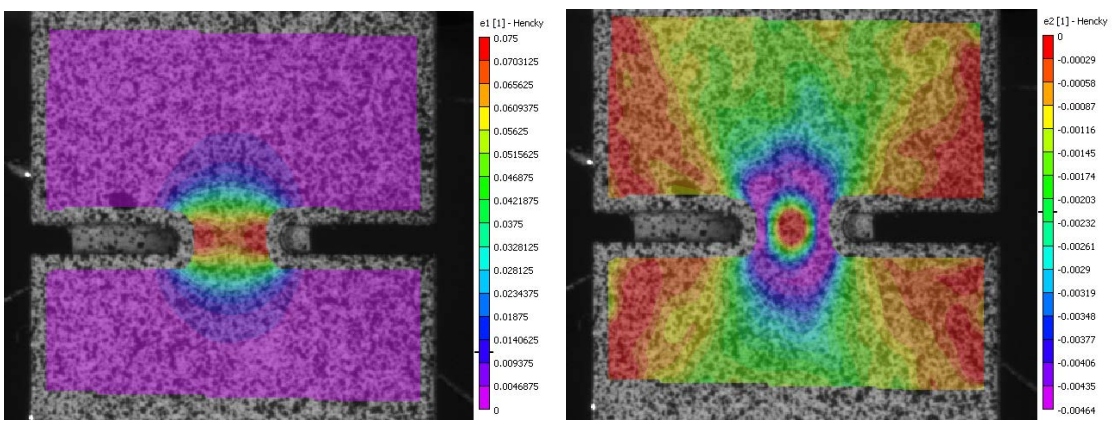

(a) (b)

Figure 14. Maximum Principal (a) and Minimum Principal (b) Strains on the Surface of a Notched, Plane Stress Tension Specimen

The axisymmetric tension test series is summarized and specimen dimensions are shown in table 5. One specimen had a smooth gage section and five others were notched with radii ranging from 14.503 to 3.048 mm. The plane strain tension test series is summarized in table 6. One smooth and two notched specimens, with notch radii of 13.97 and 4.763 mm, were tested. The experimental setup and data acquisition were identical for both the axisymmetric and plane strain test series. The experimental setup for a notched plane strain test specimen is shown in figure 15. The specimens were gripped using the hydraulic wedge grips, and the specimen was loaded with a constant axial actuator velocity to achieve a nominal strain rate of 1.0×10^{-2} s^{-1}. Actuator velocities of 0.2413 and 0.0508 mm/s were used for the axisymmetric and plane strain specimens, respectively.

Force was measured using the Lebow load cell and specimen surface strains were measured with 3D DIC. For these experiments, the 3D DIC technique was critical, since the specimen geometries contain 3D features. These features are shown in figure 16. Figure 16(a) shows the surface of an axisymmetric tension specimen with a notch radius of 6.096 mm and figure 16(b) shows the surface of a plane strain specimen with a notch radius of 13.970 mm. The surface *Z* coordinate (depth or out-of-plane coordinate) is shown in figure 16(a and b). Specimen surface strain distributions just prior to fracture are shown in figure 17. Maximum and minimum principal strains on an axisymmetric specimen with a 6.096-mm notch radius are shown in figure 17(a and b, respectively). Maximum and minimum principal strains on a wide specimen with a 13.970-mm notch radius are shown in figure 17(c and d, respectively). Experimental data from a test on an axisymmetric specimen with a 6.096-mm radius notch are shown in figure 18. History data of the force and the maximum and minimum principal surface strains at the center of the minimum specimen cross section, measured using DIC, are shown in figure 18(a). The drop in the load indicates a specimen fracture. Force versus displacement curves are shown in figure 18(b). One curve is generated using the LVDT record from the Instron frame and the second curve uses a DIC extensometer. In the latter case, the relative displacements of two points straddling the minimum notch diameter of the specimen are compared to their initial distance apart or the initial gage length of the DIC extensometer. The DIC extensometer trace is more accurate than the Instron LVDT because compliance in the machine and the grips are eliminated. The initial gage lengths of the DIC extensometers vary for the different specimen geometries tested and are summarized in table 9.

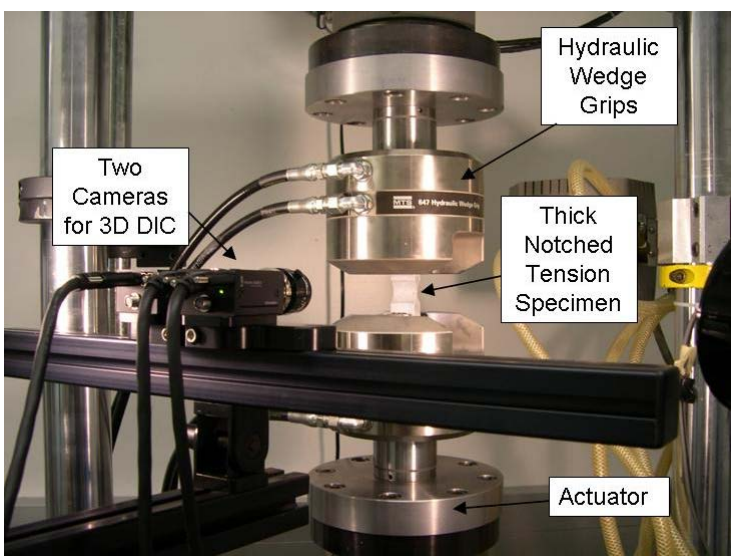

Figure 15. Experimental Setup for Axisymmetric and Plane Strain Tensile Tests

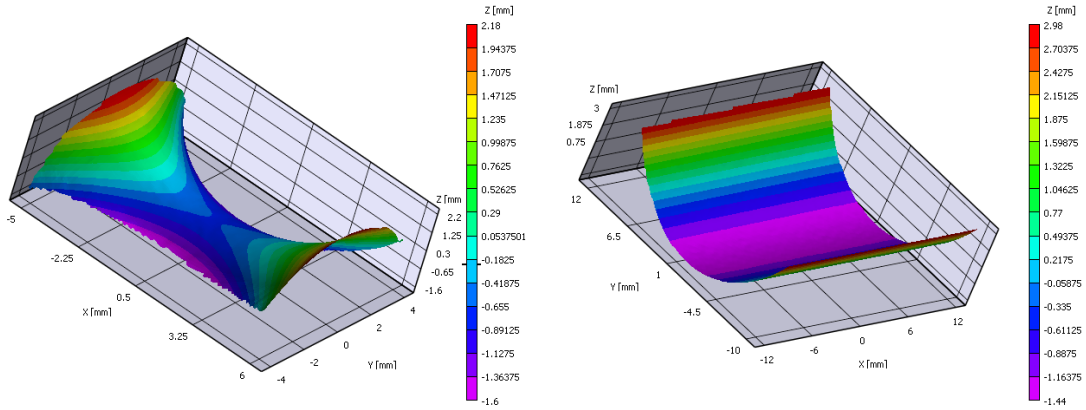

(a) (b)

Figure 16. Three-Dimensional Surface Features of (a) Notched Axisymmetric Tension Specimen and (b) Notched Plane Strain Tension Specimen

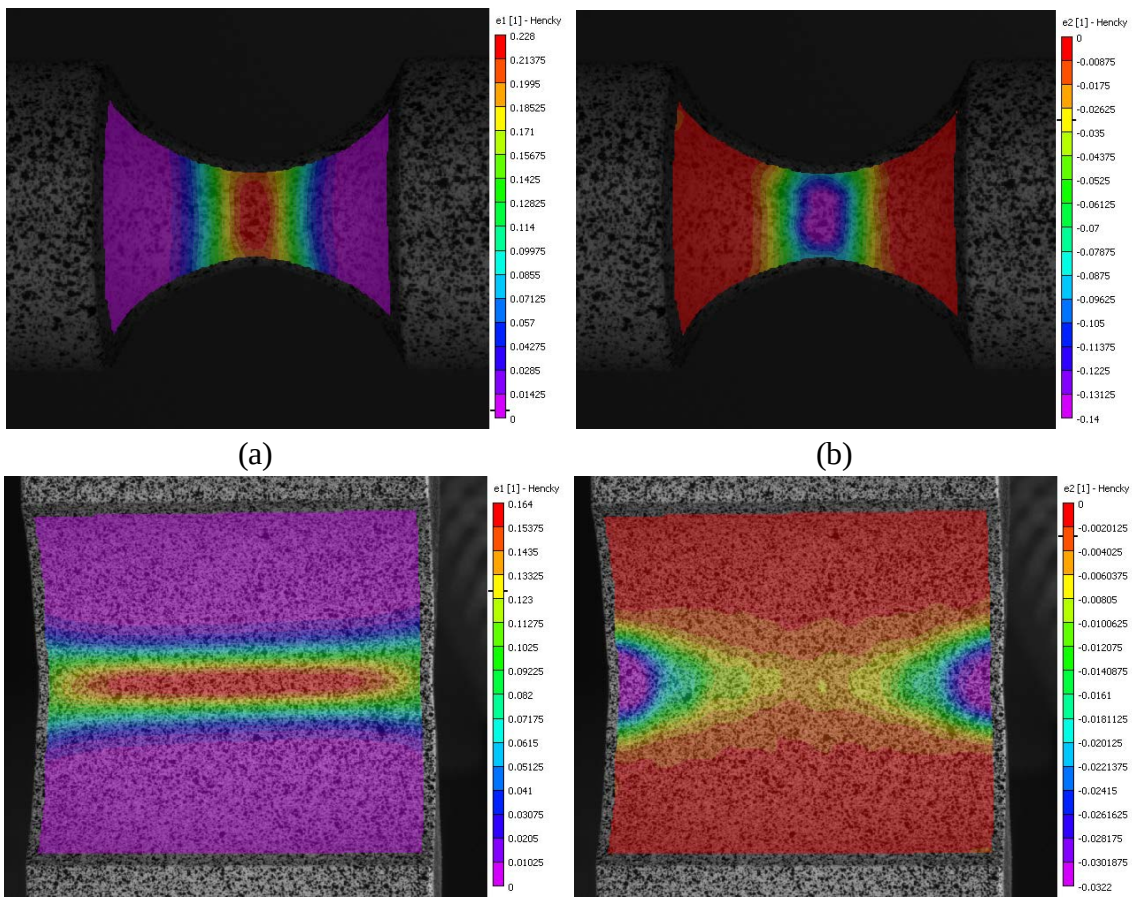

(a) (b)

(c) (d)

Figure 17. Tension Specimen Surface Strains Just Prior to Fracture: (a) Maximum and (b) Minimum Principal Strains of Notched Axisymmetric Specimen, (c) Maximum and (d) Minimum Principal Strains of Notched Plane Strain Specimen

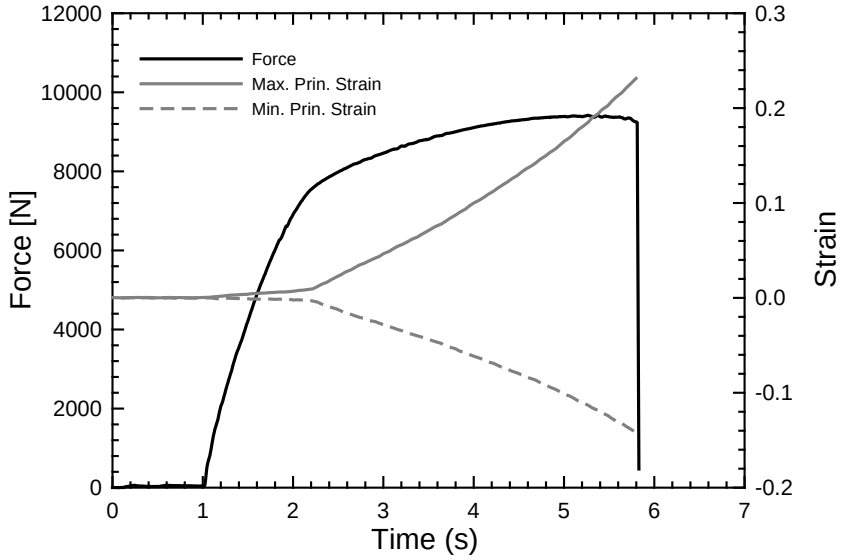

(a)

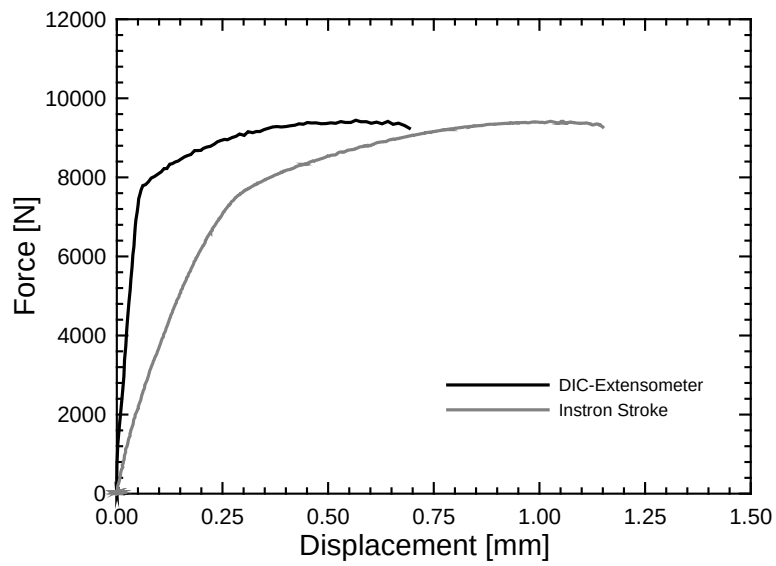

(b)

Figure 18. Sample Data From a Tension Test on Notched Axisymmetric Specimen: (a) Force and Strain History Data and (b) Force vs. Displacement Data

3.1.2 LOW-RATE COMPRESSION EXPERIMENTS.

Uniaxial compression experiments were conducted on 3.048-mm-long, 3.048-mm-diameter cylinders at three nominal strain rates using the Instron load frame. The specimen was placed between Inconel 718 pushrods and custom-designed Inconel 625 compression platens. Contact surfaces with the upper and lower platens were lubricated with molybdenum disulfide grease (see figure 10(a)) to minimize friction and barreling deformation behavior at large-plastic strains. Load was applied by imposing an upward-constant actuator velocity.

Actuator velocities for the three low strain rate experiments are:

- Strain rate: 1.0E-04 s^{-1}, actuator velocity: 3.048E-04 mm/s
- Strain rate: 1.0E-02 s^{-1}, actuator velocity: 3.048E-02 mm/s
- Strain rate: 1.0 s^{-1}, actuator velocity: 3.048 mm/s

Specimens tested at and below 150°C were instrumented with Vishay Micro-Measurements EA-06-015LA-120 strain gages (see figure 10(a)). A custom-designed, secondary LVDT fixture was used to measure the decrease in specimen length during the experiment. The fixture is shown in figure 10(b) and consists of an LVDT collar that attaches to the upper platen/pushrod and a zeroing fixture that attaches to the lower platen/pushrod. The LVDT collar accommodates a Lucas-Schaevitz part number 050 HCA LVDT. When the actuator moves upward, the screw in the zeroing fixture pushes the LVDT probe upward. This device provides more accurate specimen displacement data than the Instron integrated LVDT because it is located closer to the specimen, and a significant amount of compliance in the load frame and pushrods is eliminated from the measurement.

Sample data from a servohydraulic, uniaxial compression experiment at a nominal strain rate of 1.0 s^{-1} are shown in figure 10. Figure 19(a) shows engineering stress and strain history data and figure 19(b) shows engineering and true stress versus strain curves. Three strain traces are shown in figure 19(a). The first trace is calculated using the secondary LVDT displacement record and the second trace is from the strain gage mounted on the surface of the specimen. The strain gage provides much more accurate elastic strains than the LVDT; however, its measuring range is limited to 6%. The third trace represents a composite strain history that uses the strain gage record at low strains (preyield) and the strain calculated from the secondary LVDT record for large strains (postyield). The stress-strain curves shown in figure 19(b) use the composite strain because it is accurate in the elastic and plastic regions and covers the full range of deformation up to 30%.

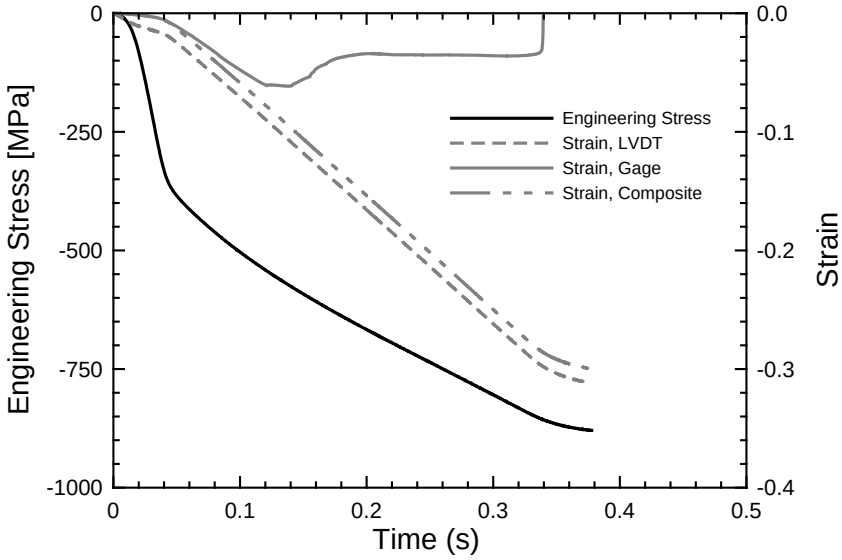

(a)

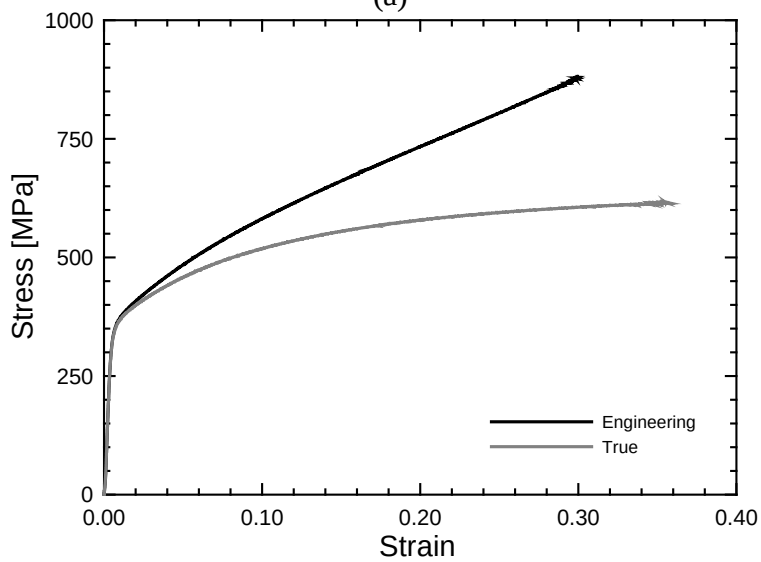

(b)

Figure 19. Sample Data From a Servohydraulic Compression Experiment: (a) Engineering Stress and Engineering Strain History Data and (b) Engineering and True Stress Strain Curves

3.1.3 LOW-RATE TORSION AND COMBINED LOADING EXPERIMENTS.

Low strain rate torsion experiments were conducted on the Instron 1321 load frame to characterize both the plastic deformation and fracture behavior of 2024-T351 aluminum under pure shear. Thin-walled tube specimens (see figure 3) were loaded using the load frame's rotational degree of freedom. The specimens were shaped like spools and fabricated so the longitudinal axis of the specimen was parallel with the thickness direction of the plate (see figure 4). The plate stock provided obvious limitations on the geometry of the specimen; the most restricting was due to the length of the specimen being limited to the thickness of the plate (12.7 mm). Short-spool specimens are difficult to grip, so adaptor fixtures were fabricated to fit

the MAR-246 steel torsion grips. The spool specimen was epoxied into upper- and lower-6061-T6 aluminum adaptors (see figure 11(a and b)). Split pins were inserted through the adaptors into the spool flanges to reinforce the epoxy bonds between the adaptors and the specimen. The specimen assembly is shown in figure 11(c). The hex-shaped ends of the adaptors were inserted into the torsion rods and Inconel set screws were used to grip the specimen (see figure 11(e)).

The experiments were conducted by imposing a constant actuator rotational velocity predetermined to achieve the desired equivalent strain rates. Load control was used on the axial channel to ensure the axial stresses in the specimen were zero. Actuator rotational velocities for the three low-rate experiments were as follows:

- Strain rate: 1.0E-04 s^{-1}, actuator rotational velocity: 3.781E-03°/s.
- Strain rate: 1.0E-02 s^{-1}, actuator rotational velocity: 3.781E-01°/s.
- Strain rate: 1.0 s^{-1}, actuator rotational velocity: 37.81°/s.

The reaction torque was measured with the Interface load cell and a custom angle of twist measurement device or torsional extensometer provided an accurate measurement of the twist angle in the specimen gage. This device, which consisted of an upper collar that housed an LVDT and a lower collar that released the LVDT probe as the actuator rotated, is shown in figure 11(d). The LVDT (Lucas-Schaevitz 050 HCA) provided a record of arc length, which can be converted to angle of twist using the distance from the LVDT probe to the center of the spool specimen. The angle of twist is $\theta = \frac{s}{r}$ where s is the arclength and r is the radius. This angle of twist measurement is more accurate than the record from the Instron integrated rotary variable differential transformer (RVDT), since it eliminates compliance in the machine and grip fixtures.

Shear stress and shear strain are calculated using the following formulas:

$$\tau = \frac{T r_m}{J} \tag{16}$$

$$\gamma = \frac{\theta r_m}{L_s} \tag{17}$$

where T is the torque, r_m is the mean gage radius, J is the polar moment of inertia and L_s is the gage length. Figure 20 shows sample data from an experiment with an equivalent strain rate of 1.0E-2 s^{-1}. History data of the shear stress and shear strain are shown in figure 20(a). Two shear strain traces are shown in the plot, one calculated from the Instron RVDT record and one calculated using the torsional extensometer device described above. The compliance in the machine clearly influences the RVDT measurement, as the shear strain accumulates too rapidly in the beginning of the experiment.

Figure 20(b) shows both shear stress versus shear strain and effective stress versus equivalent strain. Effective stress is defined by equation 5 and the equivalent strain is defined as:

$$d\bar{\varepsilon} = \left(\frac{2}{3} d\varepsilon'_{ij} d\varepsilon'_{ij} \right)^{\frac{1}{2}} \tag{18}$$

where, $d\varepsilon'_{ij}$ is the deviatoric strain tensor increment, or $d\varepsilon'_{ij} = d\varepsilon'_{ij} - \frac{1}{3} d\varepsilon_{kk} \delta_{ij}$.

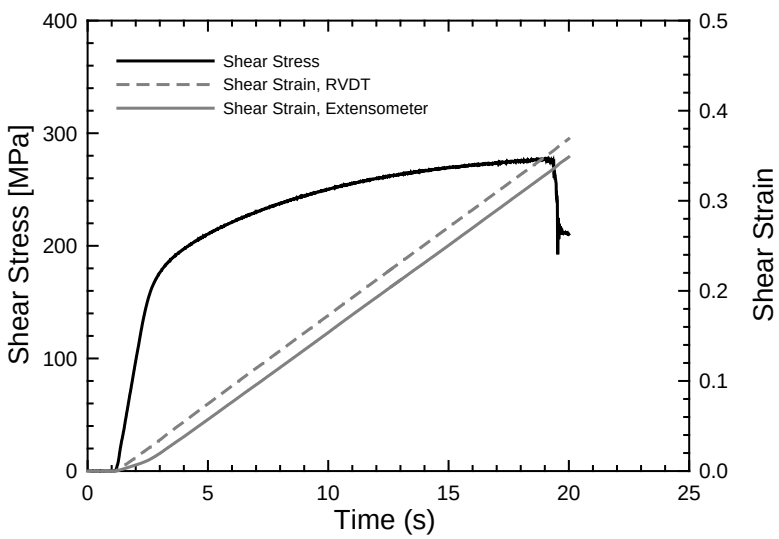

(a)

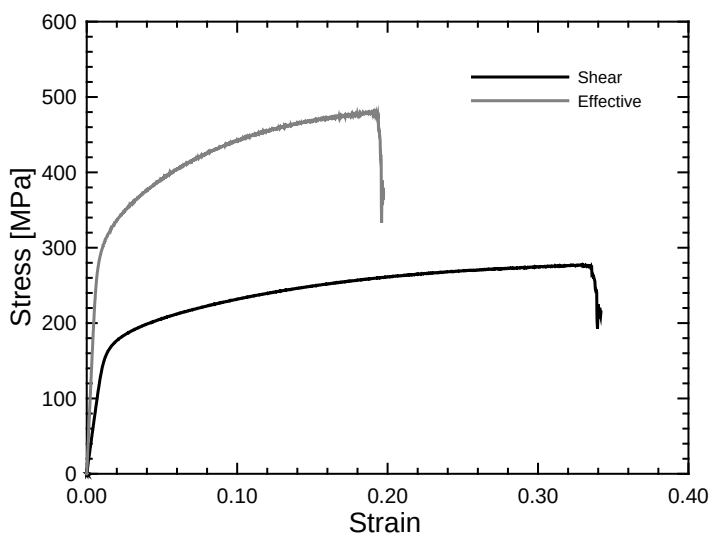

(b)

Figure 20. Sample Data From a Servohydraulic Torsion Experiment: (a) Shear Stress and Shear Strain History Data and (b) Shear and Effective Stress Strain Curves

Combined loading experiments were conducted using both the axial and rotational degrees of freedom on the Instron load frame. The dimensions of the thin-walled tube specimens used in the experiments are found in appendix D. The specimens were fabricated from a 12.7-mm-thick plate, so the axis of symmetry was parallel to the rolled axis of the plate. Specimen flanges were attached to the load frame using hydraulic wedge grips. Axial load control and torque control were used for the combined loading experiments (specimen numbers 14, 15, and 17 in table 7). The load and torque were both increased linearly with time so the axial stress–shear stress ratio, $\frac{\sigma_x}{\tau_{xy}}$, was kept nearly constant for the duration of the experiment. The pure shear experiment (specimen number 16 in table 7) was conducted using constant rotational velocity actuator motion coupled with axial load control set to zero. Torques and axial loads were measured using the interface load cell for specimen numbers 14, 15, and 16, while the Lebow cell was used for specimen number 17.

In addition to the axial stroke and rotation measurements from the LVDT and RVDT integrated into the Instron frame, DIC was used to capture surface displacement and strain data for each of these experiments. Surface strain plots for a combined-loading specimen with $\frac{\sigma_x}{\tau_{xy}} = 2.5$ are shown in figure 21. Maximum principal strains are shown in figure 21(a), and minimum principal strains are shown in figure 21(b). The white axes overlaid on the strain contours indicate the directions of the principal strains. The maximum principal strain directions are generally vertical and the minimum principal strain directions tend to be horizontal. The images clearly indicate a band of high strains in the center of the specimen gage. These images emphasize the usefulness of full-field strain information from the DIC technique. If the history of the load frame's actuator motion from the LVDT and RVDT were used to compute strain, it would be assumed that the strains were evenly distributed throughout the gage section of the specimen. This is clearly not the case (see figure 20). The result would be an average strain of significantly lower magnitude than those found in the high-strain region. Even an axial-torsional extensometer would be subject to these errors.

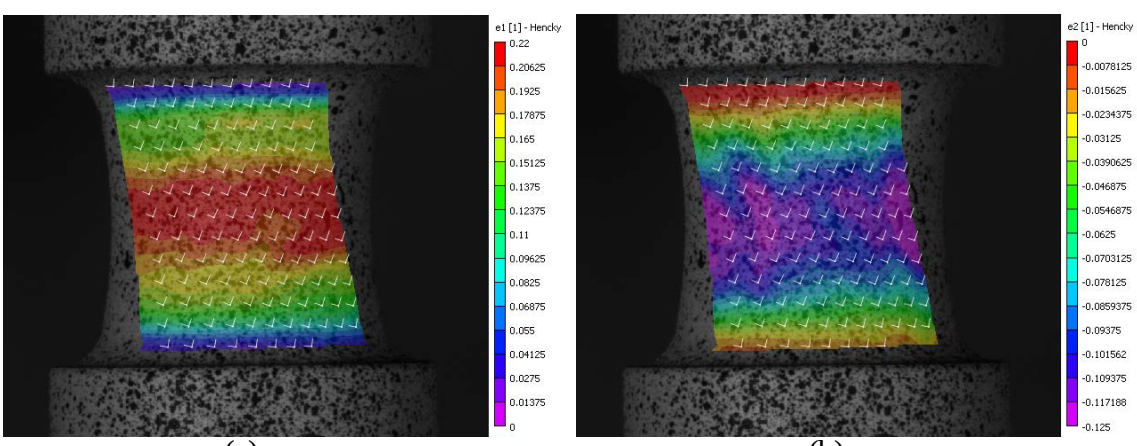

(a) (b)

Figure 21. Surface Strains on a Combined Loading Specimen: (a) Maximum Principal Strain and (b) Minimum Principal Strain

Sample data for an experiment with $\frac{\sigma_x}{\tau_{xy}}$ = 2.5 are shown in figure 22. Force versus displacement, torque versus rotation, and strain versus time are shown in figure 22(a, b, and c, respectively). In figure 22(a and b), the black traces indicate the curves generated from the MTS stroke and rotation records, while the gray traces represent data extracted from the DIC measurements. Maximum and minimum principal strains at the eventual specimen fracture region are presented in figure 22(c). These data can be used to generate a fracture locus data point. Details on the procedure are discussed in part 2 of this report [4].

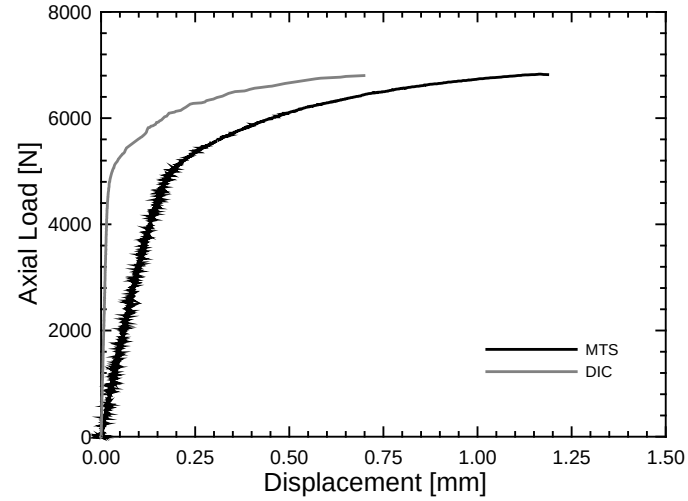

(a)

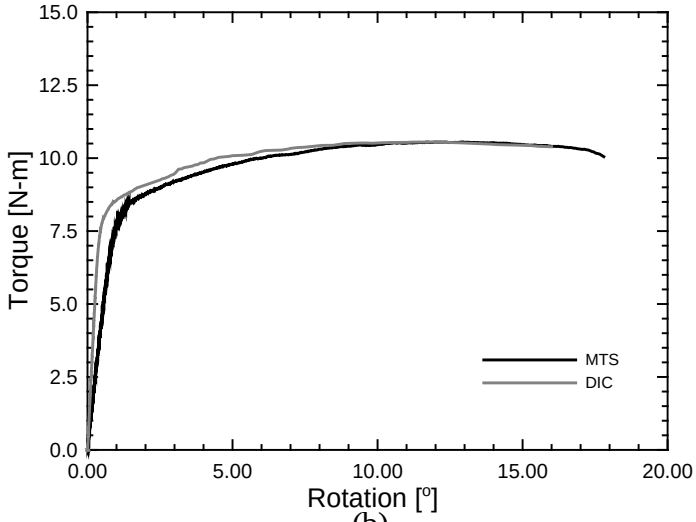

(b)

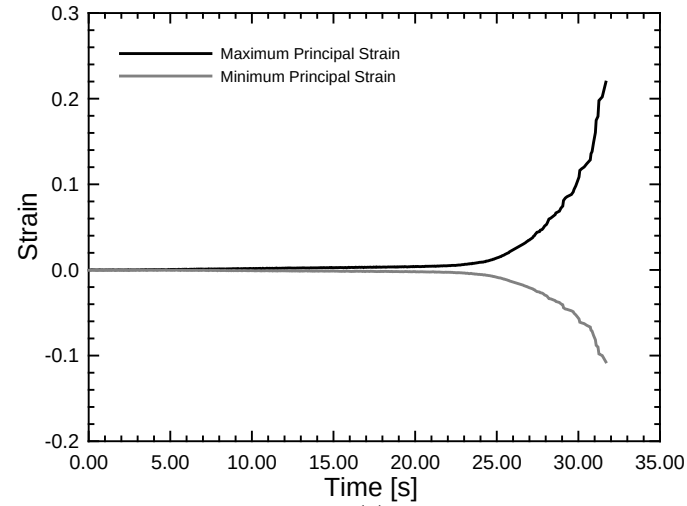

(c)

Figure 22. Experimental Data From a Combined Loading Experiment: (a) Axial Force vs. Displacement, (b) Torque vs. Rotation, and (c) Strain vs. Time

3.1.4 Low-Rate Punch Experiments.

Low-rate punch experiments were conducted under the ductile fracture test plan. These tests are summarized in table 8. Punches with three different geometries (2.39-mm radius, 4.75-mm radius, and blunt) were penetrated into 1.473-mm-thick disk specimens using the Instron load frame at a rate of 2.33E-4 m/s. The test setup is shown in figure 23. Drawings of the test fixtures are shown in appendix D. These fixtures are identical to those used in the dynamic punch test series (see section 3.2.2). The axial load was measured with the Lebow load cell. The stroke from the machine's LVDT was recorded. In addition, the relative displacement between the punch and the specimen assembly was also measured using 3D DIC. Sample data from a test using a 2.39-mm radius punch are shown in figure 24. History data are shown in figure 24(a) and the load versus displacement curve is shown in figure 24(b). The displacement data shown in figure 24 displays the relative motion between the punch and fixture measured with 3D DIC.

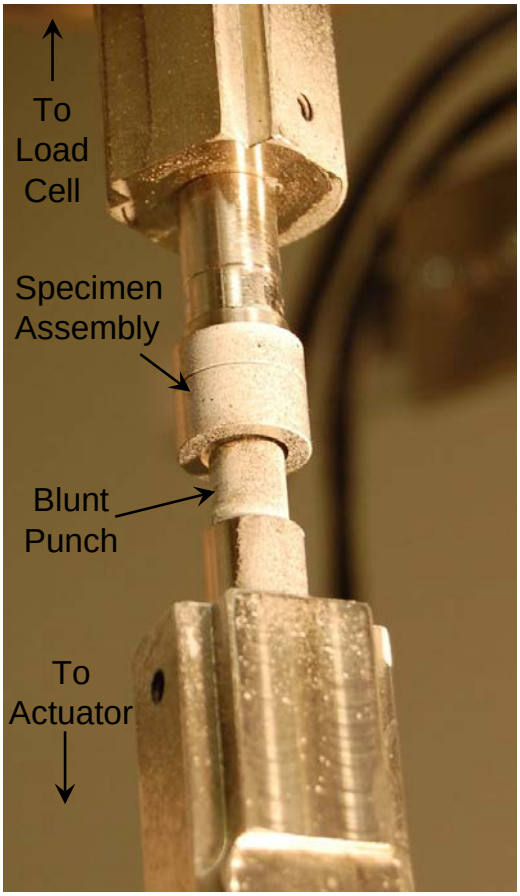

Figure 23. Low-Rate Punch Test Experimental Setup

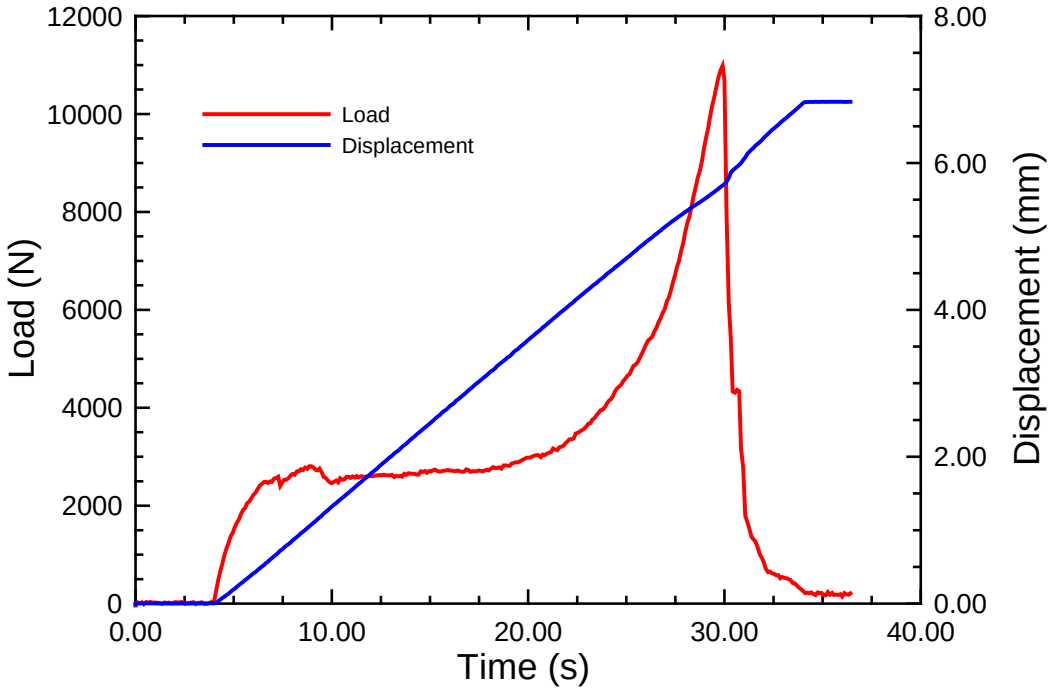

(a)

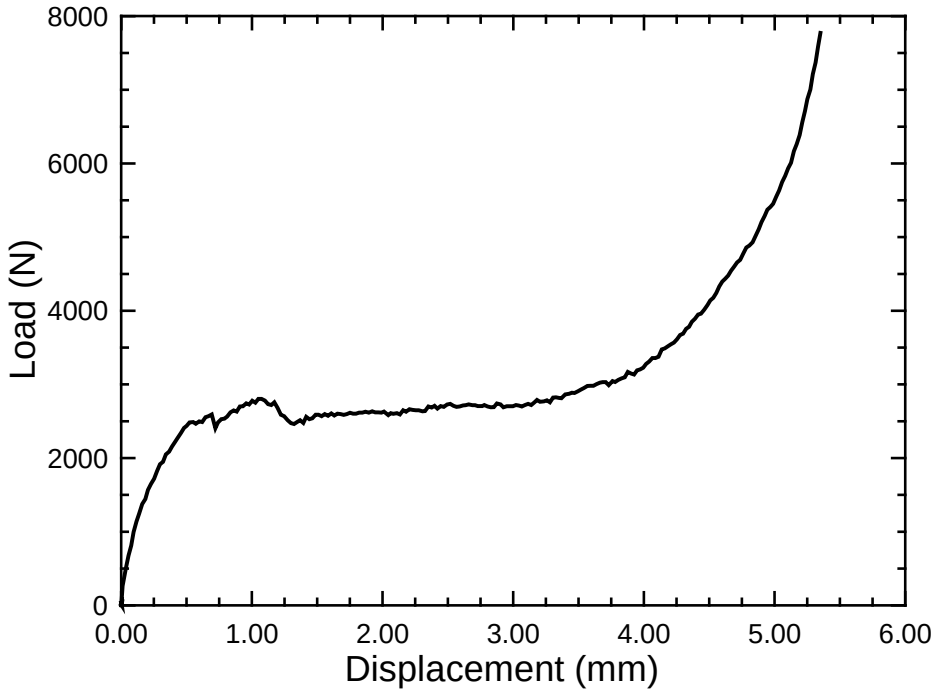

(b)

Figure 24. Low-Rate Punch Test Data: (a) History Data and (b) Load vs. Displacement Data

3.1.5 Elevated- and Low-Temperature Experiments.

Elevated- and low-temperature experiments were conducted to determine the stress versus strain dependence on temperature. Tension, compression, and torsion experiments were conducted at five temperatures: -50°C, room temperature, 150°C, 300°C, and 450°C. Two furnaces and a cryogenic chamber were used to reach these temperatures. An ATS 3620 convection furnace was used for experiments at 150°C. A Research, Inc., E4-2 infrared (IR) furnace was used for the 300°C and 450°C tests. These furnaces are shown in figure 25(a). In the picture, the front door of the ATS 3620 furnace is removed. The full 3620 furnace is shown in figure 7(b). Two cooling sleeves on the upper- and lower-push/pull rods contained flowing water to remove a significant portion of the heat that had conducted into the grips. This was necessary, especially for the upper grip, because the excess heat (if unmitigated) could negatively influence the load and torque measurements and potentially damage the load cell. The cryogenic chamber is shown in figure 25(b). Copper tubing supplied liquid nitrogen to the chamber to achieve the desired temperature. All of the mechanical fixtures used in these experiments were fabricated from high-temperature alloy steels. The push/pull rods were comprised of Inconel 718 and the torsion rods were fabricated from MAR-246. The tension grips were fabricated from Inconel 718, and compression platens were fabricated from Inconel 625. Two sets of fasteners used to attach specimens to the tension and torsion grips were comprised of A286 superalloy and Inconel 718, respectively.

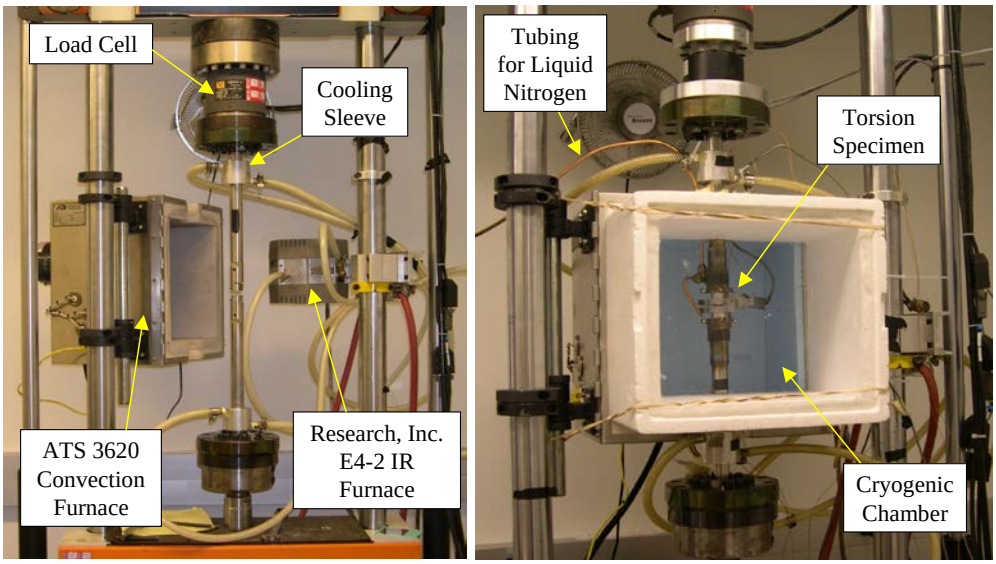

(a) (b)

Figure 25. Instron 1321 Load Frame Equipped for (a) Elevated-Temperature Testing and (b) Low-Temperature Testing

Omega type K thermocouples were used to monitor and regulate the specimen temperature in each experiment. In each type of experiment (tension, compression, and shear), multiple thermocouples were used to monitor the temperature at several different locations to identify possible temperature gradients in the furnaces or cryogenic chamber. Tension, compression, and torsion specimens instrumented with thermocouples are shown in figure 26. A tension specimen

instrumented with two thermocouples on the specimen gage is shown in figure 26(a). The thermocouples are attached to the specimen using Omega CC high-temperature cement. The tension setup also uses two additional thermocouples, one clamped to the fixture above the specimen and one clamped below the specimen. A compression test instrumented with three thermocouples is shown in figure 26(b). One thermocouple is attached directly to the specimen surface using Omega CC cement (see the inlay photograph). Two additional thermocouples are clamped to the upper and lower compression platens. A low-temperature torsion experiment is shown in figure 26(c). A thermocouple was attached to the outside wall of the tubular specimen gage with Omega CC cement. Additional thermocouples were attached to the upper and lower grips with cement.

The thermocouple on the test specimen was used with a Micristar 828-B10 controller to regulate temperature in the E4-2 IR furnace experiments. The ATS 3620 furnace had a built-in type-K thermocouple that provided feedback to an ATS AB900 temperature-control system. The chamber temperature for the low-temperature experiments was controlled manually. A four-channel Omega HH309 thermocouple data logger was used to record time histories of the various thermocouples shown in figure 26. In general, the test temperature was reached without incident and temperature gradients were minimal.

Mechanically, the experiments were conducted using the same methods described in this section. Instrumentation used for experiments at the two highest temperatures (300°C and 450°C) was limited. These temperatures exceeded the upper-level operational limit of the Epsilon 3442 extensometer, the Lucas-Schaevitz 050 HCA LVDT, and the strain gages used in the mechanical experiments. The test section of the E4-2 furnace was also too small to accommodate the extensometer and LVDT fixtures.

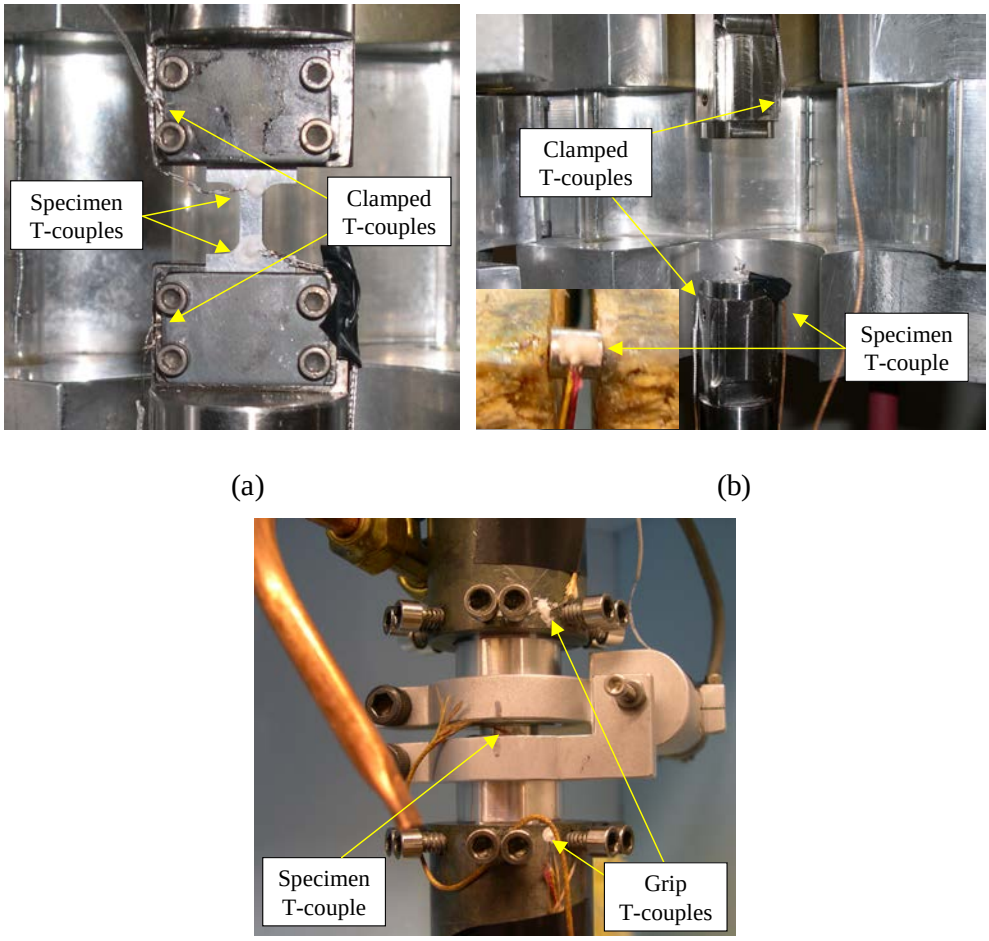

Figure 26. Elevated- or Low-Temperature Experiments Instrumented With Thermocouples (a) Tension, (b) Compression, and (c) Torsion

3.2 HIGH-STRAIN-RATE EXPERIMENTS.

High-strain-rate experiments were conducted on 2024-T351 aluminum to characterize the material's strain-rate sensitivity. The SHB or Kolsky bar apparatus is commonly used for this purpose. The SHB concept can be adapted for compression, tension, torsion, and other custom mechanical experiments at high strain rates. The available strain rate range of the technique depends on the mode of loading and on the dimensions of the actual apparatus; however, the range of 500 s^{-1} to 5000 s^{-1} is common for most SHB installations. This work employed three separate SHB setups: compression, tension, and torsion. It is uncommon for high-strain-rate data from the same material stock to be available in compression, tension, and shear; however, these tests were conducted to assure accuracy in the eventual constitutive and fracture models. This section describes the compression, tension, and torsion SHB experiments and also discusses a modification made to the compression bar apparatus to conduct dynamic punch experiments for the purposes of studying dynamic ductile fracture.

3.2.1 Compression SHB Experiments.

The compression SHB apparatus is the most common method of testing material-strength properties at high strain rates. Gray [34] provides a comprehensive overview of the experimental technique that includes the history, implementation, calibration, and data-reduction methods. The apparatus, shown in figure 27(a), consists of three round bars (incident, transmitter, and striker bar). A specimen, typically a small cylinder, is placed between the incident and transmitter bars. The interfaces between the specimen and the incident and transmitter bars are lubricated to minimize friction and keep the stress state uniaxial. A dynamic load pulse is generated by firing a striker bar into the end of the incident bar with a gas gun. The result is a square, elastic, compressive strain pulse (ε_i) that travels from the impact point toward the specimen. The amplitude of this strain pulse is proportional to the velocity of the striker bar, v:

$$\varepsilon_i = \frac{v}{2c_b} \tag{19}$$

where, c_b is the axial wave speed in an axisymmetric rod, or $c_b = \sqrt{\frac{E}{\rho}}$, where E and ρ are the elastic modulus and density of the bar, respectively. The duration of this strain pulse is twice the time required for an elastic wave to traverse the length of the striker bar. When the incident pulse reaches the specimen, the specimen undergoes plastic deformation as part of the incident pulse goes through to the transmitter bar (ε_t) and part of the wave reflects back into the incident bar as a tensile pulse (ε_r). The engineering stress in the specimen is proportional to the transmitted pulse:

$$\sigma(t) = \frac{EA\varepsilon_1(t)}{A_s} \tag{20}$$

where, A is the cross-sectional area of the transmitter bar and A_s is the initial cross-sectional area of the specimen. The strain rate in the specimen is proportional to the reflected pulse:

$$\dot{\varepsilon}(t) = \frac{\dot{u}_1(t) - \dot{u}_2(t)}{L_s} = \frac{2c_b\varepsilon_r(t)}{L_s} \tag{21}$$

where, $\dot{u}_1$ and $\dot{u}_2$ are the velocities of the ends of the incident and transmitter bars, respectively, and L_s is the length of the specimen. The engineering strain in the specimen is computed by integrating the strain rate history:

$$\varepsilon(t) = \frac{u_1(t) - u_2(t)}{L_s} = \int_0^t \varepsilon(t)\,dt \tag{22}$$

The previous analysis is known as a one-wave analysis and assumes that the specimen is in dynamic force equilibrium. This means that the force at the incident bar-specimen interface (F_1)

must be equal to the force at the transmitter bar-specimen interface (F_2). This assumption is not always true, especially shortly after specimen loading begins. At the beginning of loading, the specimen undergoes an initial "ringing-up" phase, where the load waves propagate back and forth in the specimen itself. During this phase, dynamic force equilibrium is not achieved ($F_1 \neq F_2$). Dynamic force equilibrium can be monitored by conducting a two-wave analysis. The one-wave analysis simply uses the force at the specimen-transmitter bar interface to calculate the stress history in the specimen, or:

$$F_2 = AE\varepsilon_1 \tag{23}$$

The force at the specimen-incident bar interface is:

$$F_1 = AE\left(\varepsilon_i + \varepsilon_r\right) \tag{24}$$

The dynamic equilibrium assumption made in the one-wave analysis requires that:

$$\varepsilon_t = \varepsilon_i + \varepsilon_r \tag{25}$$

A second stress history can be determined using F_1 instead of F_2. The two-wave stress history can be written as:

$$\sigma\left(t\right) = \frac{EA\left[\varepsilon_i\left(t\right) + \varepsilon_r\left(t\right)\right]}{A_s} \tag{26}$$

A photograph of the actual apparatus used in the experiments is shown in figure 27(b). The striker, incident, and transmitter bars are comprised of 12.7-mm-diameter Ti-6Al-4V. Both the incident and transmitter bars are 1886 mm long. The 616-mm-long striker bar generates a 245-μs-long, square strain pulse on impact with the incident bar. The strain pulses in the incident and transmitter bars are measured using two full Wheatstone bridges, each constructed with four Micro-Measurements ED-DY-125AC-10C strain gages (1000 Ω) positioned in the center of each bar. The positions are shown schematically in figure 27(a) as gages A and B, respectively. The bridges are powered with 15.0-V excitation using two separate HP 3611A power supplies. The output signals are conditioned with Tektronix ADA400A differential preamplifiers with a low-pass filter upper bandwidth of 100 KHz. The signals are recorded using a four-channel, 350 MHz, 8-bit Tektronix TDS5034B digital phosphor oscilloscope at a rate of 2.5E6 samples per second. Compression SHB experiments are conducted on 3.048-mm-long, 3.048-mm-diameter specimens, which is the same geometry used in the low-rate compression experiments. Molybdenum disulfide grease is used to lubricate the contact surfaces of the specimen with the incident and transmitter bars.

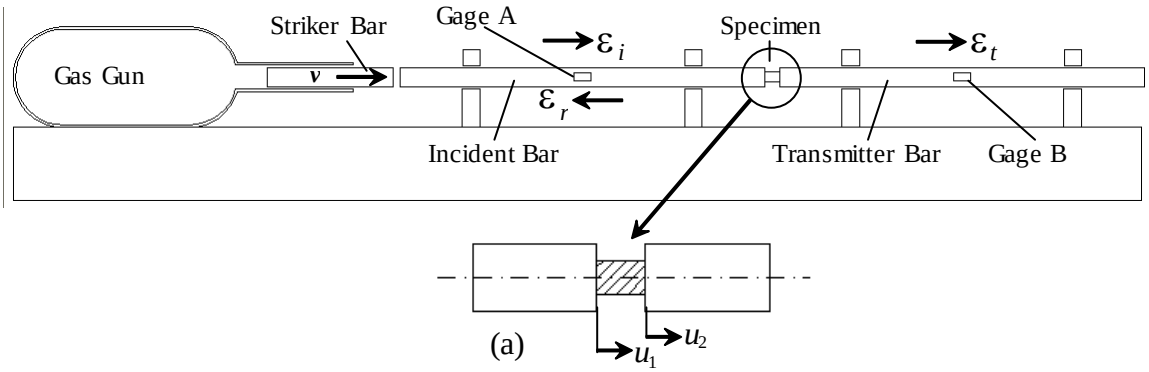

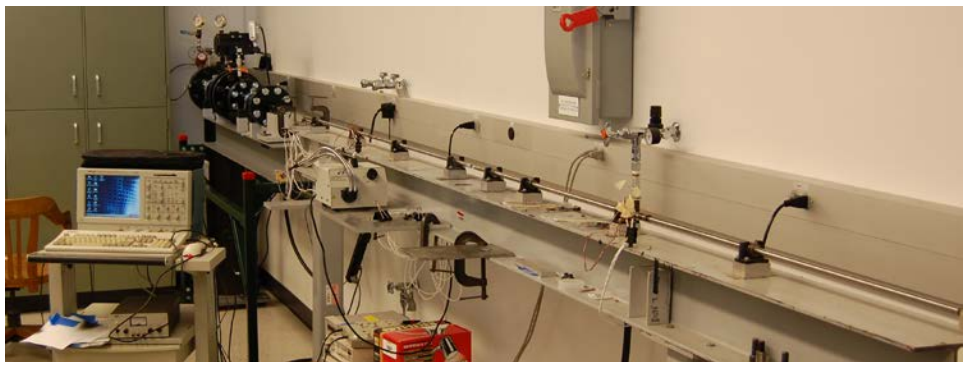

(b)

Figure 27. Compression SHB: (a) Schematic Representation of a Typical Compression SHB Apparatus and (b) Compression SHB Used in This Research

Sample data from a compression SHB experiment on a specimen fabricated from 2024-T351 aluminum are shown in figure 28. Wave data are shown in figure 28(a). The black trace is the strain history in the incident bar. Both the incident (ε_i) and reflected (ε_r) strain pulses are measured with gage A in figure 27(a). The gray trace is the strain history in the transmitter bar measured using gage B in figure 27(a). This record provides the transmitted strain pulse (ε_t). Reduced time history data of engineering stress, strain rate, and engineering strain are shown in figure 28(b). The engineering stress (black trace) is proportional to the transmitted pulse, according to equation 20. The strain rate history is proportional to the reflected pulse (see equation 21) and is not constant for the duration of the experiment. The strain rate decreases from ~2000 s^{-1} to ~1000 s^{-1} as the experiment progresses. An average strain rate of 1476.44 s^{-1} is calculated for this particular experiment. The strain history is displayed as the dashed trace. Three force versus displacement curves are shown in figure 28(c). Engineering stress-strain curves calculated using the one-wave and two-wave analyses discussed above are represented by the solid-black and dashed-black traces, respectively. For strains larger than 0.045, dynamic force equilibrium is achieved. The gray trace represents the true stress versus true strain curve of the specimen, assuming volume constancy calculated using the one-wave analysis.

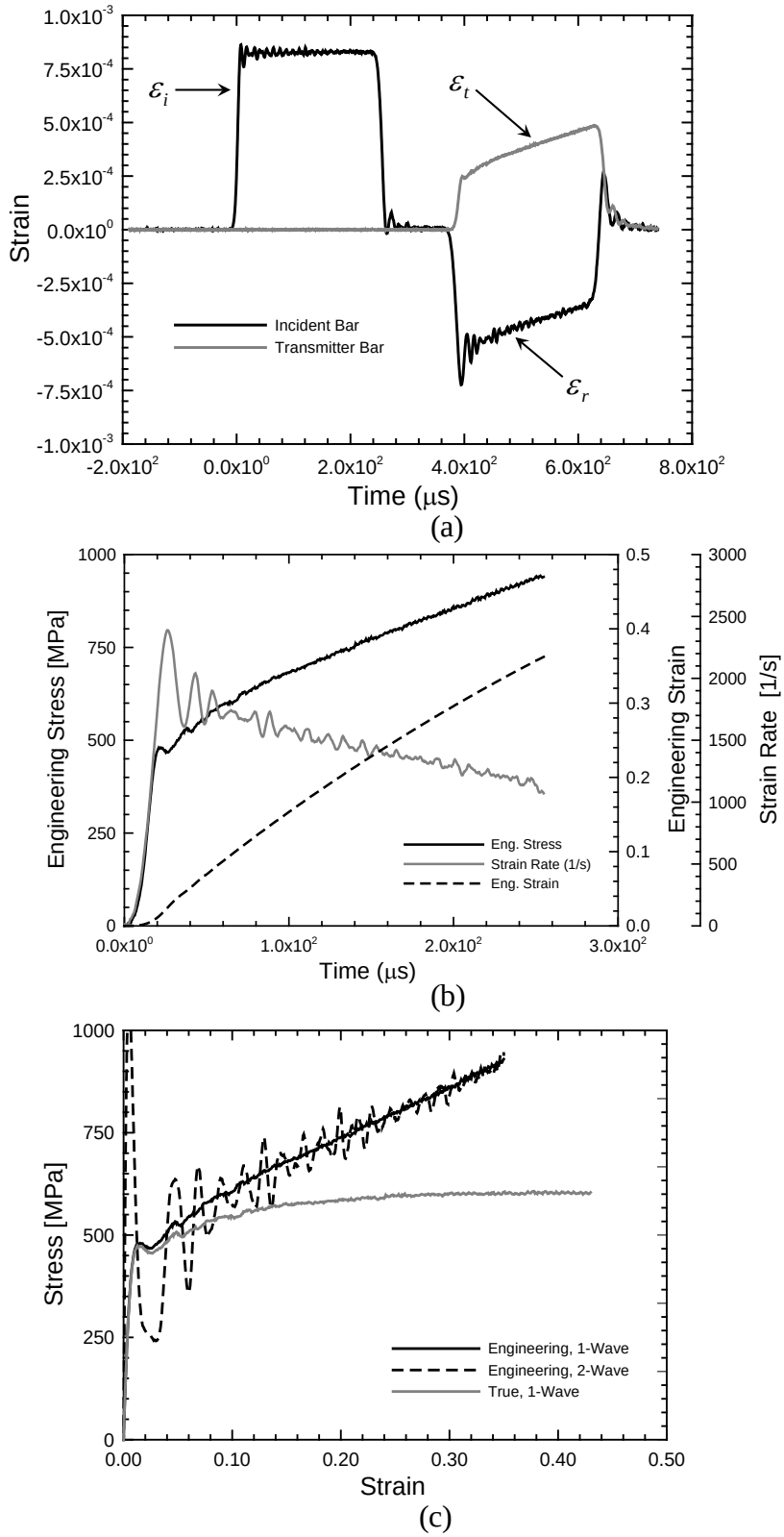

Figure 28. Sample Data From a Compression SHB Experiment on 2024-T351 Aluminum: (a) Wave Data, (b) Reduced History Data, and (c) Stress Strain Data

3.2.2 Dynamic Punch Experiments.

Punch experiments were conducted to study the dynamic ductile fracture behavior of 2024-T351 aluminum. The compression SHB apparatus described in the previous section was modified for the experiments. A hardened (HRC 47) 4340 steel punch was threaded into the end of the incident bar (see figure 29(a)). Three punch geometries were used, two with tip radii of 2.39 and 4.75 mm and one with a blunt punch geometry. A 1.473-mm-thick, 14.732-mm-diameter, 2024-T351 aluminum disk specimen was glued between two Ti-6Al-4V specimen adaptors. The specimen assembly was glued to a Ti-6Al-4V bar adaptor that was threaded into the transmitter bar. Impedance matching was implemented to minimize undesirable wave reflections at the punch-incident bar interface and the specimen assembly-transmitter bar interface. The punch displacement relative to the specimen could be unrestricted or restricted to a predetermined magnitude to investigate the failure mode evolution of the specimen. Two additional components were proposed to the setup to conduct restricted displacement dynamic punch experiments, (see figure 29(b)). A VASCOMAX C-350 stop ring was used to restrict the relative displacement of the punch into the specimen. A 7075-T6 aluminum adaptor was also added to protect the end of the incident bar from deformation after the stop ring was engaged. This technique had been used previously by researchers to limit the amount of shear strain imparted into a dynamic shear experiment on a hat-shaped specimen [31].

The analysis for this experiment is similar to that presented for standard compression SHB testing. In this case, the contact force between the specimen and the transmitter bar is proportional to the transmitted strain pulse (ε_t):

$$F_2(t) = AE\varepsilon_t(t) \tag{27}$$

The relative velocity between the punch and the specimen is proportional to the reflected strain pulse (ε_r):

$$\dot{u}(t) = \dot{u}_1(t) - \dot{u}_2(t) = 2c_b\varepsilon_r(t) \tag{28}$$

The relative displacement between the punch and the specimen is calculated by integrating the velocity history:

$$u(t) = u_1(t) - u_2(t) = \int_0^t \dot{u}(t)\,dt \tag{29}$$

Therefore, a dynamic force versus displacement curve can easily be constructed. Dynamic force equilibrium can be monitored using the two-wave analysis described in the previous section. This analysis uses the contact force between the punch and the disk specimen, or:

$$F_1(t) = AE\left[\varepsilon_i(t) + \varepsilon_r(t)\right] \tag{30}$$

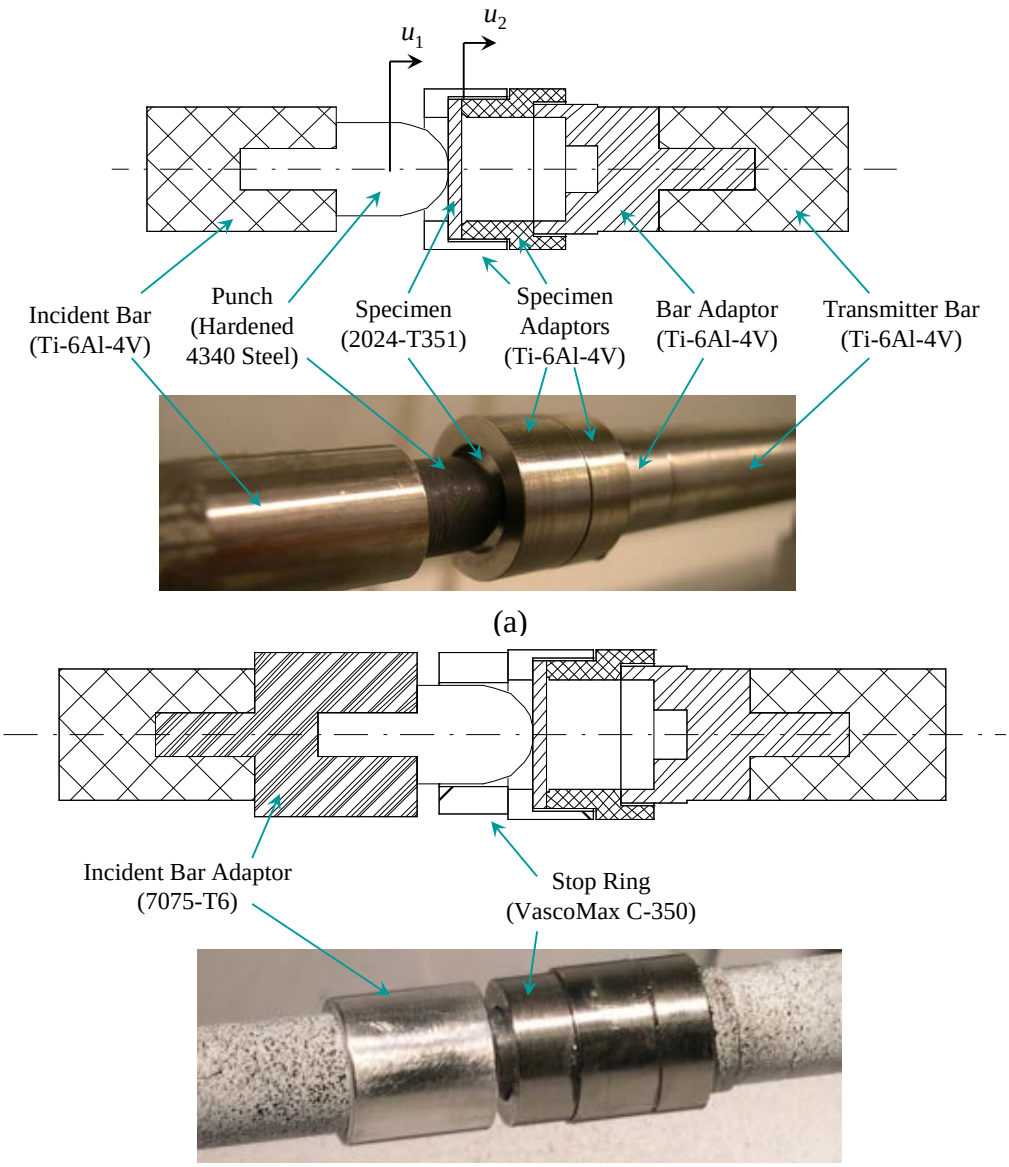

Figure 29. Experimental Setup for Dynamic Punch Test on a Compression SHB Apparatus: (a) Configured for Unrestricted Displacement and (b) Configured for Restricted Displacement

A high-speed, 3D DIC system was used to acquire an independent measurement of the relative displacement between the punch and specimen. The system, shown in figure 30, consists of two Photron SA1.1 high-speed cameras and a commercially available DIC software package. Typical frame rates for these experiments were 105,000 to 135,000 frames per second (fps).

Figure 30. High-Speed DIC Camera System

Results from an unrestricted test using the 2.39-mm-radius punch are shown in figure 31. Figure 31(a) shows wave records from the incident bar (black trace) and the transmitter bar (gray trace). Figure 31(b) shows reduced data from the same experiment. The solid trace is the contact force history between the punch and the specimen. The dashed trace is the history of the relative velocity between the punch and specimen. The relative velocity is nearly constant at 22.5 m/s for the duration of the experiment. Two relative displacement traces are also shown in figure 31(b). The first (distinguished with diamonds) is integrated from the velocity record, and the second is measured using the DIC technique. The independent relative displacement measurements agree to within 1.6% at a peak relative displacement of roughly 5.5 mm. Force versus displacement data are shown in figure 31(c). The solid trace is generated using the one-wave analysis (computed using the transmitted wave, ε_t), and the dashed trace is computed using the two-wave analysis (calculated using the sum of the incident and reflected waves, $\varepsilon_i + \varepsilon_r$). Figure 31(c) shows that dynamic force equilibrium is achieved at a displacement of roughly 0.6 mm.

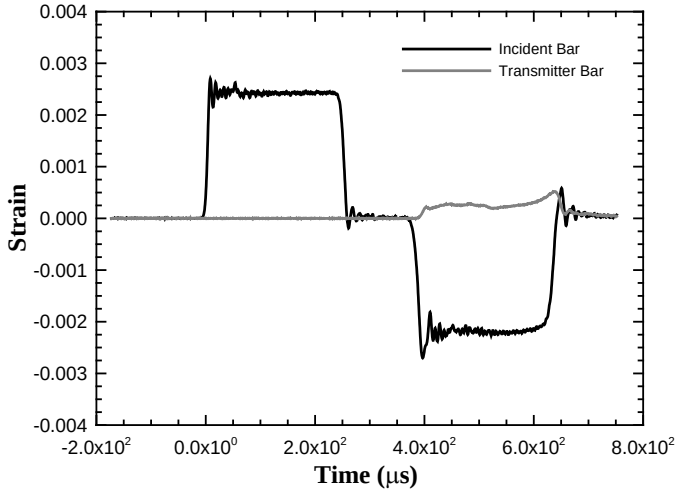

(a)

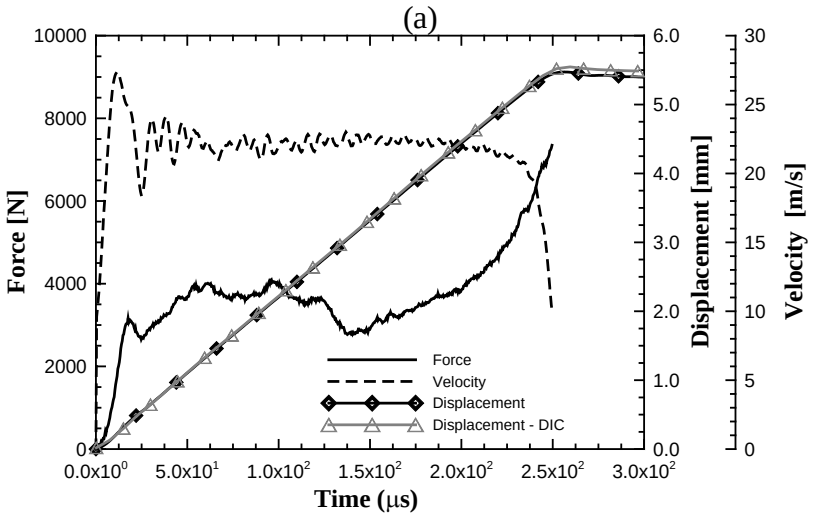

(b)

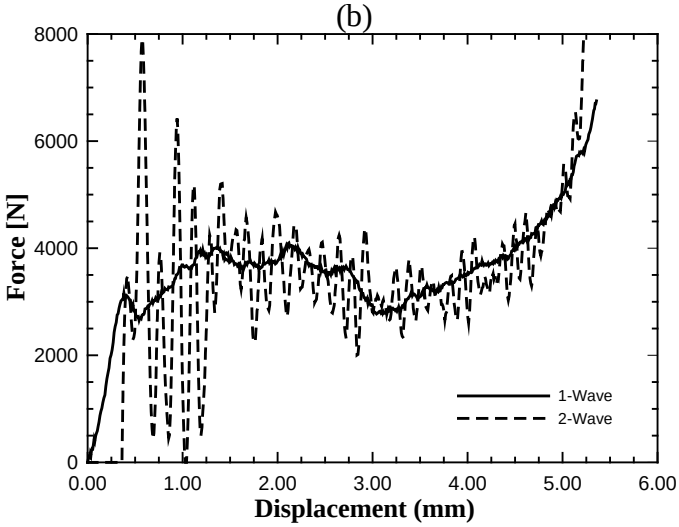

(c)

Figure 31. Experimental Results From an Unrestricted Punch Test (2.39-mm Punch Radius): (a) SHB Wave Data; (b) Reduced History Data Including Transmitted Force, Relative Velocity, and Relative Displacement; and (c) One- and Two-Wave Force vs. Displacement Data

3.2.3 Tension SHB Experiments.

This research used a direct-tension SHB apparatus [33] for dynamic tension experiments. A sketch of the apparatus is shown in figure 32. The tensile load pulse is generated by attaching a pulley fixture to the end of the incident bar. A mechanical clamp is used to grip the incident bar, and load is applied to the clamped section of the bar using a cable and a hydraulic cylinder. The section of the incident bar between the clamp and the pulley carries a static tensile load, P. The remainder of the incident bar (to the right of the clamp) is unloaded. A pin in the clamp is broken using a second hydraulic cylinder, and an elastic tensile pulse (ε_i) propagates down the incident bar from the clamp toward the specimen. The amplitude of the strain pulse is:

$$\varepsilon_i = \frac{P}{2EA} \tag{31}$$

where E and A are the elastic modulus and cross-sectional area of the incident bar, respectively. The experiment then becomes similar to the previously described compression SHB experiment. As the specimen is deformed plastically, part of the load pulse is transmitted through to the transmitter bar (ε_t) and part is reflected back into the incident bar as a compressive wave (ε_r). The transmitted pulse is proportional to the engineering stress in the specimen and the reflected pulse is proportional to the strain rate. The disadvantage of the stored-load wave generation technique is that the reflected pulse is not as easily resolved as it is for the compression SHB. The inertia of the pulley system attached to the end of the incident bar would obscure the reflected pulse if the strain gages were mounted at the center of the incident bar. Two gages, identified as gages A and B in figure 32, are mounted on the incident bar to resolve this issue. The motion of the end of the incident bar, which can be found using the method of characteristics, is:

$$\dot{u}_1(t) = \frac{1}{\rho A c_b}\left[F_A(t-t_A) + F_A(t-t_A+2t_B) - F_B(t+t_B)\right] \tag{32}$$

where $F_A(t)$ and $F_B(t)$ are the force histories in the incident bar measured by gages A and B, respectively. The durations required for an elastic wave to propagate from the specimen to gages A and B are t_A and t_B, respectively. The motion of the end of the transmitter bar is:

$$\dot{u}_2(t) = \frac{1}{\rho A c_b}\left[F_C(t+t_C)\right] \tag{33}$$

where $F_C(t)$ is the force history in the transmitter bar measured by gage C and t_C is the duration required for an elastic wave to propagate from the specimen to gage C. The strain rate for this experiment with a specimen gage length, L_s, is:

$$\dot{\varepsilon}(t) = \frac{\dot{u}_1(t) - \dot{u}_2(t)}{L_s} = \frac{1}{\rho A c_b L_s}\left[F_A(t-t_A) + F_A(t-t_A+2t_B) - F_B(t+t_B) - F_C(t+t_C)\right] \tag{34}$$

The engineering strain is simply the time integral of the strain rate (see equation 22). The engineering stress in the specimen is:

$$\sigma(t) = \frac{EA\varepsilon_t(t)}{A_s} = \frac{F_C(t+t_C)}{A_s} \tag{35}$$

where A_s is the initial cross-sectional area of the tension specimen.

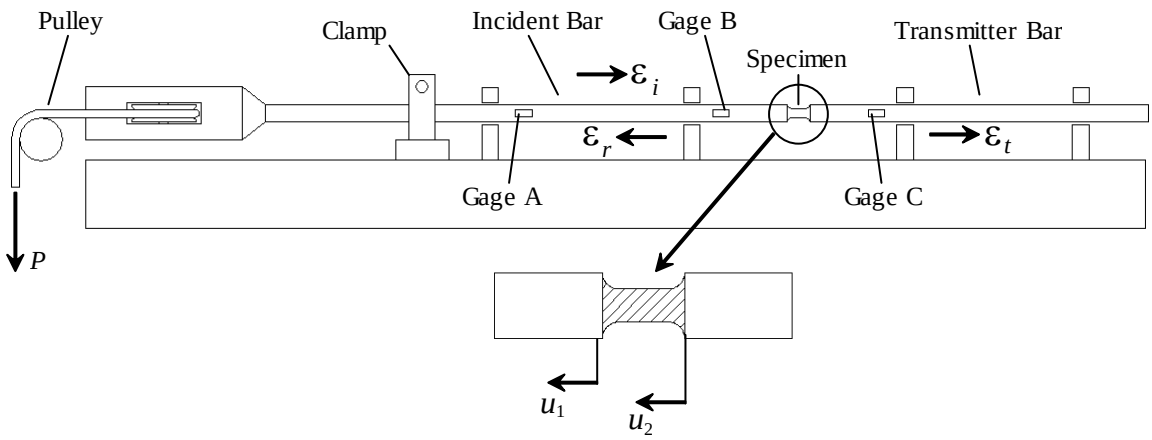

Figure 32. Sketch of a Direct-Tension SHB Apparatus

The tension SHB apparatus used for this research is shown in figure 33. The incident and transmitter bars are comprised of 12.7-mm-diameter 7075-T6 aluminum rods. The clamped section of the incident bar is 1562-mm long and stores a 630-μs load pulse. The free section of the incident bar is 1984-mm long, and the transmitter bar is 1729-mm long. The force pulses in the incident and transmitter bars are measured using three full Wheatstone bridges, each constructed with four active Micro-Measurements ED-DY-075AM-10C strain gages (1000 Ω) positioned at the locations shown schematically as gages A, B, and C (figure 32). The bridge excitation, signal conditioning, and data acquisition are identical to those used for the compression SHB apparatus. The 2024-T351 aluminum specimens with dimensions identical to those in figure 2(a) are epoxied into adaptors that are bonded between the incident and transmitter bars (see figure 31). Figure 34(a) shows the specimen instrumented with a Micro-Measurements EA-06-062AQ-350 strain gage. Figure 34(b) shows a sideview of the specimen-adaptor joint. The specimen flanges are bonded in slits in two adaptors with Emerson and Cuming TRA-BOND 2106T two-part epoxy. The adaptors are then bonded to the incident and transmitter bars, respectively. A fractured specimen is shown in figure 34(c).

Sample data from a tension SHB experiment on a 2024-T351 aluminum specimen are shown in figure 35. Wave data are shown in figure 35(a). The solid black trace is the force history in the incident bar recorded by gage A (F_A), and the dashed, black trace is the force history in the incident bar recorded by gage B (F_B). The gray trace is the force history in the transmitter bar measured using gage C (F_C). A measure of dynamic force equilibrium in the specimen is attained by comparing the force histories measured by gages B and C. Gages B and C are

positioned on the incident and transmitter bars so they are equidistant from the specimen. Since the bars are comprised of the same material, the elastic waves travel at the same velocity. Therefore, after the load pulse reaches the specimen, gage B gives a time history of force at the joint between the incident bar and the specimen. Likewise, gage C gives a time history of the joint between the specimen and the transmitter bar. After a brief rise time, the forces measured by gages B and C equilibrate at ~470 μs (figure 35(a)), showing dynamic force equilibrium in the specimen. Reduced time history data of engineering stress, strain rate, and engineering strain are shown in figure 35(b). The engineering stress (black trace) is proportional to the transmitted pulse, according to equation 35. The strain rate history, calculated with equation 34, is nearly constant at 505.401 s^{-1} for the duration of the experiment. The strain history integrated from the strain rate is displayed as the black, dashed trace, while an independent measurement from a strain gage mounted directly on the specimen is represented by the gray, dashed trace. These two independent strain measurements agree up to a strain level of 0.03, when the strain gage on the specimen fails. Engineering and true stress versus strain curves are shown in figure 35(c). The engineering stress-strain curve is calculated using equations 34, 22, and 35 and is represented by the solid black trace. The gray trace represents the true stress versus true strain curve of the specimen assuming volume constancy.

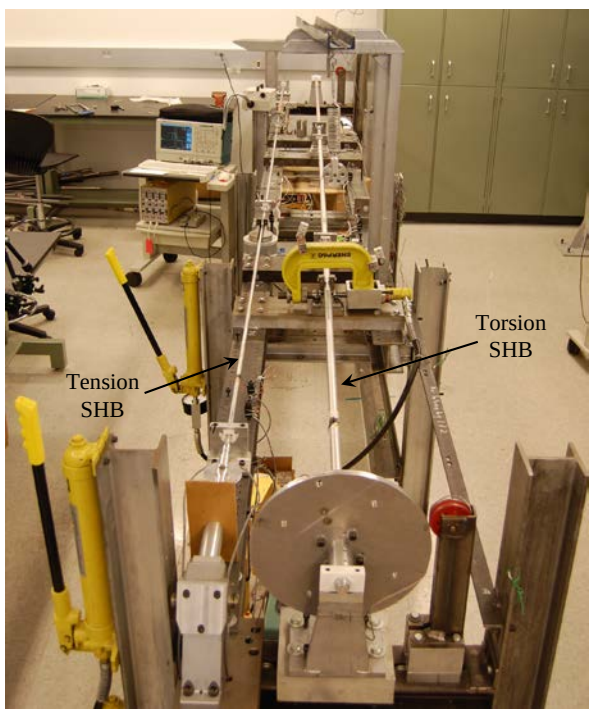

Figure 33. A Direct-Tension SHB Apparatus and a Stored-Torque Torsion SHB Apparatus

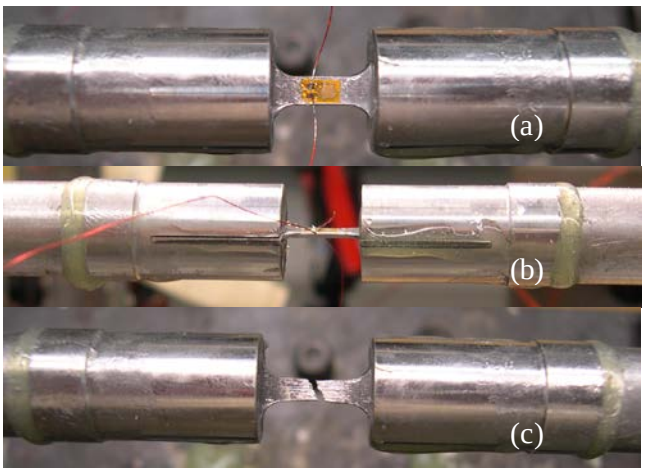

Figure 34. Specimen Attachment for a Tension SHB Experiment: (a) Top View of a Specimen Instrumented With a Strain Gage, (b) Side View of the Specimen, and (c) Post-Test Photograph

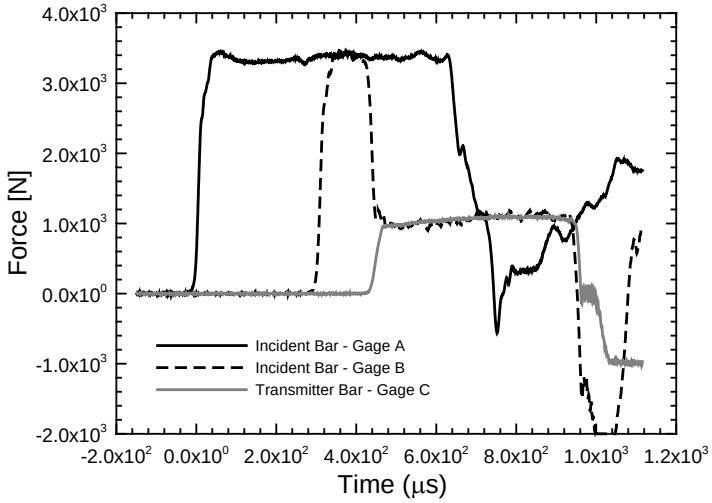

(a)

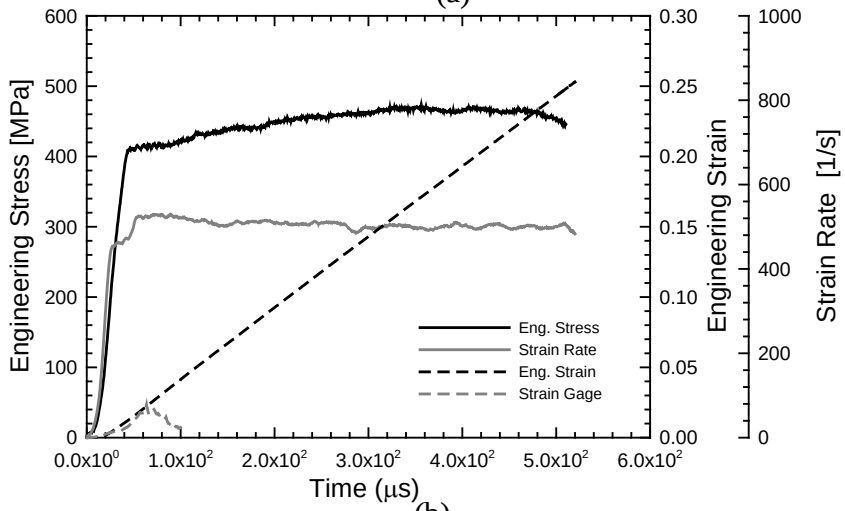

(b)

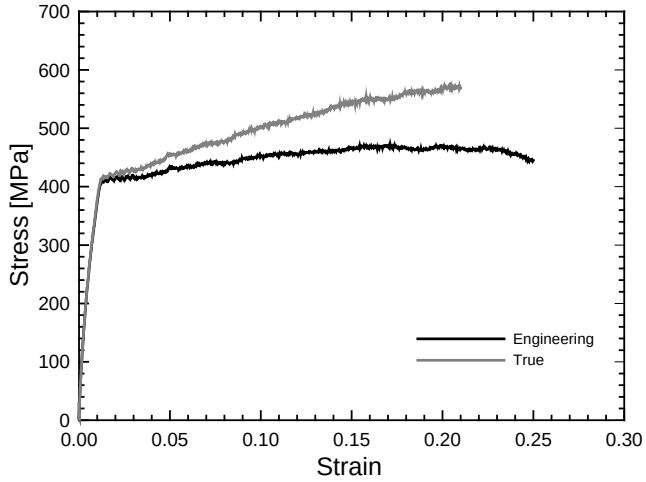

(c)

Figure 35. Specimen Data From a Tension SHB Experiment on 2024-T351 Aluminum: (a) Wave Data, (b) Reduced History Data, and (c) Stress-Strain Data

3.2.4 Torsion SHB Experiments.

This research used a stored-torque SHB [35] to characterize the rate sensitivity of 2024-T351 aluminum in shear. A sketch of the apparatus is shown in figure 36. The load pulse generation technique is similar to the one employed by the direct-tension SHB described above. The torsional load pulse is generated by attaching a torque wheel fixture to the end of the incident bar. A mechanical clamp is used to grip the incident bar, and a pure torque is applied to the wheel through a couple using a cable and a hydraulic cylinder. The section of the incident bar between the clamp and the pulley carries a static torque, T. The remainder of the incident bar (to the right of the clamp) is unloaded. A pin in the clamp is broken using a second hydraulic cylinder and an elastic shear pulse (γ_i) propagates down the incident bar from the clamp toward the specimen. The amplitude of the shear strain pulse on the surface of the bar is:

$$\gamma_i = \frac{Tr_b}{2GJ} \tag{36}$$

where r_b is the radius of the bar and G and J are the shear modulus and polar moment of inertia of the incident bar, respectively. The experiment then becomes similar to the previously described SHB experiments. As the specimen is deformed plastically, part of the load pulse is transmitted through to the transmitter bar (γ_t) and part is reflected back into the incident bar as a torsional wave in the opposite direction of the incident pulse (γ_r). The transmitted pulse is proportional to the shear stress in the specimen, and the reflected pulse is proportional to the strain rate. This technique suffers from the same disadvantage as the direct-tension bar. The inertia of the torque wheel attached to the end of the incident bar obscures the reflected pulse if the strain gages are mounted at the center of the incident bar. The issue is resolved in the same fashion as for the tension bar. Two gages, identified as gages A and B in figure 36, are mounted on the incident bar. The rotational velocity of the end of the incident bar, determined using the method of characteristics is:

$$\dot{\theta}_1(t) = \frac{1}{\rho J c_T}\left[T_A(t - t_A) + T_A(t - t_A + 2t_B) - T_B(t + t_B)\right] \tag{37}$$

where $c_T = \sqrt{\frac{G}{\rho}}$ is the transverse elastic wave speed and $T_A(t)$ and $T_B(t)$ are the torque histories in the incident bar measured by gages A and B, respectively. The durations required for a transverse elastic wave to propagate from the specimen to gages A and B are t_A and t_B, respectively. The motion of the end of the transmitter bar is:

$$\dot{\theta}_2(t) = \frac{1}{\rho J c_T}\left[T_C(t + t_C)\right] \tag{38}$$

where $T_C(t)$ is the torque history in the transmitter bar measured by gage C, and t_C is the duration required for an elastic wave to propagate from the specimen to gage C. The shear strain rate for this experiment is:

$$\dot{\gamma}(t)=\frac{r_m\left[\dot{\theta}_1(t)-\dot{\theta}_2(t)\right]}{L_s}=\frac{r_m}{\rho J c_T L_s}\left[T_A(t-t_A)+T_A(t-t_A+2t_B)-T_B(t+t_B)-T_C(t+t_C)\right] \quad (39)$$

where r_m is the mean gage radius and L_s is the gage length of the thin-walled tube specimen. The shear strain is the time integral of the strain rate or:

$$\gamma(t)=\frac{r_m\left[\theta_1(t)-\theta_2(t)\right]}{L_s}=\int_0^t \dot{\gamma}(t)\,dt \quad (40)$$

The shear stress in the specimen is:

$$\tau(t)=\frac{GJr_m\gamma_t(t)}{r_b J_s}=\frac{r_m T_C(t+t_C)}{J_s} \quad (41)$$

where J_s is the polar moment of inertia of the torsion specimen.

The torsion SHB apparatus used for this research is shown in figure 33. The incident and transmitter bars are comprised of 22.225-mm-diameter 7075-T6 aluminum rods. The clamped section of the incident bar is 1227-mm long and stores an 810-µs torsional loading pulse. The free section of the incident bar is 2283-mm long and the transmitter bar is 2026-mm long. The torque pulses in the incident and transmitter bars are measured using three full Wheatstone bridges, each constructed with four active Micro-Measurements 1000 Ω strain gages positioned at the locations shown schematically as gages A, B, and C in figure 36. The bridges are powered with 20-V excitation using three separate HP 3611A power supplies. The signal conditioning and data acquisition are identical to those used for the compression and tension bars. Spool specimens are fabricated from 2024-T351 aluminum (see figure 37(a)). The dimensions are similar to those used in the low-rate torsion experiments. The flanges of the specimens have larger outside diameters to match the impedance of the SHBs. The flanges are bonded directly to the incident and transmitter bars with Emerson and Cuming TRA-BOND 2106T two-part epoxy (see figure 37(b)). A post-test photograph of a fractured spool specimen is shown in figure 37(c).

Sample data from a torsion SHB experiment on a 2024-T351 aluminum specimen are shown in figure 38. Wave data are shown in figure 38(a). The solid black trace is the torque history in the incident bar recorded by gage A (T_A), and the dashed black trace is the torque history in the incident bar recorded by gage B (T_B). The gray trace is the torque history in the transmitter bar measured using gage C (T_C). A measure of dynamic torque equilibrium in the specimen is attained by comparing the torque histories measured by gages B and C. Gages B and C are positioned on the incident and transmitter bars so they are equidistant from the specimen. Since the bars are comprised of the same material, the elastic waves travel at the same velocity. Therefore, after the load pulse reaches the specimen, gage B records a time history of torque at the joint between the incident bar and the specimen. Likewise, gage C provides a torque history at the joint between the specimen and the transmitter bar. After a brief rise time, the torques

measured by gages B and C equilibrate at ~730 μs (figure 38(a)) showing dynamic torque equilibrium in the specimen. Reduced time history data of shear stress, shear strain rate, and shear strain are shown in figure 38(b). The shear stress (black trace) is proportional to the transmitted pulse, according to equation 41. The shear strain rate history, calculated with equation 39, ranges from 1030 s^{-1} early in the loading to 860 s^{-1} just prior to specimen failure. The average shear strain rate is 912.324 s^{-1} for the duration of the experiment. The strain history integrated from the strain rate is displayed as the black, dashed trace. Shear stress versus shear strain and effective stress versus equivalent strain curves are shown in figure 38(c). The shear stress, shear strain curve is calculated using equations 39, 40, and 41 and is represented by the solid black trace. The gray trace represents the effective stress versus equivalent strain curve calculated using equations 5 and 18.

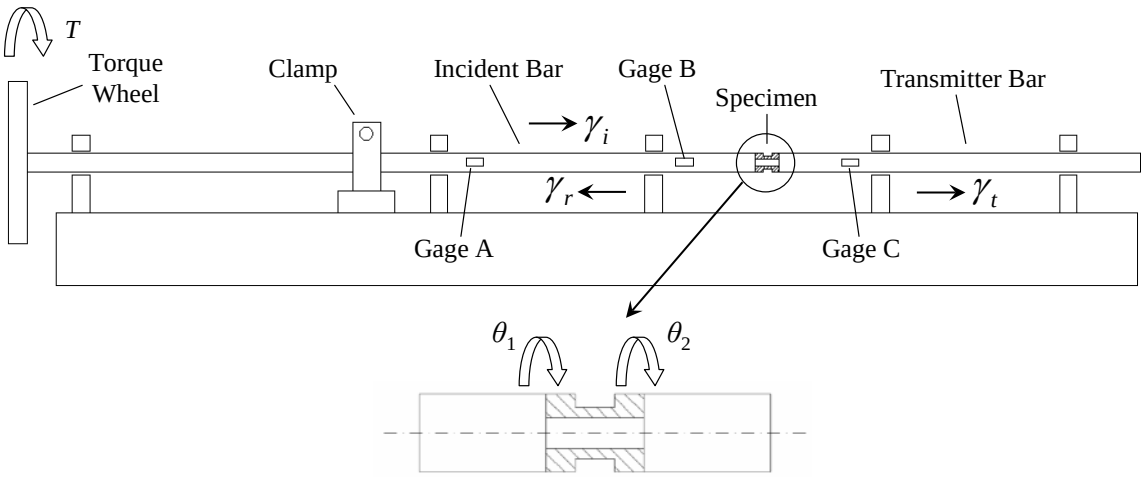

Figure 36. Sketch of a Stored-Torque SHB Apparatus

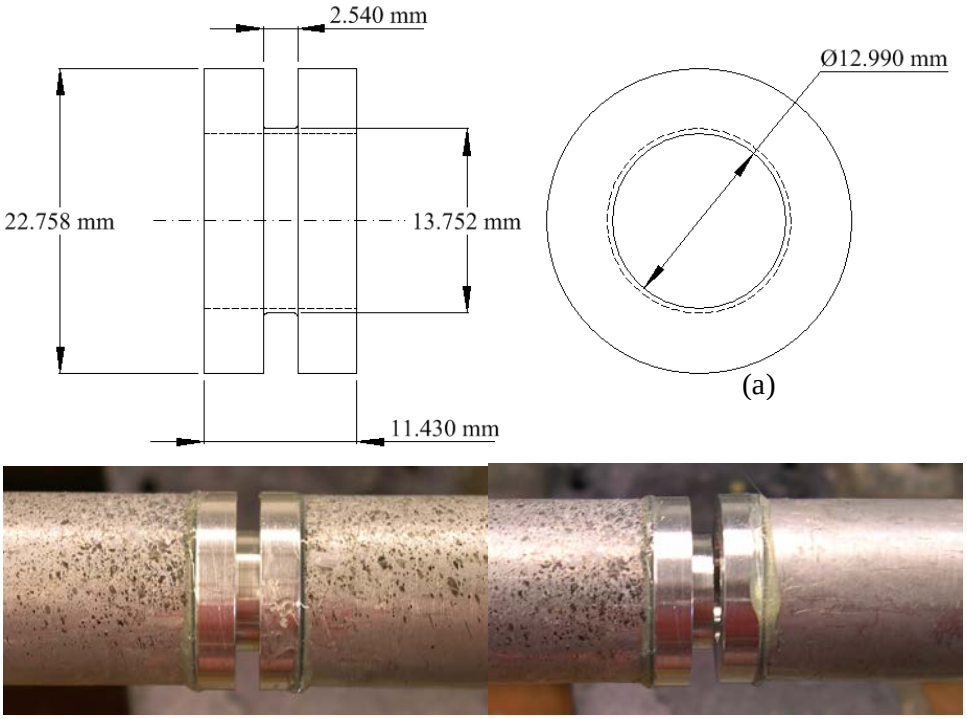

Figure 37. Spool-Shaped, Thin-Walled Tube Specimen for Torsion SHB Experiments: (a) Drawing, (b) Specimen Epoxied Between Incident and Transmitter Bars, and (c) Post-Test Photograph

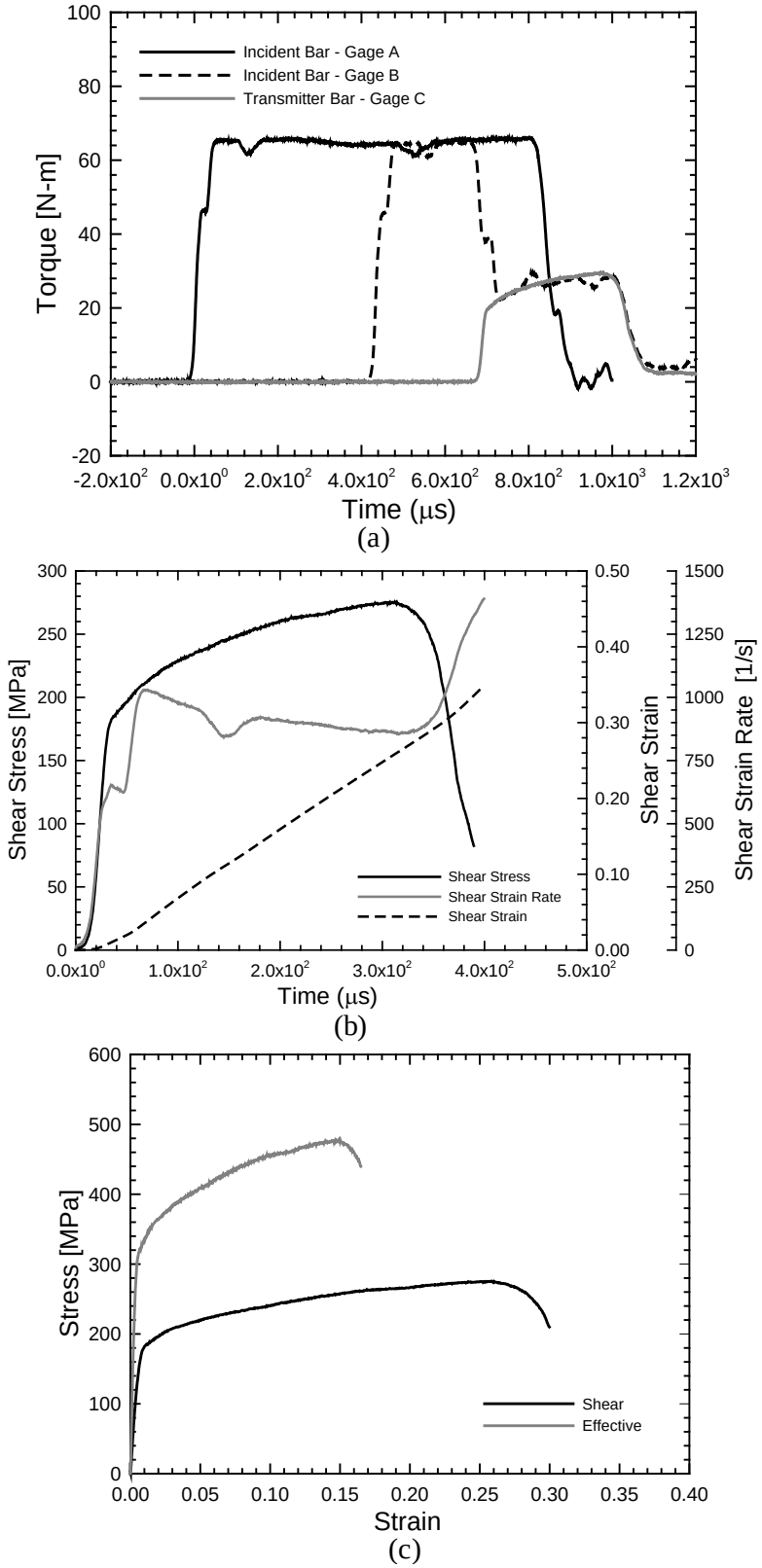

Figure 38. Specimen Data From a Torsion SHB Experiment on 2024-T351 Aluminum (a) Wave Data, (b) Reduced History Data, and (c) Stress Strain Data

3.3 DIGITAL IMAGE CORRELATION.

A 3D DIC was used to measure specimen surface displacements and strains for the majority of the experiments in the ductile fracture test program. The experimental technique and the camera system hardware used for both low- and high-strain rate tests are discussed. The details of image correlation for experimental mechanics applications are discussed thoroughly by Sutton, Orteu, and Schreier [3] and by Sutton, McNeil, and Schreier [36].

Consider a two-dimensional (2D) DIC system. In this system, a single digital camera is used to image a flat specimen that is parallel to the camera's sensor. If the specimen surface remains flat and maintains a constant working distance from the camera, the data provided by the single camera is sufficient to determine the deformation in the specimen. The main challenge of DIC, for this purpose, is to identify points in the reference frame (no deformation in the specimen) in a later frame where significant deformation has accumulated. Each image is comprised of pixels, each of which has a gray value associated with it. One pixel in the reference frame cannot be uniquely identified in the deformed frame, since there are typically many pixels in the deformed image that have exactly the same gray value as the pixel of interest in the reference image. To compensate for this, the region around the point of interest in the reference frame is included in the tracking algorithm. This region is typically referred to as a subset or a square N-by-N pixel box centered at the point of interest in the reference frame. Each pixel in the subset contains a gray value, so now there is significantly more information for a tracking algorithm to use. A nonrepetitive, high-contrast pattern is applied to the specimen surface to ensure that each subset has pixel gray value matrices distinctive enough to be identified by the tracking algorithm. This speckle pattern is typically applied using black spray paint spatter on a white spray paint base coat or vice versa. The tracking algorithm works by minimizing a sum of the squared differences (SSD) functions between the facet in the reference image and the facet in the deformed image. The SSD correlation function is written as [36]:

$$C(\bar{x},\bar{u}) = \sum \left[G(\bar{x}+\bar{u}) - F(\bar{x}) \right]^2 \tag{42}$$

where G and F are gray value matrices of the deformed and undeformed images, respectively. The $\bar{x}$ is a two-element vector specifying the center pixel location of the subset in the reference image, and $\bar{u}$ is a two-element vector specifying the horizontal and vertical displacements from the center of the subset in the reference image to the center of the potential subset in the deformed image. The tracking algorithm searches in the deformed image for a vector, $\bar{u}$, which minimizes $C(\bar{x},\bar{u})$.

The tracking algorithm described above only works well if the subset in the deformed image remains square. In many engineering applications, complex deformations arise and the subset shapes evolve significantly in the successive images. To account for this, shape functions are used to model the deformed shape of the subset. When shape functions are used to describe the deformed subset shapes, equation 43 becomes:

$$C(\bar{x},\bar{u}) = \sum \left[G\left(\xi\left(\bar{x}+\bar{u},\bar{p}\right)\right) - F\left(\bar{x}\right) \right]^2 \tag{43}$$

where ξ is the subset shape function vector that has a parameter vector $\overline{p}$. The B-spline shape functions are often used for this purpose. When all of the subsets in the reference frame are identified in the deformed image, displacement information is available at the center of each subset. Strain tensors can then be computed according to their continuum mechanics definitions. Malvern provides a good reference for the strain tensor definitions [37].

The experiments conducted in the ductile fracture test series require the use of 3D DIC because many of the specimens have 3D surface features. Three-dimensional objects cannot be resolved with only one camera. Therefore, two cameras must be used. This concept is explained by the sketch in figure 39. In the figure, the light gray trapezoids represent a mathematical model for the camera sensor. If only one camera is used, *C* in figure 39(a), a feature at point *Q* and point *R* will both be imaged on the camera's sensor at point *p*. Consequently, there is no way to differentiate between these two points using only one camera. If information from a second camera is added, *C′* in figure 39(b), the difference between *Q* and *R* can be determined. The points *Q* and *R* are imaged at point *q′* and *r′*, respectively, in the second camera's sensor. This is known as stereo-triangulation, and it is only possible if the rays from each camera are known in the same coordinate system. Therefore, the two-camera stereo rig must be calibrated in the same world coordinate system.

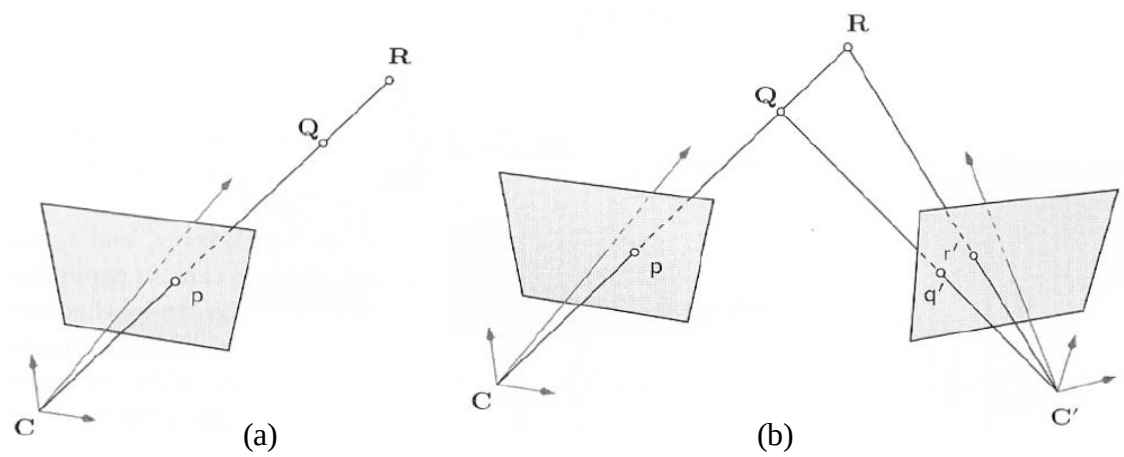

Figure 39. Sketch Showing Two Cameras Are Necessary to Resolve 3D Features: (a) One Camera and (b) Two Cameras [3]

The calibration process establishes transformations between the common world coordinate system and the sensor plane coordinate system for each camera. This consists of three separate transformations for each camera (see figure 40(a)). The first is a transformation between the 3D world (R_w) and the 3D camera coordinate system (R_c). The second is a transformation between the 3D camera system and the 2D image plane coordinate system that is located at the center of the camera sensor plane (R_r). Finally, a transformation is made between image plane coordinate system and the sensor coordinate system (R_s) where the 2D sensor-plane spatial position is transformed into pixel coordinates. In the calibration process, several camera parameters are sought. These include four intrinsic parameters that are functions of the camera focal length and the length-to-pixel conversion for the sensor plane and six extrinsic parameters that include three

components of a translation vector and three rotations required to go from R_w to R_c. Each camera is calibrated independently by capturing images of a calibration grid. For each calibration image captured, a system of equations relating the sensor position of the calibration grid points to the camera parameters is formed. The solution of these equations provides the camera parameters discussed above and the basis to transform camera sensor coordinates to world coordinates. After calibration, the transformations between both R_c to R_w and R_c to R_w in figure 40(b) are known.

Two systems were used in this research. A low-rate system was used for the ductile fracture tension test series and the combined loading test series. This system consisted of two Point Gray Research GRAS-20S4M-C cameras with 1624-by-1224 pixel resolution. The cameras were equipped with Schnieder 35-mm lenses and acquire images at a maximum rate of 19 images per second. The low-rate cameras are shown in figure 15. Sample data from the low-rate camera system is shown in figures 14, 16, 17, and 21, and in several figures in appendix E.

A high-rate system was used for the dynamic punch experiments. This system consisted of two Photron SA1.1 cameras with 1024-by-1024 pixels at full resolution. Tamron 90-mm lenses were used with the Photrons. Frame rates of 125,000 fps were achievable at a reduced resolution of 256-by-128 pixels. These settings are typical for the dynamic punch experiments conducted in this research. The high-speed camera system is shown on a custom-designed vertical-mount fixture in figure 30.

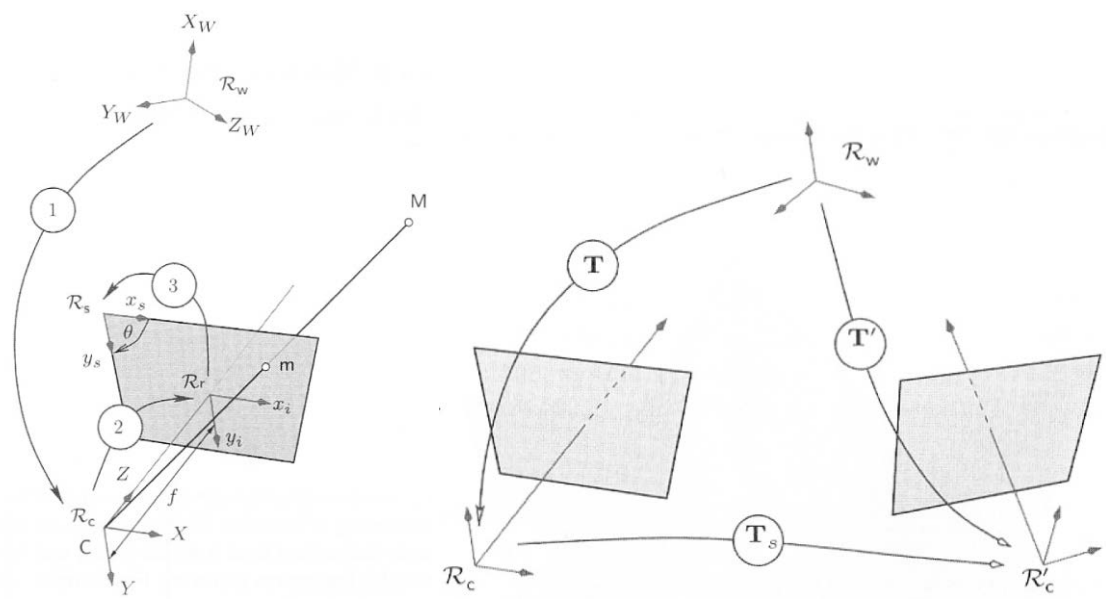

(a) (b)

Figure 40. Transformations Between Coordinate Systems for (a) a Single Camera Model and (b) a Stereo Rig Camera System [3]

3.4 DATA MANAGEMENT AND TRANSFER.

This project was a team effort that required the collaboration of several different entities. The Dynamic Mechanics of Materials Laboratory (DMML) at The Ohio State University was responsible for conducting the tests and organizing the experimental data for the test plan outlined in section 2 of this report. The team at GWU's National Crash Analysis Center (NCAC) was responsible for developing the plasticity and fracture models of MAT224. Therefore, it was necessary to transfer the data from the DMML to the NCAC. A data-transfer procedure document was developed to outline the data required for NCAC to develop the model. The data-transfer procedure document is found in appendix F.

4. EXPERIMENTAL CHARACTERIZATION OF THE PLASTIC DEFORMATION OF 2024 ALUMINUM IN TENSION, COMPRESSION, AND SHEAR.

This section discusses the data generated from the plastic deformation characterization test program shown in tables 2 and 3. The data presented are the results of the low-rate tension (on thin, smooth specimens), compression, and torsion experiments, as well as the compression, tension, and torsion SHB tests described in section 3.

4.1 EXPERIMENTAL DATA FROM 12.7-mm-THICK 2024-T351 PLATE.

Stress-strain curves from tension, compression, and torsion tests conducted on a 12.7-mm 2024-T351 plate at room temperature over a wide range of strain rates are shown in figure 41. True stress versus true strain curves from tension and compression tests are shown in figure 41(a and b, respectively). All tension and compression stress-strain curves in figure 41 were constructed from experiments on specimens oriented in the plate's rolled direction (0°). Shear stress versus shear strain curves from torsion tests are shown in figure 41(c). Figure 41 shows the material is nearly strain-rate insensitive in tension and torsion over the strain-rate ranges tested. In compression, the material is strain-rate insensitive at strain rates ranging from 1.0×10^{-4} s^{-1} to 5.0×10^{3} s^{-1}. At strain rates higher than 5.0×10^{3} s^{-1}, strain rate effects are present. Strain rates above 5.0×10^{3} s^{-1} are beyond the capabilities of the tension and torsion SHBs used in this project. It is likely that tension and shear data above 5.0×10^{3} s^{-1} would exhibit strain rate sensitivity as well.

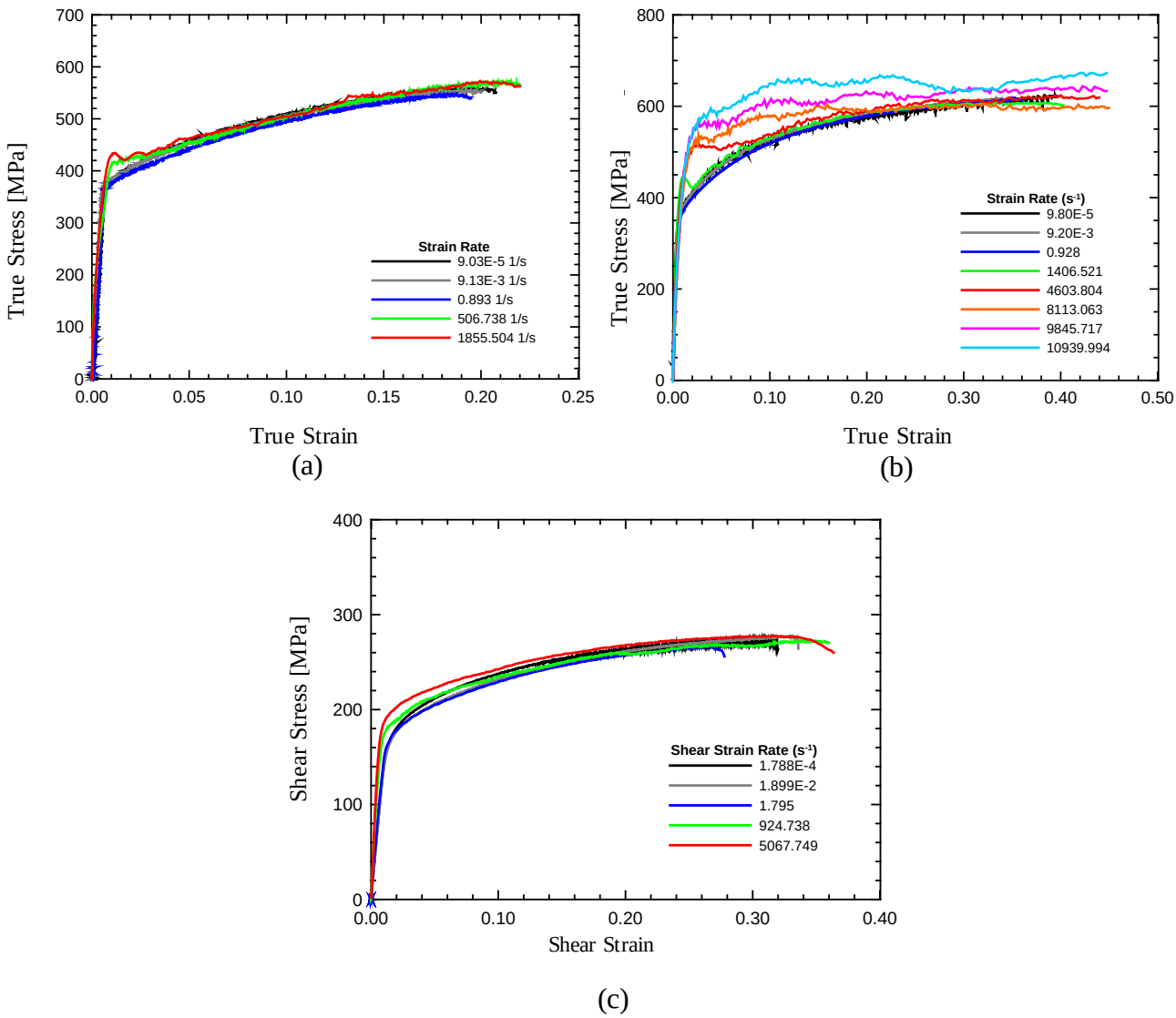

Figure 41. Stress vs. Strain Curves From (a) Tension, (b) Compression, and (c) Torsion Tests Conducted Over a Wide Range of Strain Rates on a 12.7-mm-Thick 2024-T351 Aluminum Plate

Effective stress data from tension, compression, and torsion experiments are plotted versus the logarithm of strain rate in figure 42. Stress values were extracted at two true equivalent strains (0.075 and 0.15), and are plotted versus the strain rate ($\dot{\varepsilon}$) in figure 42(a and b), respectively. Figure 42 shows the material response is insensitive to strain rate in tension compression and shear at strain rates less than 5.0×10^3 s^{-1}. In compression, at rates above 5.0×10^3 s^{-1}, rate sensitivity is evident. The repeatability of the experimental results is also shown in figure 42. Force versus displacement or torque versus rotation curves from each experiment conducted in the strain rate test series are presented in appendix D. These curves were transferred to GWU's NCAC, as outlined by the data-transfer procedure in appendix C.

Stress strain curves from tension, compression, and torsion experiments conducted at an equivalent strain rate of 1.0 s^{-1} over a wide range of temperatures are shown in figure 43. True stress versus true strain curves from tension and compression experiments are shown in figure 43 (a and b, respectively). All tension and compression stress strain curves shown in figure 43 are determined from tests on specimens oriented in the plate's rolled direction (0°). Shear stress versus shear strain curves from torsion experiments are shown in figure 43(c). The strength of 2024-T351 aluminum decreases monotonically with increasing temperature in tension, compression, and torsion. The strain-hardening behavior of the material changes significantly between 150°C and 300°C. At 150°C and below, the material exhibits strain hardening that could be well represented by a power law strain-hardening model. Above 300°C, the material exhibits near-elastic, perfectly plastic behavior. The data at 300°C shows softening behavior with increasing strain. This phenomenon is exacerbated by the necking localization in the tension data, but is also present in the compression and torsion data. The rapid onset of the necking localization in tension at 300°C limits the usefulness of the corresponding true-stress, true-strain curve in figure 43(a). Because the cross-sectional area of the specimen was not measured during the experiment, the curve is valid only to a true strain of roughly 0.10. Other researchers have observed this softening behavior and state it is due to dynamic recovery and recrystallization, where dislocations are destroyed by increasing strain and new strain-free grains are created during the deformation process [12 and 38]. Dynamic recovery is noted to have a more prominent softening effect on face-centered cubic (FCC) materials (aluminum is FCC) than body-centered cubic and hexagonal close packed materials. Also, recrystallization typically only occurs in FCC materials [38].

Stress data from tension, compression, and torsion experiments are plotted versus temperature in figure 44. Effective stress values extracted at two equivalent strains (0.075 and 0.15) are plotted versus temperature in figure 44 (a and b, respectively). In general, the compressive stress of 2024-T351 aluminum is greater than the tensile and shear stress at all temperatures tested. Repeatability of the temperature test series data is shown in figure 44. Force versus displacement or torque versus rotation curves from each experiment conducted in the temperature test series are presented in appendix G. These curves were transferred to GWU's NCAC as outlined by the data transfer procedure in appendix F.

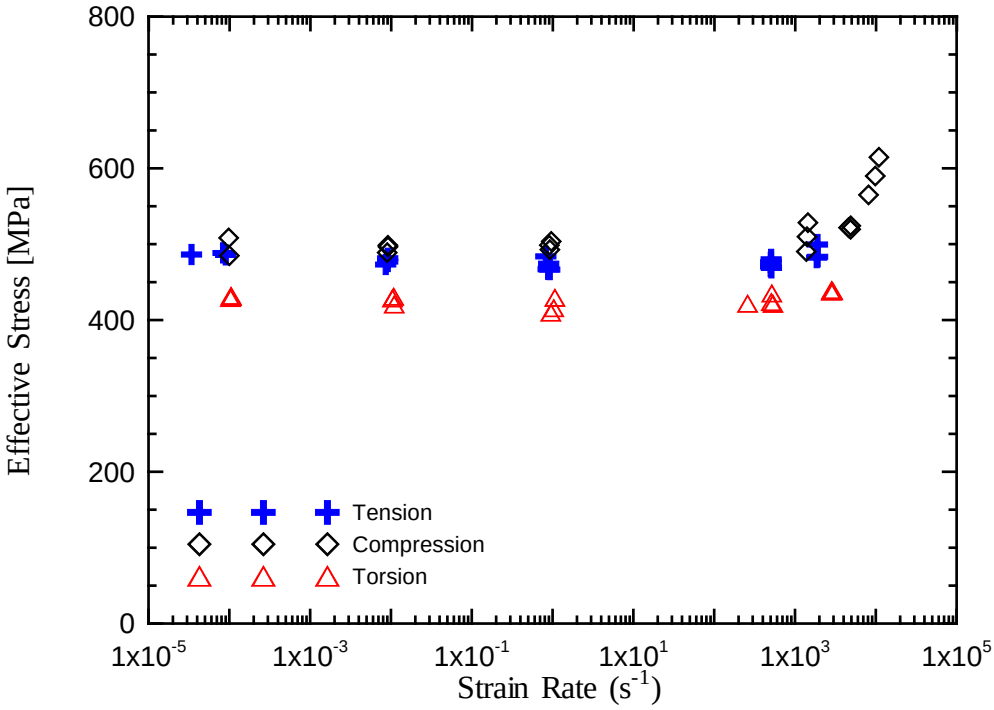

(a)

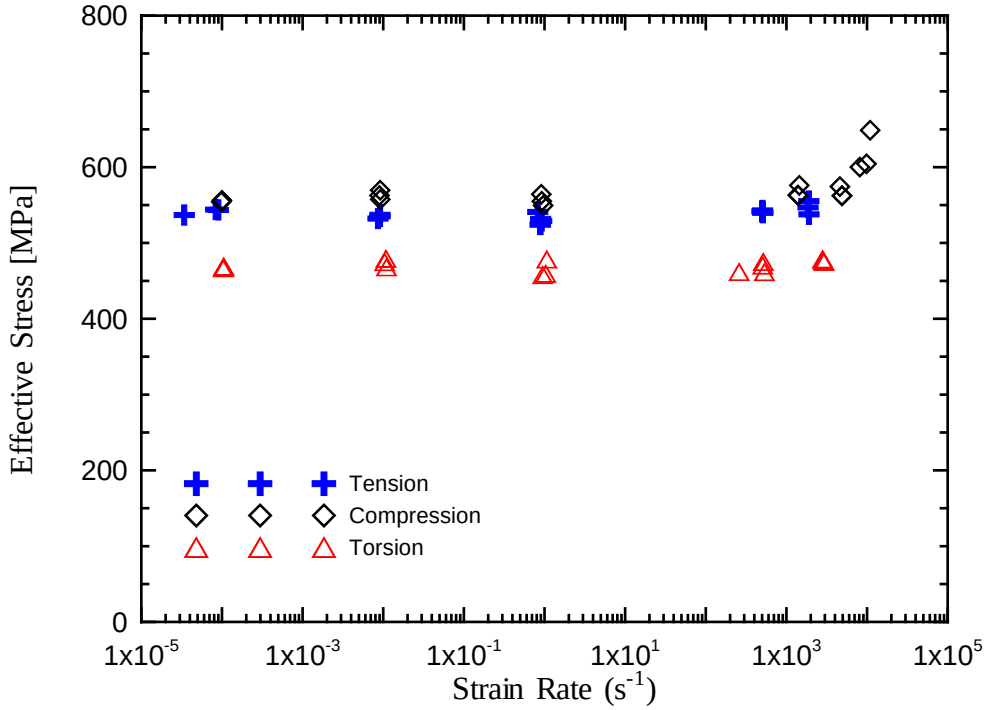

(b)

Figure 42. Effective Stress vs. Strain Rate From Tension, Compression, and Torsion Tests on a 12.7-mm-Thick 2024-T351 Aluminum Plate: (a) Effective Stress Values Extracted at Equivalent Strains of 0.075 and (b) Effective Stress Values Extracted at Equivalent Strains of 0.15

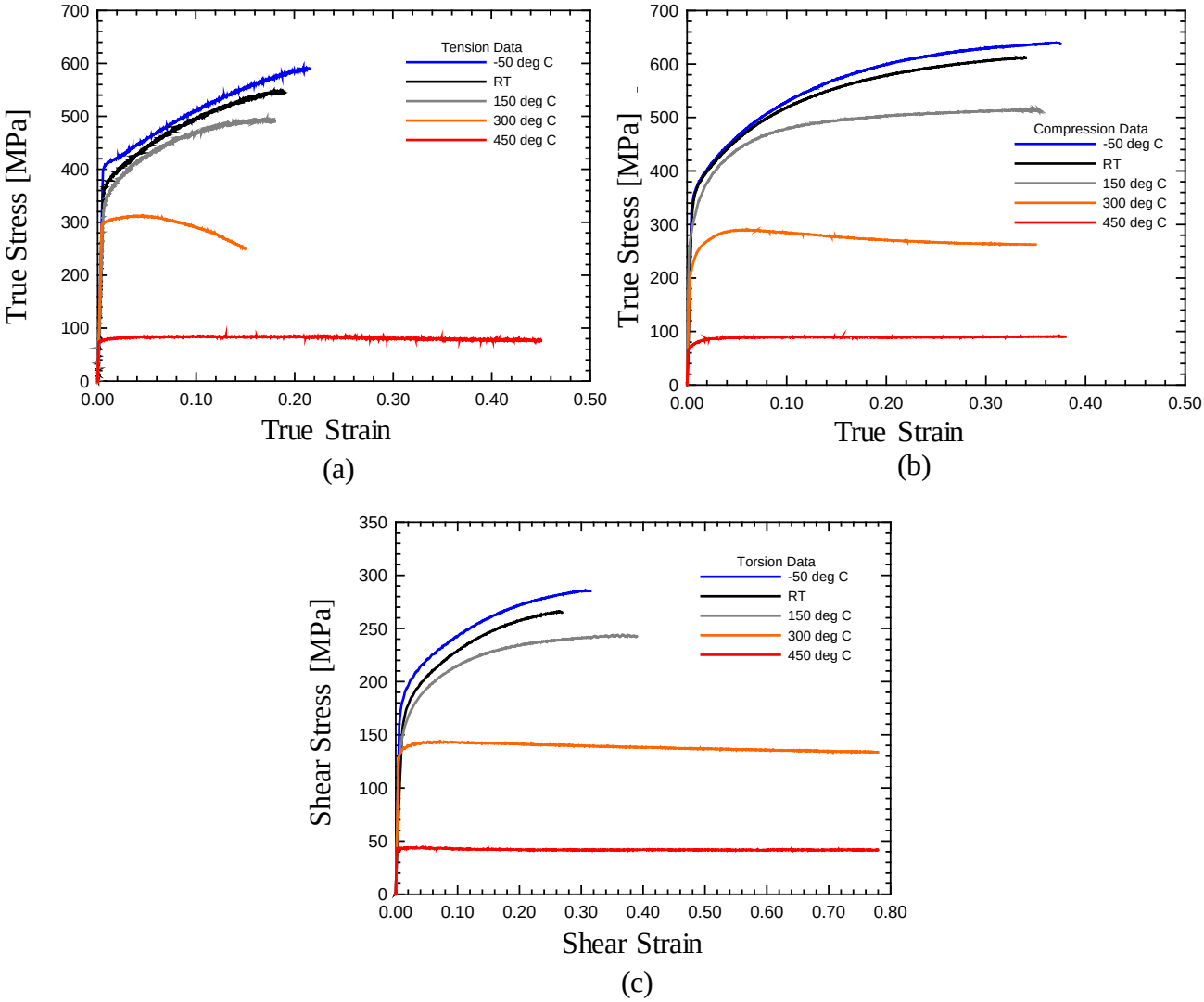

Figure 43. Stress vs. Strain Curves From (a) Tension, (b) Compression, and (c) Torsion Tests Conducted Over a Wide Range of Temperatures on 12.7-mm-Thick 2024-T351 Plate

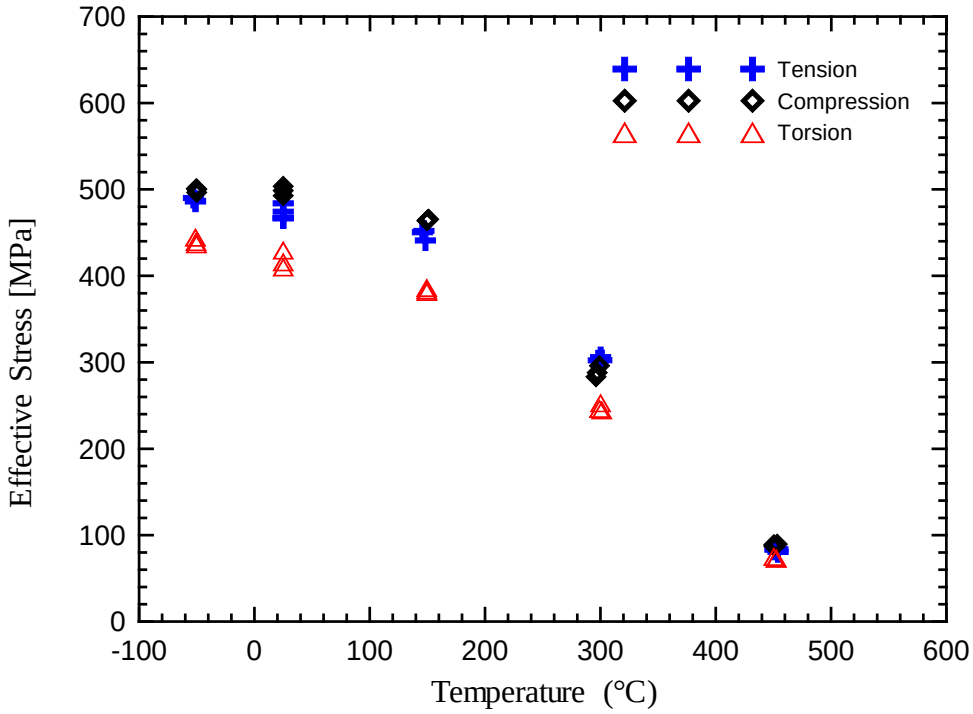

(a)

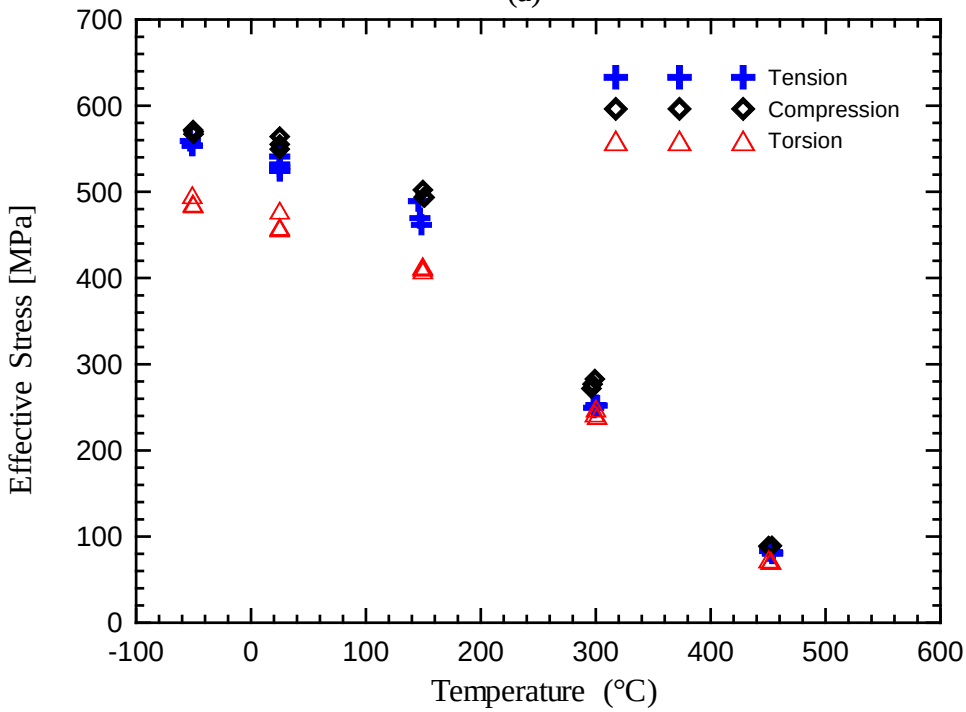

(b)

Figure 44. Stress vs. Temperature From Tension, Compression, and Torsion Tests on a 12.7-mm-Thick 2024-T351 Plate: (a) Effective Stress Values Extracted at Equivalent Strains of 0.075 and (b) Effective Stress Values Extracted at Equivalent Strains of 0.15

True stress versus true strain curves from tension and compression experiments conducted on specimens fabricated in the orientations shown in figure 4 can be observed in figure 45(a and b, respectively). The experiments shown in figure 45 were conducted at room temperature and an equivalent strain rate of 1.0 s^{-1}. In compression, the stress-strain curves are similar in the 0°, 90°, and thickness directions. The material is weaker in the ±45° directions and, clearly, the plate is anisotropic. Similar results are found in tension. The 0° and 90° strengths are nearly identical; however, the ±45° directions are weaker. In both tension and compression, the 45° stress is identical to the -45° stress, showing that the *X*-*Z* plane is a symmetry plane. This is evidence that the plate is orthotropic (has three symmetry planes), which is common for rolled aluminum material [13]. Force versus displacement curves from each experiment conducted in the anisotropy test series are presented in appendix G. These curves were transferred to GWU's NCAC as outlined by the data-transfer procedure in appendix F.

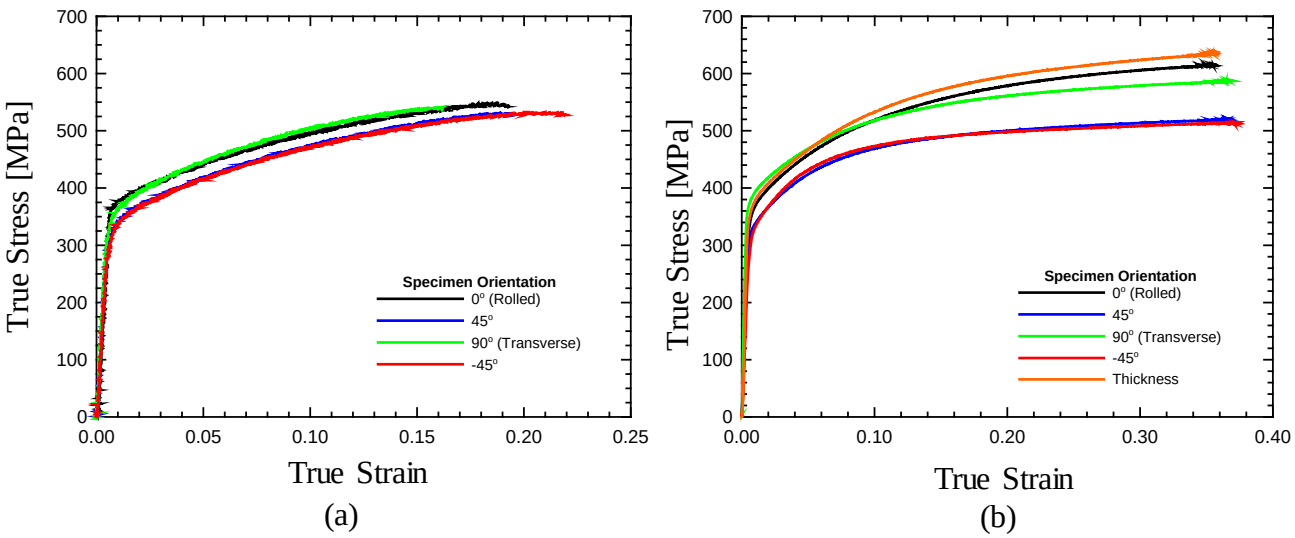

Figure 45. True Stress vs. True Strain Curves From (a) Tension and (b) Compression Tests Conducted on Specimens Fabricated in Several Orientations Within the 12.7-mm-Thick 2024-T351 Plate

Effective stress versus equivalent strain curves from select tension, compression, and torsion experiments are shown in figure 46. The effective stress is defined by equation 5 and the equivalent strain is defined by equation 18. The tension, compression, and torsion test data shown in figure 46 are from experiments conducted at an equivalent strain rate of 1.0 s^{-1} at room temperature. The tension and compression specimens are aligned in the plate's rolled direction and the torsion specimens are aligned in the plate's thickness direction (see figure 4). The comparison in figure 46 shows that simple J_2 flow theory cannot adequately describe the material behavior. The J_2 flow theory uses one universal effective stress versus equivalent plastic strain curve. The theory can model only those materials for which effective stress-strain curve in shear coincides with those in compression and tension. This is clearly not the case for 12.7-mm-thick 2024-T351 aluminum because the shear data lies well below both the tensile and compressive data. Figure 46 shows that the material has roughly the same yield point in tension and compression; however, the compression curve exhibits more strain hardening.

The torsional effective stress versus effective strain curve lies well below all of the compression and tension curves, regardless of orientation. This is evidence that the low equivalent stress from the torsion experiments cannot be due to anisotropy and specimen orientation alone.

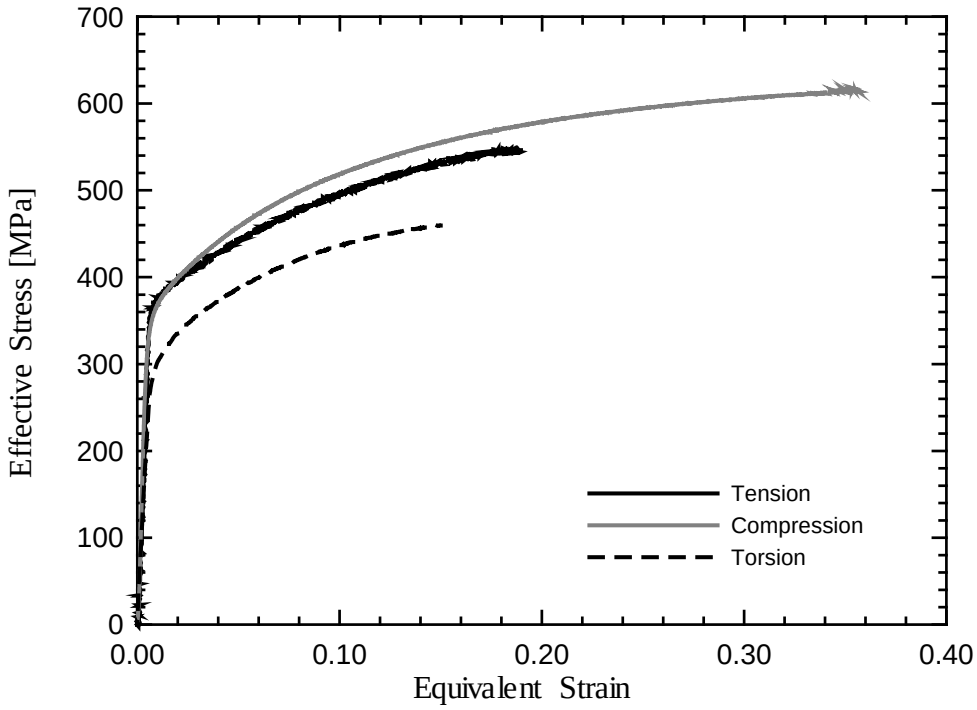

Figure 46. Comparison of Effective Stress vs. Equivalent Strain Curves From Tension, Compression, and Torsion Experiments

Averaged ratios of tensile effective stress to compressive effective stress and torsional effective stress to compressive effective stress at all five temperatures are shown in figure 47. The figure shows that the torsion-to-compression stress ratio maintains at nearly the same level over the entire temperature range. This indicates that the effective stress representation from J_2 flow theory will be inadequate to describe the material behavior at all temperatures. Interestingly, this characteristic is maintained at elevated temperatures even after the material has significantly evolved and transitioned to near-elastic, perfectly plastic behavior. Figure 47 also shows that the tensile stress is roughly 95% of the compressive stress for all temperatures except 300°C, where the tensile necking localization affects the data.

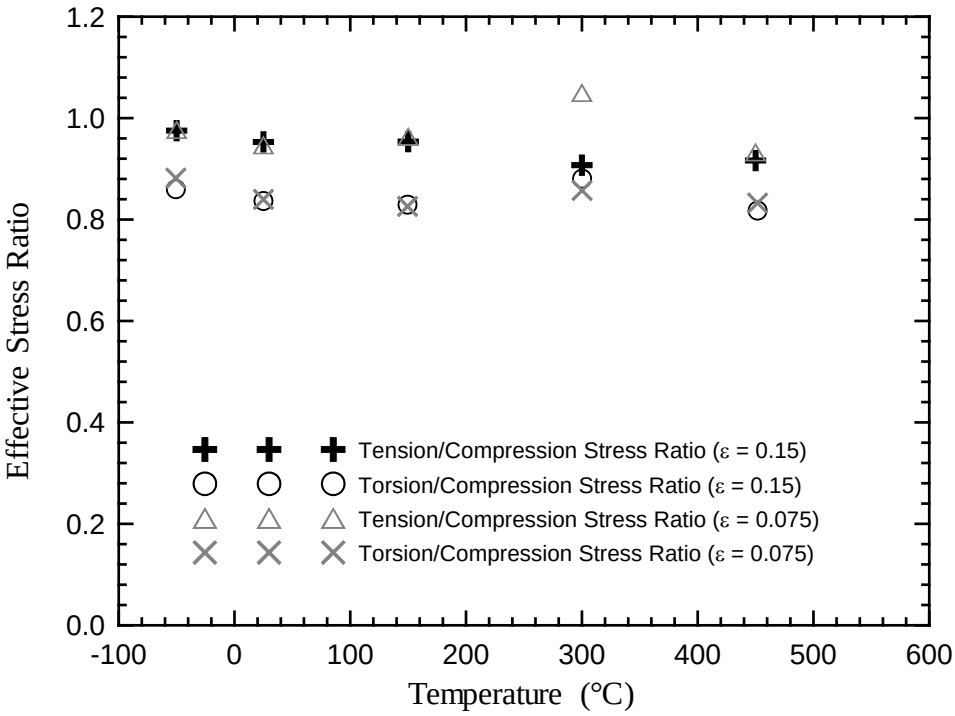

Figure 47. Tension/Compression Effective Stress Ratio and Torsion/Compression Effective Stress Ratio at Two Equivalent Strains ($\bar{\varepsilon} = 0.15$ and $\bar{\varepsilon} = 0.075$)

4.2 EXPERIMENTAL DATA FROM 6.35-mm-THICK 2024-T351 PLATE.

Results from tension and compression tests conducted on 6.35-mm-thick 2024-T351 plate are shown in figure 48 (a and b, respectively). The data shown in figure 48 are from room temperature experiments conducted on tensile and compression specimens oriented in the rolled direction of the plate (figure 3) at two strain rates (1.0 s^{-1} and 500 s^{-1} in tension and 1.0 s^{-1} and ~1200 s^{-1} in compression). Both the tension and compression data show no strain rate sensitivity with respect to the stress magnitudes. In tension, however, the fracture strains are significantly less at 1.0 s^{-1} (~0.14) than at 500 s^{-1} (~0.20). Tensile fracture strains at each strain rate were repeatable. Force versus displacement curves from each experiment conducted on the 6.35-mm-thick plate are presented in appendix G. These curves were transferred to GWU's NCAC as outlined by the data transfer procedure in appendix F.

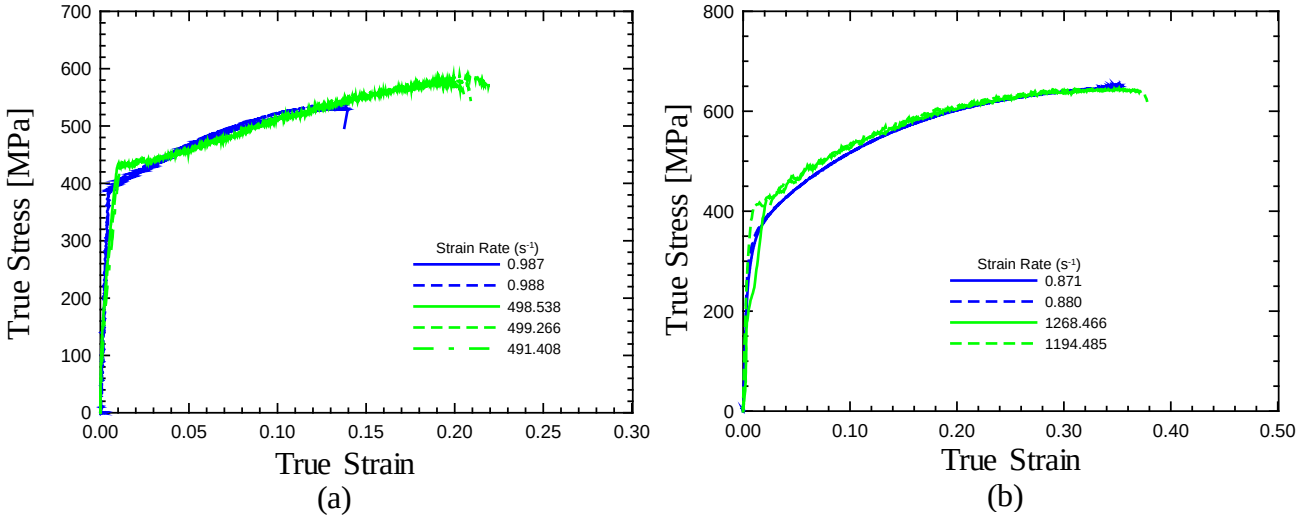

Figure 48. Stress vs. Strain Curves From (a) Tension and (b) Compression Tests Conducted at Two Strain Rates on a 6.35-mm-Thick 2024-T351 Aluminum Plate

4.3 EXPERIMENTAL DATA FROM 3.175-mm-THICK 2024-T3 SHEET.

Results from tension and compression tests conducted on a 3.175-mm-thick 2024-T3 sheet are shown in figure 49 (a and b, respectively). The data shown in figure 49 are from room temperature experiments conducted on tensile and compression samples oriented in the rolled direction of the sheet (figure 3) at two strain rates (1.0 s^{-1} and 500 s^{-1} in tension and 1.0 s^{-1} and ~1200 s^{-1} in compression). Both the tension and compression data show no strain rate sensitivity with respect to the stress magnitudes. In tension, however, the fracture strains are significantly less at 1.0 s^{-1} (between 0.13 and 0.19) than at 500 s^{-1} (~0.23). Tensile fracture strains at 500 s^{-1} were repeatable; however, fracture strains at 1.0 s^{-1} ranged from ~0.13 to 0.19. Force versus displacement curves from each experiment conducted on the 3.175-mm-thick sheet are presented in appendix G. These curves were transferred to GWU's NCAC as outlined by the data transfer procedure in appendix F.

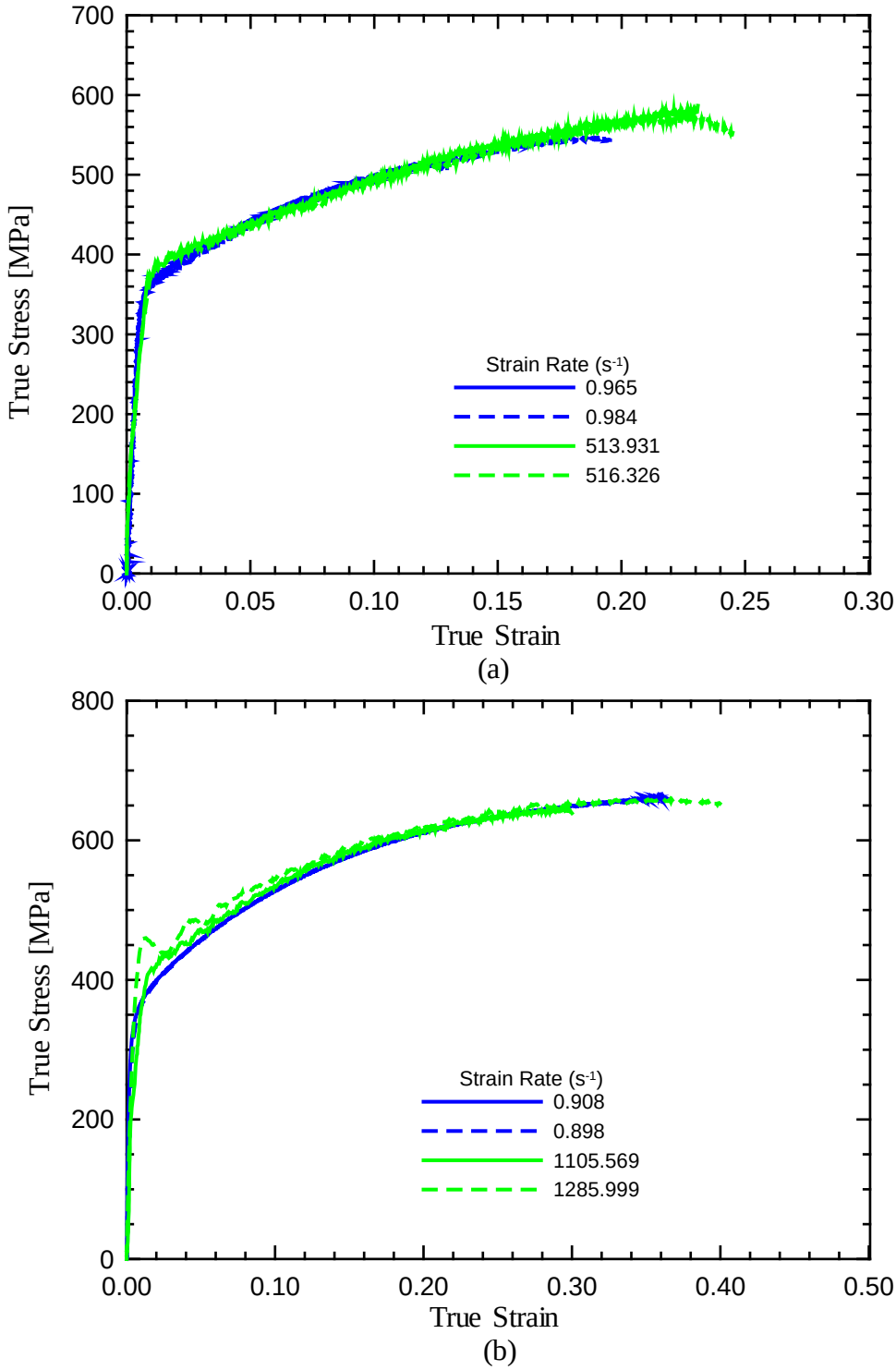

Figure 49. Stress vs. Strain Curves From (a) Tension and (b) Compression Tests Conducted at Two Strain Rates on a 3.175-mm-Thick 2024-T3 Aluminum Sheet

4.4 DATA COMPARISON: 12.7- AND 6.35-mm-THICK 2024-T351 PLATE AND 3.175-mm-THICK 2024-T3 SHEET.

Stress-strain curves from the three aluminum products are shown together in figure 50. Tension data are shown in figure 50(a) and compression data are shown in figure 50(b). Blue, green, and black traces represent the 12.7-, 6.35-, and 3.175-mm-thick stock materials, respectively. Solid traces represent data at a strain rate of ~1.0 s^{-1}, while dashed traces represent dynamic (SHB) data. In tension, the 6.35-mm-thick plate curves are slightly higher than those from the other two, which are nearly identical. At low strain rates, the tensile fracture strain of the 6.35-mm-thick plate is substantially less than that of the other two stock materials. In compression, the 3.175- and 6.35-mm-thick stocks have nearly identical response, while the 12.7-mm-thick stock exhibits less strain hardening.

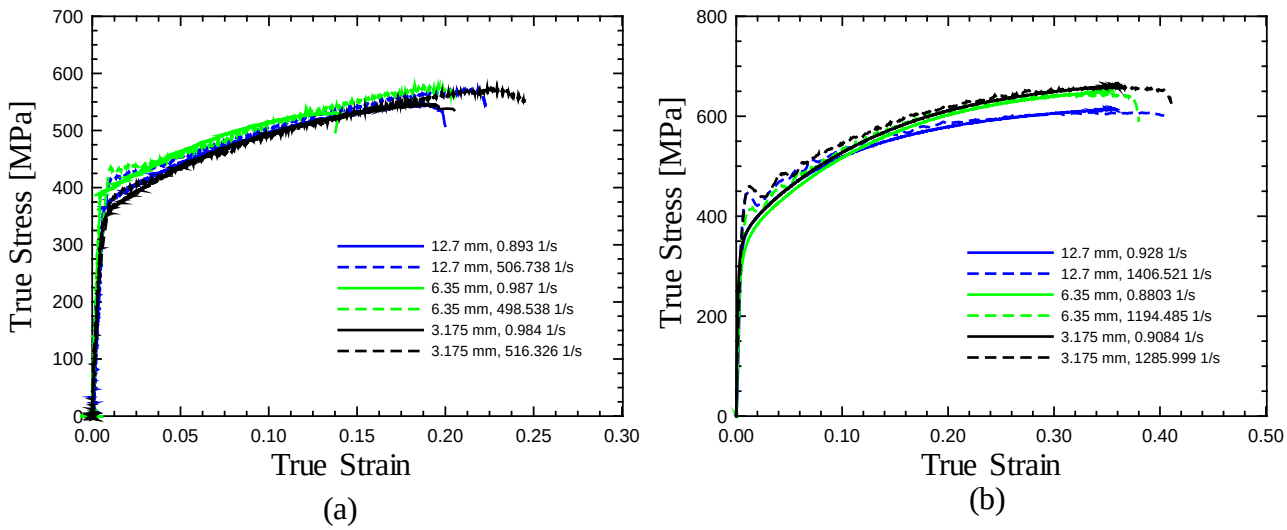

Figure 50. Stress-Strain Comparison of the Three 2024 Aluminum Stocks: (a) Tension and (b) Compression

5. DUCTILE FRACTURE OF 2024-T351 ALUMINUM.

Results of the ductile fracture test program are presented in this section. Experimental data from the tests summarized in tables 4 through 8 are used to investigate the fracture behavior of 12.7-mm-thick 2024-T351 aluminum plate. The experiments include tension tests on specimens with various geometries, pure shear (torsion) tests, combined loading (tension–torsion and compression–torsion), and the punch experiments discussed in section 2.2. The experimental techniques used for each of these experiments are discussed in section 3.

5.1 TENSION EXPERIMENTS.

The tension test data are used with a coupled experimental-numerical technique to generate data points for the fracture locus. The results of numerical simulations of the experiments are compared to experimental data to determine the stress state history and the equivalent plastic strain history of the specimen at the region where fracture initiates. Numerical simulations are

conducted using LS-DYNA. Simulated force versus displacement curves are matched to experimentally determined curves using an iterative process, which is described in part 2 of this report [4]. The experimental force versus displacement curves are presented here. These data are from the plane stress, axisymmetric, and plane strain test series summarized in tables 4, 5, and 6.

Plane stress data are presented in figure 51. Four plane-stress specimen geometries are represented in the plot. The black traces correspond to smooth dogbone specimens. Blue, red, and green traces correspond to specimens with notch radii of 4.76, 1.98, and 0.396 mm, respectively. Displacements were measured using a DIC extensometer. Initial extensometer lengths varied with the different geometries. The extensometer lengths used (for plane-stress, axisymmetric, and plane-strain specimens) are summarized in table 9. Curves from three tests on each specimen geometry are shown in the plot. These specimens are very thin (~0.76 mm) and have small cross-sectional areas; thus, minor differences in the minimum notch width and thickness (±0.025 mm) lead to spread in the load magnitudes. The displacement at failure from tests on the same geometry, however, is quite consistent. As the notch radius decreases, transverse stresses in the notch region increase. This leads to increasing axial loads and decreasing stress triaxialities. As stress triaxiality decreases, the ductility decreases, resulting in successively lesser failure displacements from SG1 to SG4.

Axisymmetric data are shown in figure 52. Six axisymmetric specimen geometries are represented in the plot. Black traces correspond to specimens with smooth gage sections. Blue, red, green, orange, and brown traces correspond to specimens with notch radii of 14.50, 9.14, 6.10, 4.47, and 3.05 mm, respectively. Displacements were measured using DIC extensometers. Axial loads for these tests are much more repeatable since the cross-sectional specimen areas are significantly larger than those from the plane stress test series. There is also good repeatability in failure displacement for each of the specimen geometry groupings. The specimens with smooth gage sections, SG5, gave the highest spread in failure displacement. The general trends observed in the plane stress data are also evident here: axial load increases and failure displacement decreases with decreasing triaxiality or decreasing notch radii.

Plane strain data from three specimen geometries are shown in figure 53. Black traces correspond to specimens with smooth gage sections. Blue and red traces correspond to specimens with notch radii of 13.97 and 4.76 mm, respectively. Load magnitudes and failure displacements from the plane strain test series were repeatable. The general trend of increasing axial load and decreasing failure displacement with decreasing triaxiality (notch radius) is observed.

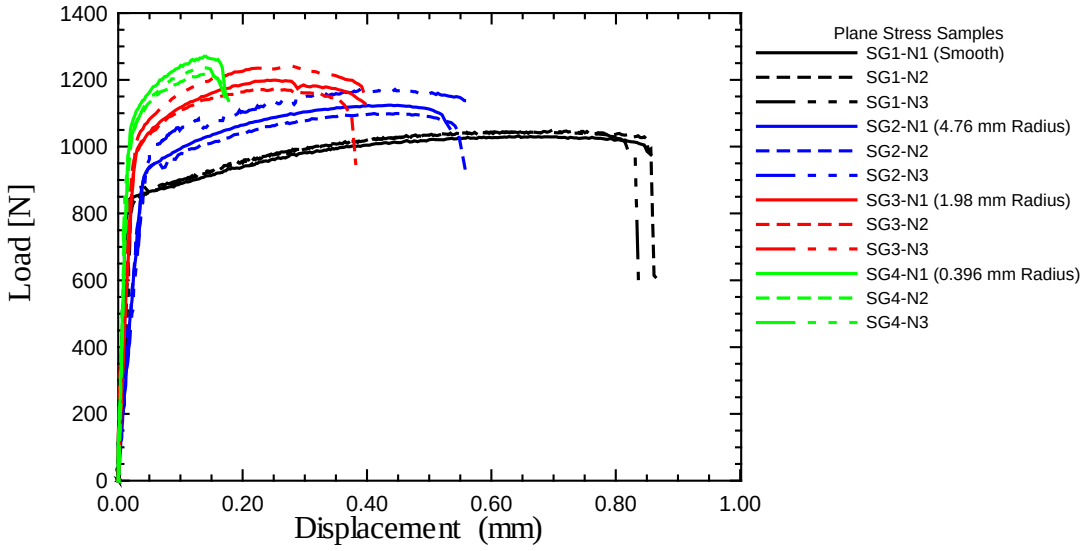

Figure 51. Load vs. Displacement Curves From the Plane Stress Tension Test Series

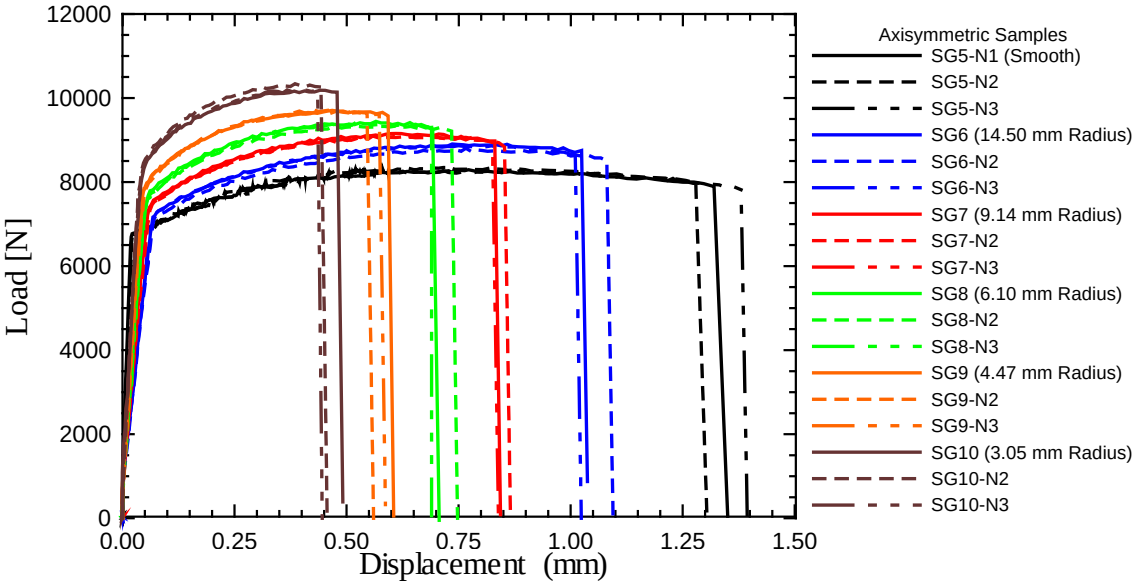

Figure 52. Load vs. Displacement Curves From the Axisymmetric Tension Test Series

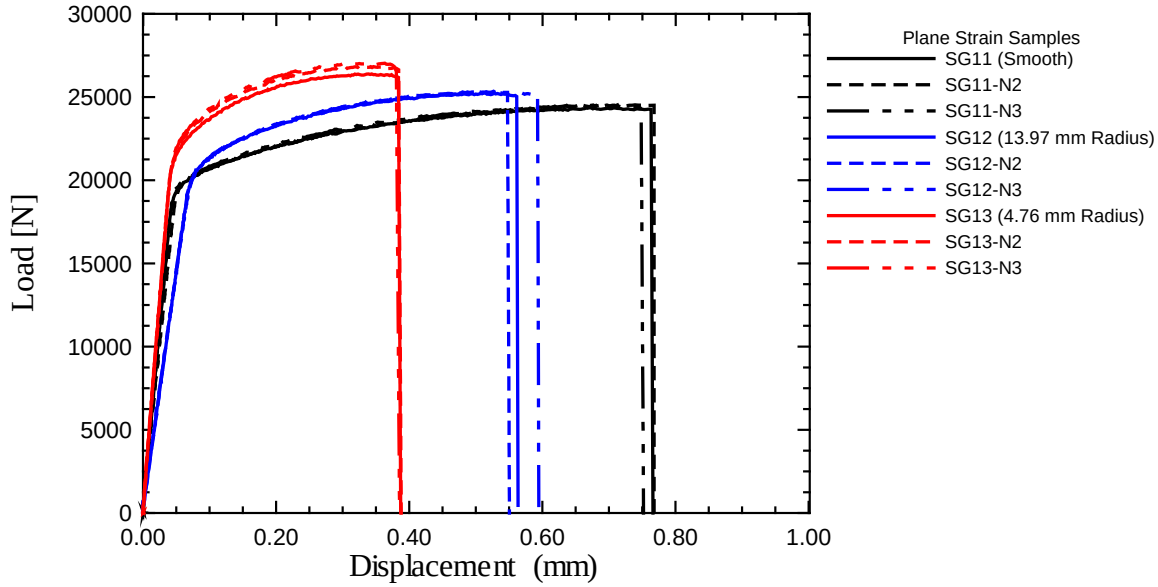

Figure 53. Load vs. Displacement Curves From the Plane Strain Tension Test Series

5.2 COMBINED LOADING EXPERIMENTS.

Combined tension-torsion and compression-torsion tests on thin-walled tubes fabricated from 2024-T351 aluminum were conducted to generate additional fracture locus data points. The combined loading experimental program is described in section 2.2 and the specifics of the experiments are described in section 3.1.3. Combined loading experiments are desirable for the purpose of constructing a fracture locus for two reasons. First, the experiment can be controlled, so the stress-state history remains nearly constant for the duration of the experiment. Second, the specimen geometry is simple enough that the stress state can be estimated using the load and torque histories, and the strain state (on the surface of the specimen) can be determined experimentally using 3D DIC. If the specimen does not buckle, the stress triaxiality and Lode parameter in the gage section can be computed directly from experimental load and torque measurements using equations 13 and 14, respectively. Surface strain data from DIC measurements can be used to determine equivalent plastic fracture strain. The tube specimen is thin; therefore, it is assumed that stress and strain gradients through the thickness of the gage section are minimal.

Parallel numerical simulations were run to determine the state of stress and the equivalent plastic fracture strain in an alternative way. Force versus displacement and torque versus rotation curves from the simulations were compared to those that were measured experimentally. The stress state and equivalent plastic fracture strain of the element where fracture initiates is tracked in the simulation. The details of this comparison are found in part 2 of this report [4]. The experimental data are presented here.

Axial load versus displacement and torque versus rotation for tests conducted at an average axial stress to shear stress ratio, $\frac{\sigma_x}{\tau_{xy}}$, of 2.59 (tension-torsion) are shown in figure 54 (a and b, respectively). Test data at an axial-stress to shear-stress ratio of 1.15 and 0.0 (pure shear and torsion) are shown in figures 55 and 56, respectively. The axial displacement and rotation data shown in figures 54, 55, and 56 were extracted from 3D DIC data by tracking the relative displacement and rotation of two points, initially 6.35 mm apart, located on the gage section of the specimen. These points are shown in figure 57. Figure 57(a) shows the initial tracking point positions, prior to any deformation, overlaid on the specimen *y*-coordinate contour. Figure 57(b) shows the tracking point positions just prior to specimen fracture overlaid on the maximum principal strain contour. Axial load versus displacement and torque versus rotation for tests conducted at an average axial stress to shear stress ratio, $\frac{\sigma_x}{\tau_{xy}}$, of -0.92 (compression-torsion) are shown in figure 57(a and b, respectively). Displacement and rotation data for the compression-shear experiments were determined from 3D DIC data by tracking the relative motion of two points, initially 3.175 mm apart, on the gage section of the specimen. These points are shown in figures 58 and 59. Tracking point positions for the remainder of the experiments are presented in appendix E.

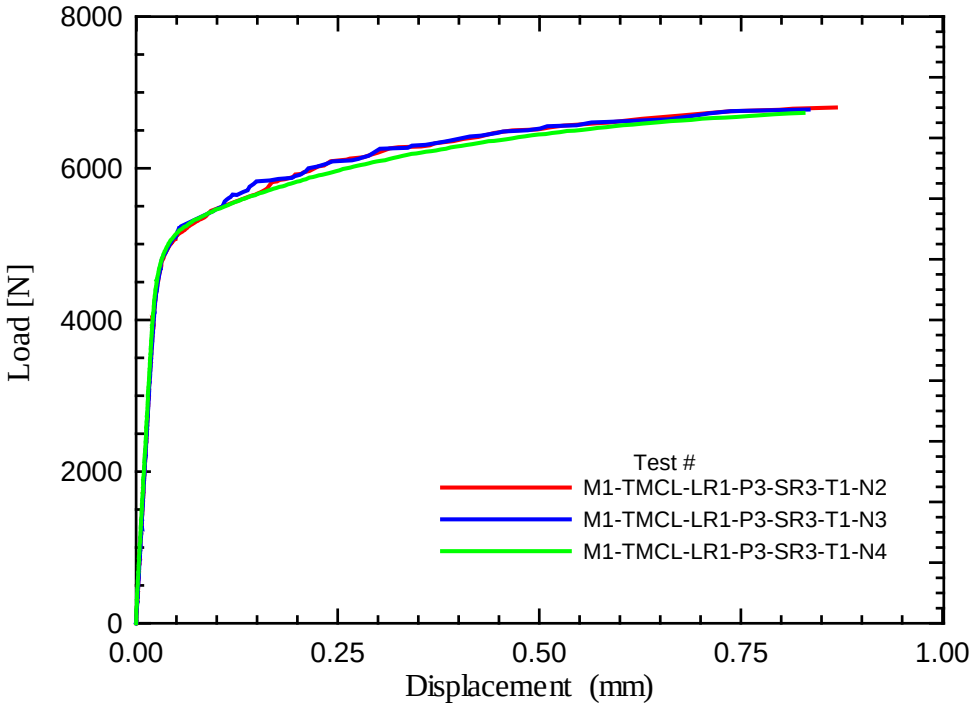

(a)

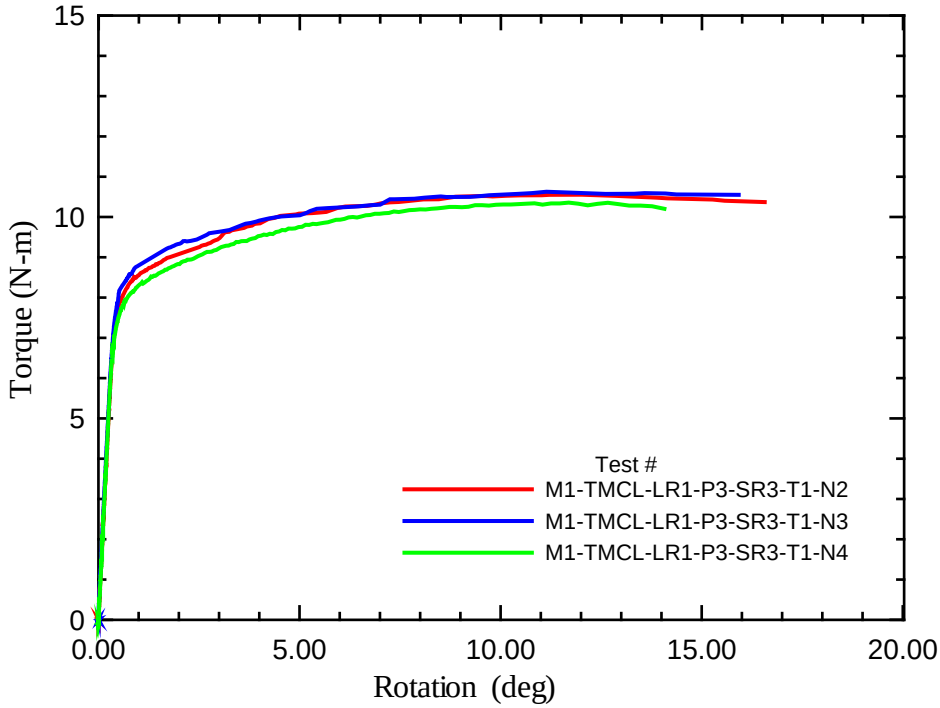

(b)

Figure 54. Experimental Data From Tension-Torsion Tests With $\frac{\sigma_x}{\tau_{xy}} = 2.59$ (a) Axial Load vs. Displacement and (b) Torque vs. Rotation

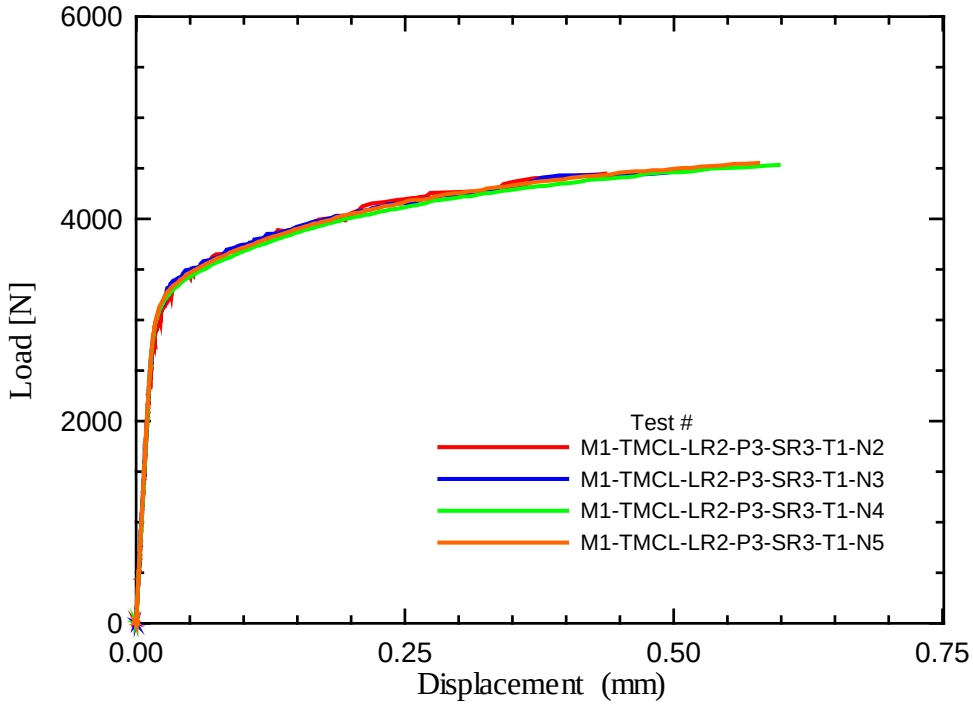

(a)

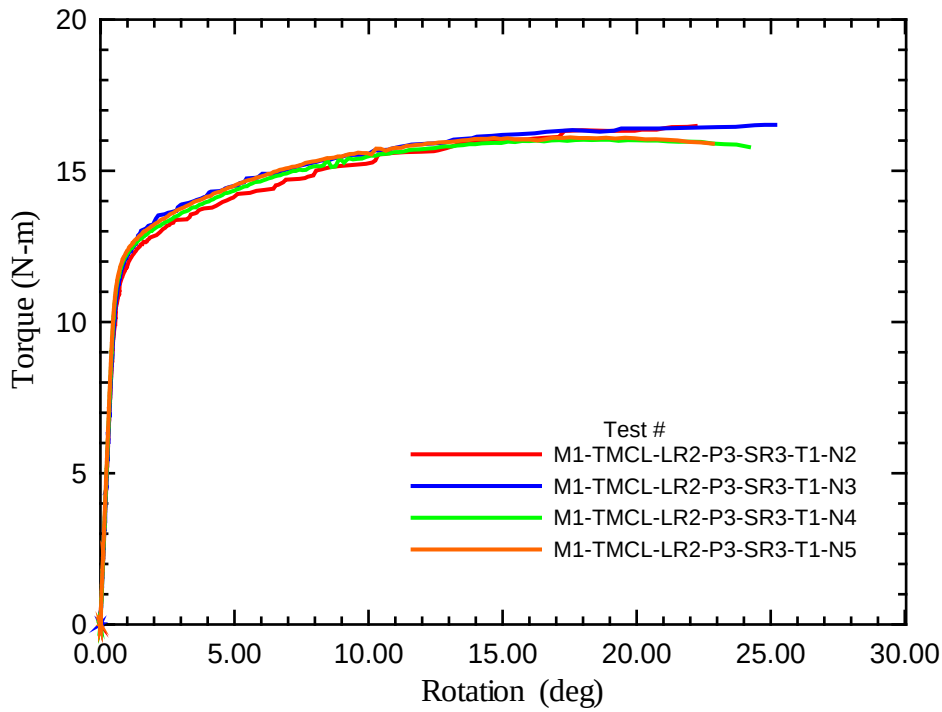

(b)

Figure 55. Experimental Data From Tension-Torsion Tests With $\frac{\sigma_x}{\tau_{xy}} = 1.15$ (a) Axial Load vs. Displacement and (b) Torque vs. Rotation

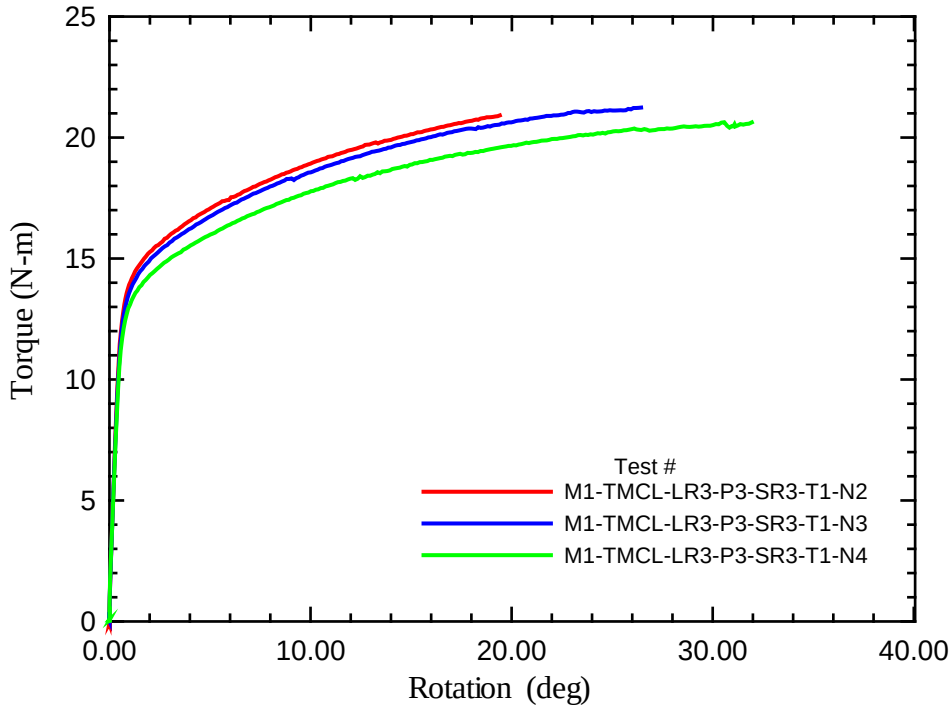

Figure 56. Torque vs. Rotation Data From Torsion Tests $\frac{\sigma_x}{\tau_{xy}} = 0.0$

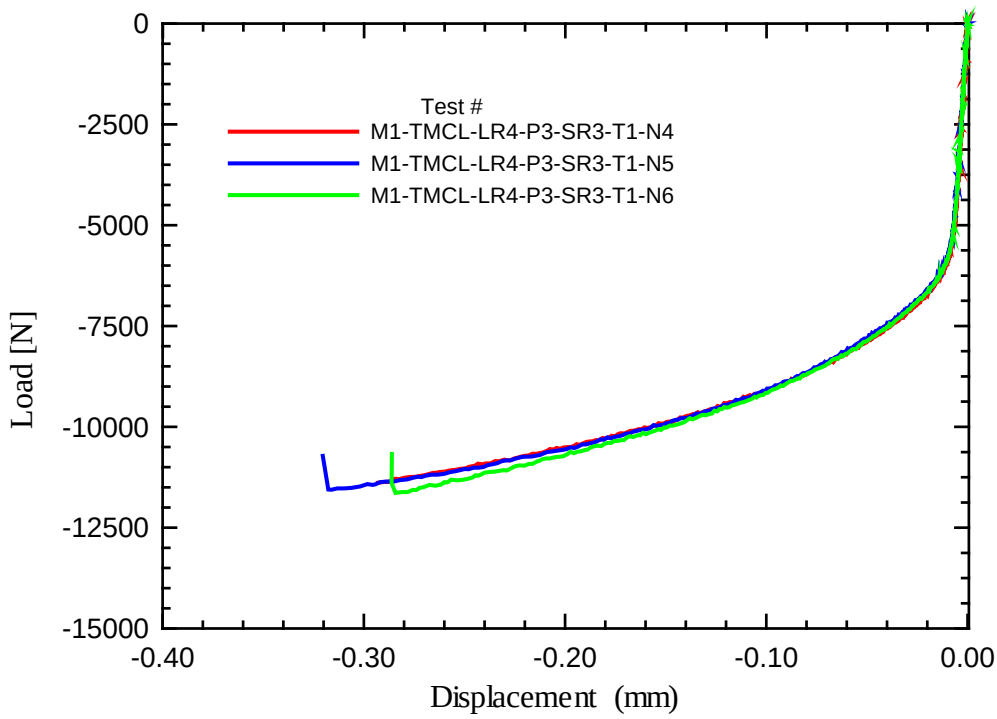

(a)

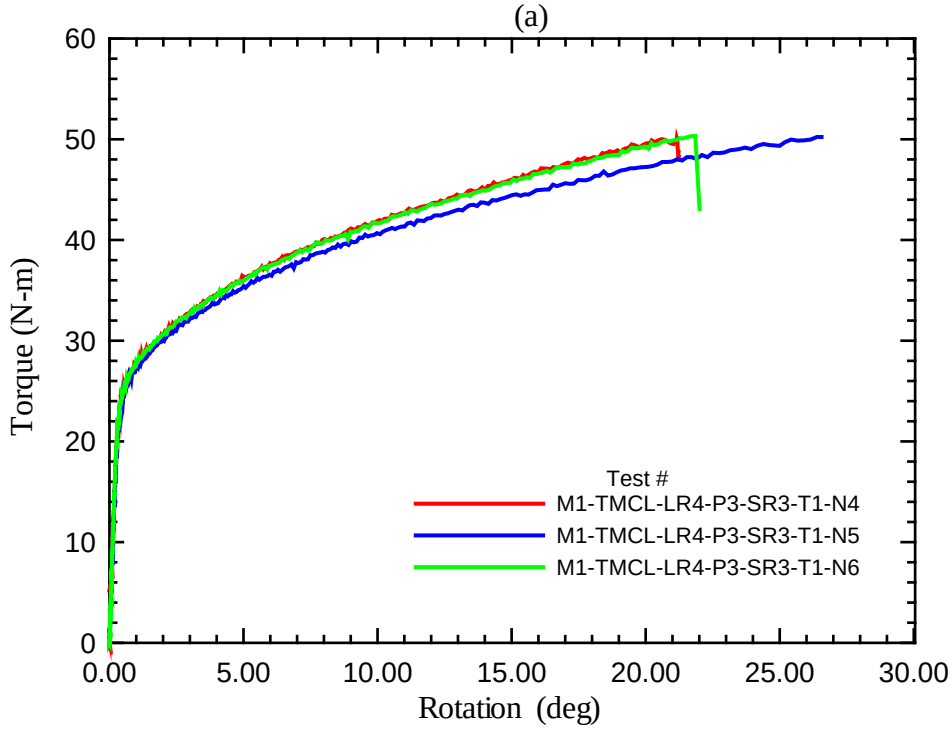

(b)

Figure 57. Experimental Data From Compression-Torsion Tests With $\frac{\sigma_x}{\tau_{xy}}$ = -0.92 (a) Axial Load vs. Displacement and (b) Torque vs. Rotation

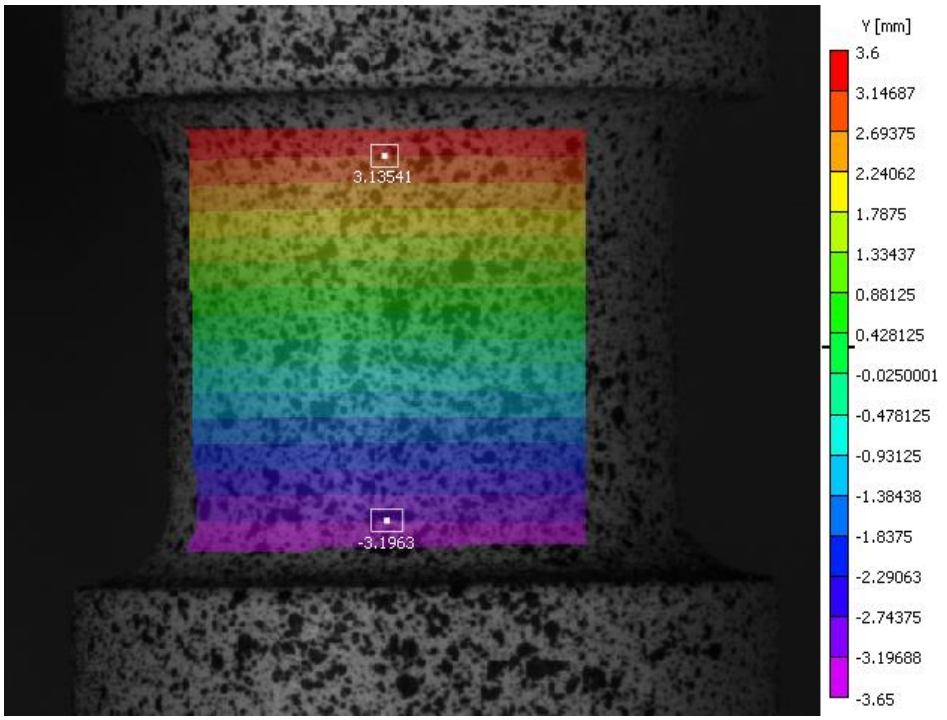

(a)

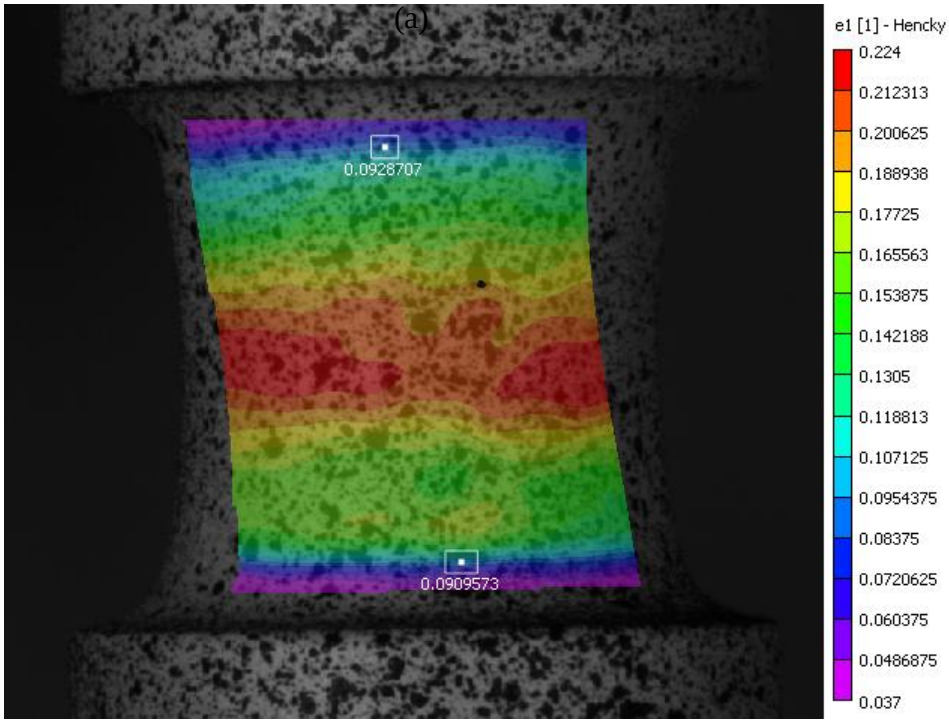

(b)

Figure 58. The 3D DIC Data From Test No. M1-CL-LR1-P3-SR3-T1-N3 (a) Initial Tracking Point Positions on *y*-Coordinate Contour and (b) Tracking Point Positions Immediately Prior to Fracture on Maximum Principal Strain Contour

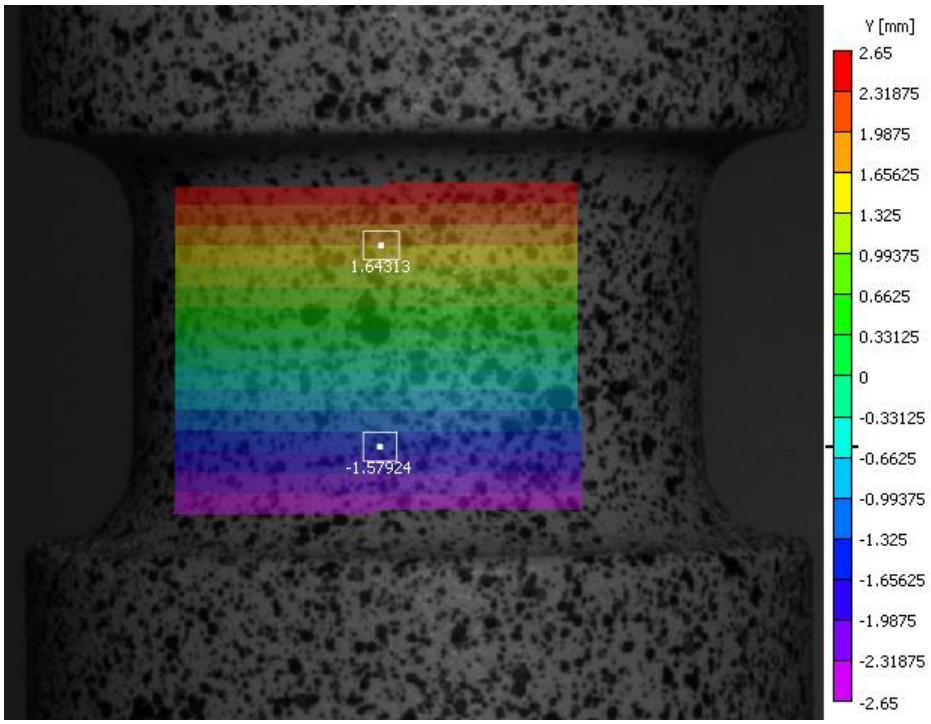

(a)

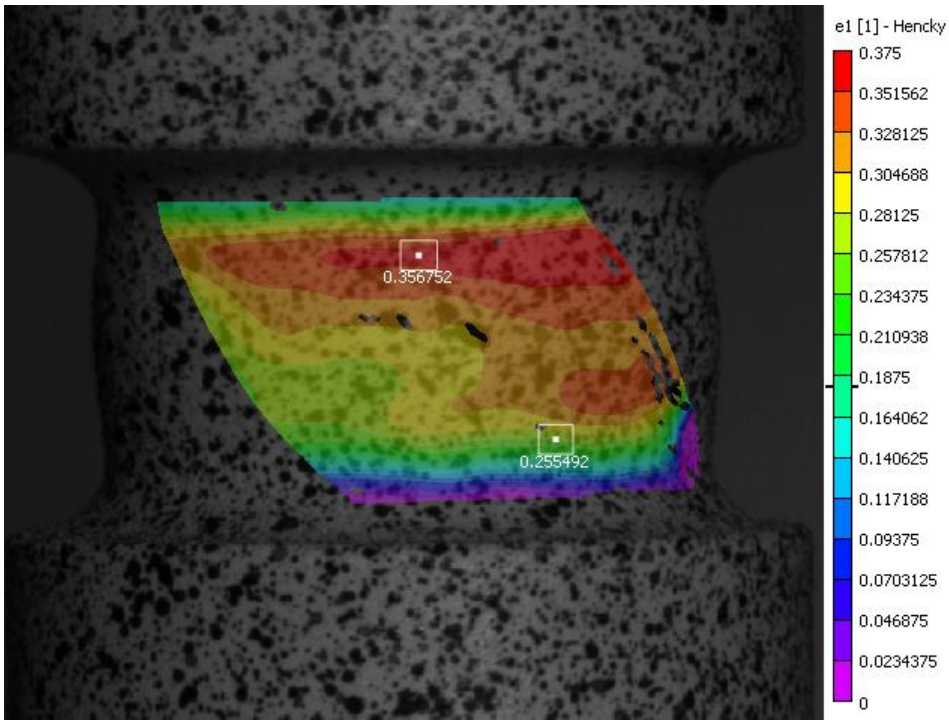

(b)

Figure 59. The 3D DIC Data From Test No. M1-CL-LR4-P3-SR3-T1-N5 (a) Initial Tracking Point Positions on *y*-Coordinate Contour and (b) Tracking Point Positions Immediately Prior to Fracture on Maximum Principal Strain Contour

5.3 PUNCH EXPERIMENTS AND RESULTS.

The ductile fracture behavior of 2024-T351 aluminum is investigated using the punch experiments listed in table 7. Numerically simulated load versus. displacement curves are compared to those determined experimentally. The details of this comparison are presented in part 2 of this report [4]. Experimental load versus displacement curves are presented here. Simulation results are used to monitor the specimen's stress state and equivalent plastic strain histories at the region of initial crack formation. Average triaxiality, product triaxiality, and Lode parameter values are computed for each experiment. These parameters, combined with the equivalent strain at the instant of crack formation, are used to determine fracture locus data points. In addition, dynamic failure mode evolution is studied by examining recovered specimens from restricted and unrestricted displacement punch experiments.

Load versus displacement curves from punch tests conducted on thin 2024-T351 aluminum disks using a punch with a 2.39-mm nose radius are shown in figure 60. The black trace in figure 60 represents a static test at a relative velocity of 2.34E-4 m/s. The red traces represent dynamic experiments conducted at an average relative velocity of 22.09 m/s. The results show some rate sensitivity in the first 3 mm of displacement. After 3 mm of displacement, the dynamic load curves generally coincide with the static curve. It is thought that the nature of the loading generates local regions of very high strain rates in the aluminum disk, resulting in increased transmitted loads. Load versus displacement curves from punch tests conducted with a 4.75-mm nose radius and a blunt punch, as shown in figures 61 and 62, respectively. Rate sensitivity is also evident in these two figures.

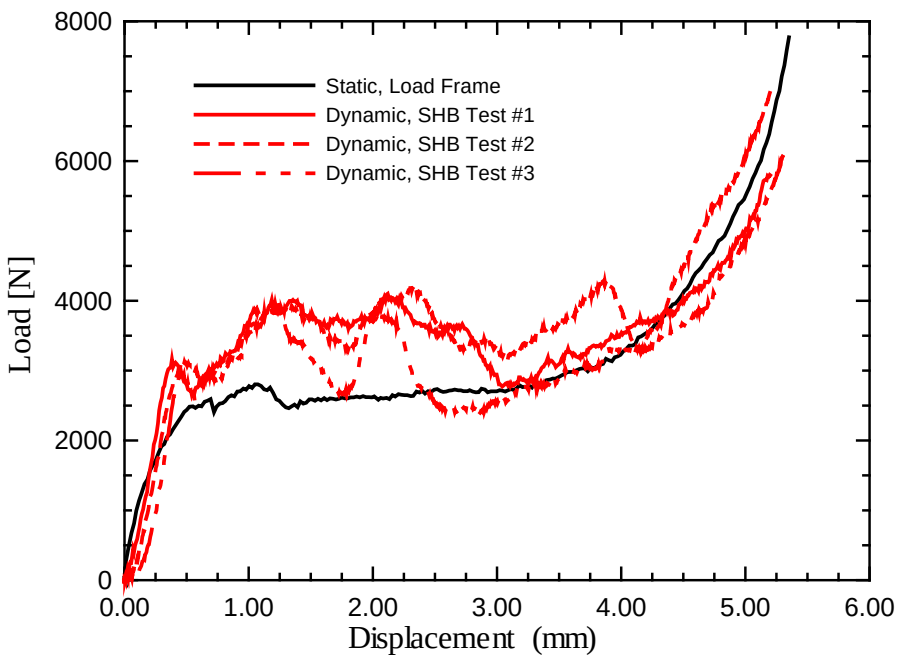

Figure 60. Load vs. Displacement Curves From Static and Dynamic Punch Tests on Thin 2024-T351 Aluminum Disks Using a Punch With a 2.39-mm Nose Radius

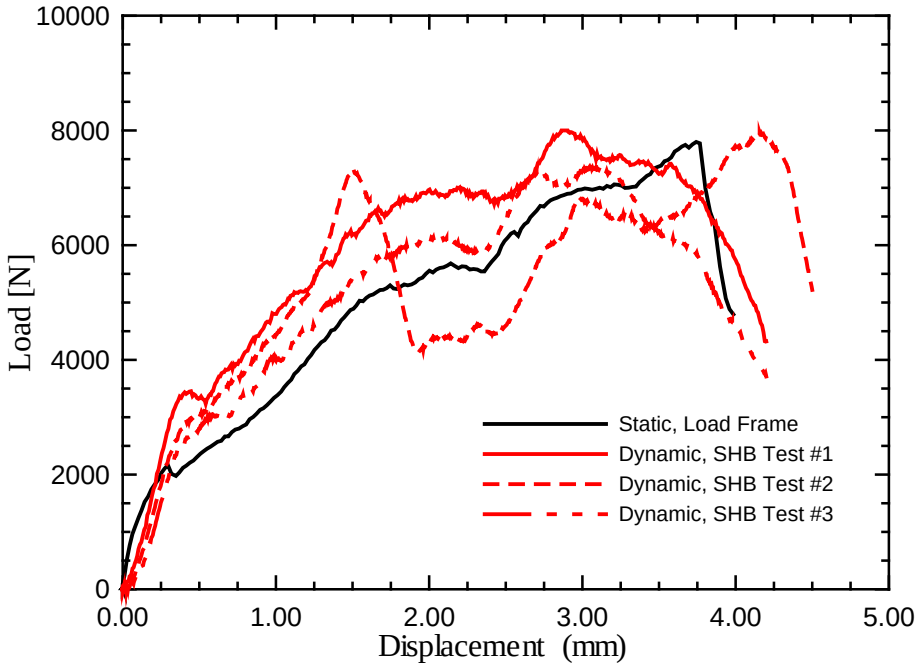

Figure 61. Load vs. Displacement Curves From Static and Dynamic Punch Tests on Thin 2024-T351 Aluminum Disks Using a Punch With a 4.75-mm Nose Radius

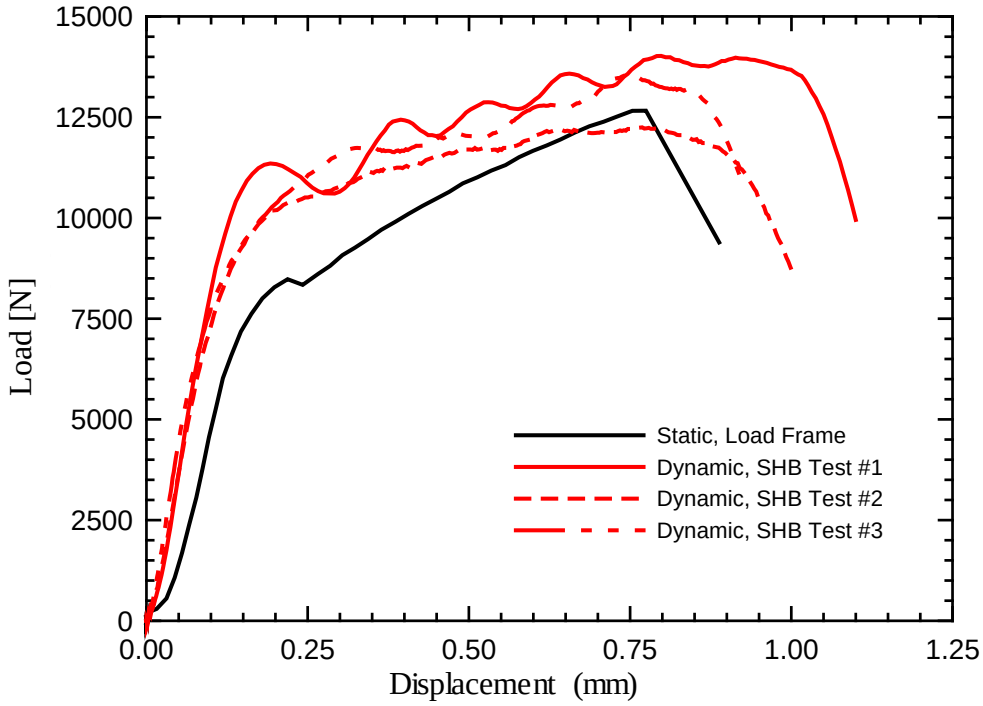

Figure 62. Load vs. Displacement Curves From Static and Dynamic Punch Tests on Thin 2024-T351 Aluminum Disks Using a Blunt Punch

The dynamic failure mode evolution of the disk specimen was studied by conducting punch tests with a predetermined displacement. These tests are described in detail in section 3.2.2. Post-test photographs of specimens tested with a 2.39-mm-radius punch are shown in figure 63. Figure 63(a) shows the rear surface of a specimen after 1.6 mm of relative displacement. The photograph shows that a circumferential crack has formed and that radial cracks are beginning to form. The formation of the circumferential crack coincides with the drop in load evident at 1.3-mm displacement in figure 60. At 2.4-mm displacement, figure 63(b), the circumferential crack has expanded and the radial cracks have grown. A plug has begun to form. A combined plugging and petaling failure mode is evident in the photograph of the specimen recovered from the unrestricted test (see figure 63(c)). The plug is surrounded by a ring comprised of eight petals.

Post-test photographs of specimens from restricted displacement experiments conducted using the 4.75-mm-radius punch are shown in figure 64. Figure 64(a) shows a circumferential crack, which is not entirely enclosed, formed in the specimen after 2.4 mm of relative displacement. Figure 64(c) shows the specimen recovered after 3.9 mm of relative displacement. A plug has nearly been ejected and small petals have formed from the development of radial cracks. The 4.75-mm-radius punch induced a combined plugging and petaling failure mode in the specimen (figure 64(d)). Seven petals have formed around the plug, two of which are still attached to the plug and five of which have been separated.

(a) (b)

(c)

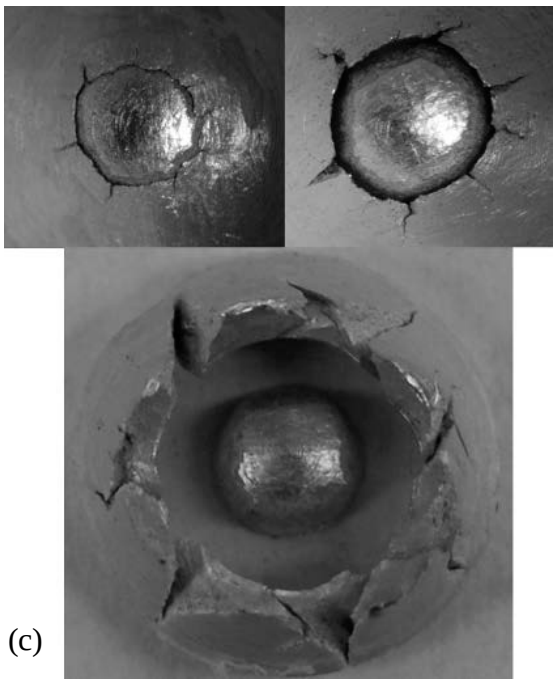

Figure 63. Failure Mode Evolution of a 2024-T351 Disk Under Load From a 2.39-mm-Radius Punch After (a) 1.6-mm Relative Displacement, (b) 2.4-mm Relative Displacement, and (c) Unrestricted Displacement

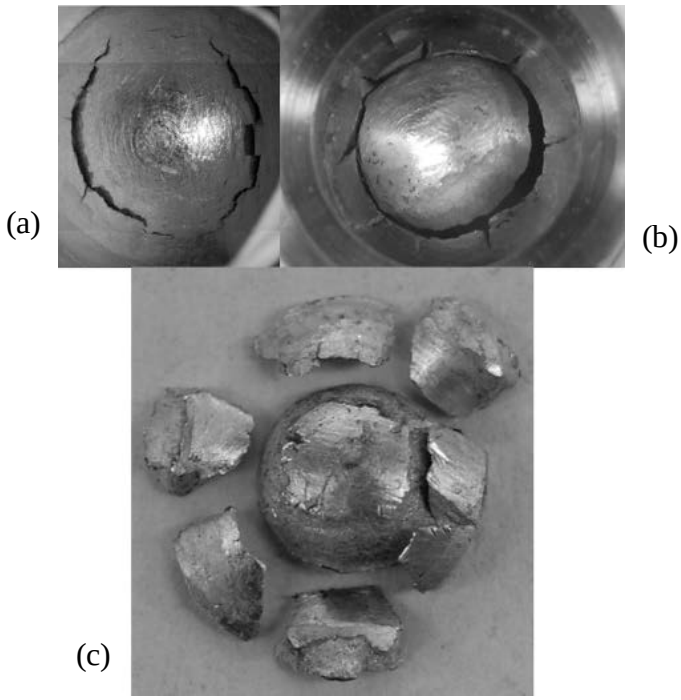

Figure 64. Failure Mode Evolution of a 2024-T351 Disk Under Load From a 4.75-mm-Radius Punch After (a) 2.4-mm Relative Displacement, (b) 3.9-mm Relative Displacement, and (c) Unrestricted Displacement

6. SUMMARY AND CONCLUSIONS.

The findings of the plastic deformation and ductile fracture experimental programs summarized here are (a) the investigation of the plastic deformation behavior of 2024 aluminum and (b) the ductile fracture behavior of 2024 aluminum.

6.1 PLASTIC DEFORMATION OF 2024 ALUMINUM.

Section 4 presents a comprehensive data set from an experimental program devised to determine the strain rate, temperature dependence, and anisotropic strength characteristics of 12.7-mm-thick 2024-T351 aluminum. In addition, limited tests were conducted on a 6.35-mm-thick 2024-T351 plate and a 3.175-mm-thick 2024-T3 sheet.

The following paragraph summarizes the results of the experiments conducted on the 12.7-mm-thick 2024-T351 plate. Tension tests over a wide range of strain rates (1.0E-4 s^{-1} to 1.8E3 s^{-1}) and temperatures (-50° to 450°C) were conducted. Tension tests were also conducted on specimens oriented in four different directions relative to the plate's rolling direction. Compression tests over a wide range of strain rates (1.0E-4 s^{-1} to 5.0E3 s^{-1}) and temperatures (-50° to 450°C) are conducted. Compression tests were also conducted on specimens oriented in five different directions relative to the plate's rolling direction. Torsion tests over a wide range of strain rates (1.0E-4 s^{-1} to 2.8E3 s^{-1}) and temperatures (-50° to 450°C) were also conducted. The results showed insignificant strain rate effect on the flow stress of the material in tension,

compression, and shear up to strain rates of about 5000 s^{-1}. In compression, rate sensitivity was evident between 5000 s^{-1} and 11000s^{-1}. The J_2 plasticity theory was not suitable for modeling the plastic deformation of the material because effective stress versus equivalent strain curves from tension, compression, and shear tests did not coincide. The material became weaker and more ductile with increasing temperature. The strain-hardening response of the material decreased significantly at 300°C, providing evidence of dynamic recovery and recrystallization. Tension, compression, and shear effective stress versus equivalent strain curves did not coincide at any temperature; in fact, the ratio of tensile strength to compressive strength and the ratio of shear strength to compressive strength were less than unity and nearly constant for all test temperatures. Experimental results from tension and compression specimens, machined in five different orientations relative to the plate-rolling direction, showed that the 2024-T351 aluminum plate had anisotropic properties with regard to plastic deformation.

Limited tests were conducted on specimens fabricated from both the 6.35-mm-thick 2024-T351 plate and the 3.175-mm-thick 2024-T3 sheet. Compression and tension tests were conducted on both material stocks at room temperature and strain rates ranging from 1.0 s^{-1} and 1200 s^{-1}. Specimens were oriented in the rolled direction of the stock material. Tensile and compressive stresses of both products were insensitive to strain rate (from 1.0 s^{-1} to 1200 s^{-1}). In tension, the fracture strains of both products were significantly less at 1.0 s^{-1} than at 500 s^{-1}. In tension, the 6.35-mm-thick plate stresses were slightly higher than those from the 12.7- and 3.175-mm-thick plate and sheet, which are nearly identical. At low strain rates, the tensile fracture strain of the 6.35-mm-thick plate was less than the other two stock materials. In compression, the 3.175- and 6.35-mm-thick stocks had nearly identical responses, while the 12.7-mm-thick stock exhibited less strain hardening (figure 50).

The data summarized above were provided to personnel at GWU's NCAC for the development of a constitutive model for 2024 aluminum for MAT224. The details of this development are found in part 2 of this report [4].

6.2 DUCTILE FRACTURE OF 2024-T351 ALUMINUM.

Section 5 presents data from a test series designed to investigate the effect of stress state on the fracture behavior of 12.7-mm-thick 2024-T351 aluminum plate. The tests included tension tests on several different specimen geometries, combined axial-torsional and pure shear experiments, and punch experiments.

Tension tests were conducted on plane-stress, axisymmetric, and plane-strain specimens for a total of 13 different specimen geometries. The plane-stress tension test series was conducted on thin specimens, one with a straight gage section and three fabricated with different notch radii. Tension tests were also conducted on axisymmetric specimens, one with a straight gage section and five with different notch radii. The plane strain tension test series was conducted on thick specimens—one with a smooth gage section and two more with different notch radii. Specimen surface displacements and strains were measured with 3D DIC. Load versus displacement curves from these experiments are shown in section 5.1. In general, the load increases and the displacements at failure decrease with decreasing stress triaxiality (notch radius).

Combined tension-torsion, compression-torsion, and pure shear experiments were also conducted. Stress-state histories in the thin-walled tube specimens were determined from load and torque cell measurements while surface displacements and strains were measured with 3D DIC. Load versus displacement data and torque versus rotation data for each test conducted are presented in section 5.2.

Static and dynamic punch tests were conducted on 1.473-mm-thick disk specimens. Punches with a 2.39- and 4.75-mm nose radii and a blunt punch were used in the test series. Tests were conducted at two different punch velocities: 2.34E-4 m/s using a load frame and ~22 m/s using a compression SHB. Rate sensitivity was evident in all of the punch experiments. This was most likely due to local regions of very high strain rates (approaching 1.5E4 s^{-1}) in the disk specimen. The dynamic failure mode evolution of the disk was investigated through a series of tests in which the punch displacements were restricted using a collar. For the 2.39-mm-radius punch, displacements were restricted to 1.6 and 2.4 mm. For the 4.75-mm-radius punch, displacements were restricted to 2.4 and 3.9 mm. The results showed the evolution of a plugging-petaling failure mode in the specimen. The specimen first exhibited a circumferential crack followed by radial cracking and petal formation. The circumferential cracks grew until a plug was formed, and the radial cracks extended until several petals were formed.

The data summarized above were provided to personnel at GWU's NCAC for the development of a fracture model for 2024 aluminum for MAT224. The details of this development are found in part 2 of this report [4].

This report presents a significant amount of data from a single 12.7-mm-thick aluminum plate and limited data from 6.35-mm-thick plate and 3.125-mm-thick sheet. Discrepancies do exist between the thicknesses and some differences in the plate and sheet products are expected during manufacture. A significant tabulated data set that resulted from this effort requires that the data minimize production lot differences as much as possible. The property variations measured are a function of the inherent material and not the fact that test A was done with plate I and test B was done with plate II. These are actual data for the sheets that are intended to verify the model through duplication of test results. Testing is the current FAA certification process. The design of new structures should include a review of the material variability and minimum material properties when using these models to apply the desired safety factors.

7. REFERENCES.

1. Lundin, S.J. et al. "Uncontained Engine Debris Fire Mitigation Test—Fuselage-Mounted Engines," Final Report to the U.S. Department of Transportation, FAA Report DOT/FAA/AR-05/3, February 2005.

2. Frankenberger, C.E., "Large Engine Uncontained Debris Analysis," FAA Report DOT/FAA/AR-99/11, May 1999.

3. Sutton, M., Orteu, J.-J., and Schreier, H.W., *Image Correlation for Shape, Motion and Deformation Measurements*, Springer, New York, New York, 2009.

4. Buyuk, M., "Development of a New Material Model in LS-DYNA, Part 2: Development of a Tabulated Thermo-Viscoplastic Material Model With Regularized Failure for Dynamic Ductile Failure Prediction of Structures Under Impact Loading," FAA Report DOT/FAA/TC-13/25, P2.

5. Livermore Software Technology Coporation, LS-DYNA Keyword User's Manual, Volumes I and II, Version 971, Livermore Software Technology Center, Livermore, California, 2007.

6. Johnson, G.R. and Cook, W.H., "A Constitutive Model and Data for Metals Subjected to Large Strains, High Strain Rates and High Temperatures," *Proceedings of the 7th International Symposium on Ballistics*, The Hague, The Netherlands, April 1983, pp. 541-547.

7. Johnson, G.R. and Cook, W.H., "Fracture Characteristics of Three Metals Subjected to Various Strains, Strain Rates, Temperatures and Pressures," *Engineering Fracture Mechanics*, Vol. 21, No. 1, 1985, pp. 31-48.

8. Li, P., Siviour, C.R., and Petrinic, N., "The Effect of Strain Rate, Specimen Geometry and Lubrication on Responses of Aluminum AA2024 in Uniaxial Compression Experiments," *Experimental Mechanics*, Vol. 49, No. 4, 2009, pp. 587-593.

9. Hodowany, J., Ravichandran, G., Rosakis, A.J., and Rosakis, P., "Partition of Plastic Work Into Heat and Stored Energy in Metals," *Experimental Mechanics*, Vol. 40, No. 2, June 2000.

10. Johnson, G.R., Hoegfeldt, J.M., Linholm, U.S., and Nagy, A., "Response of Various Metals to Large Torsional Strains Over a Large Range of Strain Rates—Part 2: Less Ductile Metals," *Transactions of the ASME*, Vol. 105, January 1983, pp. 48-53.

11. Lesuer, D. R., "Experimental Investigations of Material Models for Ti-6Al-4V Titanium and 2024-T3 Aluminum," FAA Report DOT/FAA/AR-00/25, September 2000.

12. Zhao, D. and Lampman, S., "Effects of Temperature, Hot Tension and Compression Testing," Mechanical Testing and Evaluation, Vol. 8, ASM Handbook, ASM International, 2000, pp. 152-163.

13. Barlat, F., Lege, D. J., and Brem, J.C., "A Six-Component Yield Function for Anisotropic Materials," *International Journal of Plasticity*, Vol. 7, No. 7, 1991, pp. 693-712.

14. Gilmour, K. R., Leacock, A. G., and Ashbridge, M.T.J., "The Influence of Plastic Strain Ratios on the Numerical Modelling of Stretch Forming," *Journal of Material Processing Technology*, Vol. 152, No. 1, 2004, pp. 116-125.

15. Gilmour, K. R., Leacock, A. G., and Ashbridge, M.T.J., "The Determination of the In-Plane Shear Characteristics of Aluminum Alloys," *Journal of Testing and Evaluation*, Vol. 29, No. 2, March 2001, pp. 131-137.

16. Rice, J.R. and Tracey, D.M., "On the Ductile Enlargement of Voids in Triaxial Stress Fields," *Journal of the Mechanics of Physical Solids*, Vol. 17, No. 3, 1969, pp. 201-217.

17. Hancock, J.W. and Mackenzie, A.C., "On the Mechanisms of Ductile Failure in High-Strength Steels Subjected to Multi-Axial Stress-States," *Journal of the Mechanics of Physical Solids*, Vol. 24, 1976, pp. 147-169.

18. Mackenzie, A.C., Hancock, J.W., and Brown, D.K., "On the Influence of State of Stress on Ductile Failure Initiation in High Strength Steels," *Engineering Fracture Mechanics*, Vol. 9, Nos. 2-3, 1977, pp. 167-188.

19. Bridgman, P.W., *Studies in Large Plastic Flow and Fracture, With Special Emphasis on the Effects of Hydrostatic Pressure*, Harvard University Press, Cambridge, Massachusetts, 1964.

20. Bau, Y. and Wierzbicki, T., "On Fracture Locus in the Equivalent Strain and Stress Triaxiality Space," *International Journal of Mechanical Sciences*, Vol. 46, 2004, pp. 81-98.

21. Bau, Y. and Wierzbicki, T., "A Comparative Study on Various Ductile Crack Formation Criteria," *Journal of Engineering Materials and Technology*, Vol. 126, No. 3, 2004, pp. 314-324.

22. Barsoum, I. and Faleskog, J., "Rupture Mechanisms in Combined Tension and Shear—Experiments," *International Journal of Solids and Structures*, Vol. 44, No. 17, 2007, pp. 1768-1786.

23. Carney, K.S., DuBois, P.A., Buyuk, M., and Kan, S., "Generalized, Three-Dimensional Definition, Description, and Derived Limits of the Triaxial Failure of Metals," *Journal of Aerospace Engineering*, Vol. 22, 2009.

24. Lee, Y-W, Woertz, J.C., and Wierzbicki, T., "Fracture Prediction of Thin Plates Under Hemi-Spherical Punch With Calibration and Experimental Verification," *International Journal of Mechanical Sciences*, Vol. 46, No. 5, 2004, pp. 751-781.

25. Grytten, F., Borvik, T., Hopperstad, O.S., and Langseth, M., "Quasi-Static Perforation of Thin Aluminum Plates," *International Journal of Impact Engineering*, Vol. 36, No. 3, 2009, pp. 486-497.

26. Walters, C.L., "Dynamic Bulging Technique for Testing Fracture in Intermediate Strain Rates," *Proceedings of the 2009 SEM Annual Conference and Exposition on Experimental and Applied Mechanics*, Society for Experimental Mechanics, Albuquerque, New Mexico, June, 2009.

27. Grytten, F., Børvik, T., Hopperstad, O.S., and Langseth, M., "Low Velocity Perforation of AA5083-H116 Aluminum Plates," *International Journal of Impact Engineering*, Vol. 36, No. 14, 2009, pp. 597-610.

28. Zurek, A.K., "The Study of Adiabatic Shear Band Instability in a Pearlitic 4340 Steel Using a Dynamic Punch Test," *Metallurgical and Materials Transactions A*, Vol. 25A, 1994, pp. 2483-2489.

29. Roessig, K.M. and Mason, J.J., "Adiabatic Shear Localization in the Dynamic Punch Test, Part I: Experimental Investigation," *International Journal of Plasticity*, Vol. 15, 1999, pp. 241-262.

30. Dabboussi, W. and Nemes, J.A., "Modeling of Ductile Fracture Using the Dynamic Punch Test," *International Journal of Mechanical Sciences*, Vol. 47, 2005, pp. 1282-1299.

31. Roessig, K.M. and Mason, J.J., "Adiabatic Shear Localization in the Dynamic Punch Test, Part II: Numerical Simulations," *International Journal of Plasticity*, Vol. 15, No. 3, 1999, pp. 241-262.

32. Meyers, M.A., Andrade, U.R., and Chokshi, A.H., "The Effect of Grain Size on the High-Strain, High-Strain-Rate Behavior of Copper," *Metallurgical and Materials Transactions A*, Vol. 26A, 1995, pp. 2881-2893.

33. Staab, G. H. and Gilat, A., "A Direct-Tension Split Hopkinson Bar for High Strain-Rate Testing," *Experimental Mechanics*, Vol. 31, 1991, pp. 232-235.

34. Gray, G.T., "Classic Split-Hopkinson Pressure Bar Testing," *Mechanical Testing*, Vol. 8, *ASM Handbook*, ASM International, 2000.

35. Gilat, A. "Torsional Kolsky Bar Testing," *Mechanical Testing*, Vol. 8, *ASM Handbook*, ASM International, 2000.

36. Sutton, M.A., McNeil, S.R., and Schreier, H.W., "Digital Image Correlation: Principles, Developments and Hands-on Experiment," Notes from a short course presented at the *2008 Society for Experimental Mechanics Conference*, Orlando, Florida.

37. Malvern, L.E., *Introduction to the Mechanics of a Continuous Medium*, Prentice-Hall, Inc., Englewood Cliffs, New Jersey, 1969.

38. Semiatin, S.L. and Jonas, J.J., *Formability and Workability of Metals: Plastic Instability and Flow Localization*, American Society for Metals, Metals Park, Ohio, 1984.

12.7-mm-(0.5 in)-thick 2024-T351 plate:

SHIP TO:
TW METALS
1200 BLAKE DRIVE
WICHITA, KS 67219

SOLD TO:
TW METALS INC
THE ARBORETUM
760 CONSTITUTION DRIVE
EXTON, PA 19341

KAISER ALUMINUM
Trentwood Works - Spokane, WA 99215
Phone: (800) 367-2586

CERTIFIED TEST REPORT

Serial Number
4062667

CUSTOMER PO NUMBER:	WORK PACKAGE:	CUSTOMER PART NUMBER:	SHIP RUN/LOAD ID:	GOV'T CONTRACT NUMBER:
M49144942		06251	100627/7	

KAISER ORDER NO:	LINE ITEM:	SHIP DATE:	ALLOY:	CLAD:	TEMPER:
1032601	1	21-MAR-2006	2024	BARE	T351
WEIGHT SHIPPED:	**QUANTITY:**	**B/L NUMBER:**	**GAUGE:**	**WIDTH:**	**LENGTH:**
2856 LB	8 PCS EST.	207817	0.5000 IN	48.500 IN	144.500 IN

Certified Specifications

AMS 4037/RevN
CMMP 025/RevQ
AMS-QQ-A-250/4/RevA
ASTM B 209/Rev04

TW METALS
TEST
MAR 27 2006
ACCEPTED BY

Test Code: 1504

Test Results

Lot: 352560A7 Cast 318 Drop 30 Ingot 3

Tensile:	Temper	Dir / # Tests	Ultimate KSI (MPA)	Yield KSI (MPA)	Elongation %
	T351	LT / 2 (Min:Max)	68.5 : 69.6 (472 : 480)	50.0 : 50.6 (345 : 349)	16.9 : 17.4

Chemistry:	SI	FE	CU	MN	MG	CR	ZN	TI	V	ZR		OTHER
Actual	0.08	0.22	4.47	0.59	1.37	0.01	0.18	0.02	0.01	0.01	TOT	0.04

ALLOY LIMITS

Chemistry:	SI	FE	CU	MN	MG	CR	ZN	TI	V	ZR	OTHER	MAX
2024 MIN	0.00	0.00	3.80	0.30	1.20	0.00	0.00	0.00	0.00	0.00	EACH	0.05
MAX	0.50	0.50	4.90	0.90	1.80	0.10	0.25	0.15	0.05	0.05	TOT	0.15

Aluminum Remainder

CERTIFICATION

KAISER ALUMINUM & CHEMICAL CORPORATION (KAISER) HEREBY CERTIFIES THAT METAL SHIPPED UNDER THIS ORDER WAS MELTED AND MANUFACTURED IN THE U.S.A. AND HAS BEEN INSPECTED, TESTED, AND FOUND IN CONFORMANCE WITH THE REQUIREMENTS OF THE APPLICABLE SPECIFICATIONS AS INDICATED HEREIN. ALL METAL WHICH IS SOLUTION HEAT-TREATED COMPLIES WITH AMS 2772. ANY WARRANTY IS LIMITED TO THAT SHOWN ON KAISER'S STANDARD GENERAL TERMS AND CONDITIONS OF SALE. TEST REPORTS ARE ON FILE, SUBJECT TO EXAMINATION. TEST REPORTS SHALL NOT BE REPRODUCED EXCEPT IN FULL, WITHOUT THE WRITTEN APPROVAL OF KAISER ALUMINUM & CHEMICAL CORPORATION LABORATORY. THE RECORDING OF FALSE, FICTITIOUS, OR FRAUDULANT STATEMENTS OR ENTRIES ON THE CERTIFICATE MAY BE PUNISHED AS A FELONY UNDER FEDERAL LAW. ISO-9001:2000 CERTIFIED

BILL POYNOR, LABORATORIES SUPERVISOR

Page 1 of 1

6.35-mm-(0.25 in)-thick 2024-T351 plate:

4913344 7

SHIP TO:
TW METALS
1200 BLAKE DRIVE
WICHITA, KS 67219

SOLD TO:
TW METALS INC
THE ARBORETUM
760 CONSTITUTION DRIVE
EXTON, PA 19341

KAISER ALUMINUM
Trentwood Works - Spokane, WA 99215
Phone: (800) 367-2586

CERTIFIED TEST REPORT

Serial Number
4046144

CUSTOMER PO NUMBER:	CUSTOMER PART NUMBER:	SHIPPING RUN #/LOAD ID:	GOV'T CONTRACT NUMBER:
M49133447	06232	100444/8	

KAISER ORDER NO:	LINE ITEM:	SHIP DATE:	ALLOY:	CLAD:	TEMPER:
1025400	1	16-AUG-2005	2024	BARE	T351
WEIGHT SHIPPED:	**QUANTITY:**	**B/L NUMBER:**	**GAUGE:**	**WIDTH:**	**LENGTH:**
3984 LB	22 PCS EST.	205660	0.2500 IN	48.500 IN	144.500 IN

Certified Specifications

AMS 4037/RevN AMS-QQ-A-250/4/RevA ASTM B 209/Rev04

Test Code: 1504

Test Results

Lot: 337156A4 Cast 282 Drop 11 Ingot 1

Tensile:	Temper	Dir / # Tests	Ultimate KSI (MPA)	Yield KSI (MPA)	Elongation %
	T351	LT / 2 (Min:Max)	69.4 : 70.1 (479 : 483)	48.8 : 50.5 (336 : 348)	16.6 : 17.0

Chemistry:	SI	FE	CU	MN	MG	CR	ZN	TI	V	ZR		OTHER
Actual	0.10	0.24	4.43	0.56	1.33	0.01	0.11	0.02	0.01	0.00	TOT	0.05

Lot: 337187A9 Cast 282 Drop 16 Ingot 4

Tensile:	Temper	Dir / # Tests	Ultimate KSI (MPA)	Yield KSI (MPA)	Elongation %
	T351	LT / 2 (Min:Max)	70.1 : 70.3 (483 : 485)	49.5 : 50.4 (341 : 348)	16.6 : 16.7

Chemistry:	SI	FE	CU	MN	MG	CR	ZN	TI	V	ZR		OTHER
Actual	0.10	0.28	4.65	0.59	1.38	0.03	0.12	0.02	0.01	0.00	TOT	0.04

ALLOY LIMITS

Chemistry:	SI	FE	CU	MN	MG	CR	ZN	TI	V	ZR	OTHER	MAX
2024 MIN	0.00	0.00	3.80	0.30	1.20	0.00	0.00	0.00	0.00	0.00	EACH	0.05
MAX	0.50	0.50	4.90	0.90	1.80	0.10	0.25	0.15	0.05	0.05	TOT	0.15

Aluminum Remainder

TW METALS
TEST REPORTS
AUG 22 2005
ACCEPTED BY

Page 1 of 2

49133147

KAISER ALUMINUM

Trentwood Works - Spokane, WA 99215
Phone: (800) 367-2586

CERTIFIED TEST REPORT

Serial Number
4046144

TW METALS
TEST REPORTS
AUG 22 2005
ACCEPTED BY

CERTIFICATION

KAISER ALUMINUM & CHEMICAL CORPORATION (KAISER) HEREBY CERTIFIES THAT METAL SHIPPED UNDER THIS ORDER WAS MANUFACTURED IN THE U.S.A. AND HAS BEEN INSPECTED, TESTED, AND FOUND IN CONFORMANCE WITH THE REQUIREMENTS OF THE APPLICABLE SPECIFICATIONS AS INDICATED HEREIN. ALL METAL WHICH IS SOLUTION HEAT-TREATED COMPLIES WITH AMS 2772 (MIL-H-6088). ANY WARRANTY IS LIMITED TO THAT SHOWN ON KAISER'S STANDARD GENERAL TERMS AND CONDITIONS OF SALE. TEST REPORTS ARE ON FILE, SUBJECT TO EXAMINATION. ISO-9001:2000 CERTIFIED

BILL POYNOR, LABORATORIES SUPERVISOR

Bill Poy

3.125-mm-(0.125 in)-thick 2024-T3 sheet:

From: To: Sharon
MAY-05-2006 16:49

EMO TRANS BALTO EXPORT

AMAG rolling

AMAG rolling GmbH

Abnahmeprüfzeugnis 3.1 (EN 10204)
Inspection certificate – mill certificate
AMAG rolling GmbH
Zertifiziert nach / certified to ISO/TS 16949, EN 9100, ISO 14001

Nr.: 85521763 1 / 1
Rev. 0
Seite / page: 1 von / of 2
Datum / date: 2006 04 06

Auftraggeber / orderer: TW METALS, INC, 760 CONSTITUTION DR, USA-19341 Exton,PA	Bestell Nr. / order no.: M 49143690 Datum / date: 2005 12 20
	Auftragsbest. Nr. / order confirmation no.: 558068 Datum / date: 2006 01 11
Warenempfänger / consignee: TW Metals - Wichita	Lieferschein Nr. / delivery note.: 85521763 Datum / date: 2006 04 11
Endkunde, Bestell Nr. / Your cust., ord. no.:	Akkreditiv Nr. / letter of credit no.:

Produkt/product	**Bedingungen/terms**
Form / form: sheet Werkstoff / material: 2024 Zustand / temper: T3 Dim. / dim: [inch]: 0,125x48,00x144,00 Kundenartikel-Nr / customer item no.: 05309	Techn. Lieferbedingungen / techn. spec.: AMS-QQA-250/4A, ASTM B209-04, AMS 4037 N Sondervorschrift / special terms:

AB-Pos. ord.-Pos.	BNr/Los/Teilos Lot/No./Part	Guss Nr. cast no.	Werkstoff material	Kollo packno.	Gewicht netto weight net	Stk. pcs.
01	70675/01/00	01/0013994/5	2024.4	5580680001	1227	31
01	70675/01/00	01/0013994/5	2024.4	5580680002	1234	31
01	70675/01/00	01/0013994/5	2024.4	5580680004	1231	31
01	70675/01/00	01/0013994/5	2024.4	5580680003	1232	31

Chemische Zusammensetzung / chemical composition: [%] Gewichtsanteile / weight proportion

cast no.	AMAG		Si	Fe	Cu	Mn	Mg	Cr	Ni	Zn	Ti
01/0013994/5	2024.4	Min.			3,8	0,30	1,2				
		Max.	0,50	0,50	4,9	0,9	1,8	0,10	0,05	0,25	0,15
			0,06	0,13	4,6	0,64	1,5	<0,01	<0,01	0,09	0,03

Zugversuch / tensile test

BNr/Los/Tl. Lot/No./Part	Zustand temper	Richtung direction		Rm [ksi]	Rp0.2 [ksi]	A2" [%]
			Min.	63,0	42,0	15
			Max.			
70675/01	T3	LT		66,0	47,9	18
70675/01	T3	LT		66,3	48,3	16
70675/01	T3	LT		66,4	48,3	18
70675/01	T3	LT		66,3	48,3	17
70675/01	T3	LT		66,4	48,3	16
70675/01	T3	LT		66,6	48,9	17

PSI 9

AMAG rolling GmbH, Postfach 32, A-5282 Ranshofen, Österreich – www.amag.at
AMAG rolling GmbH, P.O. Box 32, A-5282 Ranshofen, Austria – www.amag.at

TW METALS
TEST
Austry
MAY 11 2006
Burchard
ACCEPTED BY

AMAG rolling GmbH

AMAG rolling

Abnahmeprüfzeugnis 3.1 (EN 10204)
Inspection certificate – mill certificate
AMAG rolling GmbH
Zertifiziert nach / certified to ISO/TS 16949, EN 9100, ISO 14001

Nr.: 85521763 1 / 1
Rev. 0
Seite / page: 2 von / of 2
Datum / date: 2006 04 06

Elektr. Leitfähigkeit / electr. conductivity						
BNr/Los/TL Lot/No./Part	Zustand temper		dL_B [MS/m]			
		Min.				
		Max.	1,5			
70675/01	T3		0,2			

Sonstige Prüfungen / other Tests
Biegeversuch / Transverse bend test: OK.
Maßkontrolle / Dimensional Check: OK.
Oberfläche / Surface Inspection: OK.

Es wird bestätigt, dass die Lieferung geprüft wurde und den Vereinbarungen bei der Bestellung entspricht.
We hereby certify that the material described above has been tested and complies with the terms of the order contract.

Werkssachverständiger / factory specialist	Telefon / telephone	Fax / fax	E-Mail / e-mail
Rendl	+43 (7722) 801-2746	+43 (7722) 809-442	h.rendl@amag.at

Maschinell erstellt - Gültig ohne Unterschrift / Automated - valid without being signed

P520

AMAG rolling GmbH, Postfach 32, A-5282 Ranshofen, Österreich – www.amag.at
AMAG rolling GmbH, P.O. Box 32, A-5282 Ranshofen, Austria – www.amag.at

TW METALS
TEST REPORTS
Austin
MAY 1 1 2006
Burchard
ACCEPTED BY

APPENDIX B—SPECIMEN FABRICATION METHOD TEST SERIES

Tension split Hopkinson bar (SHB) specimens are typically much smaller than the standard specimens found in ASTM E8[*]. This is primarily because the strain rate is linearly proportional to the gage length of the specimen. Therefore, higher strain rates can be achieved by simply reducing the gage length of the specimen. Another factor is specimen attachment. Specimens are typically attached to SHBs using epoxy or cyanoacrylate glue (figure 34 in the main report), so the shear strength of the glue limits the transmitted force magnitude. For these reasons, specimens are typically very small (short gage lengths to achieve high strain rates and small cross-sectional areas to reduce the transmitted force). A test series was designed to determine if the surface finish of an SHB test specimen would influence the results, notably peak stresses and strains at fracture.

Tension samples (figure 2(a) in the main report) were machined using the following four different fabrication techniques:

- Machined to a surface finish of Ra 64 μin or higher, with unbroken edges. Designated SF1.
- Machined to a surface finish of Ra 32 μin or lower, with unbroken edges. Designated SF2.
- Fabricated using electrical discharge machining (EDM). The recast layer was left on the specimen and the edges were unbroken. Designated SF3.
- Machined to a surface finish of Ra 32 μin or lower with broken edges. The edges were smoothed using sandpaper. Designated SF4.

Photographs of specimen surfaces cut to these specifications are shown in figure B-1. The differences in surface finish are clearly evident. Figure B-1(a) shows the surface of an SF1 specimen. Coarse gouges from the milling machine cutting tool are evident. The SF2/SF4 finish is shown in figure B-1(b). The cutting tool marks are evident; however, they are faint. Figure B-1(c) shows the recast layer on the surface of an EDM specimen (SF3). The difference between SF2 and SF4 specimens is shown in figure B-2. The SF2 specimen has unbroken edges (figure B-2(a)), while the SF4 specimen edges are broken (figure B-2(b)).

[*] ASTM Standard E8/E8M-09, 2003, "Standard Test Methods for Tension Testing of Metallic Materials," ASTM International, West Conshohocken, Pennsylvania, 2003, DOI: 10.1520/E0008_E0008M-09, www.astm.org.

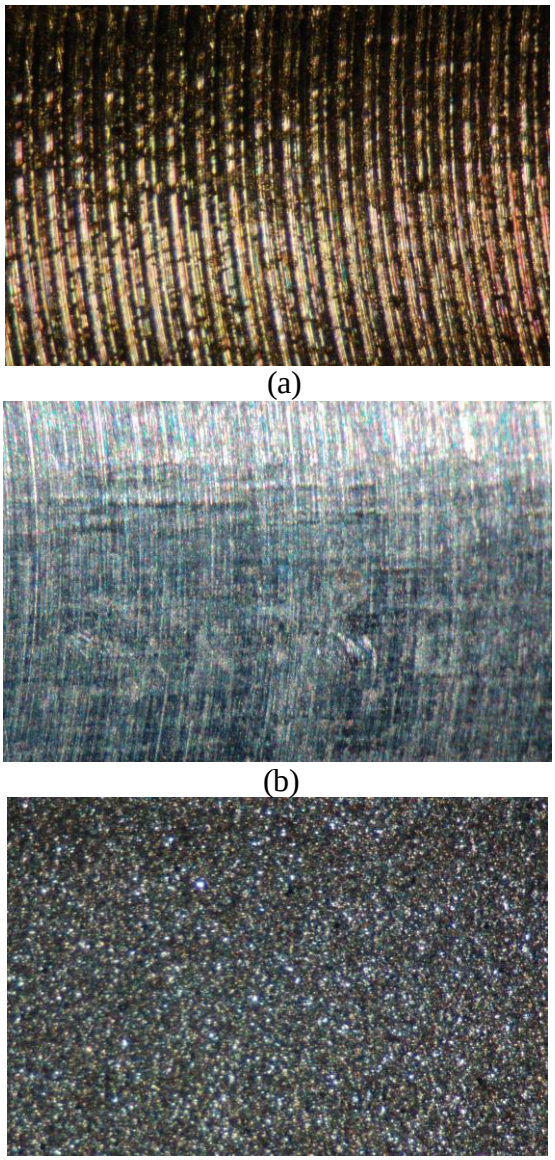

(a)

(b)

(c)

Figure B-1. Samples Cut to the Specified Surface Finish Specifications: (a) SF1, Ra – 64 µin or Higher, (b) SF2/SF3, Ra – 32 µin or Lower, and (c) SF3, EDM (2x magnification)

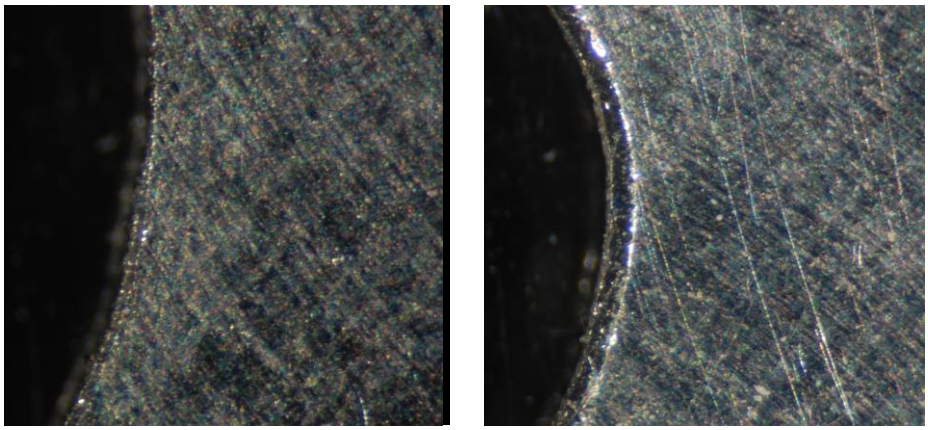

(a) (b)

Figure B-2. Samples Cut to the Specified Edge Specifications: (a) SF2, Unbroken Edges and (b) SF4, Broken Edges (2x magnification)

Tests were conducted on the tension specimens at two different strain rates: 1.0 s^{-1} using a servohydraulic load frame (see figure 9 of main document) and 1000.0 s^{-1} using a tension SHB (see figure 34 of main document). Three tests of each surface finish and strain rate combination were conducted for a total of 24 tests.

The surface finish (Ra, or the arithmetic average of absolute values) of each specimen was measured using a Mahr Federal, Inc. Pocket Surf® surface finish gage. Three surface-finish measurements, shown in figure B-3, were taken on the gage region of each specimen. The measurement locations and orientations are as follows:

- In the loading direction on the flat surface of the sample
- In the direction transverse to the loading on the flat surface of the sample
- In the loading direction on the edge surface of the sample

Average roughness range measurements of the specimens are shown in table B-1. For the SF1 specimens, all three roughness measurements were higher than 64 µin, as specified. Likewise, the SF2 and SF4 roughness measurements were all less than 32 µin. Roughness measurements on the recast layer (flat face) of the EDM specimens were over 100 µin. The edge roughness was significantly lower because the edge groove was machined into the plate first (to a specified roughness lower than 32 µin) before the EDM was used to slice the specimens to thickness (figure B-4).

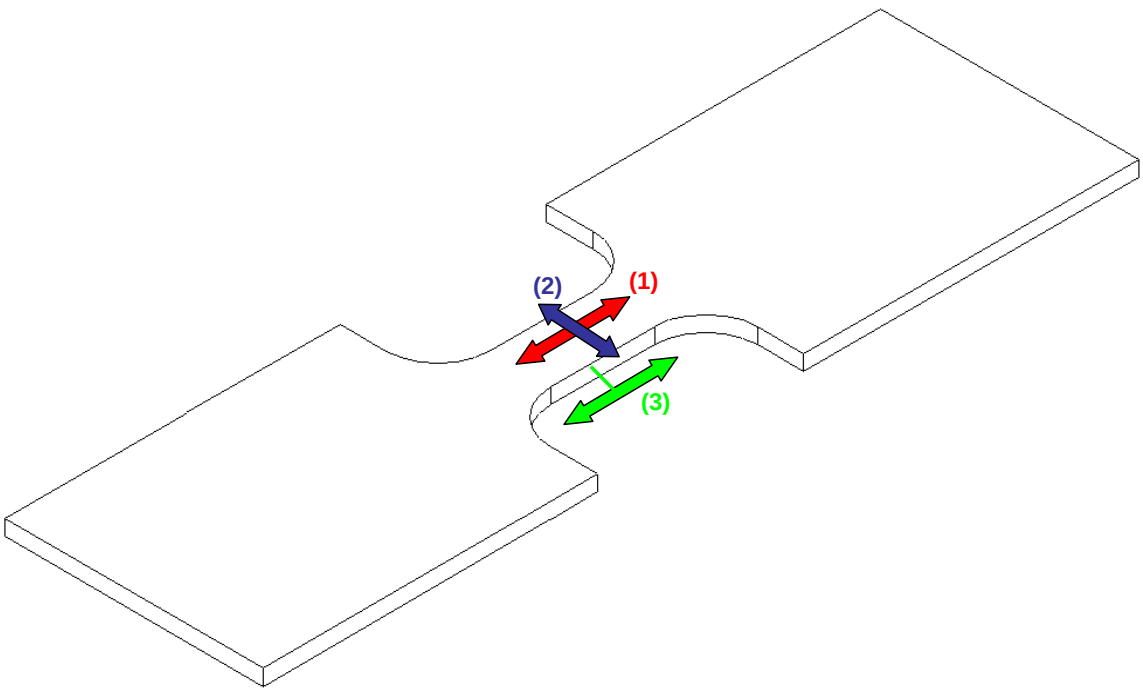

Figure B-3. Surface Roughness Measurements

Table B-1. Average Roughness Measurements

Fabrication Identifier	Fabrication Technique	Average Roughness, Ra (µin)		
		Measurement 1	Measurement 2	Measurement 3
SF1	Machined, Coarse	125-170	84-124	111-180
SF2/SF4	Machined, Smooth	13-22	8-20	16-22
SF3	EDM	107-118	107-118	15

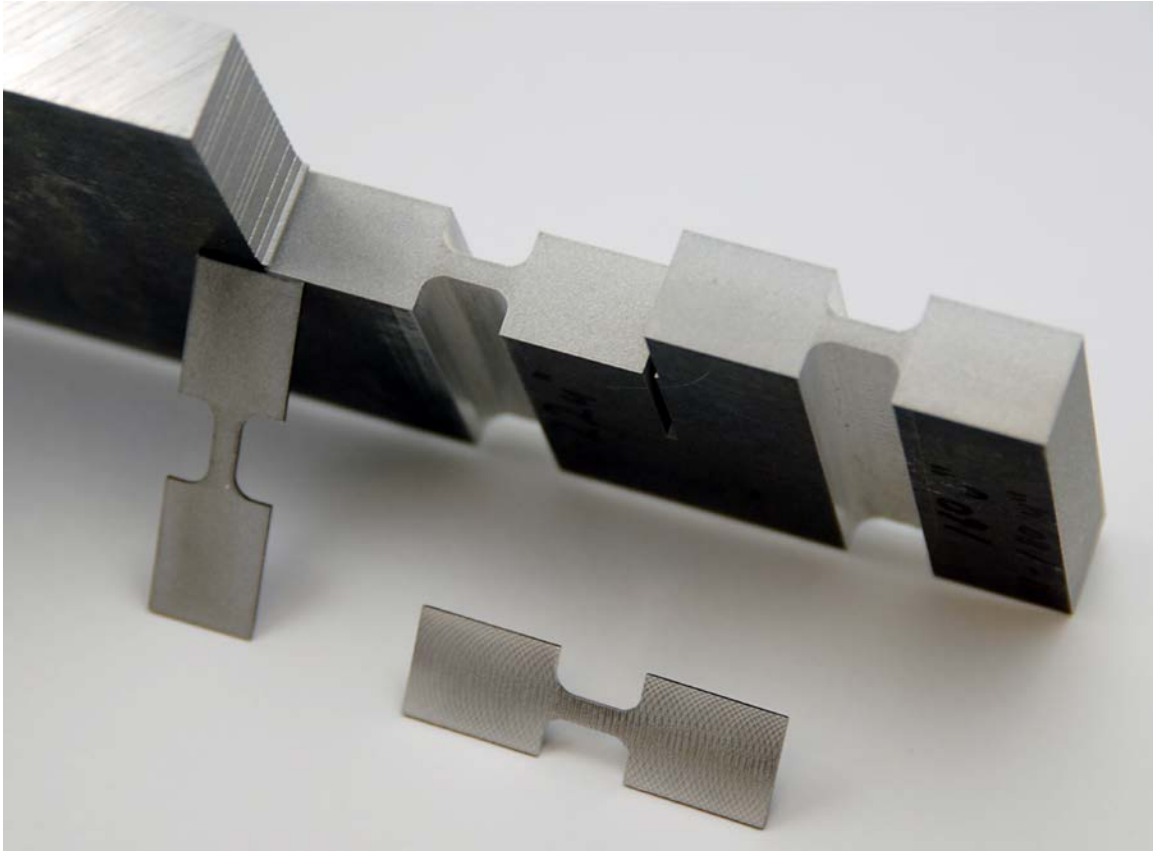

Figure B-4. The 12.7-mm-Thick 2024-T351 Aluminum Plate and Tension Specimens

Test results are shown in figures B-5 and B-6. Figure B-5(a, b, c, and d) shows engineering stress strain curves from tests conducted on SF1, SF2, SF3, and SF4 specimens, respectively. The blue curves in figure B-5 correspond to tests conducted at a strain rate of 1.0 s^{-1} and the red curves correspond to those tested at 1000.0 s^{-1}. Three curves, representing three separate tests at each rate, are shown together in each plot. The level of stress shows good repeatability for both strain rates and all four specimen fabrication methods. There is, however, some spread in the engineering fracture strain for the SF1 and SF2 specimens. At both strain rates, the fracture strains of the SF1 specimens are clearly lower than specimens fabricated to the three other specifications. This is likely because the deep machining grooves on the flat specimen face are oriented transverse to the axial load direction (figure B-1(a)). This causes stress concentrations in the grooves leading to premature fracture. The data in figure B-5 also show that stresses at 1000.0 s^{-1} are slightly higher than those at 1.0 s^{-1}. This trend is true for all four fabrication methods.

Figure B-6 shows the stress strain curves from the four different fabrication methods. Figure B-6(a and b) show data from tests at strain rates of 1.0 s^{-1} and 1000.0 s^{-1}, respectively. The stress levels from tests on all four fabrication methods are similar; however, the fracture strains from the SF1 specimens are clearly lower than those of the other specimens.

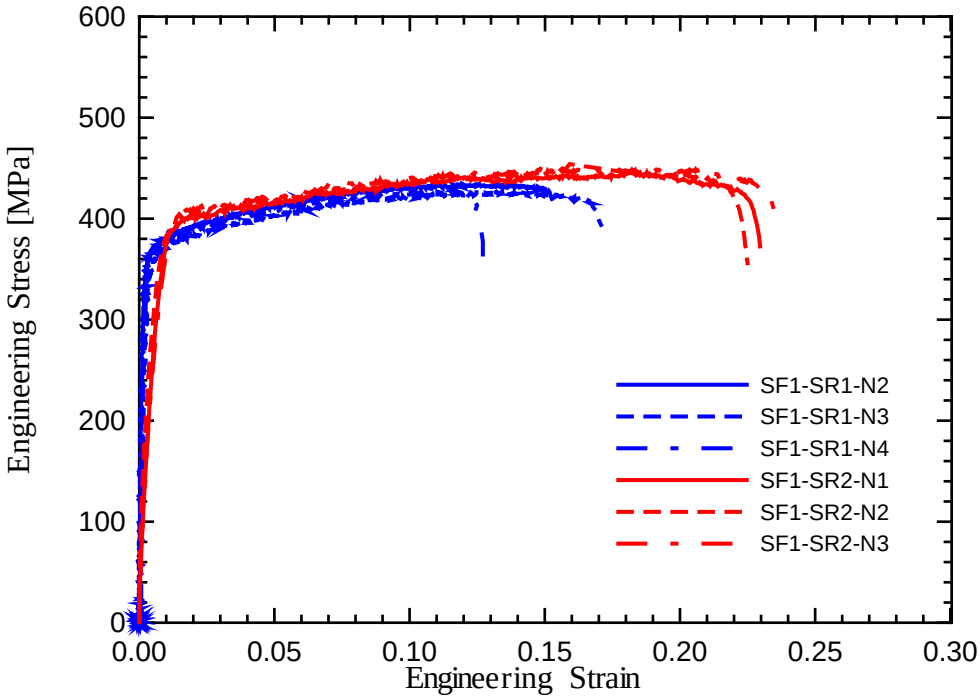

(a)

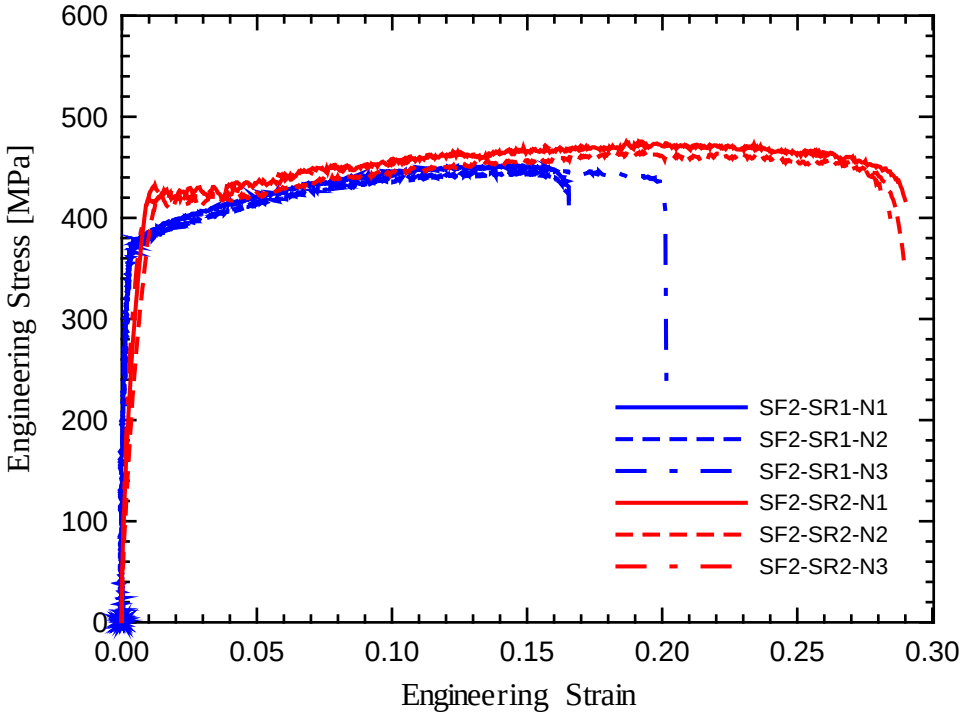

(b)

Figure B-5. Stress Strain Curves From the Specimen Fabrication Method Test Series (a) Coarse-Machined (SF1), (b) Smooth-Machined with Unbroken Edges (SF2), (c) EDM (SF3), and (d) Smooth-Machined With Broken Edges (SF4)

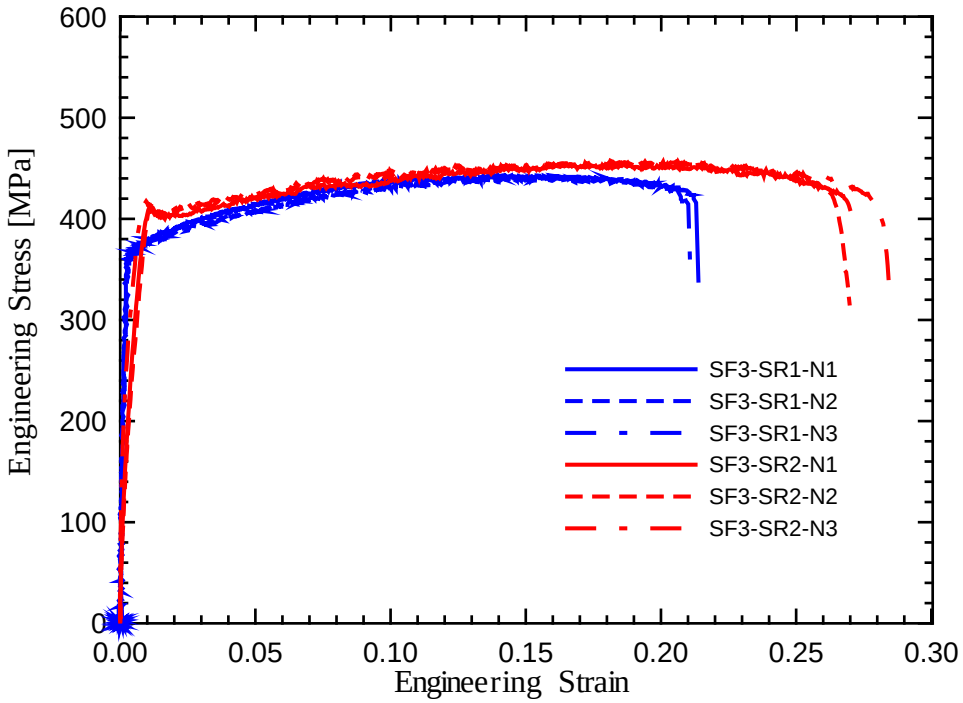

(c)

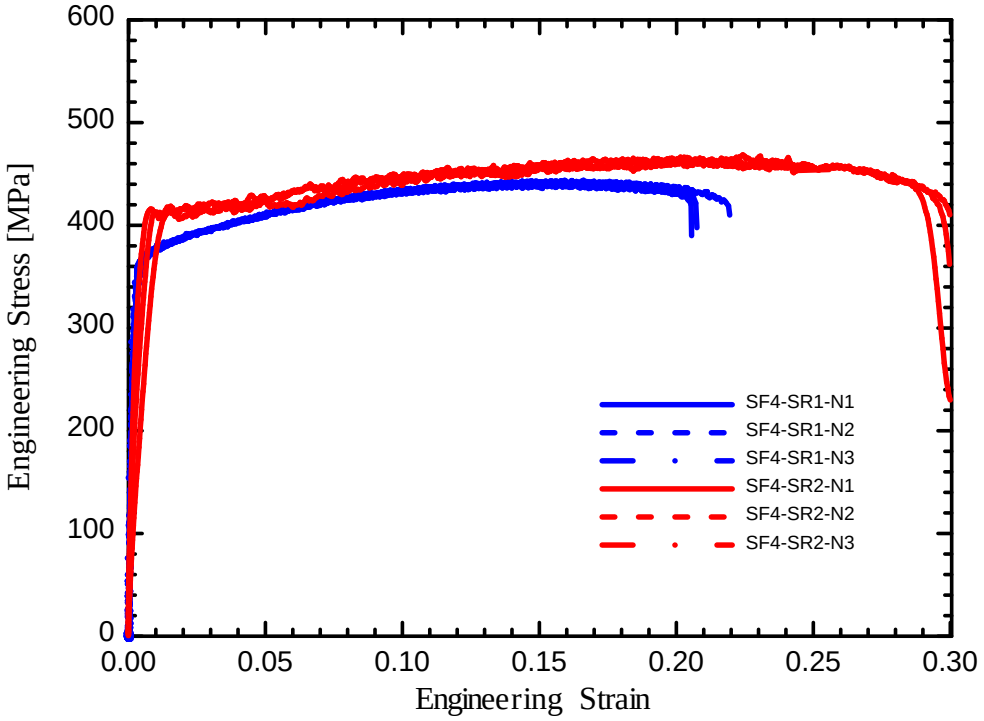

(d)

Figure B-5. Stress Strain Curves From the Specimen Fabrication Method Test Series (a) Coarse-Machined (SF1), (b) Smooth-Machined with Unbroken Edges (SF2), (c) EDM (SF3), and (d) Smooth-Machined With Broken Edges (SF4) (continued)

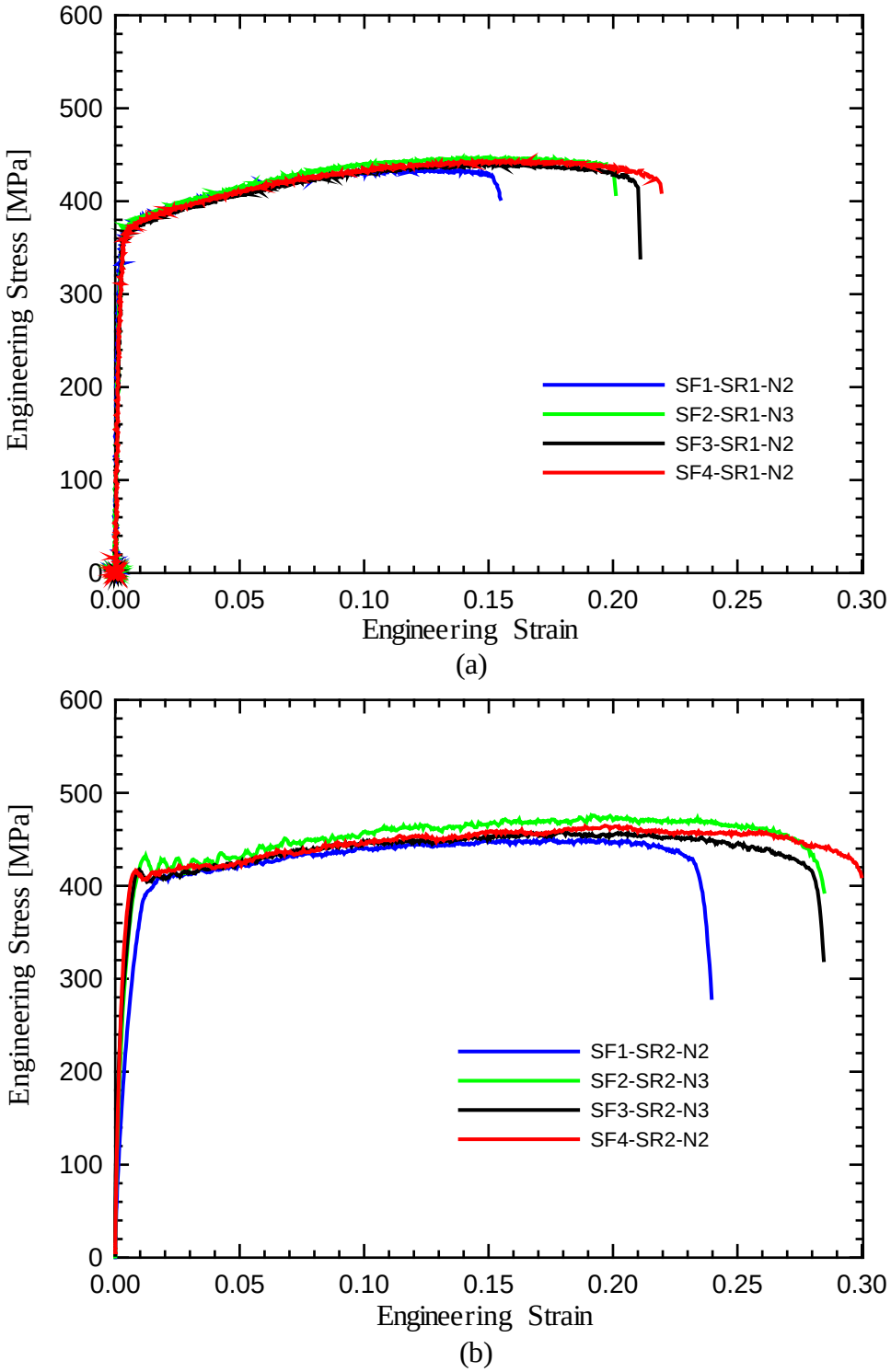

Figure B-6. Stress Strain Curves From the Specimen Fabrication Method Test Series (a) Low-Rate Data, $\dot{\varepsilon} = 1.0\ s^{-1}$ and (b) High-Rate Data, $\dot{\varepsilon} = 1000.0\ s^{-1}$

Average peak engineering stress and strain at fracture from the surface finish test series are shown in figure B-7. For all four fabrication methods, peak stresses at 1000.0 s^{-1} are higher than those at 1.0 s^{-1}. Peak stresses are highest for the smooth-machined specimens with unbroken edges (SF2), followed by smooth specimens with broken edges (SF4), EDM specimens (SF3), and the coarse-machined specimens (SF1). It is hypothesized that the SF2 specimens have higher average stresses than the SF4 specimens because breaking the edges reduces the cross-sectional area of the specimen, thus reducing the peak load. The width and thickness of each specimen were measured using calipers and micrometers, respectively, so this effective cross-sectional area decrease was not captured. The reduction in peak stresses from the SF2 specimens to the SF3 specimens is thought to occur because the thin recast layer is a heat-affected zone where the material is locally annealed, thus reducing its strength. Likewise, the deep machining gouges in the SF1 specimens reduce the specimen's cross-sectional area, much like the broken edges of the SF4 specimens. The differences in peak stress are statistically significant in all cases, except when comparing SF2 and SF4 data at 1000 s^{-1}.

The fracture strain data in figure B-7(b) shows that the SF1 specimens have significantly lower fracture strains than the SF2, SF3, and SF4 specimens. The difference is statistically significant at both 1.0 s^{-1} and 1000.0 s^{-1}. The deep gouges in the SF1 specimens create local stress concentrations that lead to premature crack initiation and fracture. Fracture strains at 1000.0 s^{-1} are higher than those at 1.0 s^{-1} for all four specimen fabrication methods. This extra dynamic ductility could be due to adiabatic heating; however, it could also be because strains are measured in different ways. The low-rate strains are measured using a 4-mm extensometer, and the high-rate strains are calculated from the waves measured from the SHB apparatus.

The results in figure B-7 show that the surface roughness has an effect on the test results. However, it is important to note that the fabrication method also plays a critical role. This is apparent when the results of the coarse-machined (SF1) specimens are compared to the EDM (SF3) specimens. Table B-1 shows that the SF1 and SF3 samples have similar surface roughness. However, the SF3 specimens have clearly sustained higher peak stresses and fracture strains. The distribution of the roughness clearly has an effect. The deep gouges of the SF1 specimens have prominent orientations in the width direction of the specimen (see figure B-1(a)), and the pitting of the EDM recast layer is uniformly distributed (see figure B-1(c)). The roughness distribution of the SF1 specimens negatively impacts both the strength and ductility of the specimen. On the other hand, the roughness distribution of the EDM specimens impacts the strength of the specimen less and has no impact on specimen ductility.

The results of this study show that the specimen fabrication method had an effect on both the peak engineering stress and strain at fracture. The coarse-machined (SF1) specimens had lower peak stresses and fracture strains than the other specimens. The smooth-machined, unbroken (SF2) specimens had higher peak stresses than those with broken edges (SF4) and those fabricated with the EDM (SF3). The ductilities of the SF2, SF3, and SF4 specimens were all roughly equivalent.

The main result of this study was that the tension specimens used to produce the data in sections 4 and 5 of the main report were fabricated using traditional machining methods to a surface finish better than 32 µin with unbroken edges.

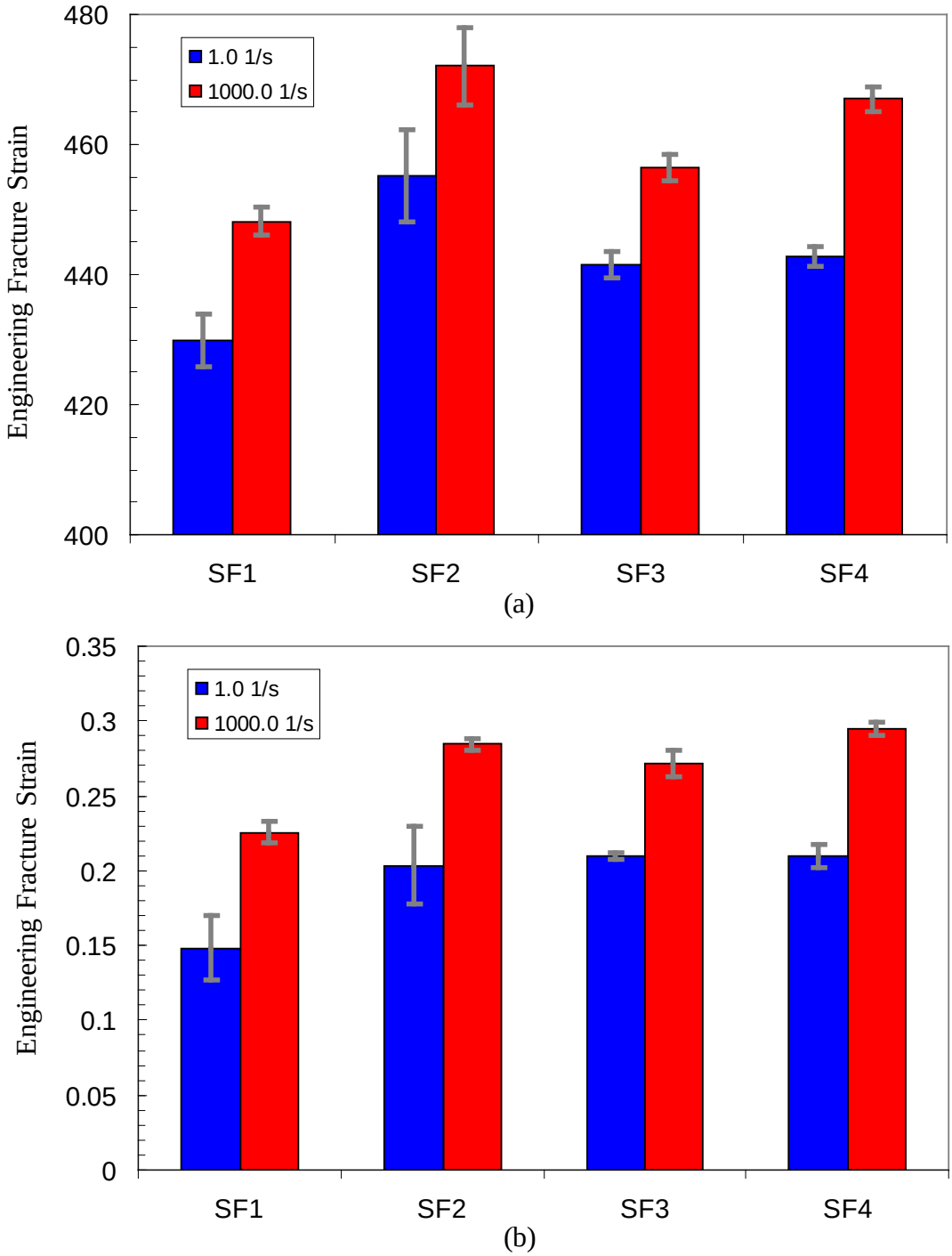

Figure B-7. Average Data From the Specimen Fabrication Method Test Series (a) Peak Engineering Stress and (b) Engineering Strain at Fracture

APPENDIX C—TEST NAMING CONVENTION

This appendix describes the naming scheme for all of the tests conducted. The naming scheme follows:

M*X*-TM*X*-P*X*-SG*X*-O*X*-SR*X*-T*X*-N*X*,

where the *X*s signify the specifics of the test, outlined in the following list:

- M*X* is the material identifier. The number 1 signifies 2024 aluminum, and 2 and 3 signify Ti-6Al-4V and Inconel 718, respectively. This report contains only data for 2024 aluminum (M1).

- TM*X* is the test mode identifier.

  - TMT indicates a tensile test.
  - TMC indicates a compression test.
  - TMS indicates a shear (torsion) test.
  - TMCL indicates a combined loading test (tension torsion or compression torsion).
  - TMP1 indicates a sharp radius punch test.
  - TMP2 indicates an intermediate radius punch test.
  - TMP3 indicates a blunt punch test.

- P*X* is the plate/sheet stock origin of the test specimen

  - P1 indicates 0.125 in 2024-T3 sheet.
  - P2 indicates 0.25 in 2024-T351 plate.
  - P3 indicates 0.5 in 2024-T351 plate.

- SG*X* indicates the specimen geometry. This identifier applies only to tension tests (see tables 4, 5, and 6).

  - SG1 though SG4 indicate plane stress tension tests on thin, flat specimens with various gage section geometries (see table 4 of main document).

  - SG5 through SG10 indicate tension tests on axisymmetric specimens with various gage section geometries (see table 5 of main document).

  - SG11 through SG13 indicate plane strain tension tests on wide specimens with with various gage section geometries (see table 6 of main document).

- O*X* indicates the sample's orientation with respect to the original sheet or plate.

  - O1 indicates the specimen is aligned in the rolled direction of the sheet/plate.

- O2 indicates the specimen is aligned +45° to the rolled direction of the sheet/plate.

- O3 indicates the specimen is aligned transverse (90°) to the rolled direction of the sheet/plate.

- O4 indicates the specimen is aligned -45° to the rolled direction of the sheet/plate.

- O5 indicates the specimen is aligned in the thickness direction of the sheet/plate (compression only).

- SR*X* indicates the strain rate of the test (see table 2).

  - SR1: $\dot{\varepsilon} = 1.0E\text{-}4\ s^{-1}$
  - SR2: $\dot{\varepsilon} = 1.0E\text{-}2\ s^{-1}$
  - SR3: $\dot{\varepsilon} = 1.0\ s^{-1}$
  - SR4:
    - Tension/Torsion: $\dot{\varepsilon} = 500.0\ s^{-1}$
    - Compression: $\dot{\varepsilon} = 1500.0\ s^{-1}$
  - SR5:

    - Tension: $\dot{\varepsilon} = 1800.0\ s^{-1}$
    - Compression: $\dot{\varepsilon} = 5000.0\ s^{-1}$
    - Torsion: $\dot{\varepsilon} = 2800.0\ s^{-1}$

  - SR6: $\dot{\varepsilon} = 8000.0\ s^{-1}$ (compression only)
  - SR7: $\dot{\varepsilon} = 10000.0\ s^{-1}$ (compression only)
  - SR8: $\dot{\varepsilon} = 11000.0\ s^{-1}$ (compression only)

- T*X* indicates the test temperature (see table 2).

  - T1: Room Temperature
  - T2: 150°C
  - T3: 300°C
  - T4: 450°C
  - T5: -50°C

- NX indicates the test number. Typically, three tests of each condition were conducted (N1, N2, and N3).

The combined loading tests (TMCL) have an additional identifier, LR*X* or load ratio, that specifies the ratio of axial stress to shear stress, or $\frac{\sigma_x}{\tau_{xy}}$. The four load ratios are:

- LR1: $\frac{\sigma_x}{\tau_{xy}} = 2.587$ (tension-torsion)
- LR2: $\frac{\sigma_x}{\tau_{xy}} = 1.148$ (tension-torsion)
- LR3: $\frac{\sigma_x}{\tau_{xy}} = 0.0$ (torsion)
- LR4: $\frac{\sigma_x}{\tau_{xy}} = -0.920$ (compression-torsion)

Table C-1. Complete Test Series

Tension													
	Test #	Test Mode (Tension, Torsion, Compression, etc.)	Apparatus	Material Stock Identifier	Specimen Geometry	Specimen Gage Fabrication Orientation	Strain Rate (1/s)	Temperature (˚C)	Test Complete? (y/n)	Gauge Length (in)	Gauge Width (in)	Gauge Thickness (in)	Notes
1	M1-TMT-P3-SG1-O1-SR1-T1-N1	Tension	Instron	P3 (0.5")	Flat Dogbone	Rolled Direction	1.00E-04	RT	y	0.200	0.121	0.029	Testing Complete
2	M1-TMT-P3-SG1-O1-SR1-T1-N2	Tension	Instron	P3 (0.5")	Flat Dogbone	Rolled Direction	1.00E-04	RT	y	0.200	0.119	0.030	
3	M1-TMT-P3-SG1-O1-SR1-T1-N3	Tension	Instron	P3 (0.5")	Flat Dogbone	Rolled Direction	1.00E-04	RT	y	0.200	0.120	0.030	
4	M1-TMT-P3-SG1-O1-SR2-T1-N1	Tension	Instron	P3 (0.5")	Flat Dogbone	Rolled Direction	1.00E-02	RT	y	0.200	0.121	0.030	
5	M1-TMT-P3-SG1-O1-SR2-T1-N2	Tension	Instron	P3 (0.5")	Flat Dogbone	Rolled Direction	1.00E-02	RT	y	0.200	0.120	0.030	
6	M1-TMT-P3-SG1-O1-SR2-T1-N3	Tension	Instron	P3 (0.5")	Flat Dogbone	Rolled Direction	1.00E-02	RT	y	0.200	0.120	0.031	
7	M1-TMT-P3-SG1-O1-SR3-T1-N1	Tension	Instron	P3 (0.5")	Flat Dogbone	Rolled Direction	1.00E+00	RT	y	0.200	0.120	0.030	
8	M1-TMT-P3-SG1-O1-SR3-T1-N2	Tension	Instron	P3 (0.5")	Flat Dogbone	Rolled Direction	1.00E+00	RT	y	0.200	0.120	0.030	
9	M1-TMT-P3-SG1-O1-SR3-T1-N3	Tension	Instron	P3 (0.5")	Flat Dogbone	Rolled Direction	1.00E+00	RT	y	0.200	0.119	0.031	
10	M1-TMT-P3-SG1-O1-SR3-T2-N1	Tension	Instron	P3 (0.5")	Flat Dogbone	Rolled Direction	1.00E+00	150	y	0.200	0.121	0.030	
11	M1-TMT-P3-SG1-O1-SR3-T2-N2	Tension	Instron	P3 (0.5")	Flat Dogbone	Rolled Direction	1.00E+00	150	y	0.200	0.121	0.030	
12	M1-TMT-P3-SG1-O1-SR3-T2-N3	Tension	Instron	P3 (0.5")	Flat Dogbone	Rolled Direction	1.00E+00	150	y	0.200	0.121	0.030	
13	M1-TMT-P3-SG1-O1-SR3-T3-N1	Tension	Instron	P3 (0.5")	Flat Dogbone	Rolled Direction	1.00E+00	300	y	0.200	0.121	0.030	
14	M1-TMT-P3-SG1-O1-SR3-T3-N2	Tension	Instron	P3 (0.5")	Flat Dogbone	Rolled Direction	1.00E+00	300	y	0.200	0.120	0.030	
15	M1-TMT-P3-SG1-O1-SR3-T3-N3	Tension	Instron	P3 (0.5")	Flat Dogbone	Rolled Direction	1.00E+00	300	y	0.200	0.121	0.030	
16	M1-TMT-P3-SG1-O1-SR3-T4-N1	Tension	Instron	P3 (0.5")	Flat Dogbone	Rolled Direction	1.00E+00	450	y	0.200	0.120	0.030	
17	M1-TMT-P3-SG1-O1-SR3-T4-N2	Tension	Instron	P3 (0.5")	Flat Dogbone	Rolled Direction	1.00E+00	450	y	0.200	0.120	0.030	
18	M1-TMT-P3-SG1-O1-SR3-T4-N3	Tension	Instron	P3 (0.5")	Flat Dogbone	Rolled Direction	1.00E+00	450	y	0.200	0.120	0.030	
19	M1-TMT-P3-SG1-O1-SR3-T5-N1	Tension	Instron	P3 (0.5")	Flat Dogbone	Rolled Direction	1.00E+00	-50	y	0.200	0.120	0.030	Testing Complete
20	M1-TMT-P3-SG1-O1-SR3-T5-N2	Tension	Instron	P3 (0.5")	Flat Dogbone	Rolled Direction	1.00E+00	-50	y	0.200	0.120	0.031	
21	M1-TMT-P3-SG1-O1-SR3-T5-N3	Tension	Instron	P3 (0.5")	Flat Dogbone	Rolled Direction	1.00E+00	-50	y	0.200	0.120	0.030	
22	M1-TMT-P3-SG1-O1-SR4-T1-N1	Tension	SHB	P3 (0.5")	Flat Dogbone	Rolled Direction	5.00E+02	RT	y	0.200	0.120	0.029	Testing Complete

23	M1-TMT-P3-SG1-O1-SR4-T1-N2	Tension	SHB	P3 (0.5")	Flat Dogbone	Rolled Direction	5.00E+02	RT	y	0.200	0.119	0.031	
24	M1-TMT-P3-SG1-O1-SR4-T1-N3	Tension	SHB	P3 (0.5")	Flat Dogbone	Rolled Direction	5.00E+02	RT	y	0.200	0.119	0.031	
25	M1-TMT-P3-SG1-O1-SR5-T1-N1	Tension	SHB	P3 (0.5")	Flat Dogbone	Rolled Direction	2.00E+03	RT	y	0.200	0.120	0.030	
26	M1-TMT-P3-SG1-O1-SR5-T1-N2	Tension	SHB	P3 (0.5")	Flat Dogbone	Rolled Direction	2.00E+03	RT	y	0.200	0.121	0.031	
27	M1-TMT-P3-SG1-O1-SR5-T1-N3	Tension	SHB	P3 (0.5")	Flat Dogbone	Rolled Direction	2.00E+03	RT	y	0.200	0.120	0.030	
28	M1-TMT-P3-SG1-O2-SR3-T1-N1	Tension	Instron	P3 (0.5")	Flat Dogbone	45˚	1.00E+00	RT	y	0.200	0.124	0.030	Testing Complete
29	M1-TMT-P3-SG1-O2-SR3-T1-N2	Tension	Instron	P3 (0.5")	Flat Dogbone	45˚	1.00E+00	RT	y	0.200	0.123	0.031	
30	M1-TMT-P3-SG1-O3-SR3-T1-N1	Tension	Instron	P3 (0.5")	Flat Dogbone	Transverse	1.00E+00	RT	y	0.200	0.120	0.030	
31	M1-TMT-P3-SG1-O3-SR3-T1-N2	Tension	Instron	P3 (0.5")	Flat Dogbone	Transverse	1.00E+00	RT	y	0.200	0.120	0.030	
32	M1-TMT-P3-SG1-O4-SR3-T1-N1	Tension	Instron	P3 (0.5")	Flat Dogbone	135˚	1.00E+00	RT	y	0.200	0.125	0.031	
33	M1-TMT-P3-SG1-O4-SR3-T1-N2	Tension	Instron	P3 (0.5")	Flat Dogbone	135˚	1.00E+00	RT	y	0.200	0.125	0.031	
	Test #	Test Mode (Tension, Torsion, Compression, etc.)	Apparatus	Material Stock Identifier	Specimen Geometry	Specimen Gage Fabrication Orientation	Strain Rate (1/s)	Temperature (˚C)	Test Complete? (y/n)	Gauge Radius (in)	Gauge Width (in)	Gauge Thickness (in)	
34	M1-TMT-P3-SG2-O1-SR3-T1-N1	Tension	Instron	P3 (0.5")	2D Large Notch	Rolled Direction	1.00E+00	RT	y	0.188	0.120	0.030	Testing Complete
35	M1-TMT-P3-SG2-O1-SR3-T1-N2	Tension	Instron	P3 (0.5")	2D Large Notch	Rolled Direction	1.00E+00	RT	y	0.188	0.121	0.031	
36	M1-TMT-P3-SG2-O1-SR3-T1-N3	Tension	Instron	P3 (0.5")	2D Large Notch	Rolled Direction	1.00E+00	RT	y	0.189	0.118	0.030	
37	M1-TMT-P3-SG3-O1-SR3-T1-N1	Tension	Instron	P3 (0.5")	2D Intermediate Notch	Rolled Direction	1.00E+00	RT	y	0.077	0.121	0.031	
38	M1-TMT-P3-SG3-O1-SR3-T1-N2	Tension	Instron	P3 (0.5")	2D Intermediate Notch	Rolled Direction	1.00E+00	RT	y	0.079	0.121	0.031	
39	M1-TMT-P3-SG3-O1-SR3-T1-N3	Tension	Instron	P3 (0.5")	2D Intermediate Notch	Rolled Direction	1.00E+00	RT	y	0.078	0.124	0.030	
40	M1-TMT-P3-SG4-O1-SR3-T1-N1	Tension	Instron	P3 (0.5")	2D Small Notch	Rolled Direction	1.00E+00	RT	y	0.015	0.127	0.030	
41	M1-TMT-P3-SG4-O1-SR3-T1-N2	Tension	Instron	P3 (0.5")	2D Small Notch	Rolled Direction	1.00E+00	RT	y	0.015	0.123	0.030	
42	M1-TMT-P3-SG4-O1-SR3-T1-N3	Tension	Instron	P3 (0.5")	2D Small Notch	Rolled Direction	1.00E+00	RT	y	0.015	0.124	0.030	

	Test #	Test Mode (Tension, Torsion, Compression, etc.)	Apparatus	Material Stock Identifier	Specimen Geometry	Specimen Gage Fabrication Orientation	Strain Rate (1/s)	Temperature (˚C)	Test Complete? (y/n)	Gauge Length (in)	Gauge Diameter (in)		
43	M1-TMT-P3-SG5-O1-SR3-T1-N1	Tension	Instron	P3 (0.5")	Axisymmetric Smooth	Rolled Direction	1.00E+00	RT	y	0.950	0.187		Testing Complete
44	M1-TMT-P3-SG5-O1-SR3-T1-N2	Tension	Instron	P3 (0.5")	Axisymmetric Smooth	Rolled Direction	1.00E+00	RT	y	0.950	0.187		
45	M1-TMT-P3-SG5-O1-SR3-T1-N3	Tension	Instron	P3 (0.5")	Axisymmetric Smooth	Rolled Direction	1.00E+00	RT	y	0.950	0.186		
46	M1-TMT-P3-SG6-O1-SR3-T1-N1	Tension	Instron	P3 (0.5")	Axisymmetric Notch #1	Rolled Direction	1.00E+00	RT	y	0.571	0.187		
47	M1-TMT-P3-SG6-O1-SR3-T1-N2	Tension	Instron	P3 (0.5")	Axisymmetric Notch #1	Rolled Direction	1.00E+00	RT	y	0.571	0.187		
48	M1-TMT-P3-SG6-O1-SR3-T1-N3	Tension	Instron	P3 (0.5")	Axisymmetric Notch #1	Rolled Direction	1.00E+00	RT	y	0.571	0.187		
49	M1-TMT-P3-SG7-O1-SR3-T1-N1	Tension	Instron	P3 (0.5")	Axisymmetric Notch #2	Rolled Direction	1.00E+00	RT	y	0.360	0.187		
50	M1-TMT-P3-SG7-O1-SR3-T1-N2	Tension	Instron	P3 (0.5")	Axisymmetric Notch #2	Rolled Direction	1.00E+00	RT	y	0.360	0.187		
51	M1-TMT-P3-SG7-O1-SR3-T1-N3	Tension	Instron	P3 (0.5")	Axisymmetric Notch #2	Rolled Direction	1.00E+00	RT	y	0.360	0.187		
52	M1-TMT-P3-SG8-O1-SR3-T1-N1	Tension	Instron	P3 (0.5")	Axisymmetric Notch #3	Rolled Direction	1.00E+00	RT	y	0.240	0.187		
53	M1-TMT-P3-SG8-O1-SR3-T1-N2	Tension	Instron	P3 (0.5")	Axisymmetric Notch #3	Rolled Direction	1.00E+00	RT	y	0.240	0.187		
54	M1-TMT-P3-SG8-O1-SR3-T1-N3	Tension	Instron	P3 (0.5")	Axisymmetric Notch #3	Rolled Direction	1.00E+00	RT	y	0.240	0.187		
55	M1-TMT-P3-SG9-O1-SR3-T1-N1	Tension	Instron	P3 (0.5")	Axisymmetric Notch #4	Rolled Direction	1.00E+00	RT	y	0.176	0.188		
56	M1-TMT-P3-SG9-O1-SR3-T1-N2	Tension	Instron	P3 (0.5")	Axisymmetric Notch #4	Rolled Direction	1.00E+00	RT	y	0.176	0.188		
57	M1-TMT-P3-SG9-O1-SR3-T1-N3	Tension	Instron	P3 (0.5")	Axisymmetric Notch #4	Rolled Direction	1.00E+00	RT	y	0.176	0.188		
58	M1-TMT-P3-SG10-O1-SR3-T1-N1	Tension	Instron	P3 (0.5")	Axisymmetric Notch #5	Rolled Direction	1.00E+00	RT	y	0.120	0.188		
59	M1-TMT-P3-SG10-O1-SR3-T1-N2	Tension	Instron	P3 (0.5")	Axisymmetric Notch #5	Rolled Direction	1.00E+00	RT	y	0.120	0.188		
60	M1-TMT-P3-SG10-O1-SR3-T1-N3	Tension	Instron	P3 (0.5")	Axisymmetric Notch #5	Rolled Direction	1.00E+00	RT	y	0.120	0.188		

	Test #	Test Mode (Tension, Torsion, Compression, etc.)	Apparatus	Material Stock Identifier	Specimen Geometry	Specimen Gage Fabrication Orientation	Strain Rate (1/s)	Temperature (˚C)	Test Complete? (y/n)	Gauge Radius (in)	Gauge Width (in)	Gauge Thickness (in)	
61	M1-TMT-P3-SG11-O1-SR3-T1-N1	Tension	Instron	P3 (0.5")	Plane Strain (thick dogbone)	Rolled Direction	1.00E+00	RT	y	0.200	0.081	0.999	
62	M1-TMT-P3-SG11-O1-SR3-T1-N2	Tension	Instron	P3 (0.5")	Plane Strain (thick dogbone)	Rolled Direction	1.00E+00	RT	y	0.200	0.080	0.998	
63	M1-TMT-P3-SG11-O1-SR3-T1-N3	Tension	Instron	P3 (0.5")	Plane Strain (thick dogbone)	Rolled Direction	1.00E+00	RT	y	0.200	0.079	0.997	
64	M1-TMT-P3-SG12-O1-SR3-T1-N1	Tension	Instron	P3 (0.5")	Plane Strain (thick large notch)	Rolled Direction	1.00E+00	RT	y	0.550	0.081	0.999	
65	M1-TMT-P3-SG12-O1-SR3-T1-N2	Tension	Instron	P3 (0.5")	Plane Strain (thick large notch)	Rolled Direction	1.00E+00	RT	y	0.550	0.080	0.998	
66	M1-TMT-P3-SG12-O1-SR3-T1-N3	Tension	Instron	P3 (0.5")	Plane Strain (thick large notch)	Rolled Direction	1.00E+00	RT	y	0.550	0.080	0.998	
67	M1-TMT-P3-SG13-O1-SR3-T1-N1	Tension	Instron	P3 (0.5")	Plane Strain (thick small notch)	Rolled Direction	1.00E+00	RT	y	0.188	0.081	0.999	
68	M1-TMT-P3-SG13-O1-SR3-T1-N2	Tension	Instron	P3 (0.5")	Plane Strain (thick small notch)	Rolled Direction	1.00E+00	RT	y	0.188	0.080	0.998	
69	M1-TMT-P3-SG13-O1-SR3-T1-N3	Tension	Instron	P3 (0.5")	Plane Strain (thick small notch)	Rolled Direction	1.00E+00	RT	y	0.188	0.081	0.998	Testing Complete
	Test #	Test Mode (Tension, Torsion, Compression, etc.)	Apparatus	Material Stock Identifier	Specimen Geometry	Specimen Gage Fabrication Orientation	Strain Rate (1/s)	Temperature (˚C)	Test Complete? (y/n)	Gauge Length (in)	Gauge Width (in)	Gauge Thickness (in)	
70	M1-TMT-P2-SG1-O1-SR3-T1-N1	Tension	Instron	P2 (0.25")	Flat Dogbone	Rolled Direction	1.00E+00	RT	y	0.200	0.120	0.031	Testing Complete
71	M1-TMT-P2-SG1-O1-SR3-T1-N2	Tension	Instron	P2 (0.25")	Flat Dogbone	Rolled Direction	1.00E+00	RT	y	0.200	0.120	0.031	
72	M1-TMT-P2-SG1-O1-SR4-T1-N1	Tension	SHB	P2 (0.25")	Flat Dogbone	Rolled Direction	5.00E+02	RT	y	0.200	0.119	0.031	
73	M1-TMT-P2-SG1-O1-SR4-T1-N2	Tension	SHB	P2 (0.25")	Flat Dogbone	Rolled Direction	5.00E+02	RT	y	0.200	0.119	0.031	
74	M1-TMT-P1-SG1-O1-SR3-T1-N1	Tension	Instron	P1 (0.125")	Flat Dogbone	Rolled Direction	1.00E+00	RT	y	0.200	0.120	0.031	
75	M1-TMT-P1-SG1-O1-SR3-T1-N2	Tension	Instron	P1 (0.125")	Flat Dogbone	Rolled Direction	1.00E+00	RT	y	0.200	0.120	0.031	
76	M1-TMT-P1-SG1-O1-SR4-T1-N1	Tension	SHB	P1 (0.125")	Flat Dogbone	Rolled Direction	5.00E+02	RT	y	0.200	0.119	0.031	

77	M1-TMT-P1-SG1-O1-SR4-T1-N2	Tension	SHB	P1 (0.125")	Flat Dogbone	Rolled Direction	5.00E+02	RT	y	0.200	0.120	0.031	
Tension (Surface Finish Test Series)													
	Test #	Test Mode (Tension, Torsion, Compression, etc.)	Apparatus	Material Stock Identifier	Specimen Geometry	Specimen Gage Fabrication Orientation	Strain Rate (1/s)	Temperature (˚C)	Test Complete? (y/n)	Gauge Length (in)	Gauge Width (in)	Gauge Thickness (in)	
78	M1-SF1-SR1-N1	Tension	Instron	P3 (0.5")	Flat Dogbone	Rolled Direction	1.00E+00	RT	y	0.200	0.119	0.029	SF1 - 2024-T351 Aluminum, Machined with surface roughness range: Ra - 84 to 180 Testing Complete
79	M1-SF1-SR1-N2	Tension	Instron	P3 (0.5")	Flat Dogbone	Rolled Direction	1.00E+00	RT	y	0.200	0.120	0.029	
80	M1-SF1-SR1-N3	Tension	Instron	P3 (0.5")	Flat Dogbone	Rolled Direction	1.00E+00	RT	y	0.200	0.120	0.030	
81	M1-SF1-SR1-N4	Tension	Instron	P3 (0.5")	Flat Dogbone	Rolled Direction	1.00E+00	RT	y	0.200	0.120	0.026	
82	M1-SF1-SR2-N1	Tension	SHB	P3 (0.5")	Flat Dogbone	Rolled Direction	1.00E+03	RT	y	0.200	0.119	0.029	
83	M1-SF1-SR2-N2	Tension	SHB	P3 (0.5")	Flat Dogbone	Rolled Direction	1.00E+03	RT	y	0.200	0.120	0.030	
84	M1-SF1-SR2-N3	Tension	SHB	P3 (0.5")	Flat Dogbone	Rolled Direction	1.00E+03	RT	y	0.200	0.119	0.029	
85	M1-SF2-SR1-N1	Tension	Instron	P3 (0.5")	Flat Dogbone	Rolled Direction	1.00E+00	RT	y	0.200	0.119	0.029	SF2 - 2024-T351 Aluminum, Machined with surface roughness range: Ra - 8 to 20 (edges unbroken) Testing Complete
86	M1-SF2-SR1-N2	Tension	Instron	P3 (0.5")	Flat Dogbone	Rolled Direction	1.00E+00	RT	y	0.200	0.121	0.029	
87	M1-SF2-SR1-N3	Tension	Instron	P3 (0.5")	Flat Dogbone	Rolled Direction	1.00E+00	RT	y	0.200	0.121	0.030	
88	M1-SF2-SR2-N1	Tension	SHB	P3 (0.5")	Flat Dogbone	Rolled Direction	1.00E+03	RT	y	0.200	0.121	0.029	
89	M1-SF2-SR2-N2	Tension	SHB	P3 (0.5")	Flat Dogbone	Rolled Direction	1.00E+03	RT	y	0.200	0.119	0.029	
90	M1-SF2-SR2-N3	Tension	SHB	P3 (0.5")	Flat Dogbone	Rolled Direction	1.00E+03	RT	y	0.200	0.120	0.029	
91	M1-SF3-SR1-N1	Tension	Instron	P3 (0.5")	Flat Dogbone	Rolled Direction	1.00E+00	RT	y	0.200	0.121	0.030	SF3 - 2024-T351 Aluminum, EDM with surface roughness range: Ra - 107 to 118 Testing Complete
92	M1-SF3-SR1-N2	Tension	Instron	P3 (0.5")	Flat Dogbone	Rolled Direction	1.00E+00	RT	y	0.200	0.121	0.030	
93	M1-SF3-SR1-N3	Tension	Instron	P3 (0.5")	Flat Dogbone	Rolled Direction	1.00E+00	RT	y	0.200	0.121	0.030	
94	M1-SF3-SR2-N1	Tension	SHB	P3 (0.5")	Flat Dogbone	Rolled Direction	1.00E+03	RT	y	0.200	0.121	0.030	
95	M1-SF3-SR2-N2	Tension	SHB	P3 (0.5")	Flat Dogbone	Rolled Direction	1.00E+03	RT	y	0.200	0.121	0.030	
96	M1-SF3-SR2-N3	Tension	SHB	P3 (0.5")	Flat Dogbone	Rolled Direction	1.00E+03	RT	y	0.200	0.121	0.030	
97	M1-SF4-SR1-N1	Tension	Instron	P3 (0.5")	Flat Dogbone	Rolled Direction	1.00E+00	RT	y	0.200	0.120	0.029	SF2 - 2024-T351 Aluminum, Machined with surface roughness range: Ra - 8 to 20 (edges broken) Testing Complete
98	M1-SF4-SR1-N2	Tension	Instron	P3 (0.5")	Flat Dogbone	Rolled Direction	1.00E+00	RT	y	0.200	0.120	0.030	
99	M1-SF4-SR1-N3	Tension	Instron	P3 (0.5")	Flat Dogbone	Rolled Direction	1.00E+00	RT	y	0.200	0.120	0.029	
100	M1-SF4-SR2-N1	Tension	SHB	P3 (0.5")	Flat Dogbone	Rolled Direction	1.00E+03	RT	y	0.200	0.119	0.029	
101	M1-SF4-SR2-N2	Tension	SHB	P3 (0.5")	Flat Dogbone	Rolled Direction	1.00E+03	RT	y	0.200	0.120	0.029	
102	M1-SF4-SR2-N3	Tension	SHB	P3 (0.5")	Flat Dogbone	Rolled Direction	1.00E+03	RT	y	0.200	0.119	0.029	
	Compression												
	Test #	Test Mode (Tension, Torsion, Compression, etc.)	Apparatus	Material Stock Identifier	Specimen Geometry	Specimen Gage Fabrication Orientation	Strain Rate (1/s)	Temperature (˚C)	Test Complete? (y/n)	Gauge Length (in)	Gauge Diameter (in)		
103	M1-TMC-P3-SG1-O1-SR1-T1-N1	Compression	Instron	P3 (0.5")	Cylinder	Rolled Direction	1.00E-04	RT	y	0.120	0.120		Testing Complete
104	M1-TMC-P3-SG1-O1-SR1-T1-N2	Compression	Instron	P3 (0.5")	Cylinder	Rolled Direction	1.00E-04	RT	y	0.119	0.120		
105	M1-TMC-P3-SG1-O1-SR1-T1-N3	Compression	Instron	P3 (0.5")	Cylinder	Rolled Direction	1.00E-04	RT	y	0.120	0.120		
106	M1-TMC-P3-SG1-O1-SR2-T1-N1	Compression	Instron	P3 (0.5")	Cylinder	Rolled Direction	1.00E-02	RT	y	0.120	0.120		
107	M1-TMC-P3-SG1-O1-SR2-T1-N2	Compression	Instron	P3 (0.5")	Cylinder	Rolled Direction	1.00E-02	RT	y	0.120	0.119		
108	M1-TMC-P3-SG1-O1-SR2-T1-N3	Compression	Instron	P3 (0.5")	Cylinder	Rolled Direction	1.00E-02	RT	y	0.120	0.120		

109	M1-TMC-P3-SG1-O1-SR3-T1-N1	Compression	Instron	P3 (0.5")	Cylinder	Rolled Direction	1.00E+00	RT	y	0.120	0.120		
110	M1-TMC-P3-SG1-O1-SR3-T1-N2	Compression	Instron	P3 (0.5")	Cylinder	Rolled Direction	1.00E+00	RT	y	0.122	0.120		
111	M1-TMC-P3-SG1-O1-SR3-T1-N3	Compression	Instron	P3 (0.5")	Cylinder	Rolled Direction	1.00E+00	RT	y	0.118	0.120		
112	M1-TMC-P3-SG1-O1-SR3-T2-N1	Compression	Instron	P3 (0.5")	Cylinder	Rolled Direction	1.00E+00	150	y	0.120	0.120		Testing Complete
113	M1-TMC-P3-SG1-O1-SR3-T2-N2	Compression	Instron	P3 (0.5")	Cylinder	Rolled Direction	1.00E+00	150	y	0.119	0.119		
114	M1-TMC-P3-SG1-O1-SR3-T2-N3	Compression	Instron	P3 (0.5")	Cylinder	Rolled Direction	1.00E+00	150	y	0.121	0.120		
115	M1-TMC-P3-SG1-O1-SR3-T3-N1	Compression	Instron	P3 (0.5")	Cylinder	Rolled Direction	1.00E+00	300	y	0.121	0.120		
116	M1-TMC-P3-SG1-O1-SR3-T3-N2	Compression	Instron	P3 (0.5")	Cylinder	Rolled Direction	1.00E+00	300	y	0.121	0.120		
117	M1-TMC-P3-SG1-O1-SR3-T3-N3	Compression	Instron	P3 (0.5")	Cylinder	Rolled Direction	1.00E+00	300	y	0.121	0.121		
118	M1-TMC-P3-SG1-O1-SR3-T4-N1	Compression	Instron	P3 (0.5")	Cylinder	Rolled Direction	1.00E+00	450	y	0.121	0.120		
119	M1-TMC-P3-SG1-O1-SR3-T4-N2	Compression	Instron	P3 (0.5")	Cylinder	Rolled Direction	1.00E+00	450	y	0.121	0.119		
120	M1-TMC-P3-SG1-O1-SR3-T4-N3	Compression	Instron	P3 (0.5")	Cylinder	Rolled Direction	1.00E+00	450	y	0.123	0.120		
121	M1-TMC-P3-SG1-O1-SR3-T5-N1	Compression	Instron	P3 (0.5")	Cylinder	Rolled Direction	1.00E+00	-50	y	0.120	0.120		Testing Complete
122	M1-TMC-P3-SG1-O1-SR3-T5-N2	Compression	Instron	P3 (0.5")	Cylinder	Rolled Direction	1.00E+00	-50	y	0.120	0.120		
123	M1-TMC-P3-SG1-O1-SR3-T5-N3	Compression	Instron	P3 (0.5")	Cylinder	Rolled Direction	1.00E+00	-50	y	0.120	0.120		
124	M1-TMC-P3-SG1-O1-SR4-T1-N1	Compression	SHB	P3 (0.5")	Cylinder	Rolled Direction	5.00E+02	RT	y	0.122	0.122		Testing Complete
125	M1-TMC-P3-SG1-O1-SR4-T1-N2	Compression	SHB	P3 (0.5")	Cylinder	Rolled Direction	5.00E+02	RT	y	0.121	0.121		
126	M1-TMC-P3-SG1-O1-SR4-T1-N3	Compression	SHB	P3 (0.5")	Cylinder	Rolled Direction	5.00E+02	RT	y	0.121	0.121		
127	M1-TMC-P3-SG1-O1-SR5-T1-N1	Compression	SHB	P3 (0.5")	Cylinder	Rolled Direction	5.00E+03	RT	y	0.121	0.121		
128	M1-TMC-P3-SG1-O1-SR5-T1-N2	Compression	SHB	P3 (0.5")	Cylinder	Rolled Direction	5.00E+03	RT	y	0.121	0.120		
129	M1-TMC-P3-SG1-O1-SR5-T1-N3	Compression	SHB	P3 (0.5")	Cylinder	Rolled Direction	5.00E+03	RT	y	0.120	0.120		
130	M1-TMC-P3-SG1-O2-SR3-T1-N1	Compression	Instron	P3 (0.5")	Cylinder	45˚	1.00E+00	RT	y	0.121	0.120		Testing Complete
131	M1-TMC-P3-SG1-O2-SR3-T1-N2	Compression	Instron	P3 (0.5")	Cylinder	45˚	1.00E+00	RT	y	0.120	0.120		
132	M1-TMC-P3-SG1-O3-SR3-T1-N1	Compression	Instron	P3 (0.5")	Cylinder	Transverse	1.00E+00	RT	y	0.121	0.120		
133	M1-TMC-P3-SG1-O3-SR3-T1-N2	Compression	Instron	P3 (0.5")	Cylinder	Transverse	1.00E+00	RT	y	0.120	0.120		
134	M1-TMC-P3-SG1-O4-SR3-T1-N1	Compression	Instron	P3 (0.5")	Cylinder	135˚	1.00E+00	RT	y	0.119	0.120		

135	M1-TMC-P3-SG1-O4-SR3-T1-N2	Compression	Instron	P3 (0.5")	Cylinder	135°	1.00E+00	RT	y	0.121	0.120		
136	M1-TMC-P3-SG1-O5-SR3-T1-N1	Compression	Instron	P3 (0.5")	Cylinder	Through Thickness	1.00E+00	RT	y	0.121	0.121		
137	M1-TMC-P3-SG1-O5-SR3-T1-N2	Compression	Instron	P3 (0.5")	Cylinder	Through Thickness	1.00E+00	RT	y	0.121	0.120		
138	M1-TMC-P2-SG1-O1-SR3-T1-N1	Compression	Instron	P2 (0.25")	Cylinder	Rolled Direction	1.00E+00	RT	y	0.121	0.121		Testing Complete
139	M1-TMC-P2-SG1-O1-SR3-T1-N2	Compression	Instron	P2 (0.25")	Cylinder	Rolled Direction	1.00E+00	RT	y	0.120	0.121		
140	M1-TMC-P2-SG1-O1-SR4-T1-N1	Compression	SHB	P2 (0.25")	Cylinder	Rolled Direction	5.00E+02	RT	y	0.121	0.121		
141	M1-TMC-P2-SG1-O1-SR4-T1-N2	Compression	SHB	P2 (0.25")	Cylinder	Rolled Direction	5.00E+02	RT	y	0.121	0.120		
142	M1-TMC-P1-SG1-O1-SR3-T1-N1	Compression	Instron	P1 (0.125")	Cylinder	Rolled Direction	1.00E+00	RT	y	0.121	0.121		
143	M1-TMC-P1-SG1-O1-SR3-T1-N2	Compression	Instron	P1 (0.125")	Cylinder	Rolled Direction	1.00E+00	RT	y	0.121	0.121		
144	M1-TMC-P1-SG1-O1-SR4-T1-N1	Compression	SHB	P1 (0.125")	Cylinder	Rolled Direction	5.00E+02	RT	y	0.121	0.121		
145	M1-TMC-P1-SG1-O1-SR4-T1-N2	Compression	SHB	P1 (0.125")	Cylinder	Rolled Direction	5.00E+02	RT	y	0.121	0.121		
146	M1-TMC-P3-SG2-O1-SR4-T1-N1	Compression	SHB	P3 (0.5")	Cylinder (G2)	Rolled Direction	5.00E+02	RT	y	0.200	0.200		Testing Complete
147	M1-TMC-P3-SG2-O1-SR4-T1-N2	Compression	SHB	P3 (0.5")	Cylinder (G2)	Rolled Direction	5.00E+02	RT	y	0.200	0.200		
148	M1-TMC-P3-SG2-O1-SR4-T1-N3	Compression	SHB	P3 (0.5")	Cylinder (G2)	Rolled Direction	5.00E+02	RT	y	0.200	0.200		
149	M1-TMC-P3-SG3-O1-SR4-T1-N1	Compression	SHB	P3 (0.5")	Cylinder (G3)	Rolled Direction	5.00E+02	RT	y	0.152	0.200		
150	M1-TMC-P3-SG3-O1-SR4-T1-N2	Compression	SHB	P3 (0.5")	Cylinder (G3)	Rolled Direction	5.00E+02	RT	y	0.150	0.200		
151	M1-TMC-P3-SG3-O1-SR4-T1-N3	Compression	SHB	P3 (0.5")	Cylinder (G3)	Rolled Direction	5.00E+02	RT	y	0.150	0.199		
152	M1-TMC-P3-SG4-O1-SR4-T1-N1	Compression	SHB	P3 (0.5")	Cylinder (G4)	Rolled Direction	5.00E+02	RT	y	0.250	0.200		
153	M1-TMC-P3-SG4-O1-SR4-T1-N2	Compression	SHB	P3 (0.5")	Cylinder (G4)	Rolled Direction	5.00E+02	RT	y	0.250	0.200		
154	M1-TMC-P3-SG4-O1-SR4-T1-N3	Compression	SHB	P3 (0.5")	Cylinder (G4)	Rolled Direction	5.00E+02	RT	y	0.250	0.200		
Shear (Torsion)													
	Test #	Test Mode (Tension, Torsion, Compression, etc.)	Apparatus	Material Stock Identifier	Specimen Geometry	Specimen Gage Fabrication Orientation	Strain Rate (1/s)	Temperature (˚C)	Test Complete? (y/n)	Gauge Length (in)	Inside Diameter (in)	Gauge Thickness (in)	
155	M1-TMS-P3-SR1-T1-N1	Shear (Torsion)	Instron	P3 (0.5")	Spool	Through Thickness	1.00E-04	RT	y	0.101	0.510	0.020	Testing Complete
156	M1-TMS-P3-SR1-T1-N2	Shear (Torsion)	Instron	P3 (0.5")	Spool	Through Thickness	1.00E-04	RT	y	0.100	0.510	0.020	
157	M1-TMS-P3-SR1-T1-N3	Shear (Torsion)	Instron	P3 (0.5")	Spool	Through Thickness	1.00E-04	RT	y	0.100	0.510	0.021	

158	M1-TMS-P3-SR2-T1-N1	Shear (Torsion)	Instron	P3 (0.5")	Spool	Through Thickness	1.00E-02	RT	y	0.100	0.510	0.021	
159	M1-TMS-P3-SR2-T1-N2	Shear (Torsion)	Instron	P3 (0.5")	Spool	Through Thickness	1.00E-02	RT	y	0.100	0.510	0.021	
160	M1-TMS-P3-SR2-T1-N3	Shear (Torsion)	Instron	P3 (0.5")	Spool	Through Thickness	1.00E-02	RT	y	0.100	0.510	0.020	
161	M1-TMS-P3-SR3-T1-N1	Shear (Torsion)	Instron	P3 (0.5")	Spool	Through Thickness	1.00E+00	RT	y	0.101	0.511	0.020	
162	M1-TMS-P3-SR3-T1-N2	Shear (Torsion)	Instron	P3 (0.5")	Spool	Through Thickness	1.00E+00	RT	y	0.101	0.511	0.014	
163	M1-TMS-P3-SR3-T1-N3	Shear (Torsion)	Instron	P3 (0.5")	Spool	Through Thickness	1.00E+00	RT	y	0.100	0.511	0.020	
164	M1-TMS-P3-SR3-T2-N1	Shear (Torsion)	Instron	P3 (0.5")	Spool	Through Thickness	1.00E+00	150	y	0.100	0.511	0.020	Testing Complete
165	M1-TMS-P3-SR3-T2-N2	Shear (Torsion)	Instron	P3 (0.5")	Spool	Through Thickness	1.00E+00	150	y	0.100	0.511	0.020	
166	M1-TMS-P3-SR3-T2-N3	Shear (Torsion)	Instron	P3 (0.5")	Spool	Through Thickness	1.00E+00	150	y	0.100	0.511	0.021	
167	M1-TMS-P3-SR3-T3-N1	Shear (Torsion)	Instron	P3 (0.5")	Spool	Through Thickness	1.00E+00	300	y	0.100	0.511	0.021	
168	M1-TMS-P3-SR3-T3-N2	Shear (Torsion)	Instron	P3 (0.5")	Spool	Through Thickness	1.00E+00	300	y	0.100	0.511	0.020	
169	M1-TMS-P3-SR3-T3-N3	Shear (Torsion)	Instron	P3 (0.5")	Spool	Through Thickness	1.00E+00	300	y	0.100	0.511	0.020	
170	M1-TMS-P3-SR3-T4-N1	Shear (Torsion)	Instron	P3 (0.5")	Spool	Through Thickness	1.00E+00	450	y	0.100	0.511	0.020	
171	M1-TMS-P3-SR3-T4-N2	Shear (Torsion)	Instron	P3 (0.5")	Spool	Through Thickness	1.00E+00	450	y	0.101	0.511	0.021	
172	M1-TMS-P3-SR3-T4-N3	Shear (Torsion)	Instron	P3 (0.5")	Spool	Through Thickness	1.00E+00	450	y	0.100	0.511	0.020	
173	M1-TMS-P3-SR3-T5-N1	Shear (Torsion)	Instron	P3 (0.5")	Spool	Through Thickness	1.00E+00	-50	y	0.100	0.511	0.020	Testing Complete
174	M1-TMS-P3-SR3-T5-N2	Shear (Torsion)	Instron	P3 (0.5")	Spool	Through Thickness	1.00E+00	-50	y	0.100	0.511	0.020	
175	M1-TMS-P3-SR3-T5-N3	Shear (Torsion)	Instron	P3 (0.5")	Spool	Through Thickness	1.00E+00	-50	y	0.100	0.511	0.020	
176	M1-TMS-P3-SR4-T1-N1	Shear (Torsion)	SHB	P3 (0.5")	Spool	Through Thickness	5.00E+02	RT	y	0.105	0.511	0.015	Testing Complete
177	M1-TMS-P3-SR4-T1-N2	Shear (Torsion)	SHB	P3 (0.5")	Spool	Through Thickness	5.00E+02	RT	y	0.105	0.511	0.015	
178	M1-TMS-P3-SR4-T1-N3	Shear (Torsion)	SHB	P3 (0.5")	Spool	Through Thickness	5.00E+02	RT	y	0.053	0.511	0.015	
179	M1-TMS-P3-SR5-T1-N1	Shear (Torsion)	SHB	P3 (0.5")	Spool	Through Thickness	3.00E+03	RT	y	0.054	0.511	0.016	
180	M1-TMS-P3-SR5-T1-N2	Shear (Torsion)	SHB	P3 (0.5")	Spool	Through Thickness	3.00E+03	RT	y	0.053	0.511	0.016	
181	M1-TMS-P3-SR5-T1-N3	Shear (Torsion)	SHB	P3 (0.5")	Spool	Through Thickness	3.00E+03	RT	y	0.053	0.511	0.016	

Punch Tests

	Test #	Test Mode (Tension, Torsion, Compression, etc.)	Apparatus	Material Stock Identifier	Specimen Geometry	Specimen Gage Fabrication Orientation	Strain Rate (1/s)	Temperature (˚C)	Test Complete? (y/n)	Specimen Thickness (in)			
182	M1-TMP1-P3-SR1-T1-N1	Punch #1	SHB	P3 (0.5")	Circular Plate	N/A	High Rate	RT	y	0.058			Static punch tests were completed. Dynamic punch experiments with three punch geometries into 0.058" thick specimens were completed. Testing Complete
183	M1-TMP1-P3-SR1-T1-N2	Punch #1	SHB	P3 (0.5")	Circular Plate	N/A	High Rate	RT	y	0.058			
184	M1-TMP1-P3-SR1-T1-N3	Punch #1	SHB	P3 (0.5")	Circular Plate	N/A	High Rate	RT	y	0.058			
185	M1-TMP2-P3-SR1-T1-N1	Punch #4	SHB	P3 (0.5")	Circular Plate	N/A	High Rate	RT	y	0.058			
186	M1-TMP2-P3-SR1-T1-N2	Punch #4	SHB	P3 (0.5")	Circular Plate	N/A	High Rate	RT	y	0.058			
187	M1-TMP2-P3-SR1-T1-N3	Punch #4	SHB	P3 (0.5")	Circular Plate	N/A	High Rate	RT	y	0.058			
188	M1-TMP3-P3-SR1-T1-N1	Punch #6	SHB	P3 (0.5")	Circular Plate	N/A	High Rate	RT	y	0.058			
189	M1-TMP3-P3-SR1-T1-N2	Punch #6	SHB	P3 (0.5")	Circular Plate	N/A	High Rate	RT	y	0.058			
190	M1-TMP3-P3-SR1-T1-N3	Punch #6	SHB	P3 (0.5")	Circular Plate	N/A	High Rate	RT	y	0.058			
191	M1-TMP1-P3-SR2-T1-N1	Punch #1	Instron	P3 (0.5")	Circular Plate	N/A	Low Rate	RT	y	0.059			
192	M1-TMP2-P3-SR2-T1-N1	Punch #4	Instron	P3 (0.5")	Circular Plate	N/A	Low Rate	RT	y	0.059			
193	M1-TMP3-P3-SR2-T1-N1	Punch #6	Instron	P3 (0.5")	Circular Plate	N/A	Low Rate	RT	y	0.059			

Combined Loading Tests

	Test #	Test Mode (Tension, Torsion, Compression, etc.)	Apparatus	Material Stock Identifier	Specimen Geometry	Specimen Gage Fabrication Orientation	Strain Rate (1/s)	Temperature (˚C)	Test Complete? (y/n)	Inner Diameter (in)	Outer Diameter (in)	Gauge Length (in)	
194	M1-TMCL-LR1-P3-SR3-T1-N1	Combined Loading	Instron	P3 (0.5")	Spool	Rolled Direction	1.00E+00	RT	y	0.313	0.361	0.250	Combined loading tests load a spool specimen in a state of tension/compression and torsion (shear). Four loading cases are used (LR1 and LR2 - Tension/Torsion, LR3 - Torsion, LR4 - Compression/Torsion). LR (Load Ratio) represents the ratio of axial stress to shear stress in the specimen. Testing Complete
195	M1-TMCL-LR1-P3-SR3-T1-N2	Combined Loading	Instron	P3 (0.5")	Spool	Rolled Direction	1.00E+00	RT	y	0.312	0.361	0.250	
196	M1-TMCL-LR1-P3-SR3-T1-N3	Combined Loading	Instron	P3 (0.5")	Spool	Rolled Direction	1.00E+00	RT	y	0.312	0.361	0.250	
197	M1-TMCL-LR2-P3-SR3-T1-N1	Combined Loading	Instron	P3 (0.5")	Spool	Rolled Direction	1.00E+00	RT	y	0.313	0.361	0.250	
198	M1-TMCL-LR2-P3-SR3-T1-N2	Combined Loading	Instron	P3 (0.5")	Spool	Rolled Direction	1.00E+00	RT	y	0.312	0.361	0.250	
199	M1-TMCL-LR2-P3-SR3-T1-N3	Combined Loading	Instron	P3 (0.5")	Spool	Rolled Direction	1.00E+00	RT	y	0.312	0.361	0.250	
200	M1-TMCL-LR3-P3-SR3-T1-N1	Combined Loading	Instron	P3 (0.5")	Spool	Rolled Direction	1.00E+00	RT	y	0.314	0.361	0.250	
201	M1-TMCL-LR3-P3-SR3-T1-N2	Combined Loading	Instron	P3 (0.5")	Spool	Rolled Direction	1.00E+00	RT	y	0.314	0.361	0.250	

202	M1-TMCL-LR3-P3-SR3-T1-N3	Combined Loading	Instron	P3 (0.5")	Spool	Rolled Direction	1.00E+00	RT	y	0.313	0.361	0.250	
203	M1-TMCL-LR4-P3-SR3-T1-N4	Combined Loading	Instron	P3 (0.5")	Spool	Rolled Direction	1.00E+00	RT	y	0.250	0.361	0.125	
204	M1-TMCL-LR4-P3-SR3-T1-N5	Combined Loading	Instron	P3 (0.5")	Spool	Rolled Direction	1.00E+00	RT	y	0.250	0.361	0.125	
205	M1-TMCL-LR4-P3-SR3-T1-N6	Combined Loading	Instron	P3 (0.5")	Spool	Rolled Direction	1.00E+00	RT	y	0.250	0.361	0.125	

Yellow = Added to assess the anisotropy of the plate material

Teal = Added to assess the failure strain dependence on state of stress

Blue = Added cold temperature test at the request of team members

Green = Added to assess the effects of inertia and friction on compressive SHB tests

199 tests have been conducted as of 12/1/09

APPENDIX D—DRAWINGS OF TEST SPECIMENS AND FIXTURES USED IN THE DUCTILE FRACTURE TEST SERIES

Drawings of each specimen used in the ductile fracture test series are presented in this appendix. These include the following tables, which can be found in the main report: plane stress (table 4), axisymmetric (table 5), plane strain (table 6), tension, and the combined axial-torsional specimens (table 7). Drawings of the specimen and the fixtures used in the punch test series (table 8) are also presented. Drawing dimensions are in inches, as when presented to the machine shop for fabrication.

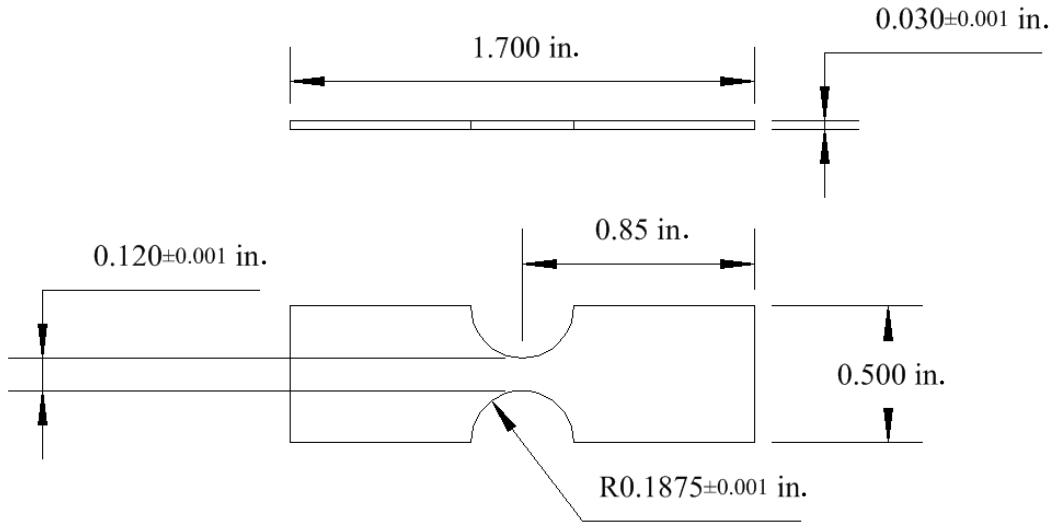

Figure D-1. Plane Stress Tension Specimen With a Large Notch (specimen #2)

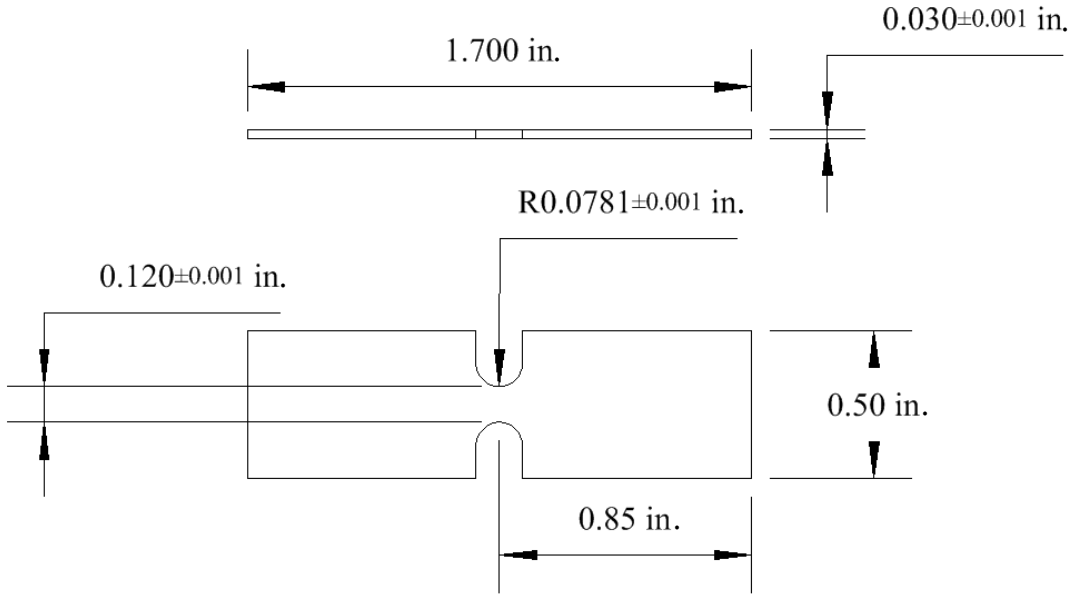

Figure D-2. Plane Stress Tension Specimen With an Intermediate Notch (specimen #3)

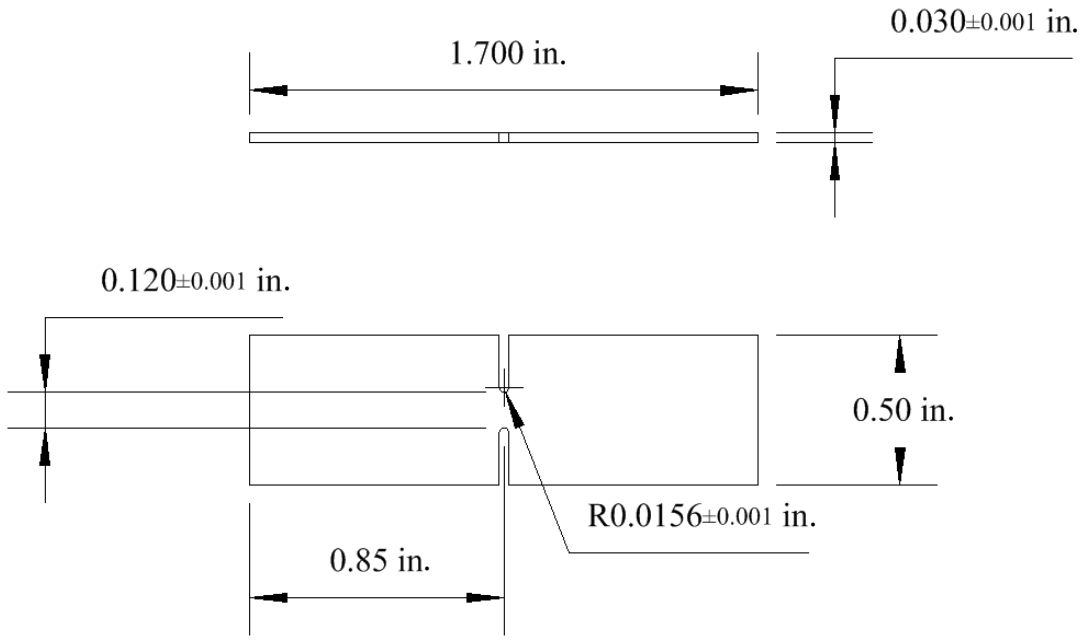

Figure D-3. Plane Stress Tension Specimen With a Small Notch (specimen #4)

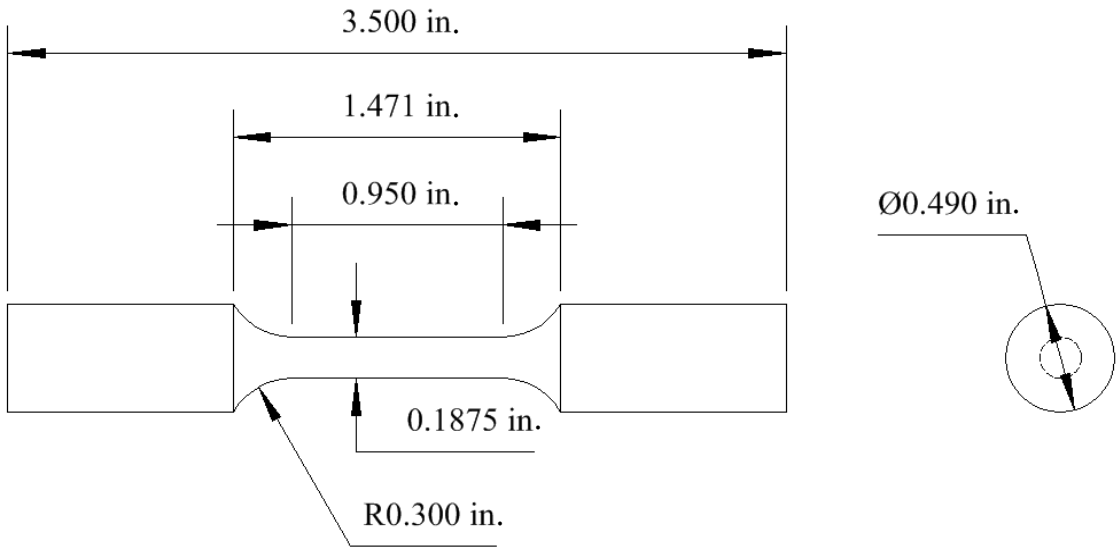

Figure D-4. Axisymmetric Tension Specimen With a Smooth Gage Section (specimen #5)

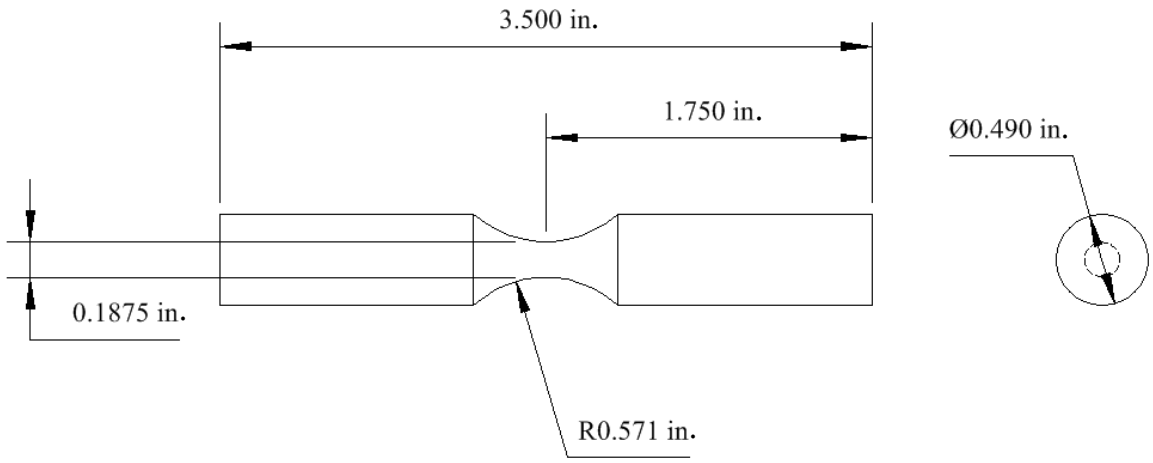

Figure D-5. Axisymmetric Tension Specimen With a Notch (specimen #6)

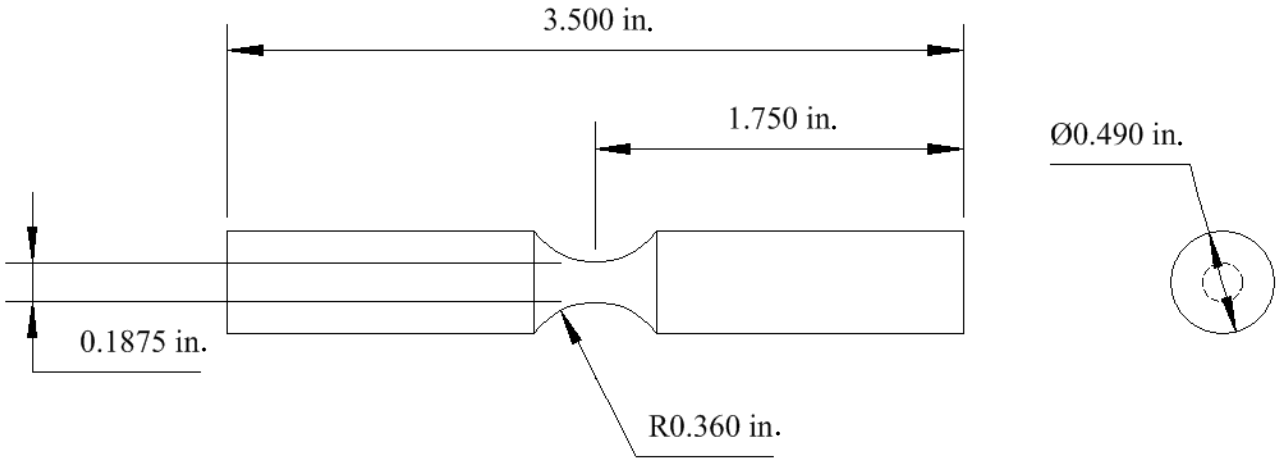

Figure D-6. Axisymmetric Tension Specimen With a Notch (specimen #7)

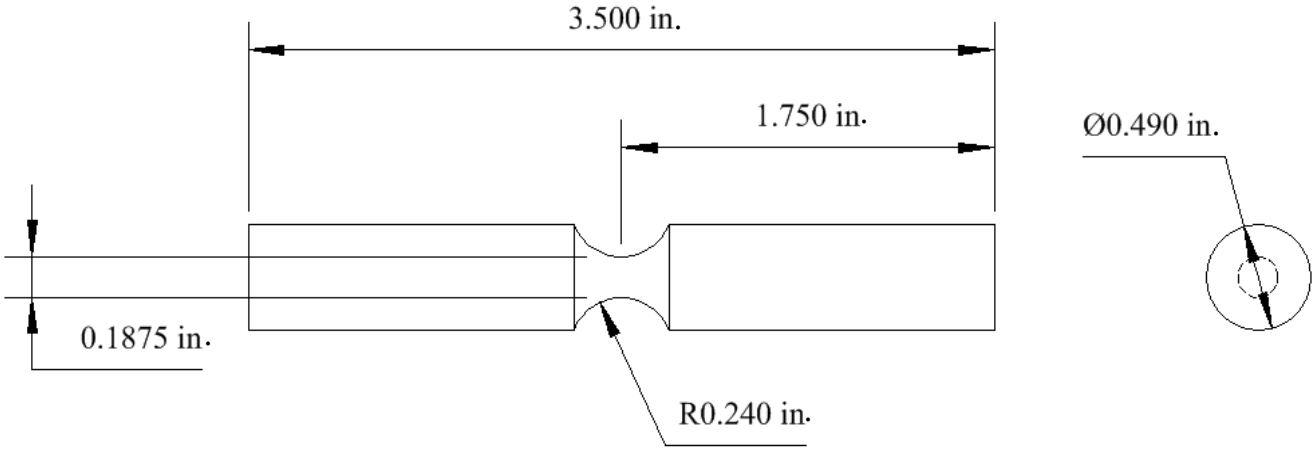

Figure D-7. Axisymmetric Tension Sample With a Notch (specimen #8)

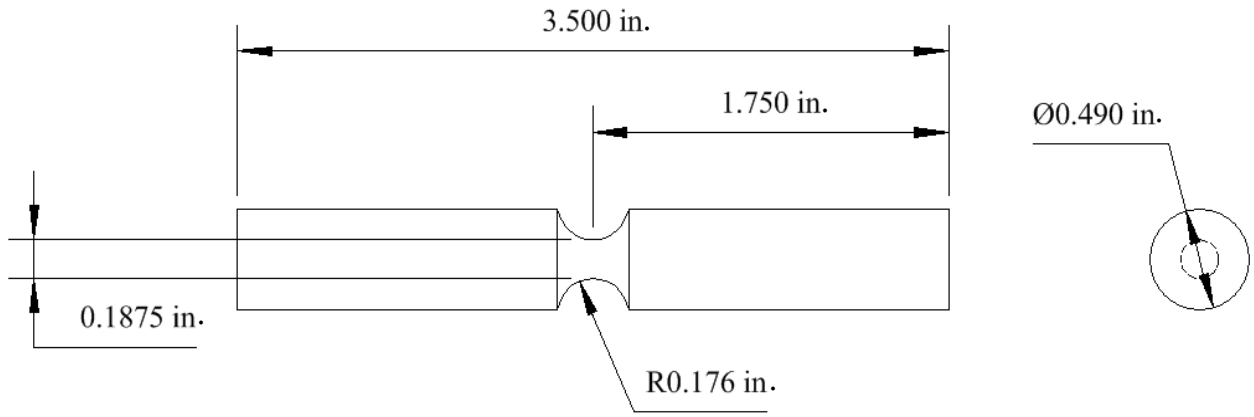

Figure D-8. Axisymmetric Tension Specimen With a Notch (specimen #9)

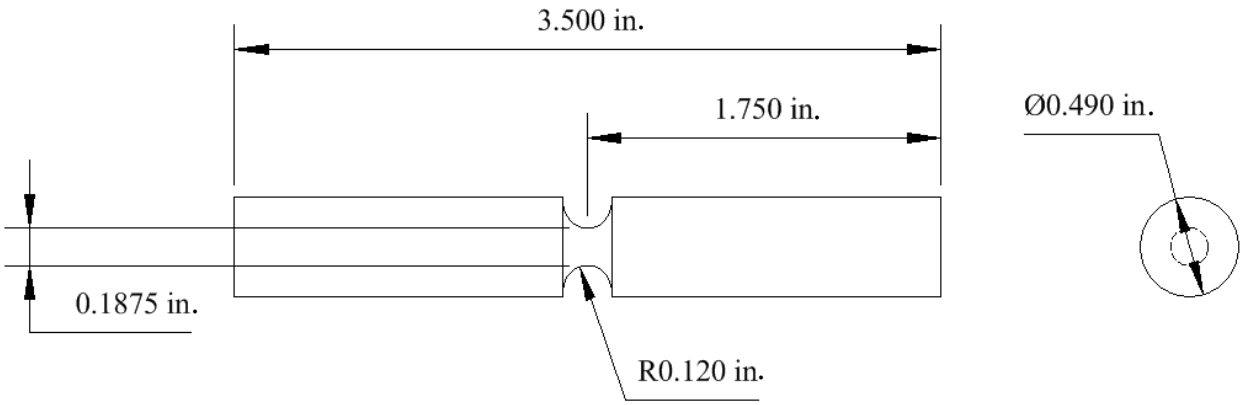

Figure D-9. Axisymmetric Tension Specimen With a Notch (specimen #10)

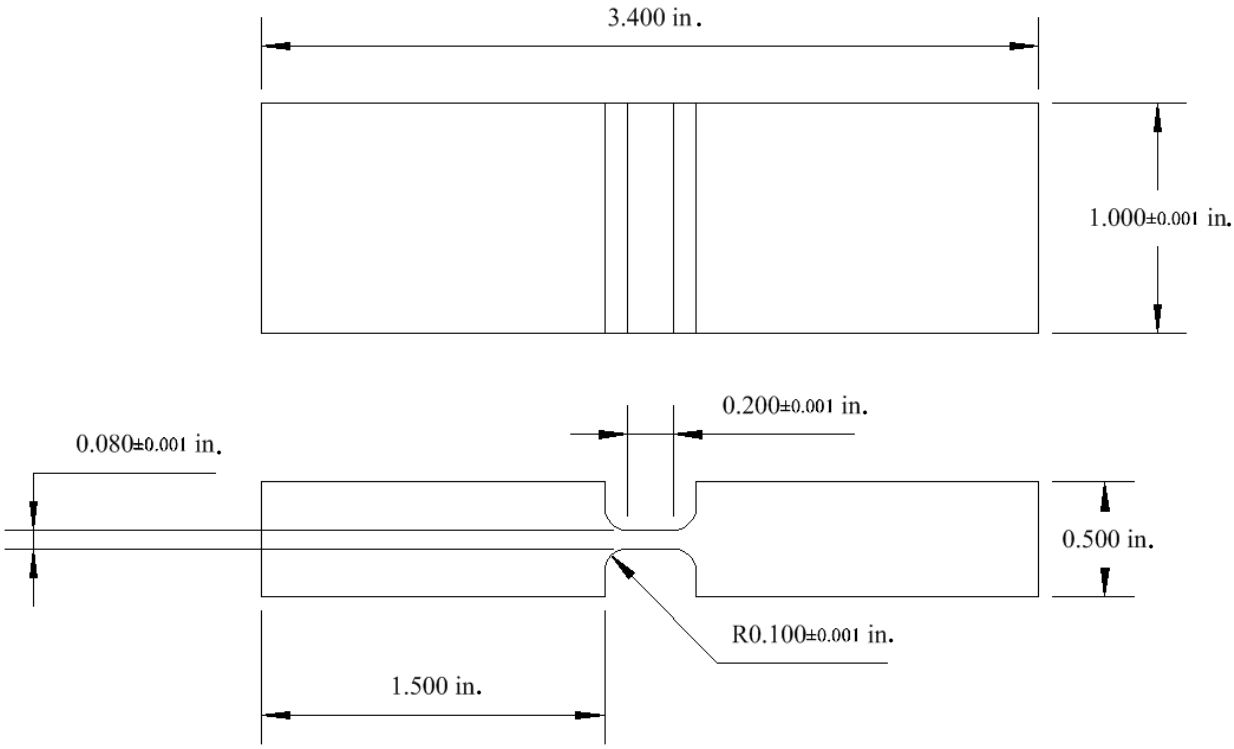

Figure D-10. Plane Strain Tension Specimen With a Smooth Gage Section (specimen #11)

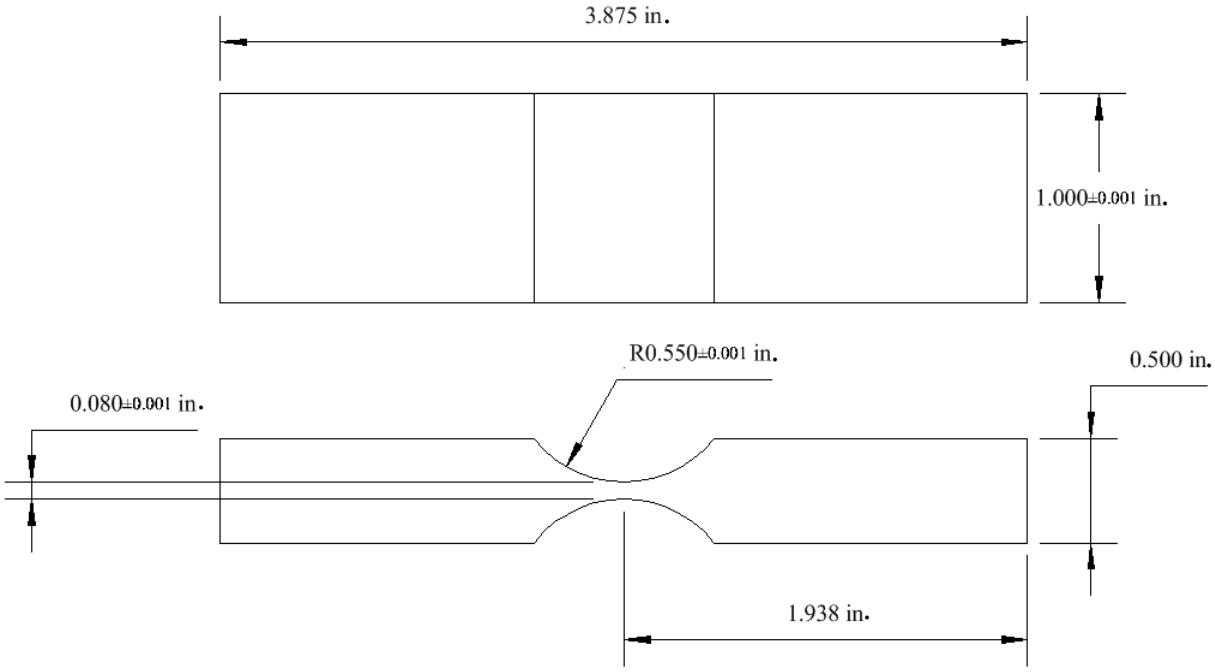

Figure D-11. Plane Strain Tension Specimen With a Large Notch (specimen #12)

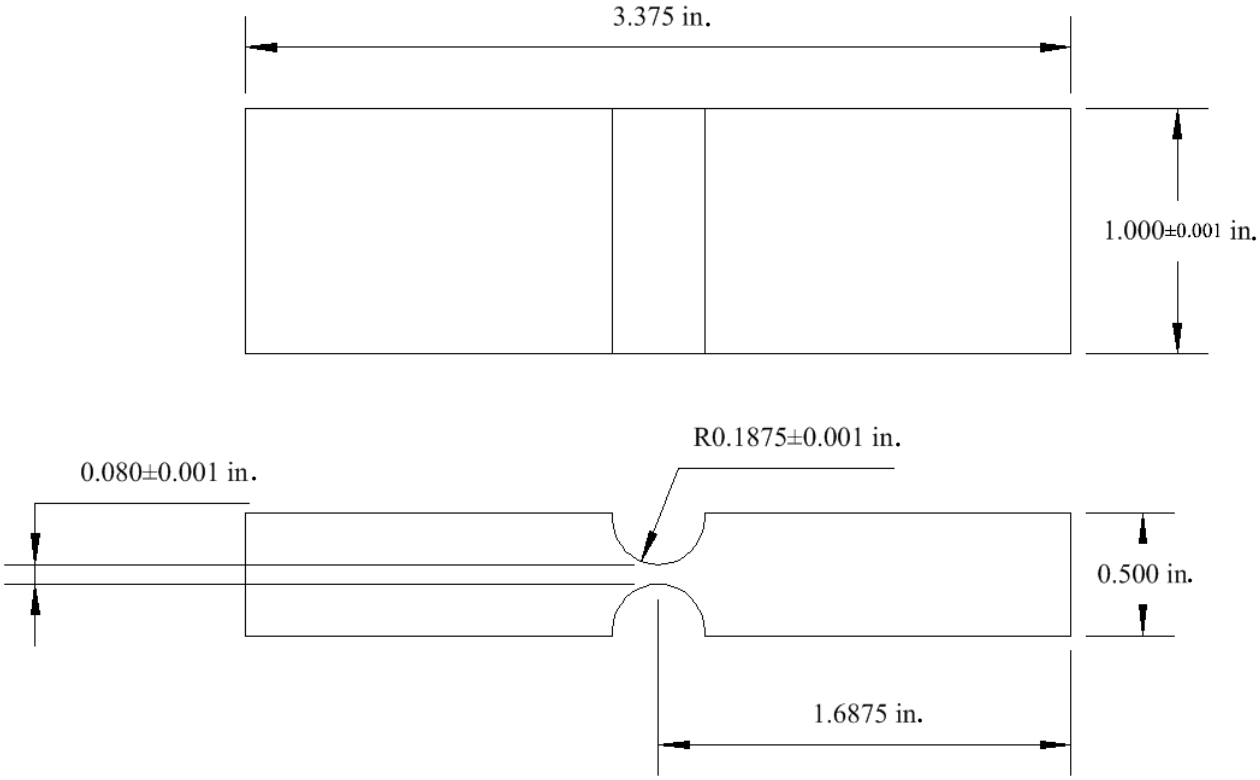

Figure D-12. Plane Strain Tension Specimen With a Small Notch (specimen #13)

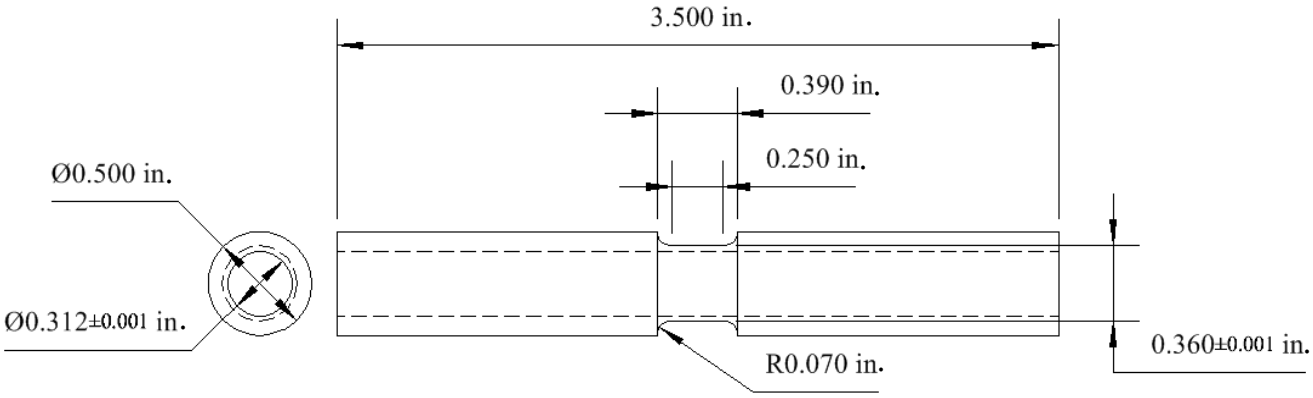

Figure D-13. Combined Tension-Torsion Specimens (specimens #14, 15, and 16)

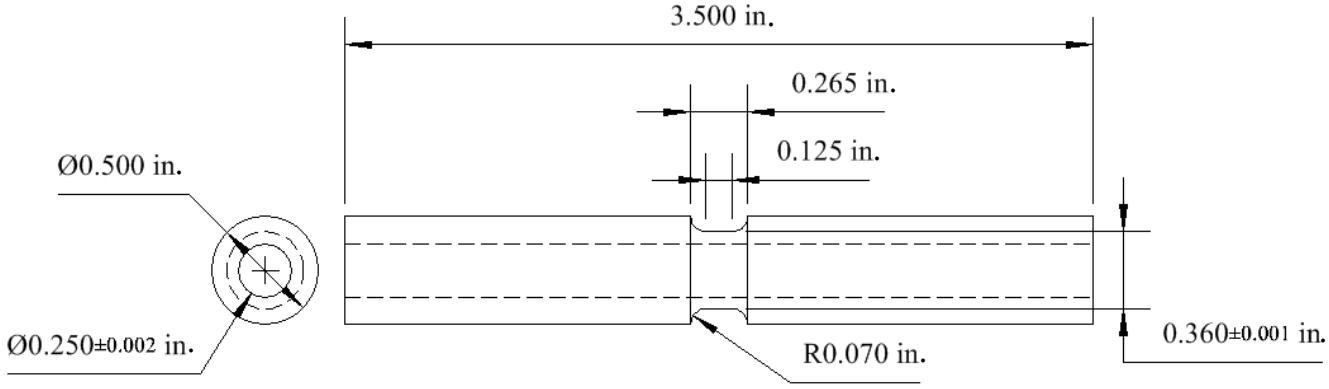

Figure D-14. Combined Compression-Torsion Specimens (specimens #14 through 16)

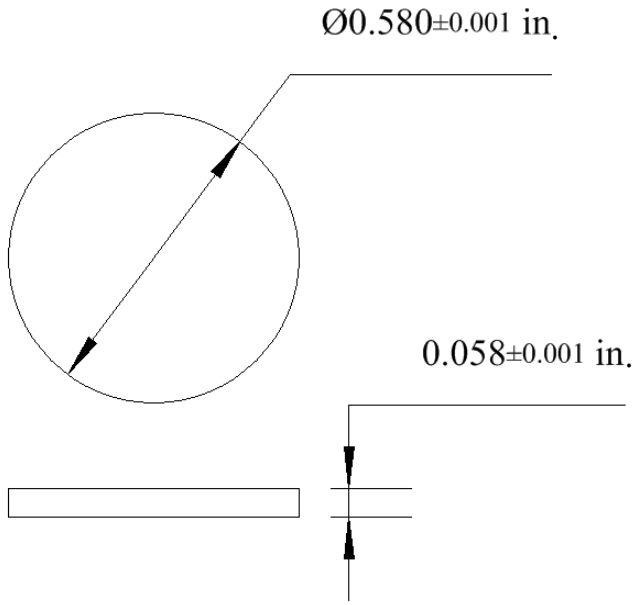

Figure D-15. Punch Test Specimen

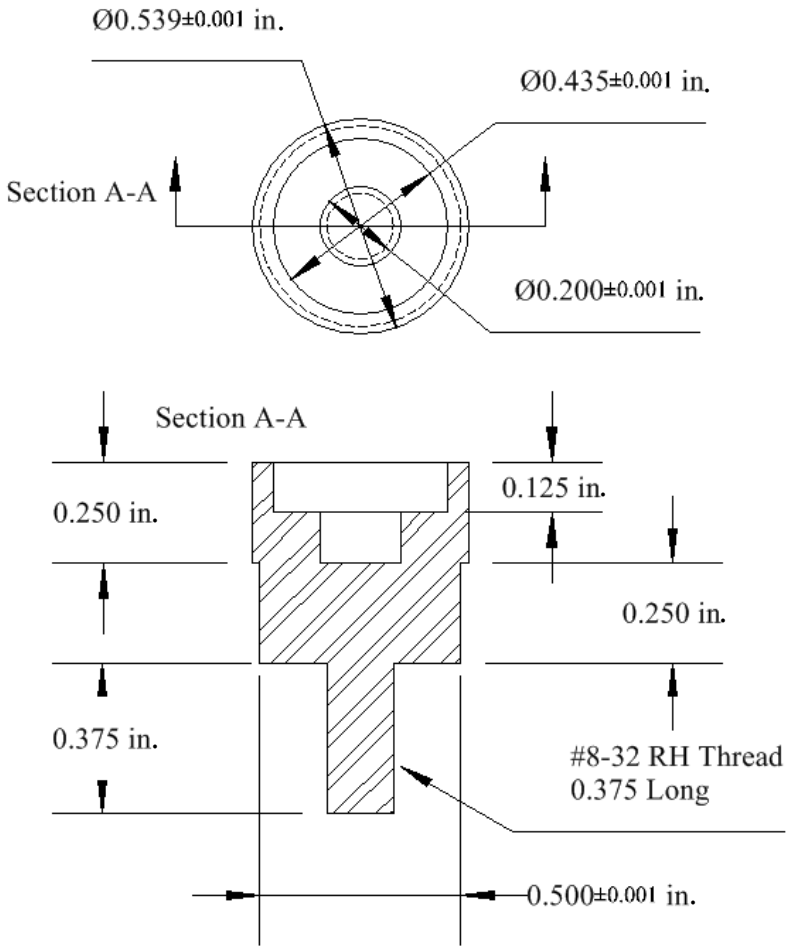

Figure D-16. Punch Test Fixture—Bar Adaptor

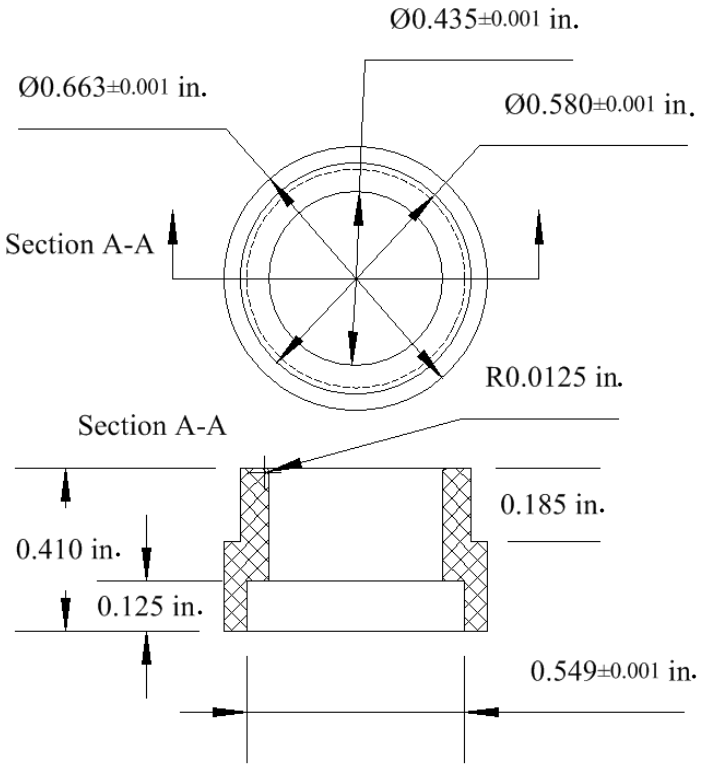

Figure D-17. Punch Test Fixture—Specimen Support Adaptor

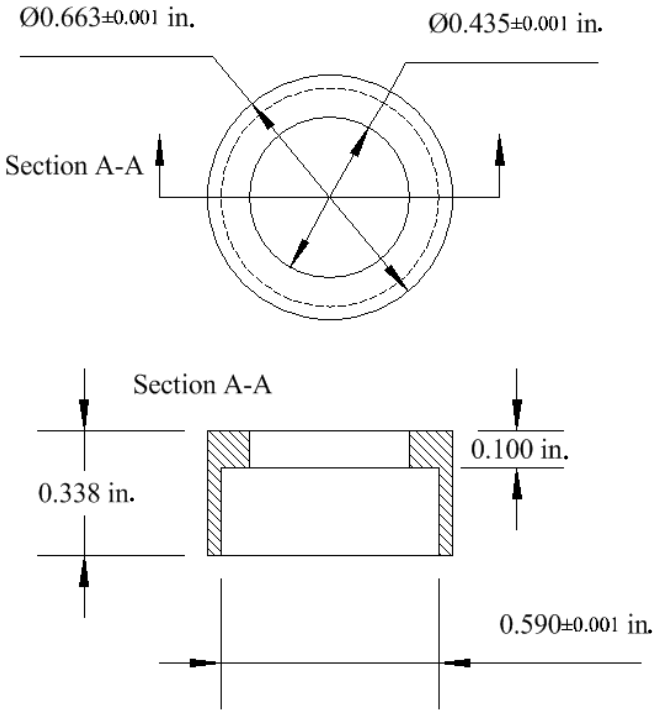

Figure D-18. Punch Test Fixture—Specimen Lock Adaptor

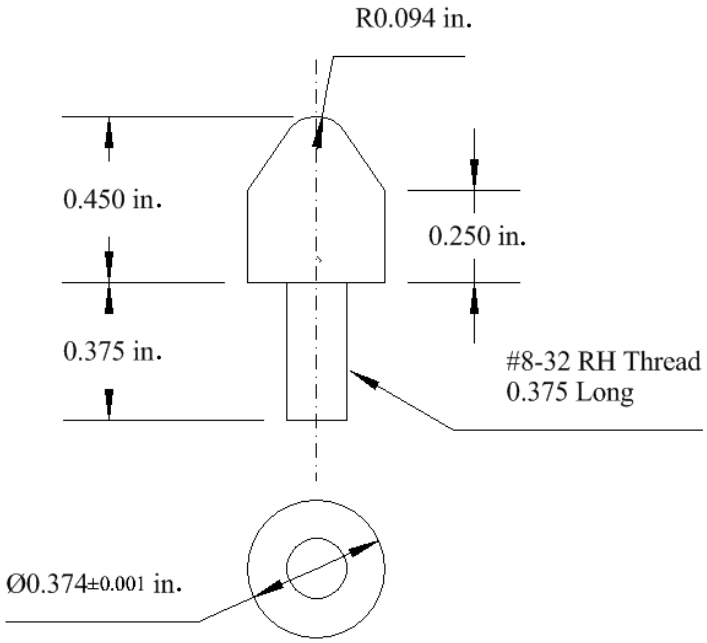

Figure D-19. Punch #1

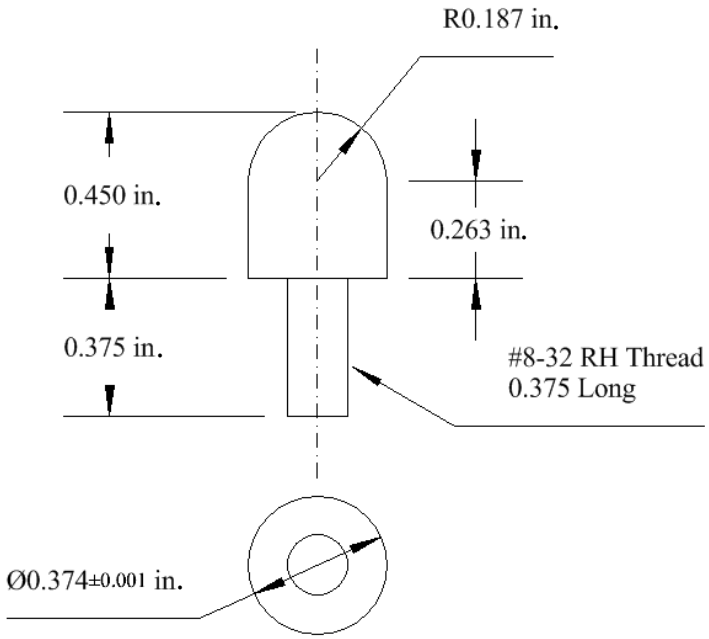

Figure D-20. Punch #2

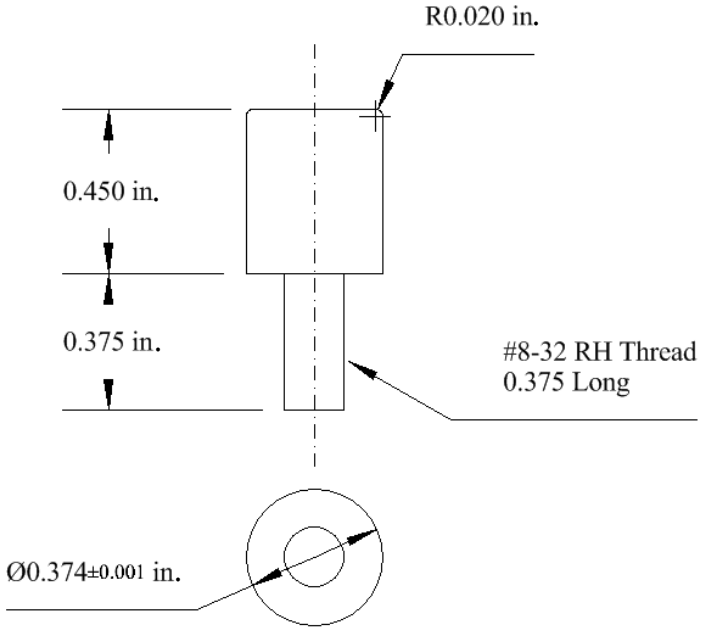

Figure D-21. Punch #3

APPENDIX E—FRACTURE TEST SERIES DIC EXTENSOMETER POSITIONS AND STRAIN CONTOURS PRIOR TO FRACTURE

Additional data from the tension ductile fracture test series are presented in this appendix. For each experiment outlined in 4 through 7 of the main document, the maximum and minimum principal surface strain contours just prior to specimen fracture are shown. In addition, the initial positions of the points used to extract extensometer data are also shown.

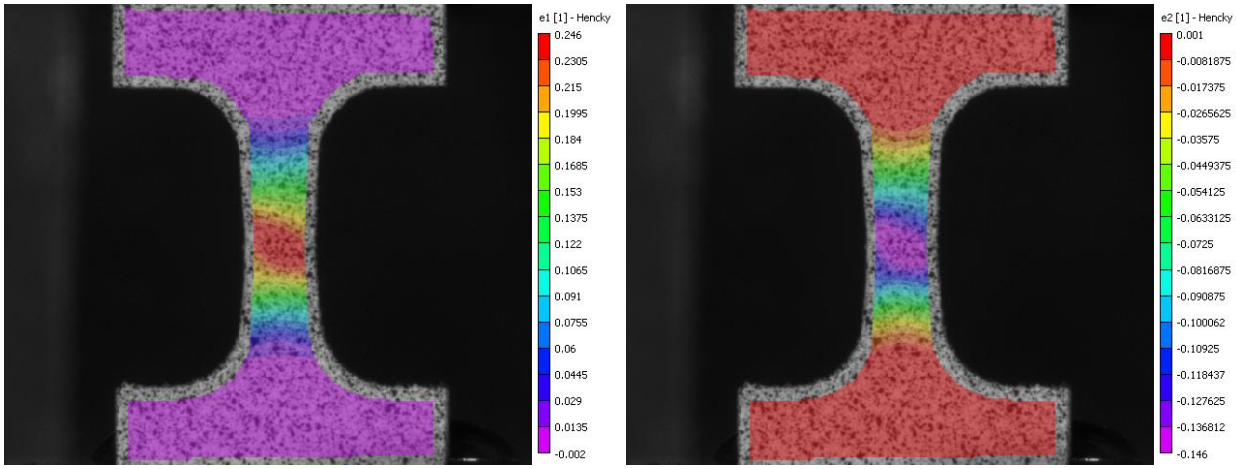

(a) (b)

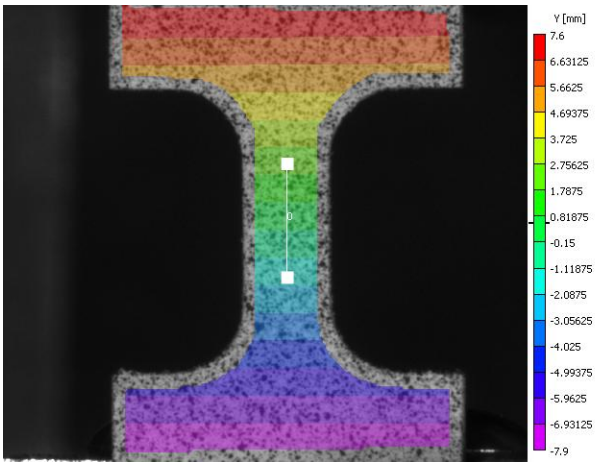

(c)

Figure E-1. Digital Image Correlation (DIC) Data From Test #M1-TMT-P3-SG1-O1-SR2-T1-N4: (a) Maximum Principal and (b) Minimum Principal Strain Contours Immediately Prior to Fracture, and (c) Initial Extensometer Position

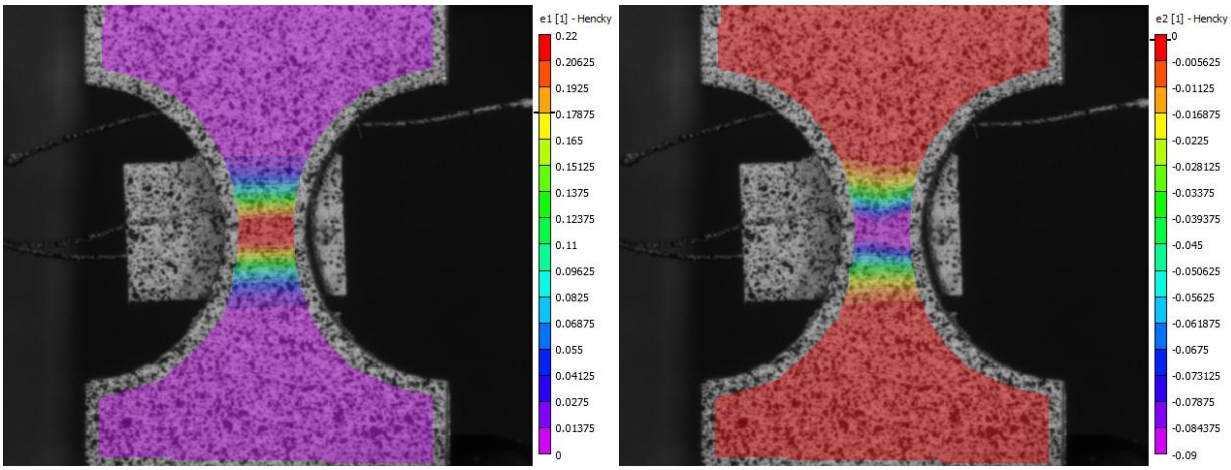

(a) (b)

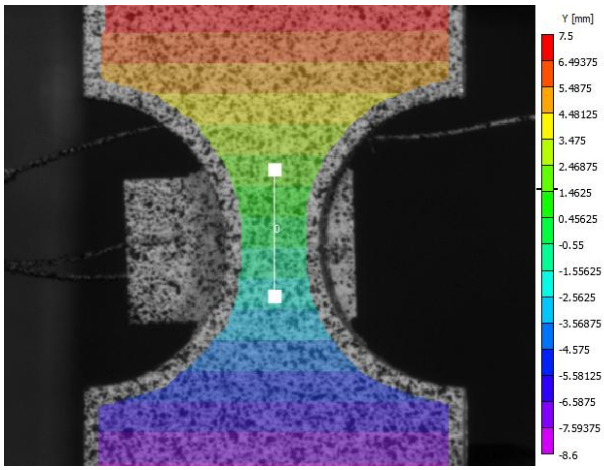

(c)

Figure E-2. The DIC Data From Test # M1-TMT-P3-SG2-O1-SR3-T1-N5: (a) Maximum Principal and (b) Minimum Principal Strain Contours Immediately Prior to Fracture, and (c) Initial Extensometer Position

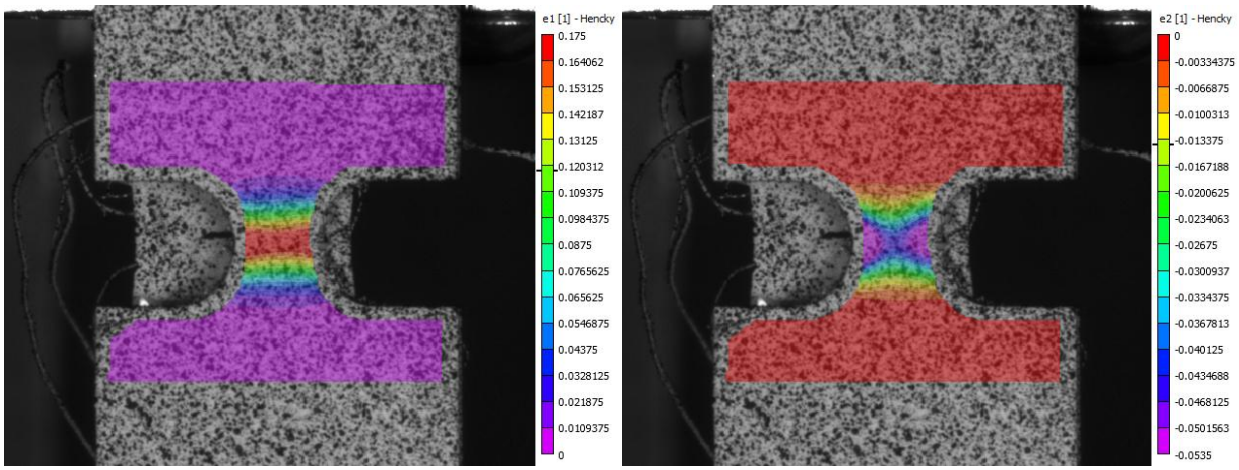

(a) (b)

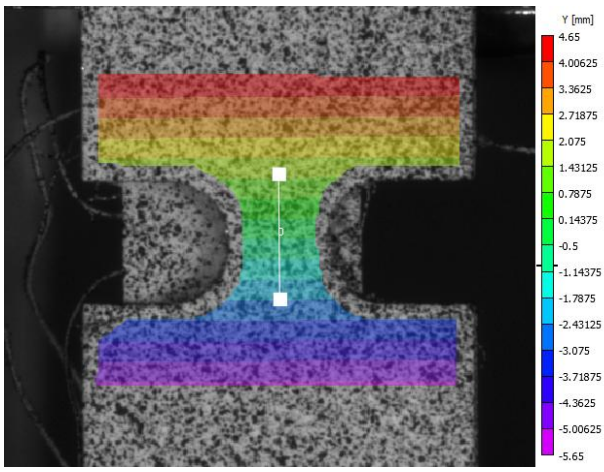

(c)

Figure E-3. The DIC Data From Test # M1-TMT-P3-SG3-O1-SR3-T1-N5: (a) Maximum Principal and (b) Minimum Principal Strain Contours Immediately Prior to Fracture, and (c) Initial Extensometer Position

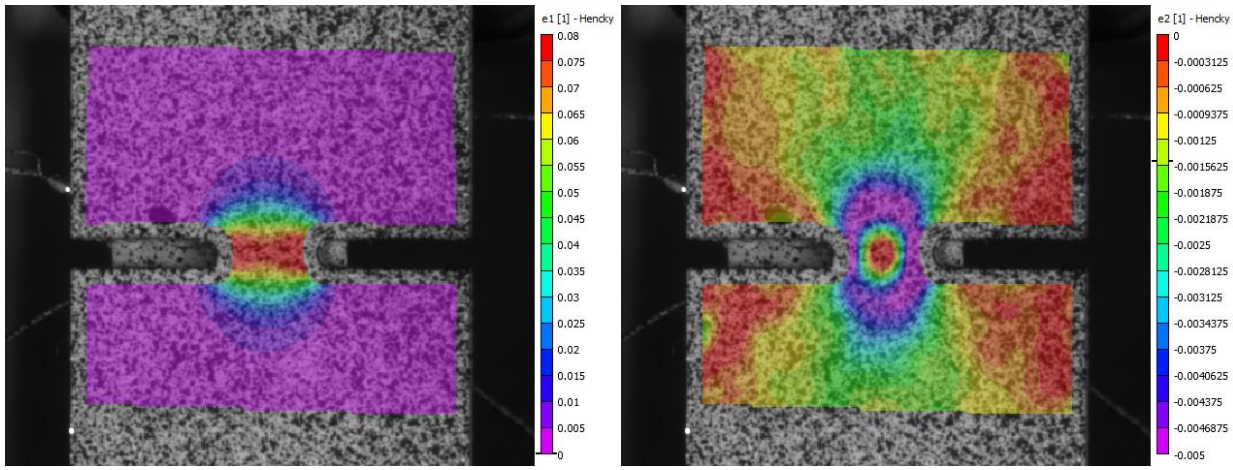

(a) (b)

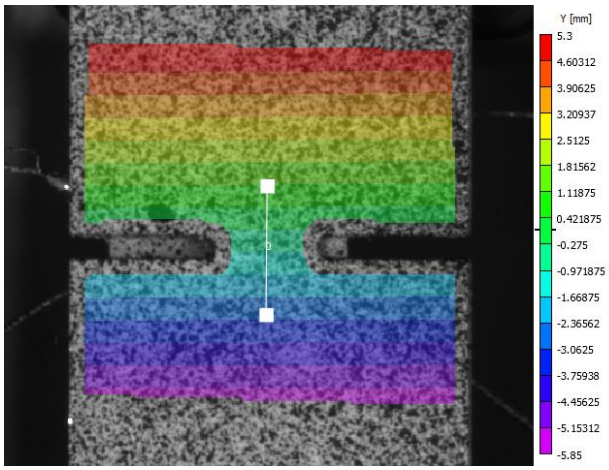

(c)

Figure E-4. The DIC Data From Test # M1-TMT-P3-SG4-O1-SR3-T1-N5: (a) Maximum Principal and (b) Minimum Principal Strain Contours Immediately Prior to Fracture, and (c) Initial Extensometer Position

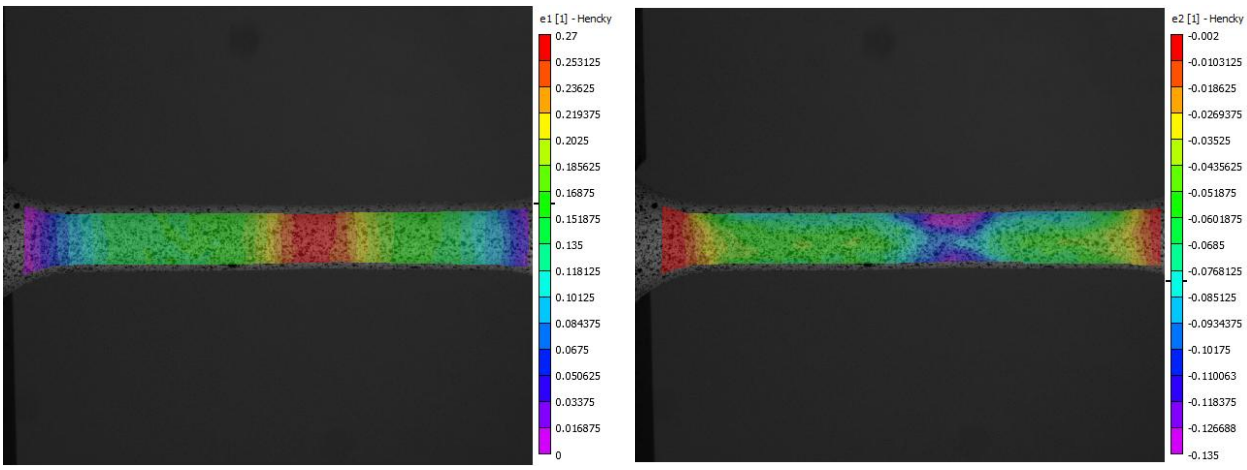

(a) (b)

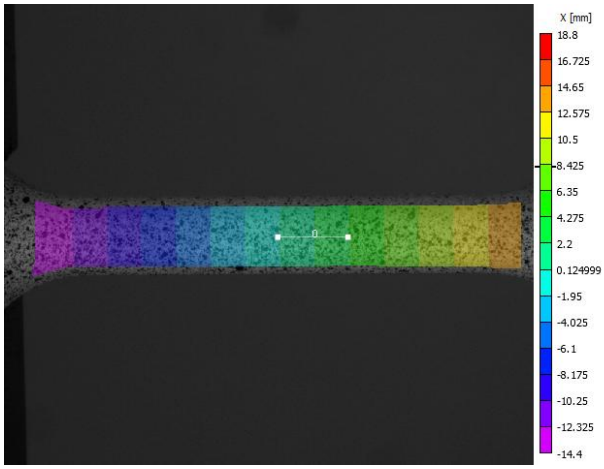

(c)

Figure E-5. The DIC Data From Test # M1-TMT-P3-SG5-O1-SR3-T1-N2: (a) Maximum Principal and (b) Minimum Principal Strain Contours Immediately Prior to Fracture, and (c) Initial Extensometer Position

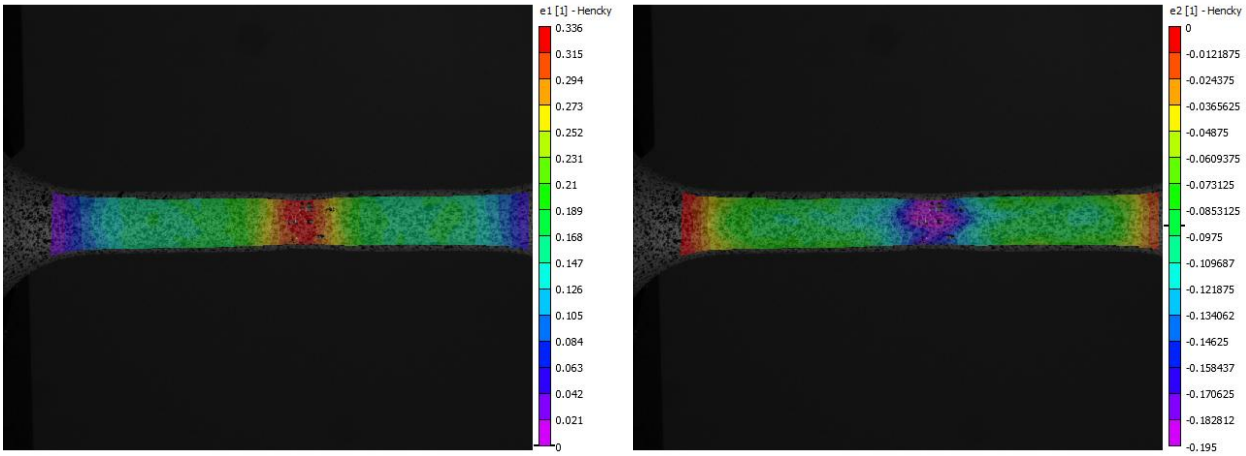

(a) (b)

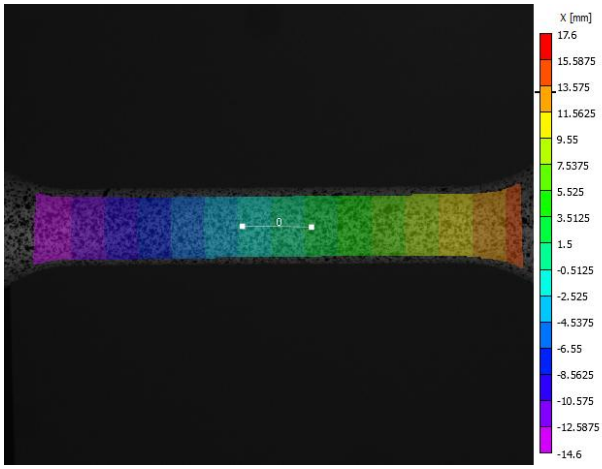

(c)

Figure E-6. The DIC Data From Test # TMT-P3-SG5-O1-SR3-T1-N3: (a) Maximum Principal and (b) Minimum Principal Strain Contours Immediately Prior to Fracture, and (c) Initial Extensometer Position

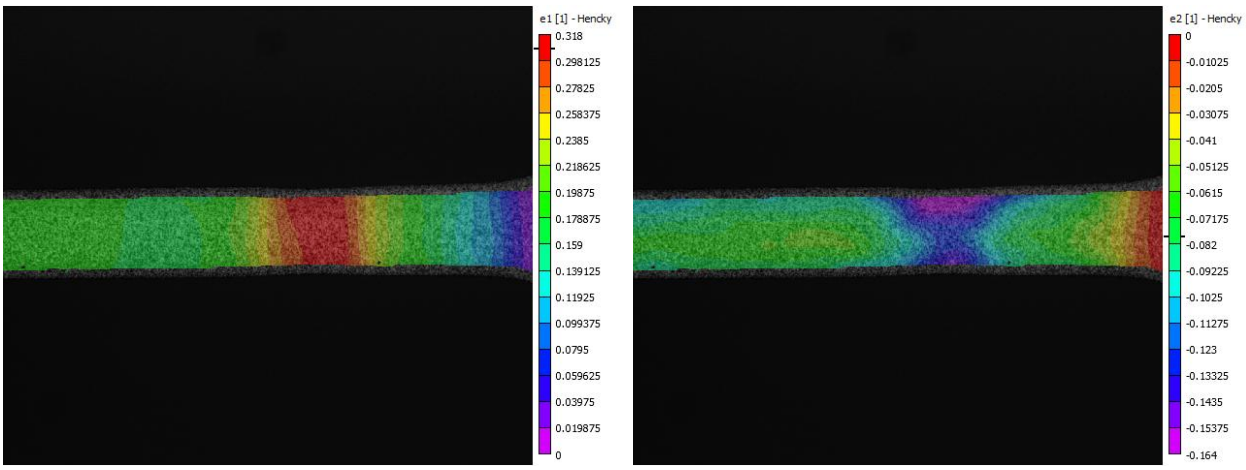

(a) (b)

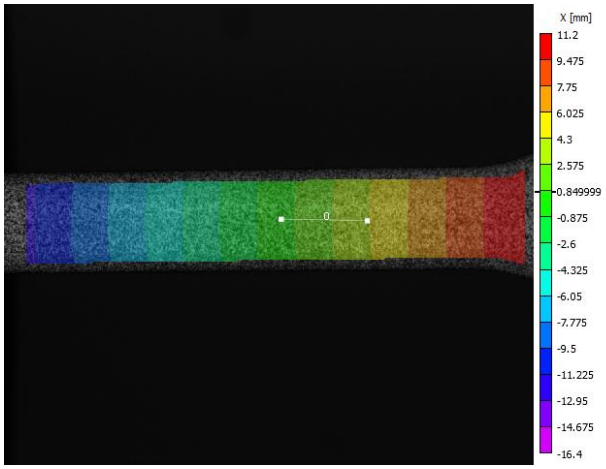

(c)

Figure E-7. The DIC Data From Test # M1-TMT-P3-SG5-O1-SR3-T1-N4: (a) Maximum Principal and (b) Minimum Principal Strain Contours Immediately Prior to Fracture, and (c) Initial Extensometer Position

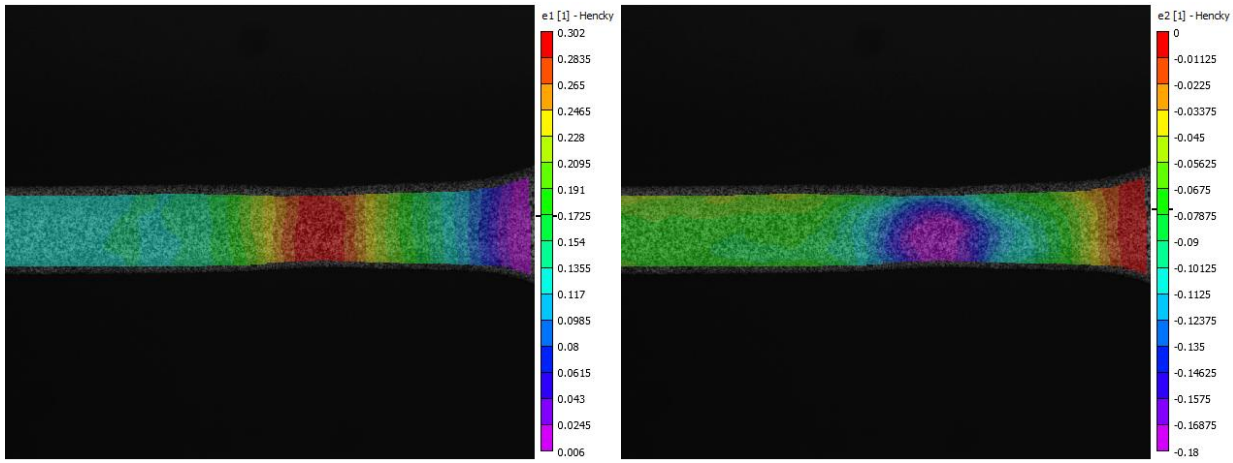

(a) (b)

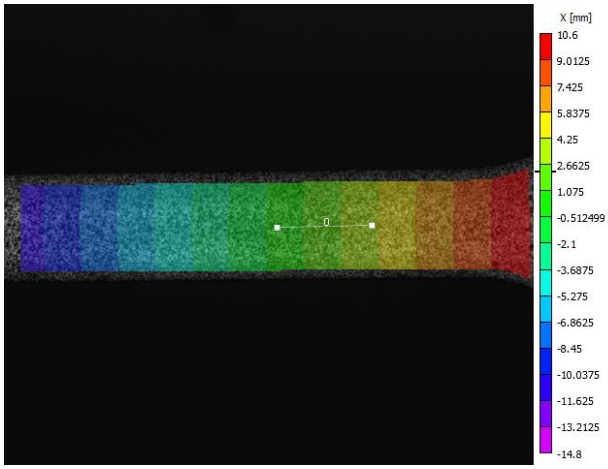

(c)

Figure E-8. The DIC Data From Test # M1-TMT-P3-SG5-O1-SR3-T1-N5: (a) Maximum Principal and (b) Minimum Principal Strain Contours Immediately Prior to Fracture, and (c) Initial Extensometer Position

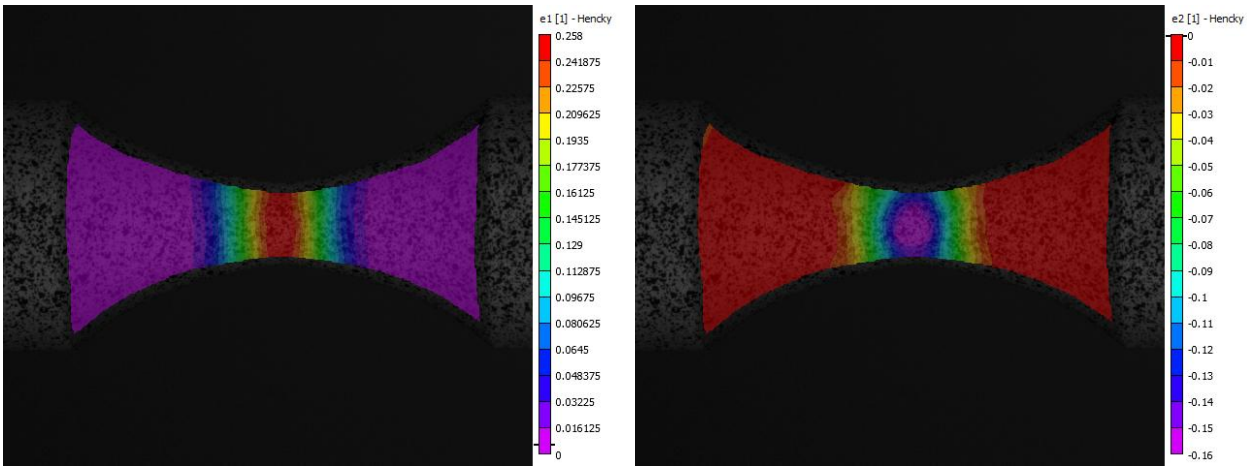

(a) (b)

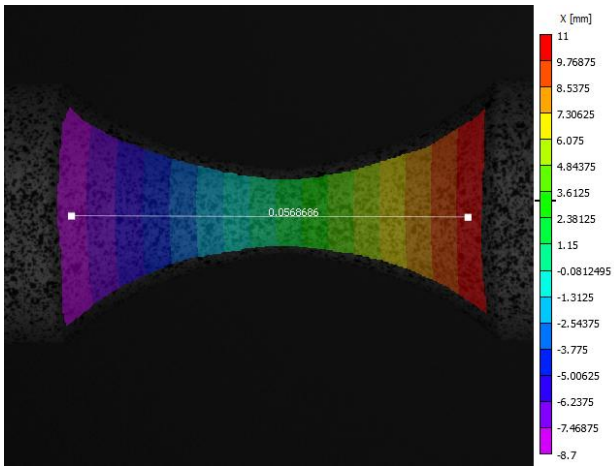

(c)

Figure E-9. The DIC Data From Test # M1-TMT-P3-SG6-O1-SR3-T1-N3: (a) Maximum Principal and (b) Minimum Principal Strain Contours Immediately Prior to Fracture, and (c) Initial Extensometer Position

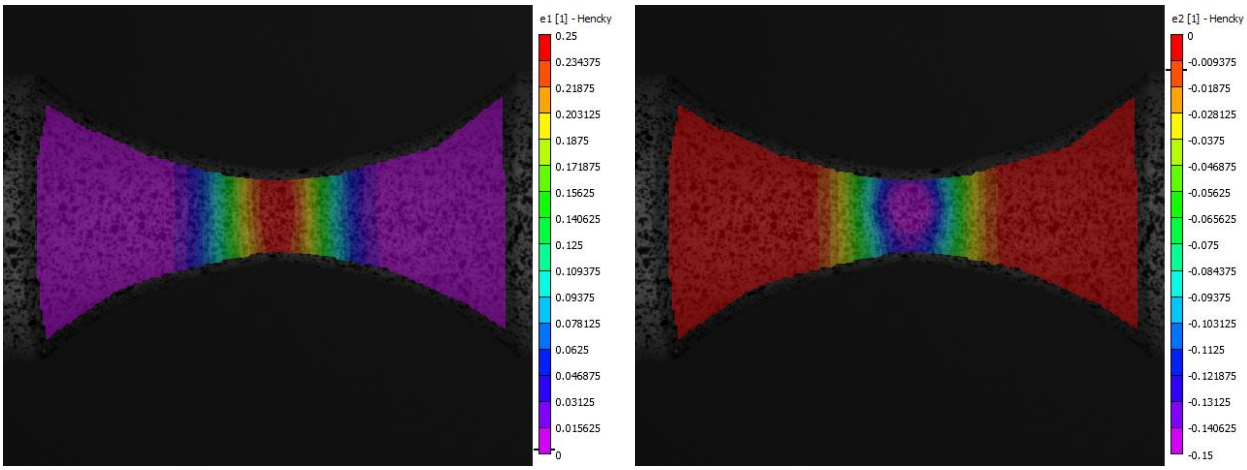

(a) (b)

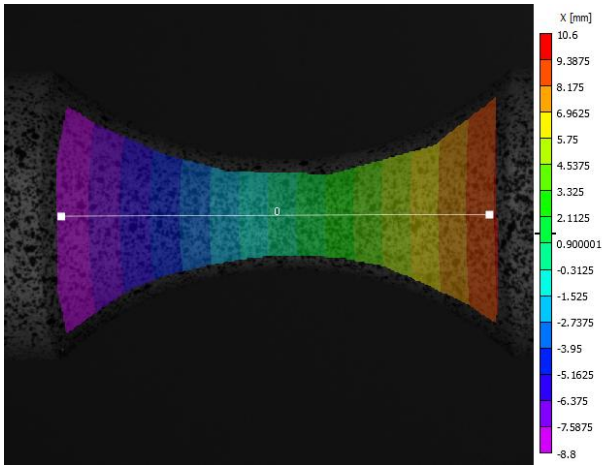

(c)

Figure E-10. The DIC Data From Test # M1-TMT-P3-SG6-O1-SR3-T1-N4: (a) Maximum Principal and (b) Minimum Principal Strain Contours Immediately Prior to Fracture, and (c) Initial Extensometer Position

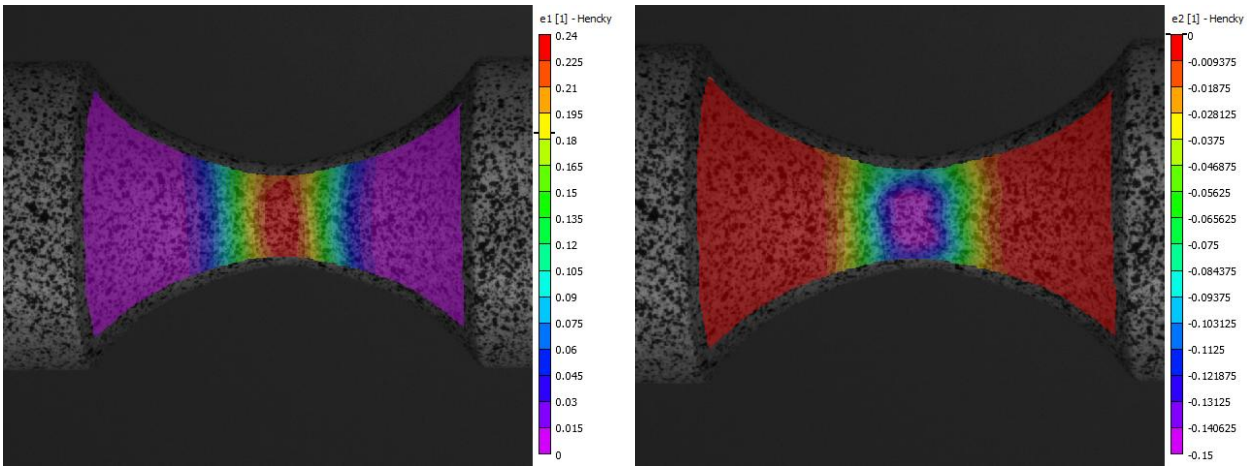

(a) (b)

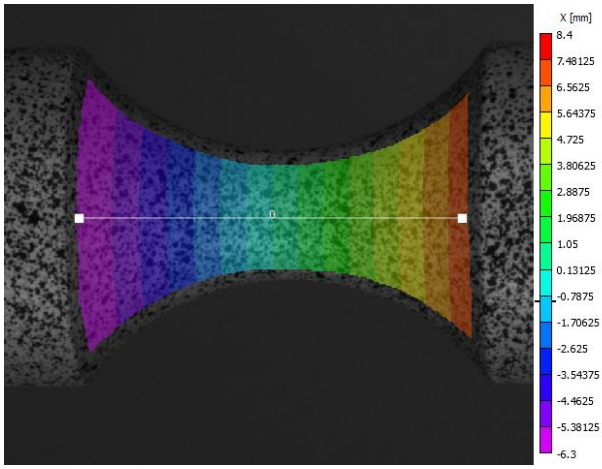

(c)

Figure E-11. The DIC Data From Test # M1-TMT-P3-SG7-O1-SR3-T1-N2: (a) Maximum Principal and (b) Minimum Principal Strain Contours Immediately Prior to Fracture, and (c) Initial Extensometer Position

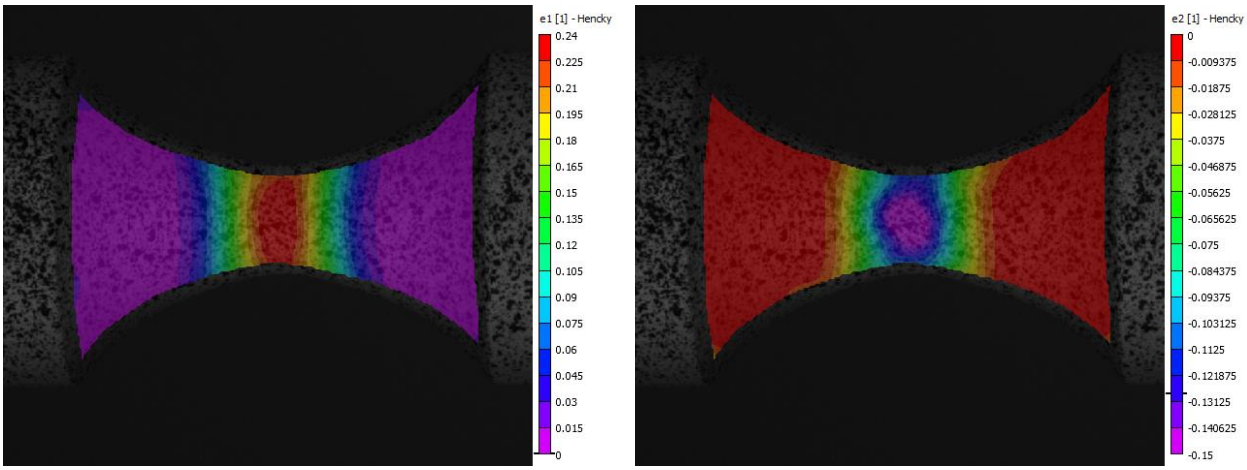

(a) (b)

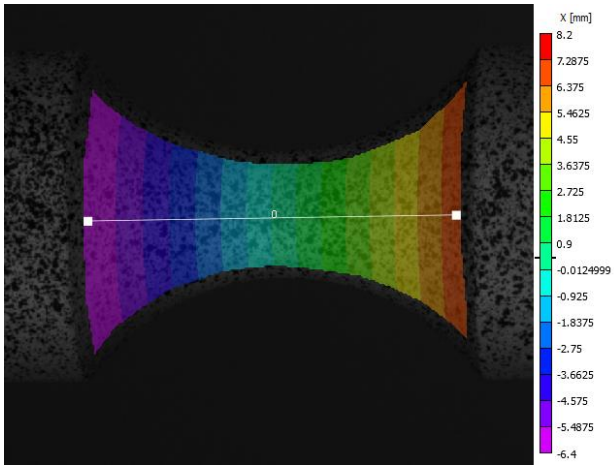

(c)

Figure E-12. The DIC Data From Test # M1-TMT-P3-SG7-O1-SR3-T1-N3: (a) Maximum Principal and (b) Minimum Principal Strain Contours Immediately Prior to Fracture, and (c) Initial Extensometer Position

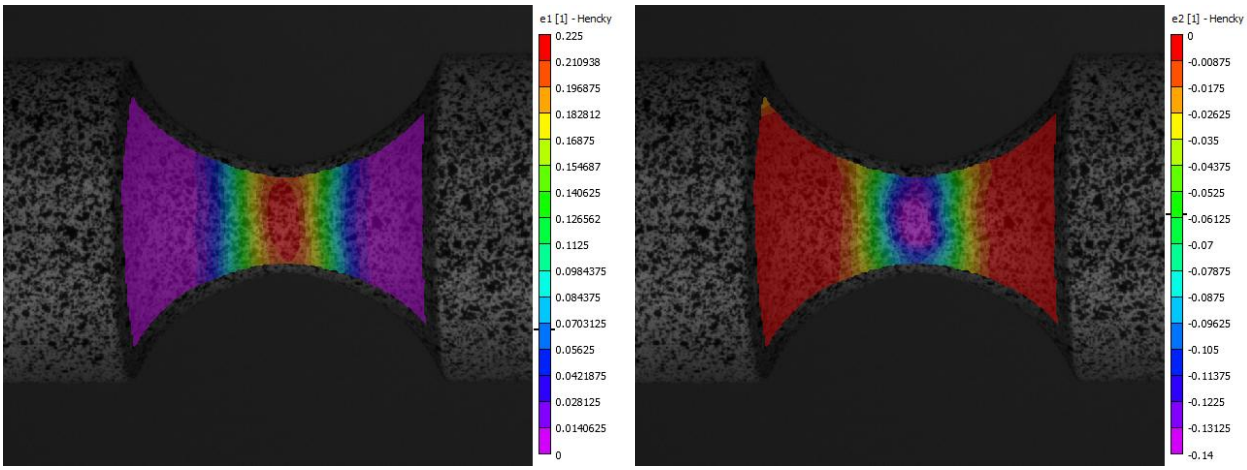

(a) (b)

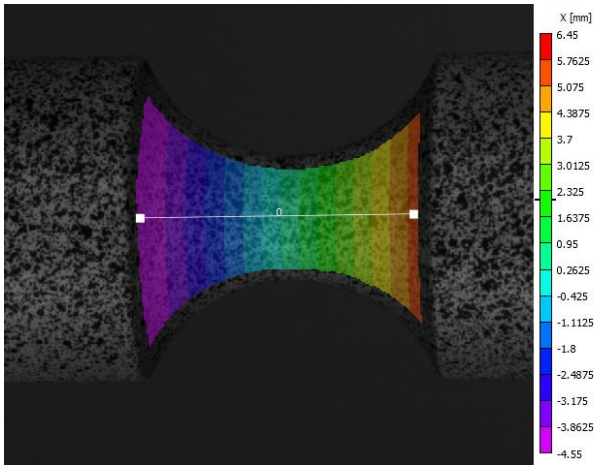

(c)

Figure E-13. The DIC Data From Test # M1-TMT-P3-SG8-O1-SR3-T1-N2: (a) Maximum Principal and (b) Minimum Principal Strain Contours Immediately Prior to Fracture, and (c) Initial Extensometer Position

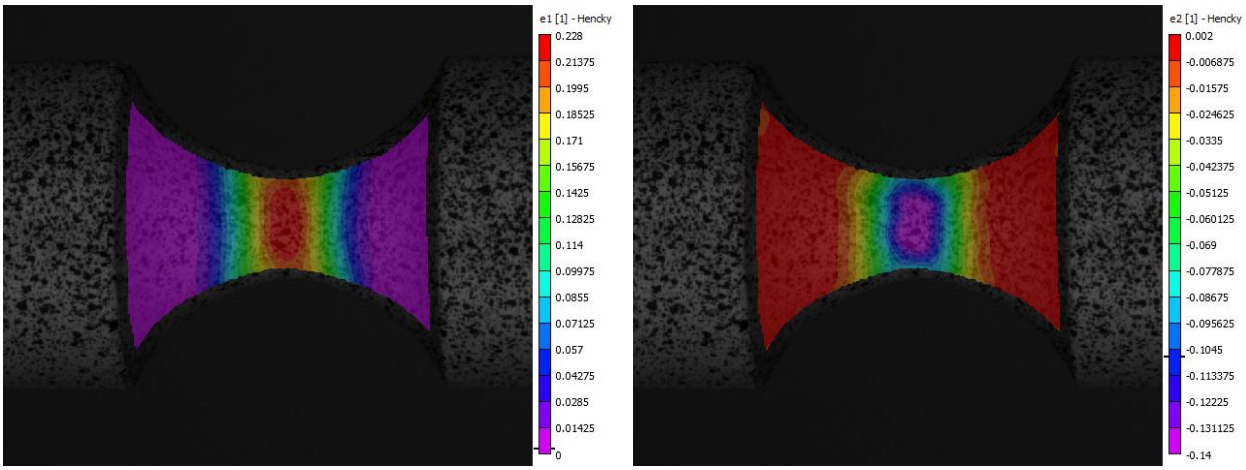

(a) (b)

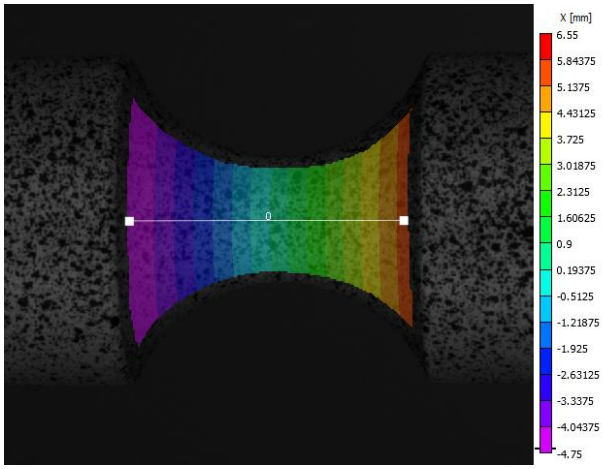

(c)

Figure E-14. The DIC Data From Test # M1-TMT-P3-SG8-O1-SR3-T1-N3: (a) Maximum Principal and (b) Minimum Principal Strain Contours Immediately Prior to Fracture, and (c) Initial Extensometer Position

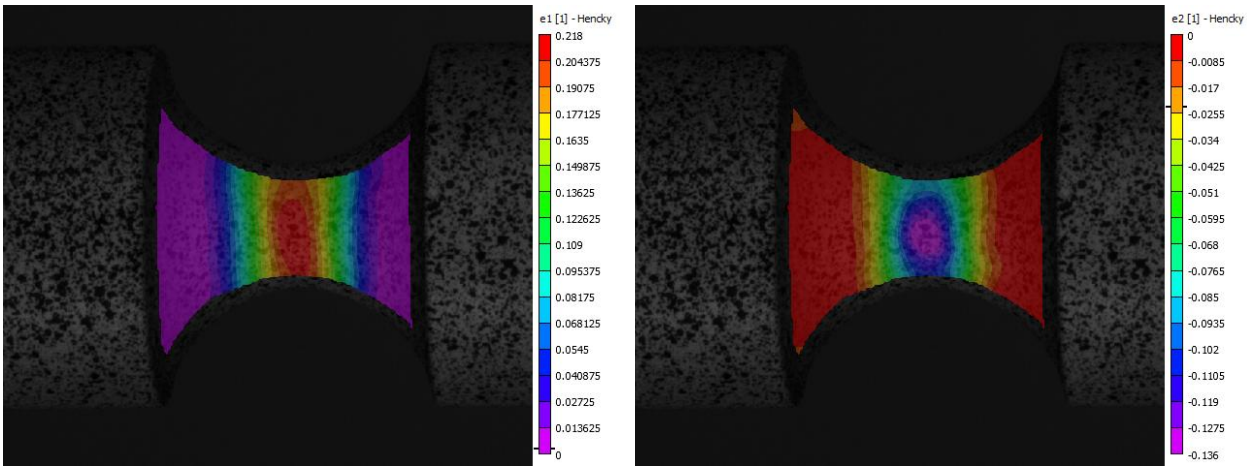

(a) (b)

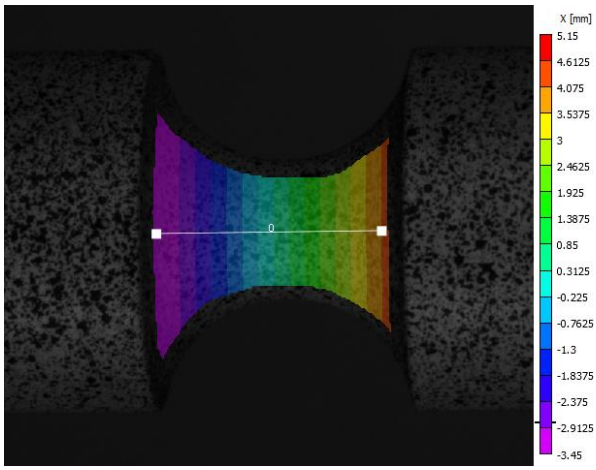

(c)

Figure E-15. The DIC Data From Test # M1-TMT-P3-SG9-O1-SR3-T1-N2: (a) Maximum Principal and (b) Minimum Principal Strain Contours Immediately Prior to Fracture, and (c) Initial Extensometer Position

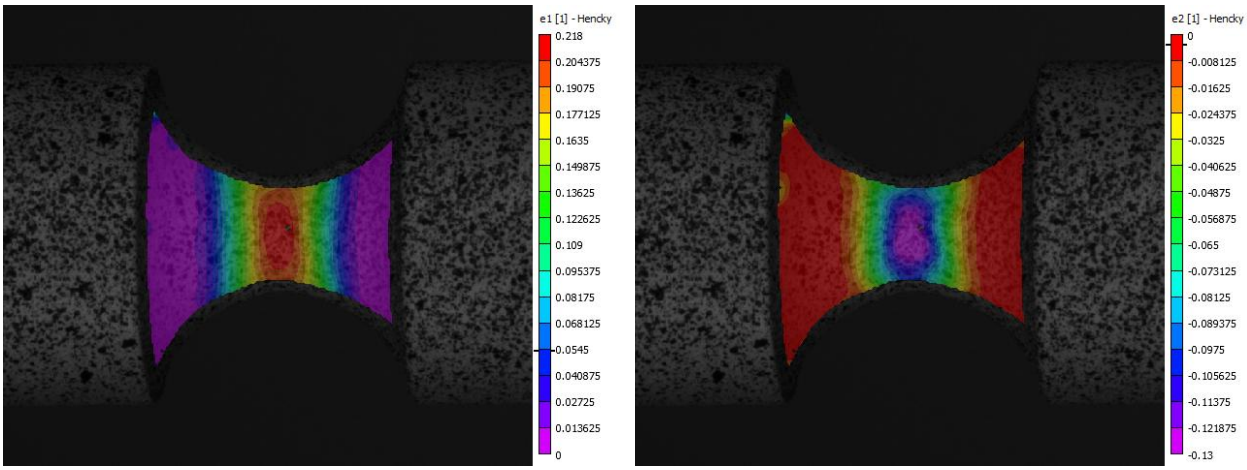

(a) (b)

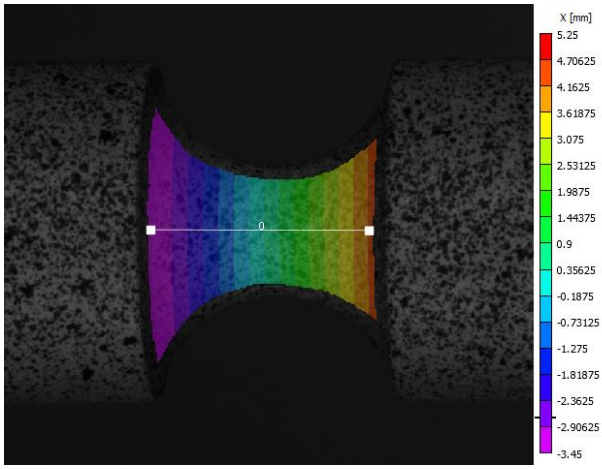

(c)

Figure E-16. The DIC Data From Test # M1-TMT-P3-SG9-O1-SR3-T1-N3: (a) Maximum Principal and (b) Minimum Principal Strain Contours Immediately Prior to Fracture, and (c) Initial Extensometer Position

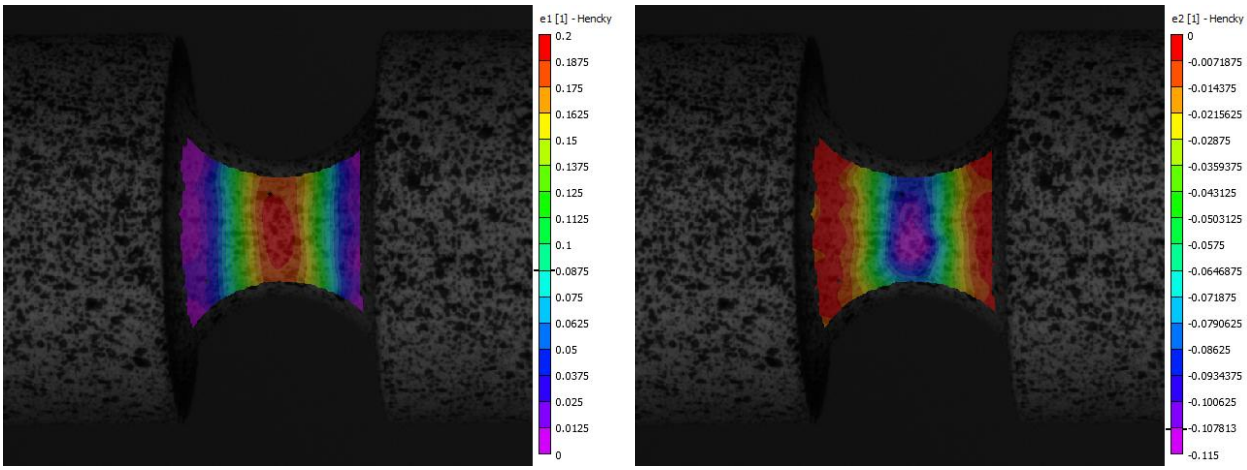

(a) (b)

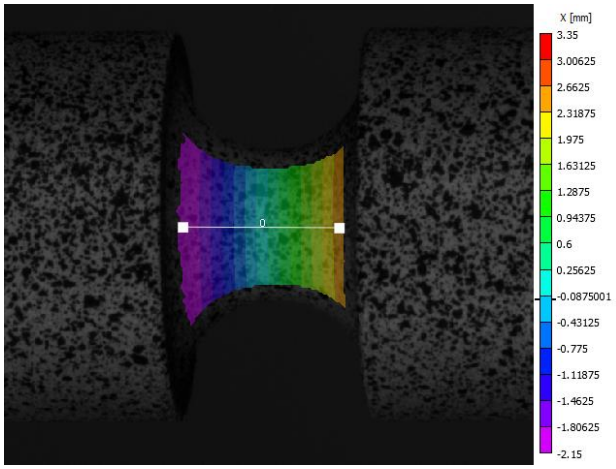

(c)

Figure E-17. The DIC Data From Test # M1-TMT-P3-SG10-O1-SR3-T1-N1: (a) Maximum Principal and (b) Minimum Principal Strain Contours Immediately Prior to Fracture, and (c) Initial Extensometer Position

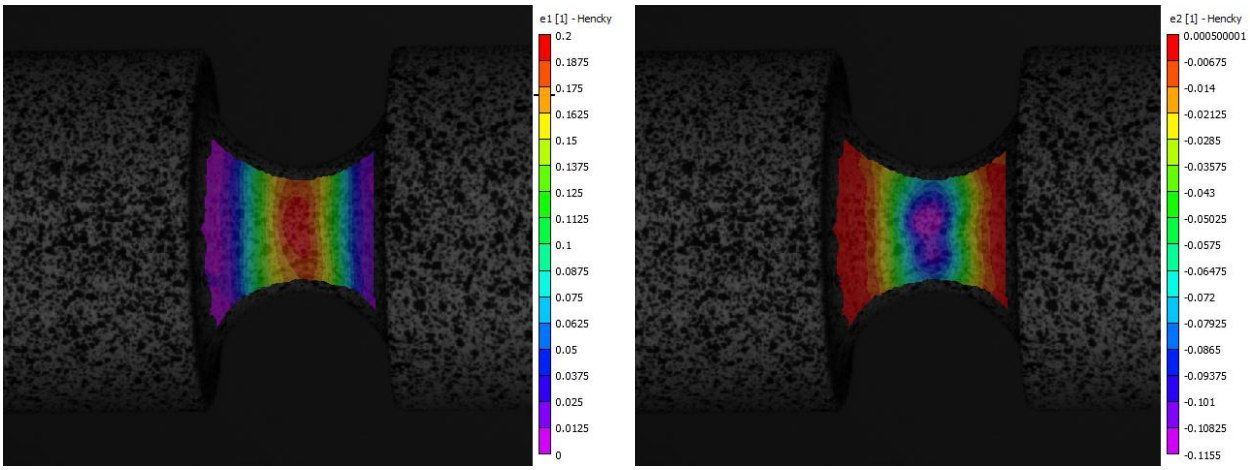

(a) (b)

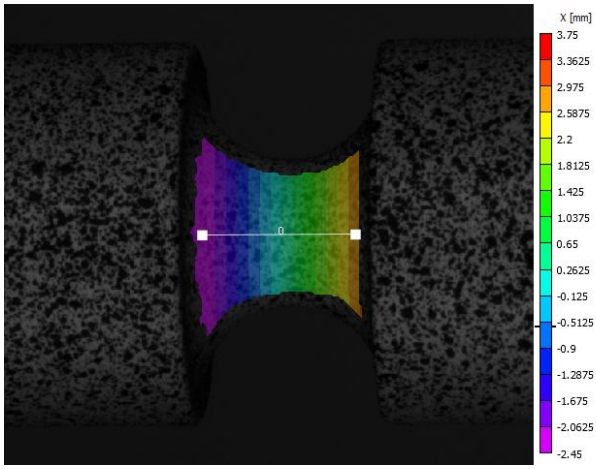

(c)

Figure E-18. The DIC Data From Test # M1-TMT-P3-SG10-O1-SR3-T1-N2: (a) Maximum Principal and (b) Minimum Principal Strain Contours Immediately Prior to Fracture, and (c) Initial Extensometer Position

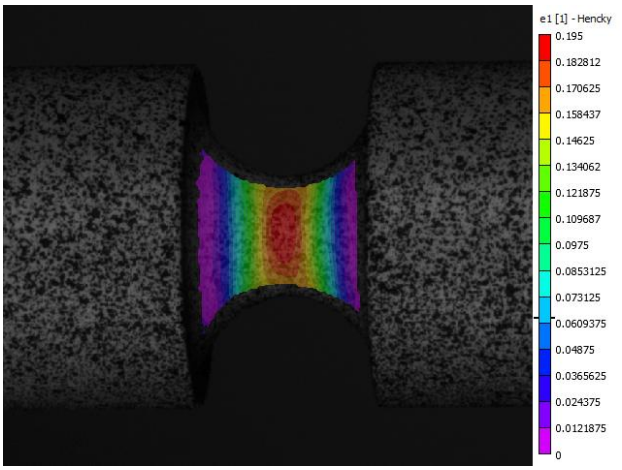

(a)

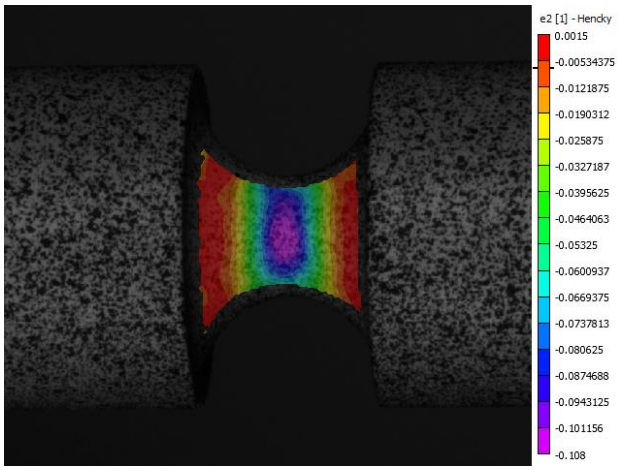

(b)

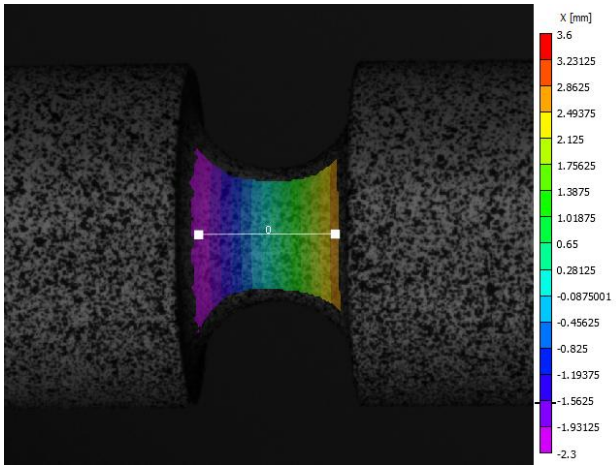

(c)

Figure E-19. The DIC Data from Test # M1-TMT-P3-SG10-O1-SR3-T1-N3: (a) Maximum Principal and (b) Minimum Principal Strain Contours Immediately Prior to Fracture, and (c) Initial Extensometer Position

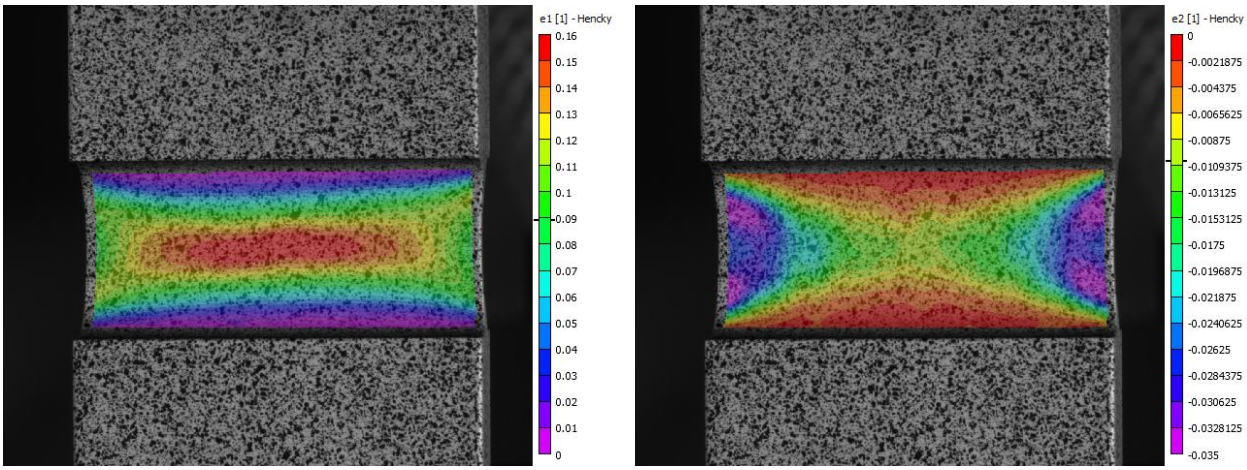

(a) (b)

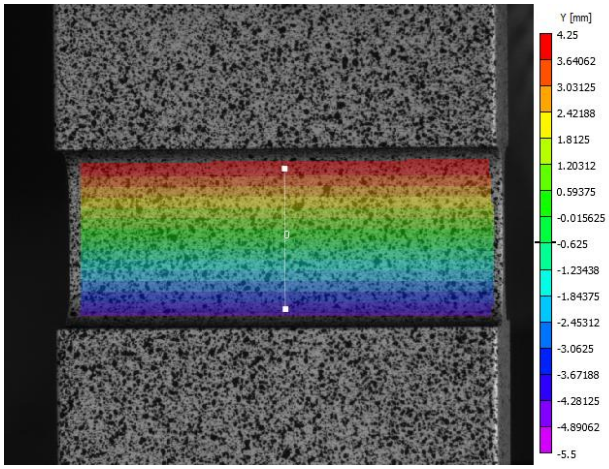

(c)

Figure E-20. The DIC Data From Test # M1-TMT-P3-SG11-O1-SR3-T1-N1: (a) Maximum Principal and (b) Minimum Principal Strain Contours Immediately Prior to Fracture, and (c) Initial Extensometer Position

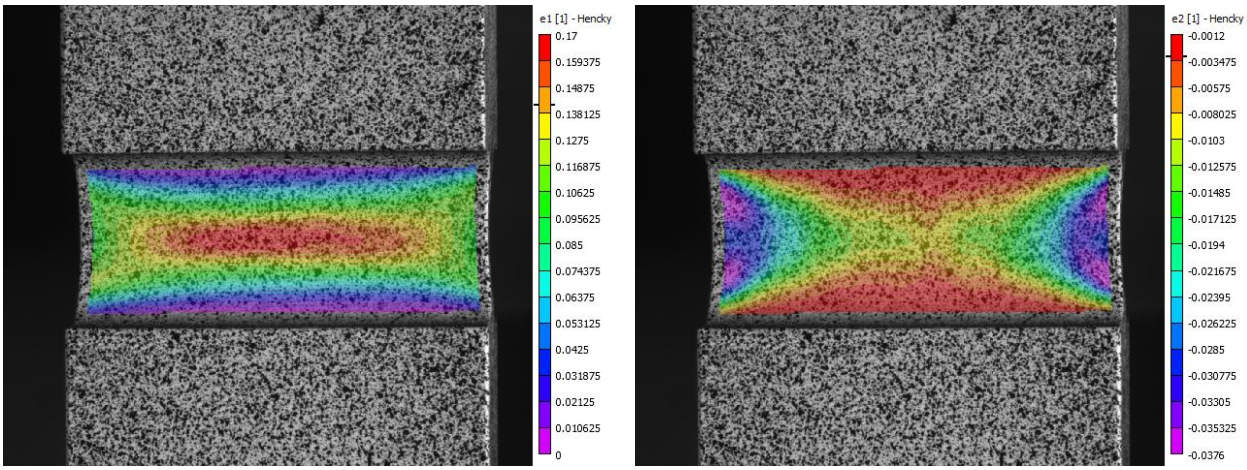

(a) (b)

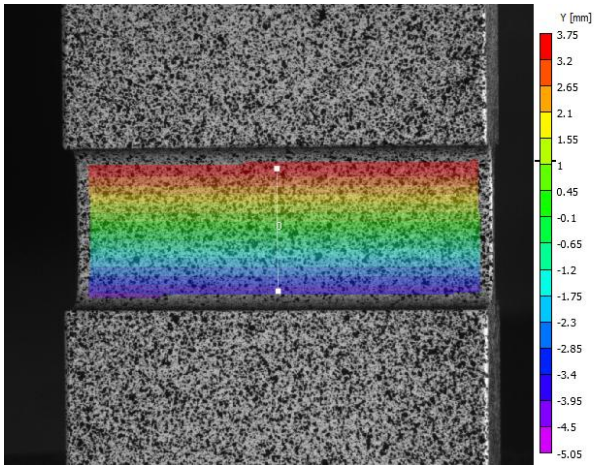

(c)

Figure E-21. The DIC Data From Test # M1-TMT-P3-SG11-O1-SR3-T1-N2: (a) Maximum Principal and (b) Minimum Principal Strain Contours Immediately Prior to Fracture, and (c) Initial Extensometer Position

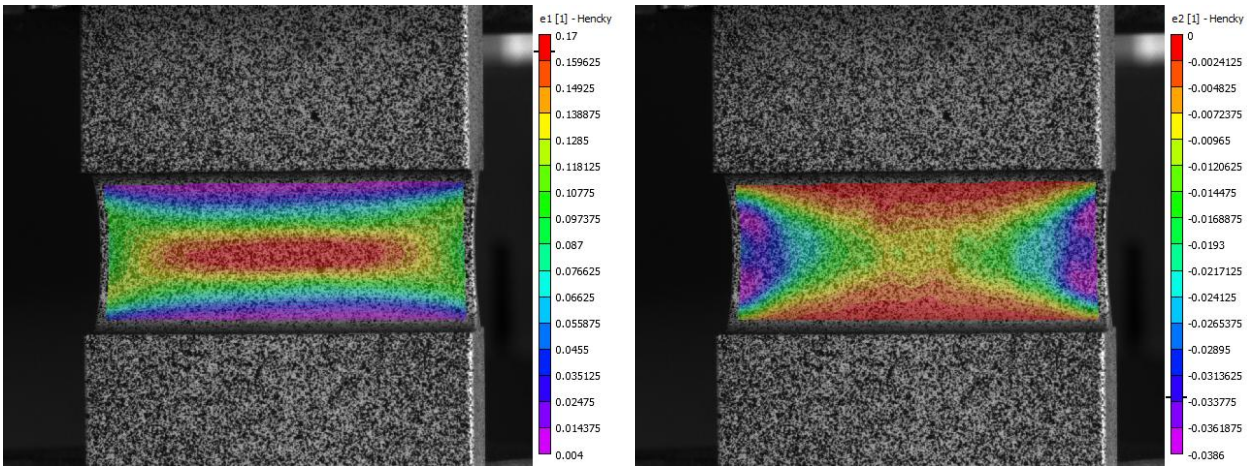

(a) (b)

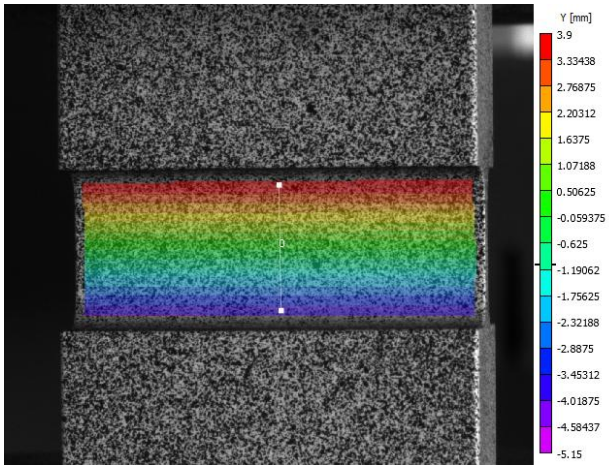

(c)

Figure E-22. The DIC Data From Test # M1-TMT-P3-SG11-O1-SR3-T1-N3: (a) Maximum Principal and (b) Minimum Principal Strain Contours Immediately Prior to Fracture, and (c) Initial Extensometer Position

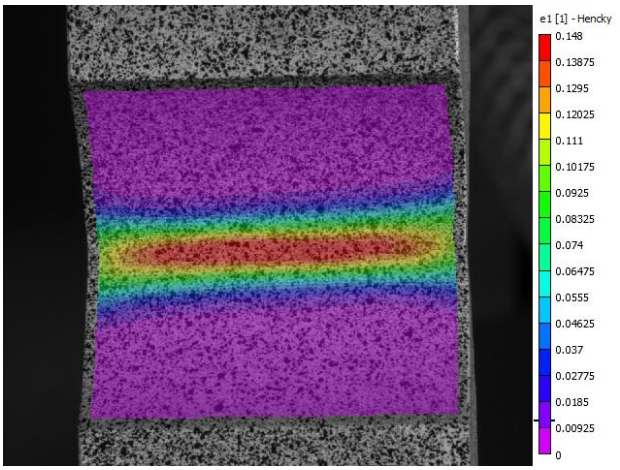

(a)

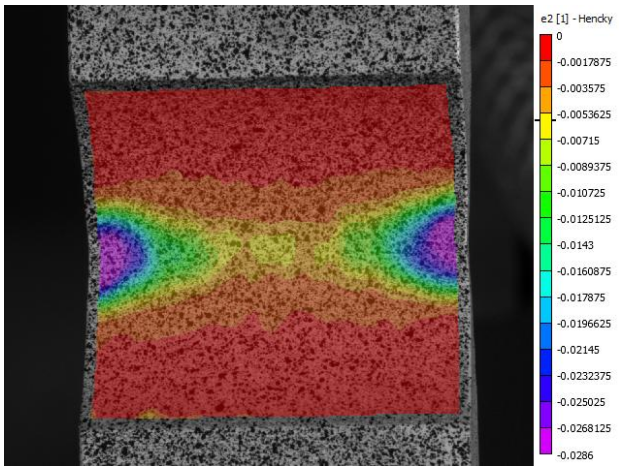

(b)

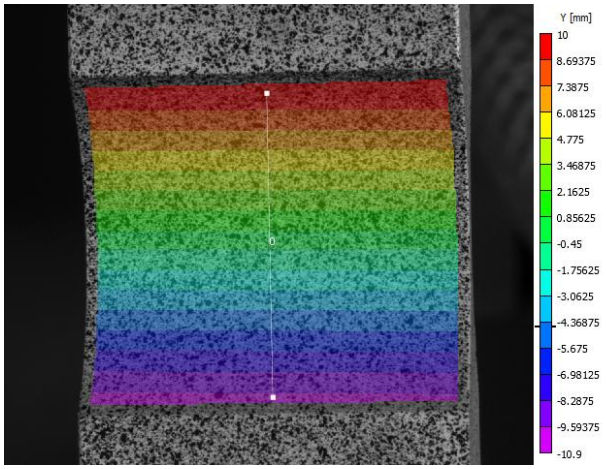

(c)

Figure E-23. The DIC Data From Test # M1-TMT-P3-SG12-O1-SR3-T1-N1: (a) Maximum Principal and (b) Minimum Principal Strain Contours Immediately Prior to Fracture, and (c) Initial Extensometer Position

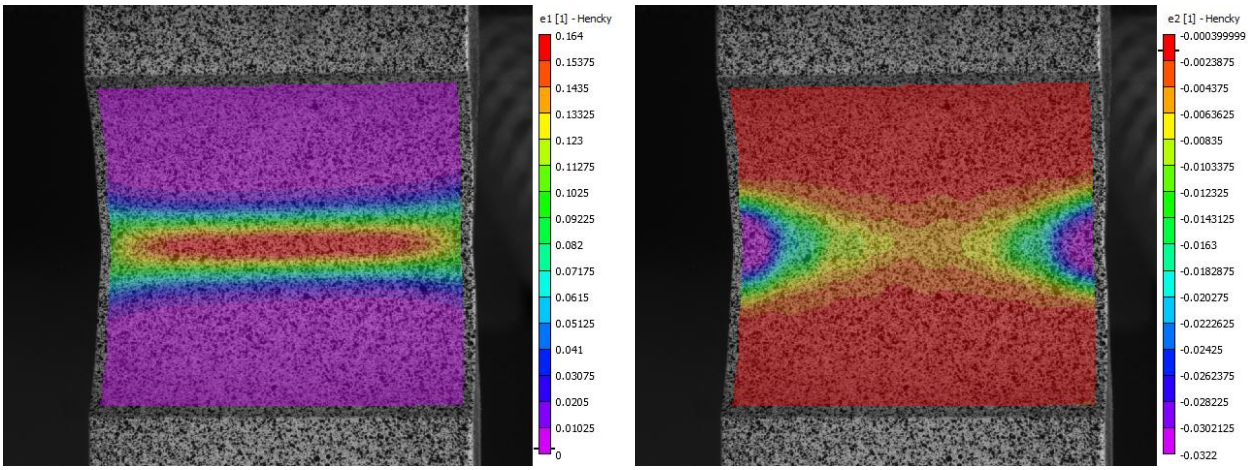

(a) (b)

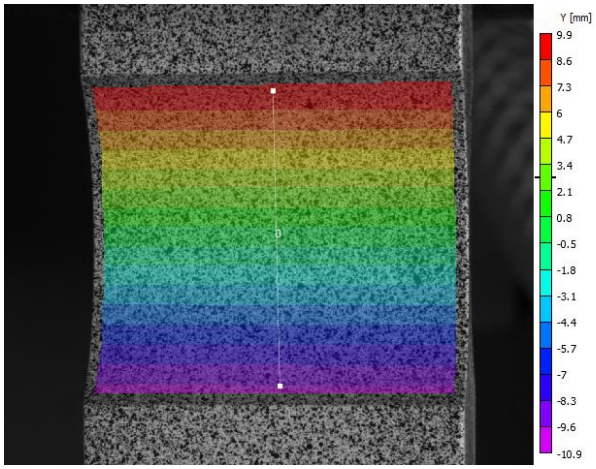

(c)

Figure E-24. The DIC Data From Test # M1-TMT-P3-SG12-O1-SR3-T1-N2: (a) Maximum Principal and (b) Minimum Principal Strain Contours Immediately Prior to Fracture, and (c) Initial Extensometer Position

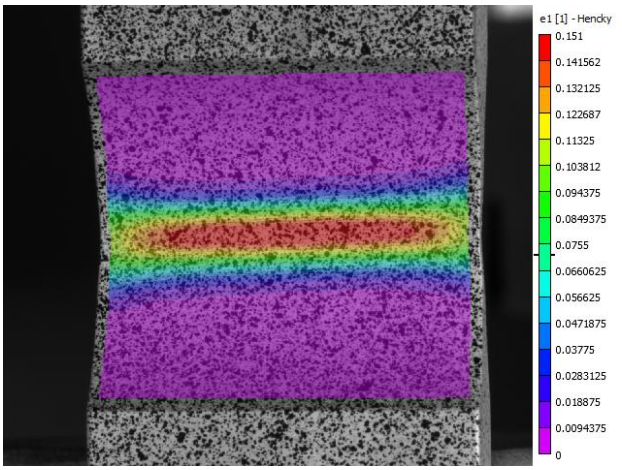

(a)

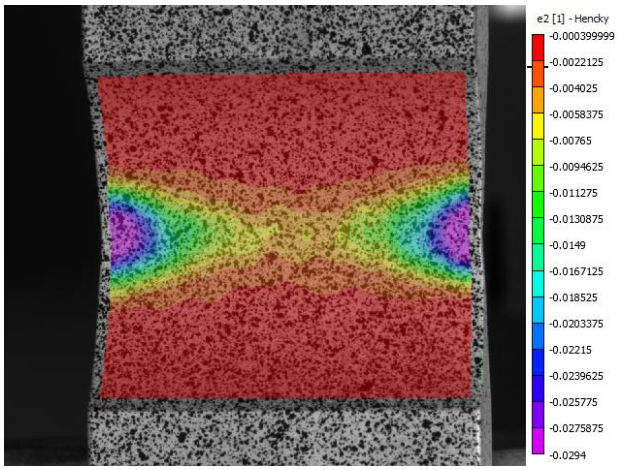

(b)

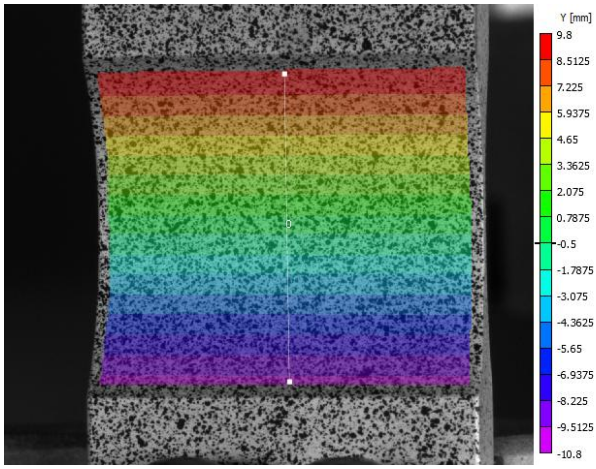

(c)

Figure E-25. The DIC Data From Test # M1-TMT-P3-SG12-O1-SR3-T1-N3: (a) Maximum Principal and (b) Minimum Principal Strain Contours Immediately Prior to Fracture, and (c) Initial Extensometer Position

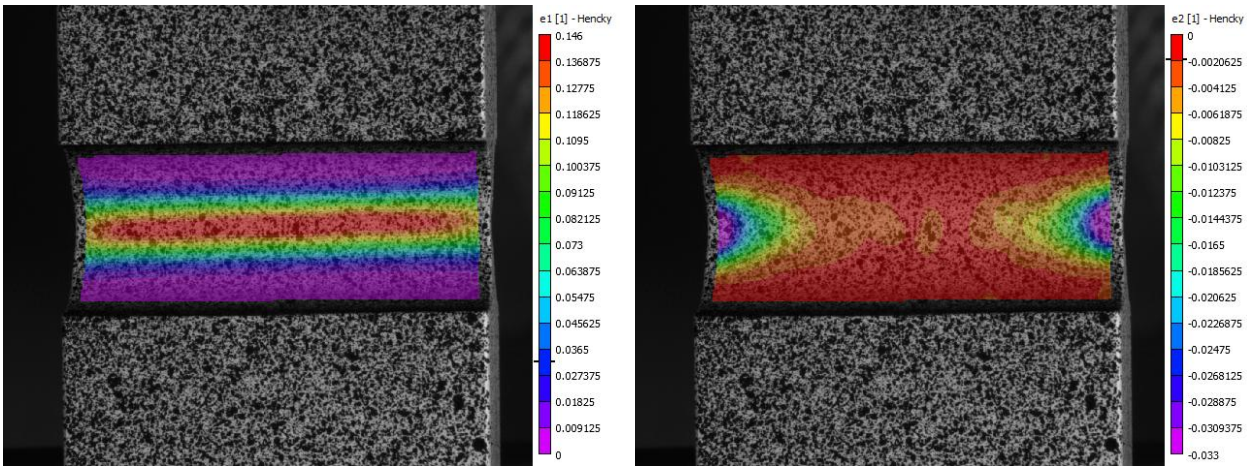

(a) (b)

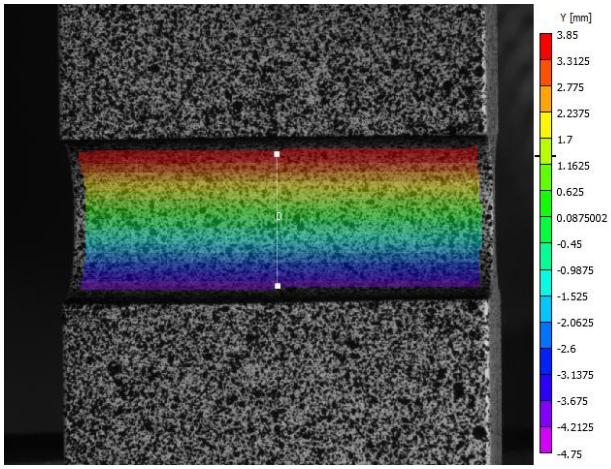

(c)

Figure E-26. The DIC Data From Test # M1-TMT-P3-SG13-O1-SR3-T1-N1: (a) Maximum Principal and (b) Minimum Principal Strain Contours Immediately Prior to Fracture, and (c) Initial Extensometer Position

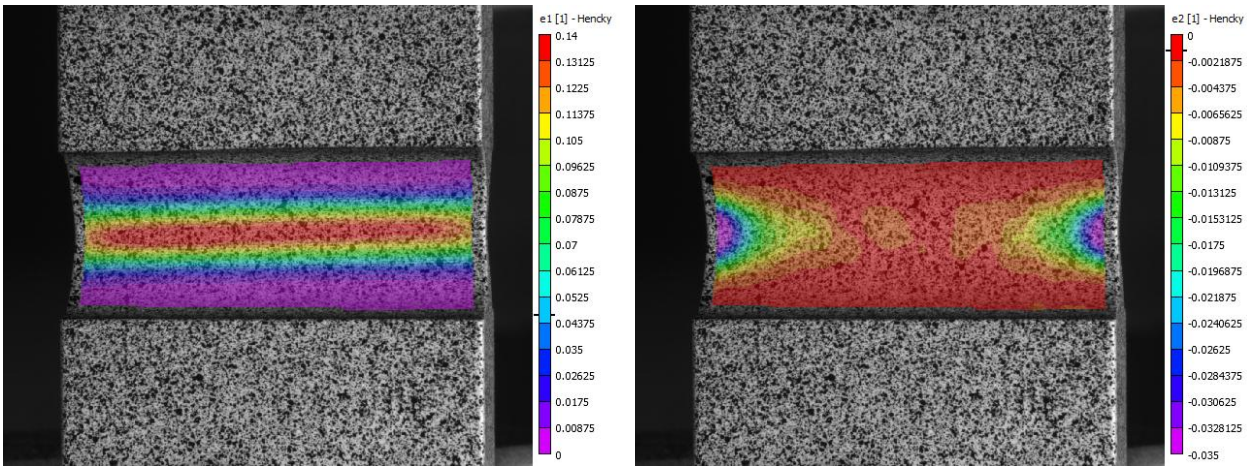

(a) (b)

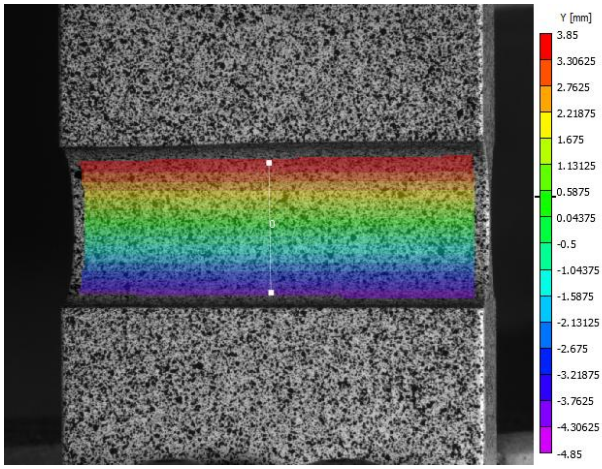

(c)

Figure E-27. The DIC Data From Test # M1-TMT-P3-SG13-O1-SR3-T1-N2: (a) Maximum Principal and (b) Minimum Principal Strain Contours Immediately Prior to Fracture, and (c) Initial Extensometer Position

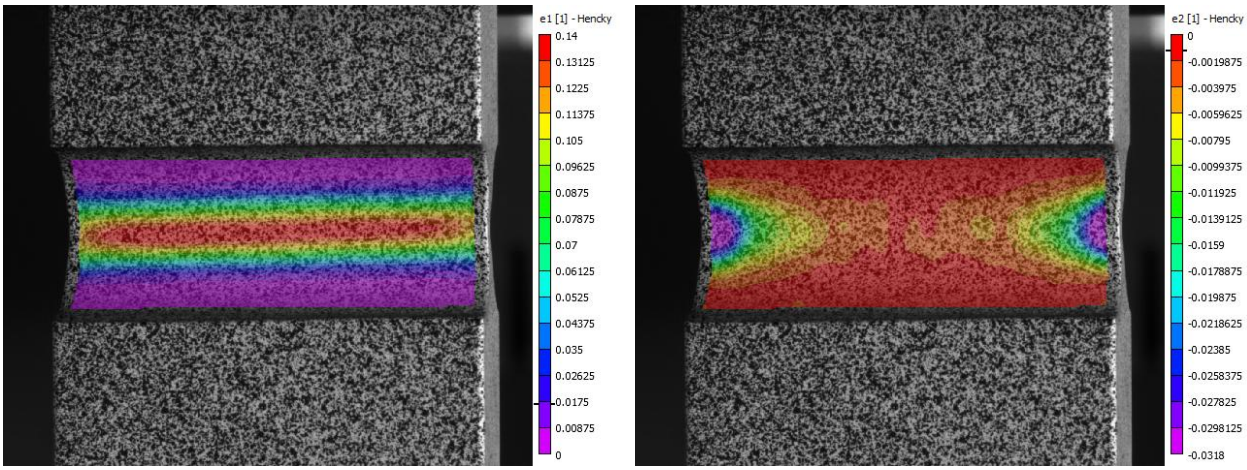

(a) (b)

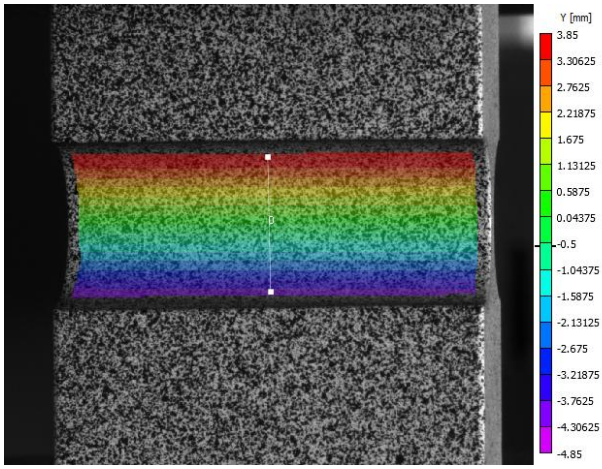

(c)

Figure E-28. The DIC Data From Test # M1-TMT-P3-SG13-O1-SR3-T1-N3: (a) Maximum Principal and (b) Minimum Principal Strain Contours Immediately Prior to Fracture, and (c) Initial Extensometer Position

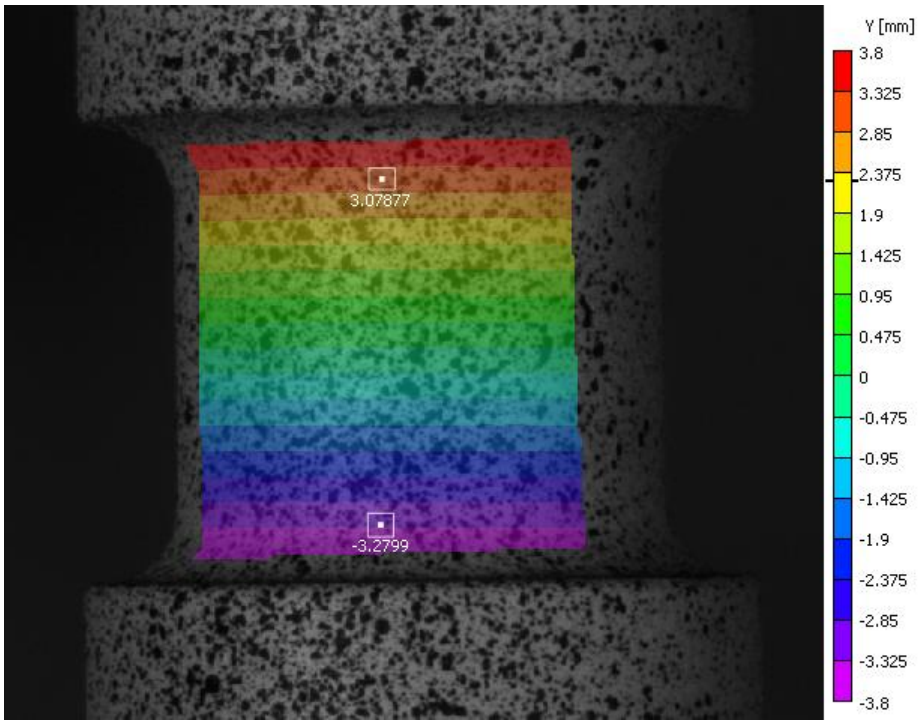

(a)

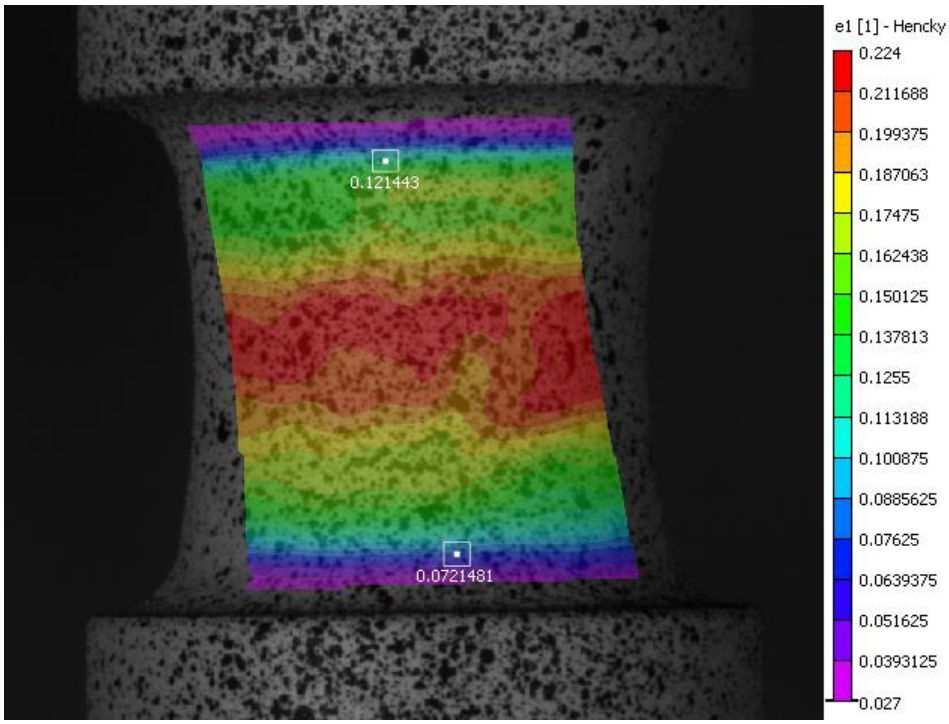

(b)

Figure E-29. The DIC Data From Test #M1-TMCL-LR1-P3-SR3-T1-N2: (a) Initial Tracking Point Positions on *y*-Coordinate Contour, (b) Tracking Point Positions Immediately Prior to Fracture on Maximum Principal Strain Contour

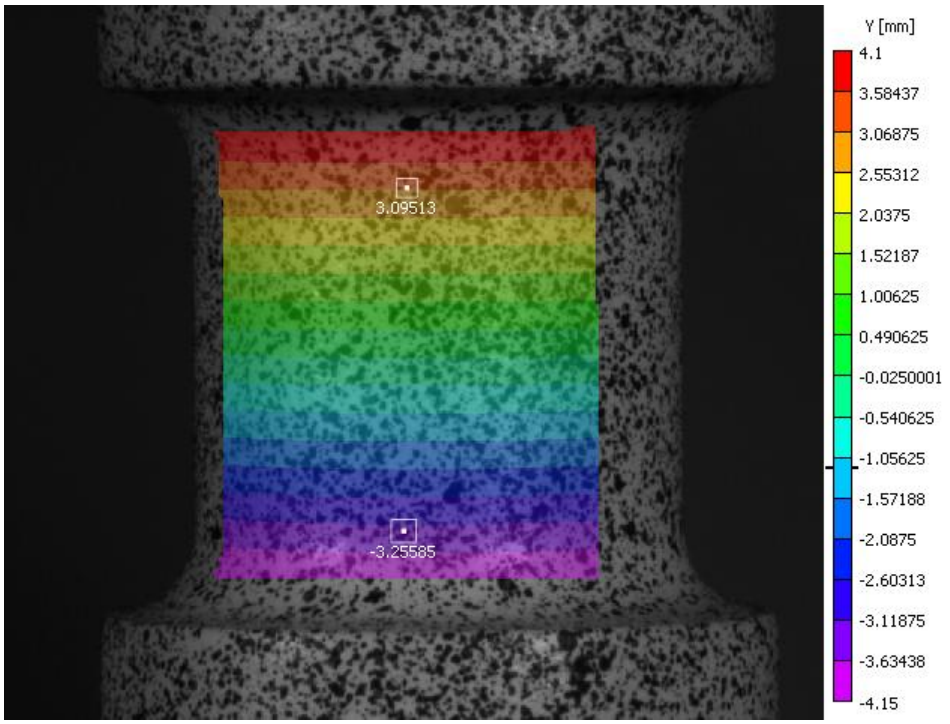

(a)

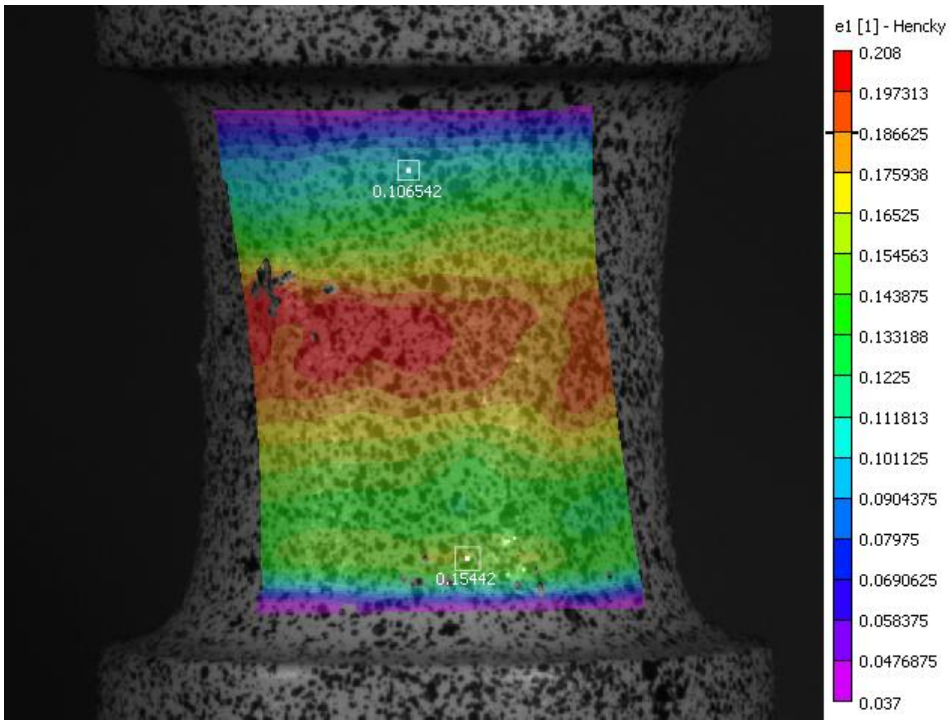

(b)

Figure E-30. The DIC Data From Test # M1-TMCL-LR1-P3-SR3-T1-N4: (a) Initial Tracking Point Positions on *y*-Coordinate Contour, (b) Tracking Point Positions Immediately Prior to Fracture on Maximum Principal Strain Contour

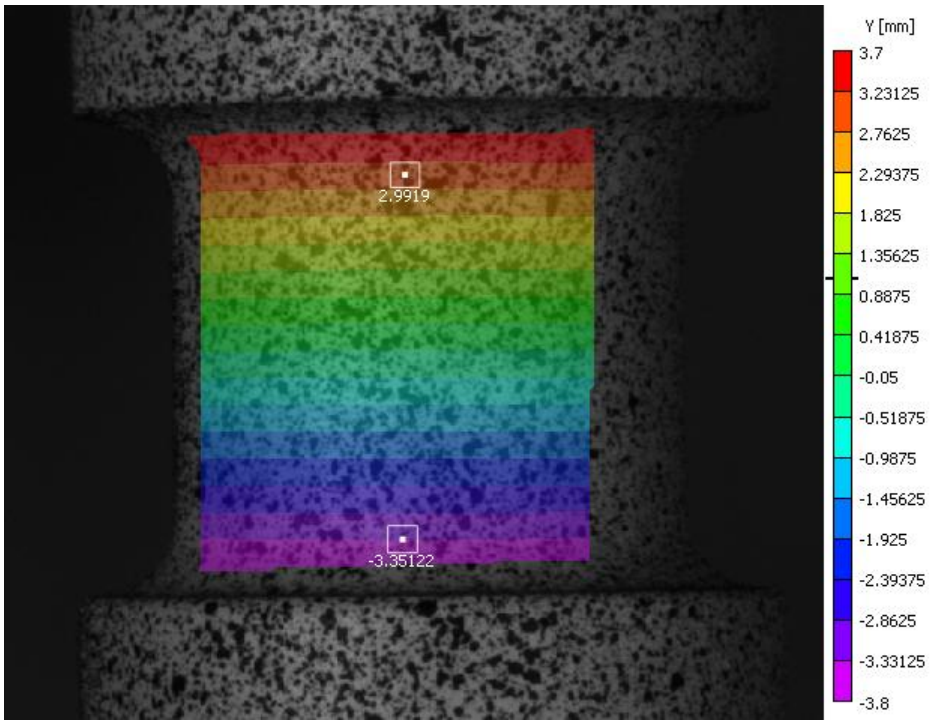

(a)

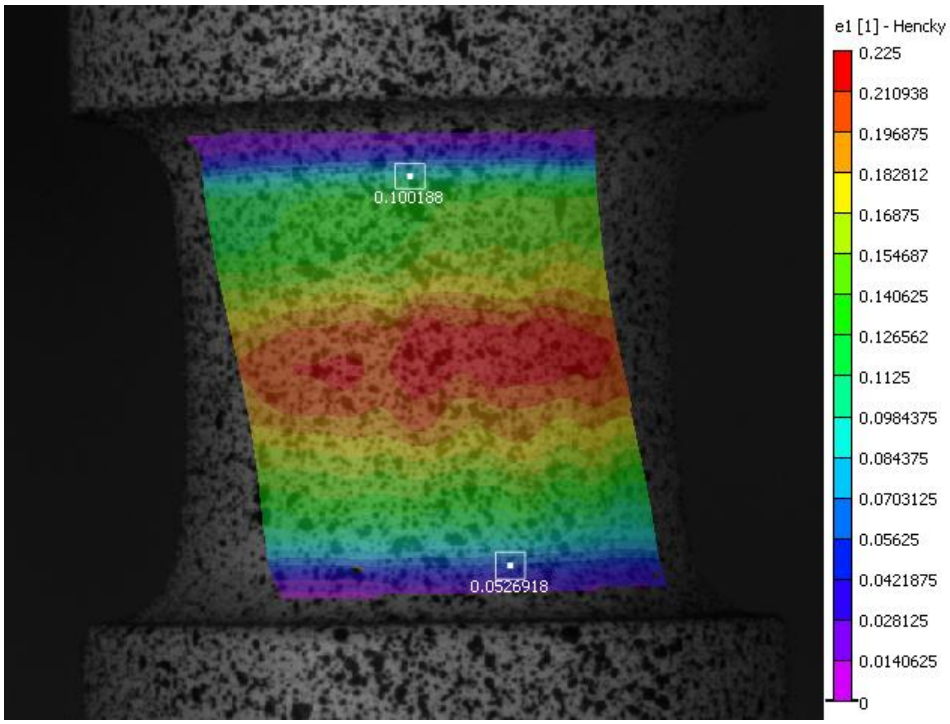

(b)

Figure E-31. The DIC Data From Test # M1-TMCL-LR2-P3-SR3-T1-N2: (a) Initial Tracking Point Positions on *y*-Coordinate Contour, (b) Tracking Point Positions Immediately Prior to Fracture on Maximum Principal Strain Contour

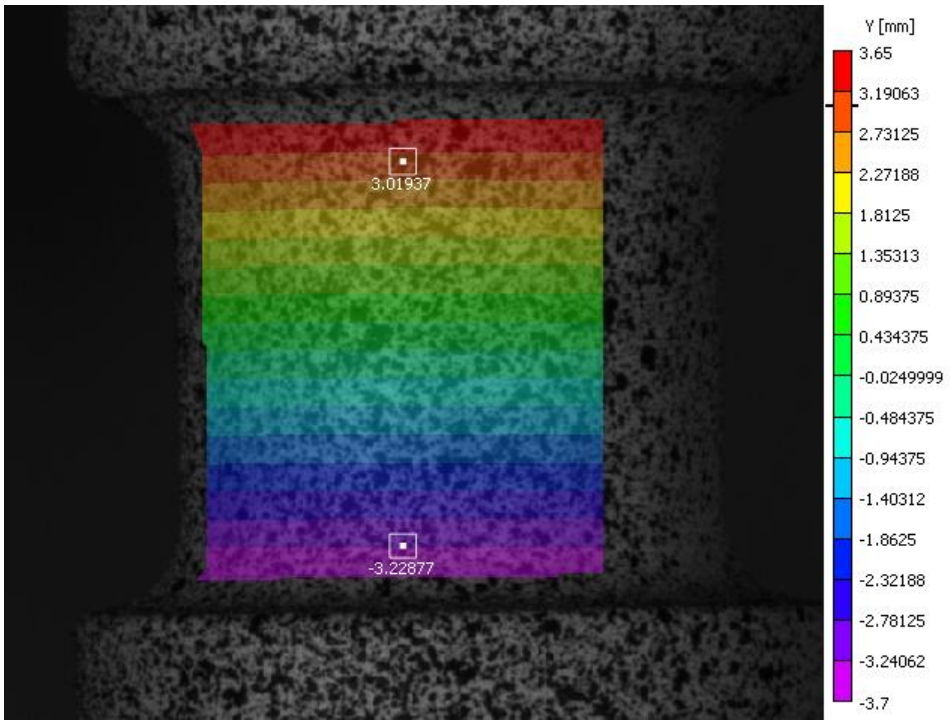

(a)

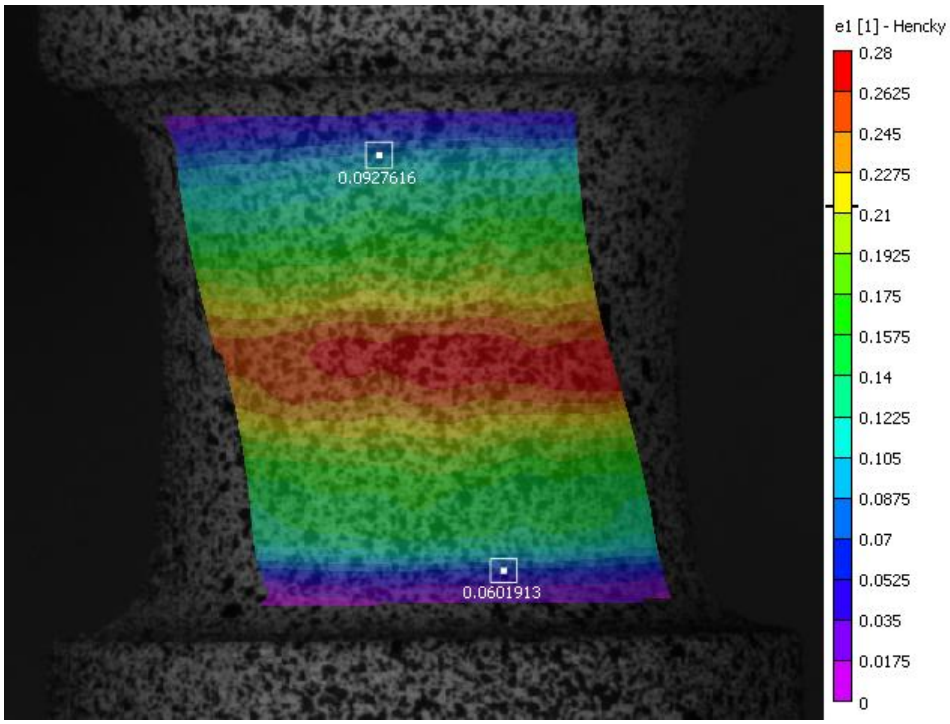

(b)

Figure E-32. The DIC Data From Test # M1-TMCL-LR2-P3-SR3-T1-N3: (a) Initial Tracking Point Positions on *y*-Coordinate Contour, (b) Tracking Point Positions Immediately Prior to Fracture on Maximum Principal Strain Contour

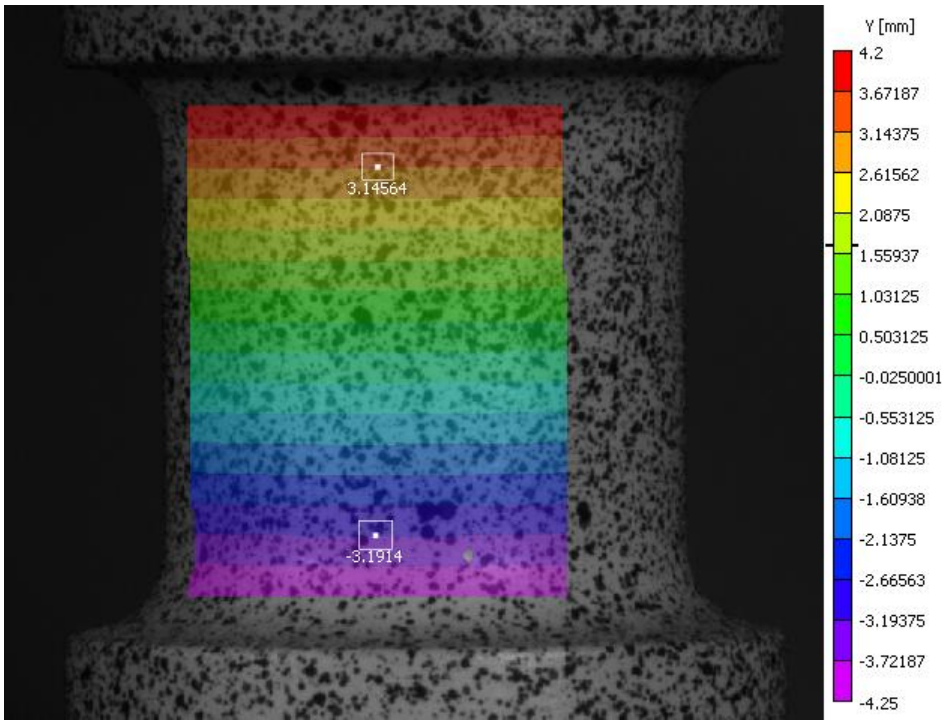

(a)

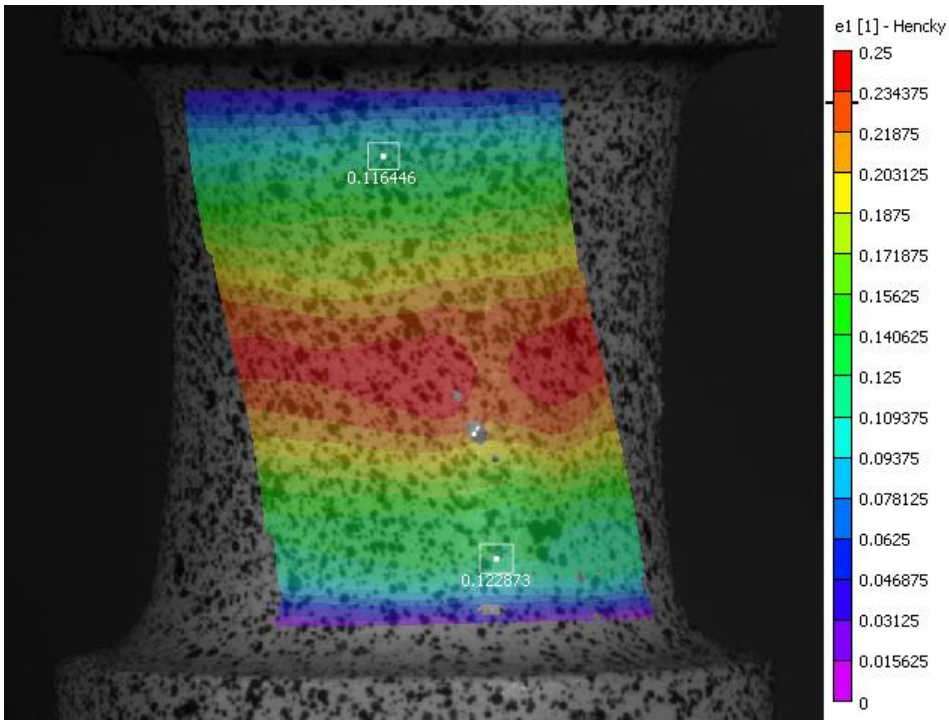

(b)

Figure E-33. The DIC Data From Test # M1-TMCL-LR2-P3-SR3-T1-N4: (a) Initial Tracking Point Positions on *y*-Coordinate Contour, (b) Tracking Point Positions Immediately Prior to Fracture on Maximum Principal Strain Contour

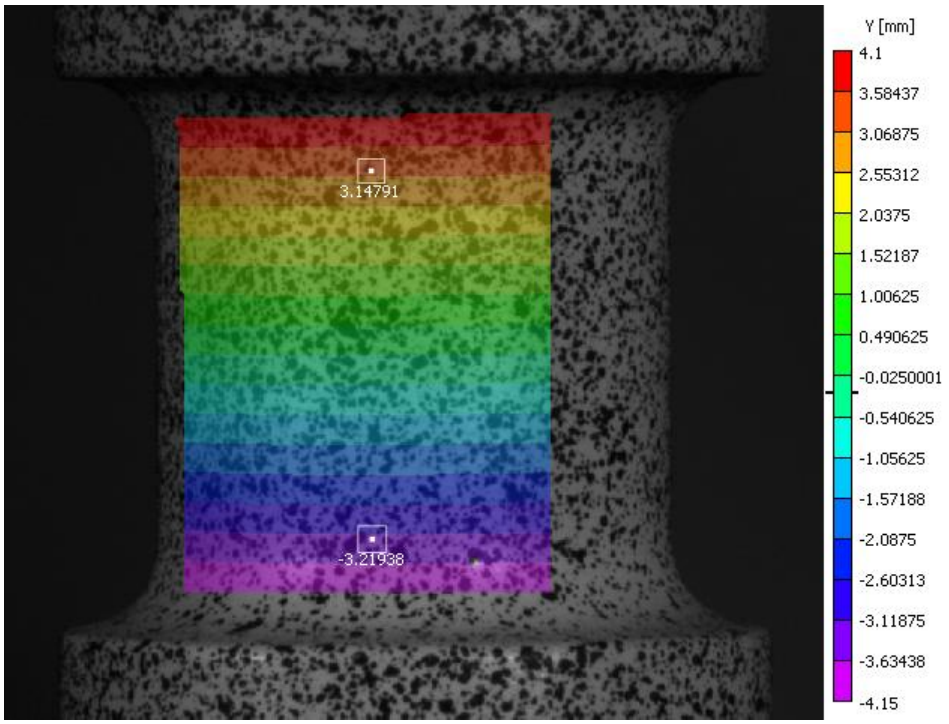

(a)

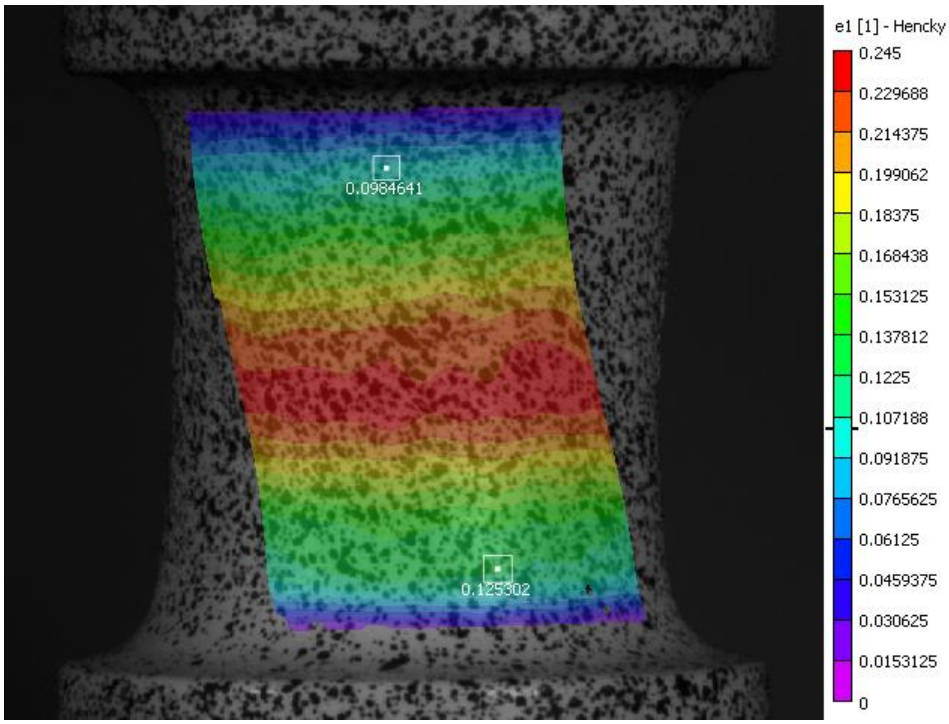

(b)

Figure E-34. The DIC Data From Test # M1-TMCL-LR2-P3-SR3-T1-N5: (a) Initial Tracking Point Positions on *y*-Coordinate Contour, (b) Tracking Point Positions Immediately Prior to Fracture on Maximum Principal Strain Contour

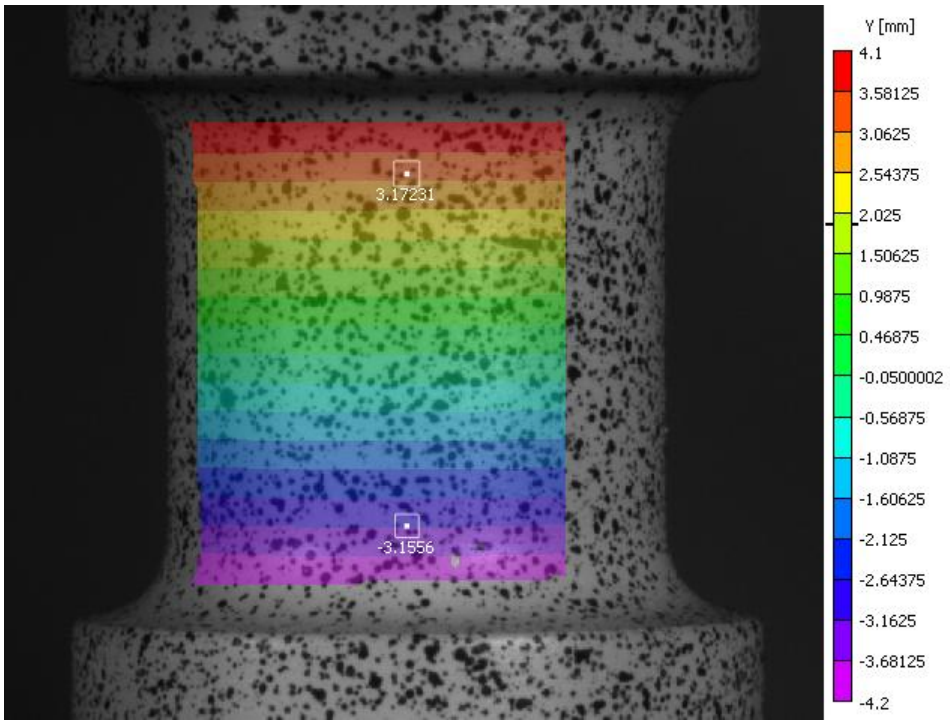

(a)

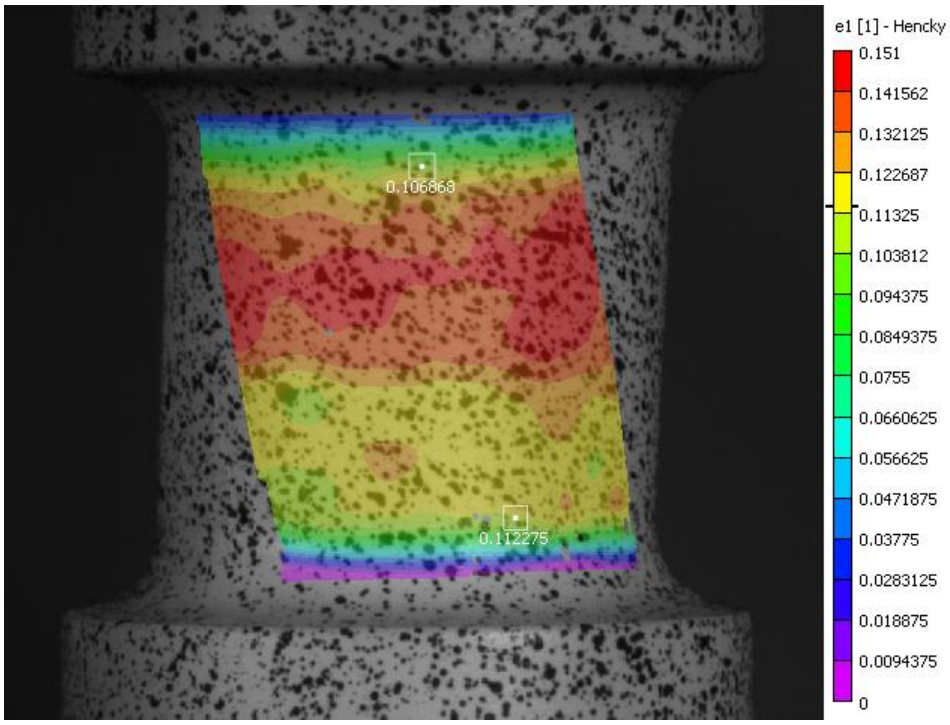

(b)

Figure E-35. The DIC Data From Test # M1-TMCL-LR3-P3-SR3-T1-N2: (a) Initial Tracking Point Positions on *y*-Coordinate Contour, (b) Tracking Point Positions Immediately Prior to Fracture on Maximum Principal Strain Contour

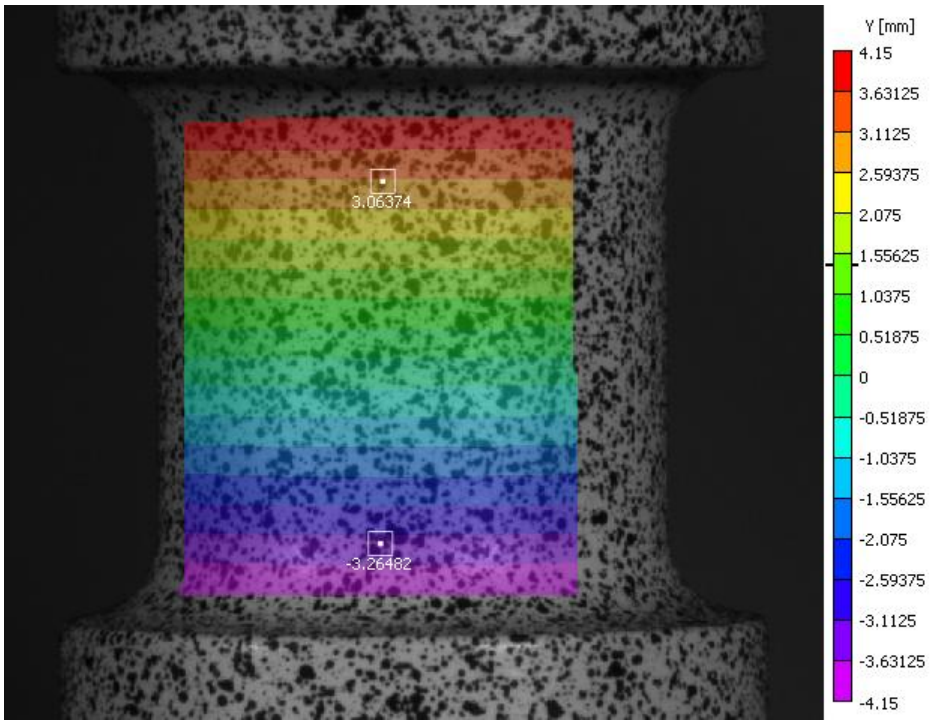

(a)

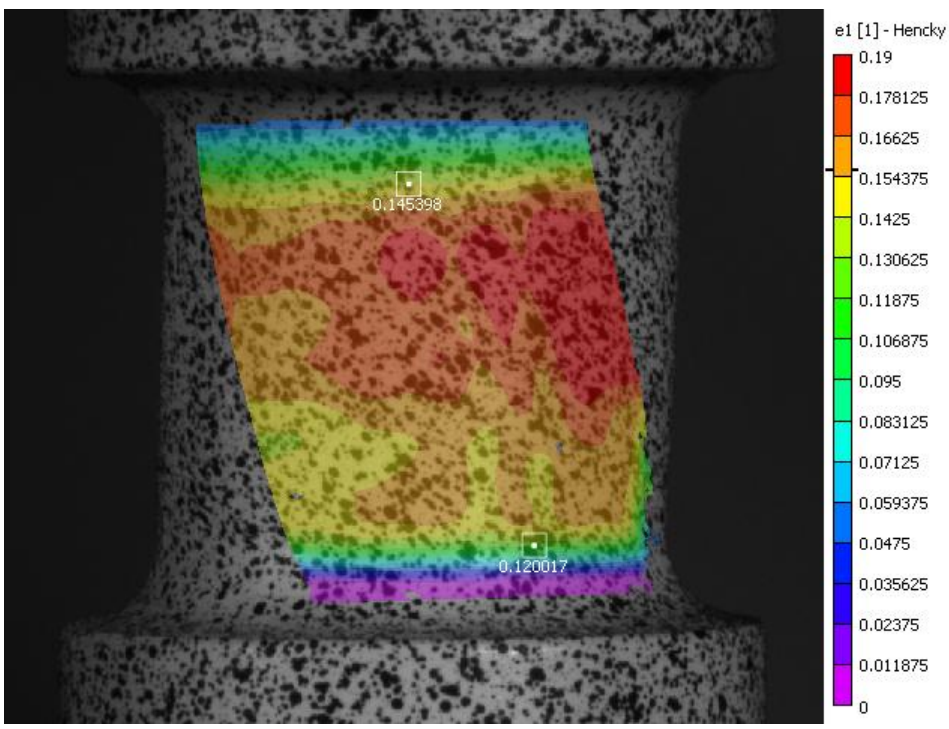

(b)

Figure E-36. The DIC Data From Test # M1-TMCL-LR3-P3-SR3-T1-N3: (a) Initial Tracking Point Positions on *y*-Coordinate Contour, (b) Tracking Point Positions Immediately Prior to Fracture on Maximum Principal Strain Contour

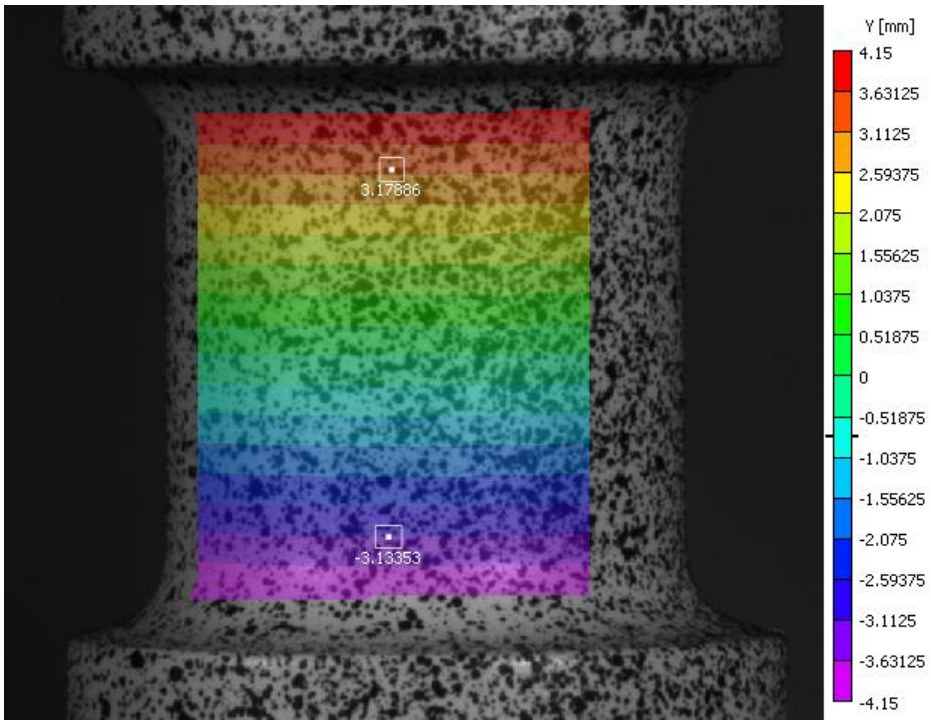

(a)

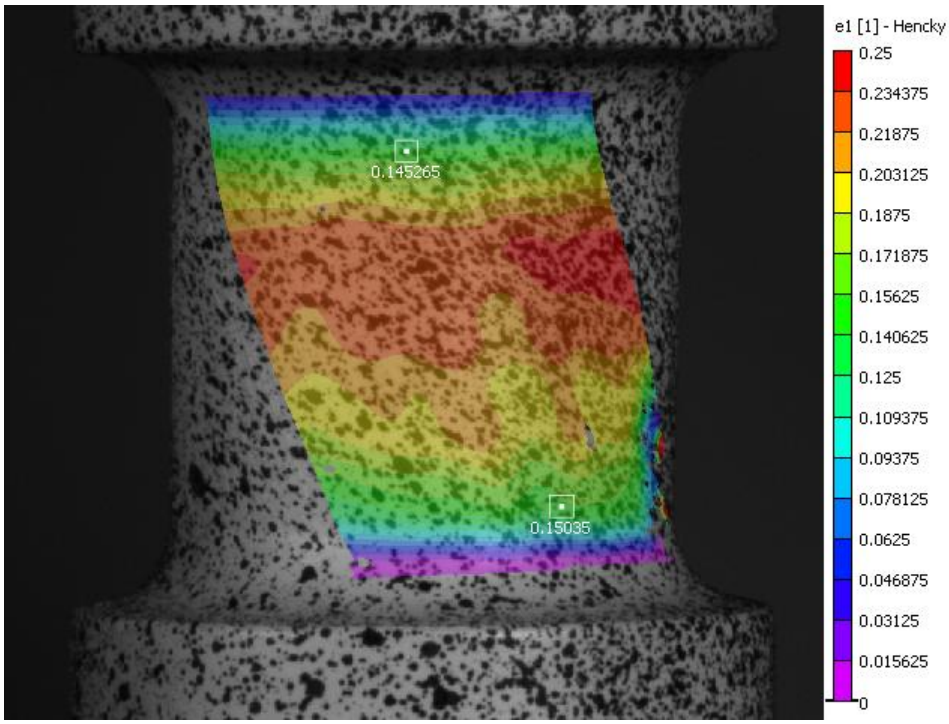

(b)

Figure E-37. The DIC Data From Test # M1-TMCL-LR3-P3-SR3-T1-N4: (a) Initial Tracking Point Positions on *y*-Coordinate Contour, (b) Tracking Point Positions Immediately Prior to Fracture on Maximum Principal Strain Contour

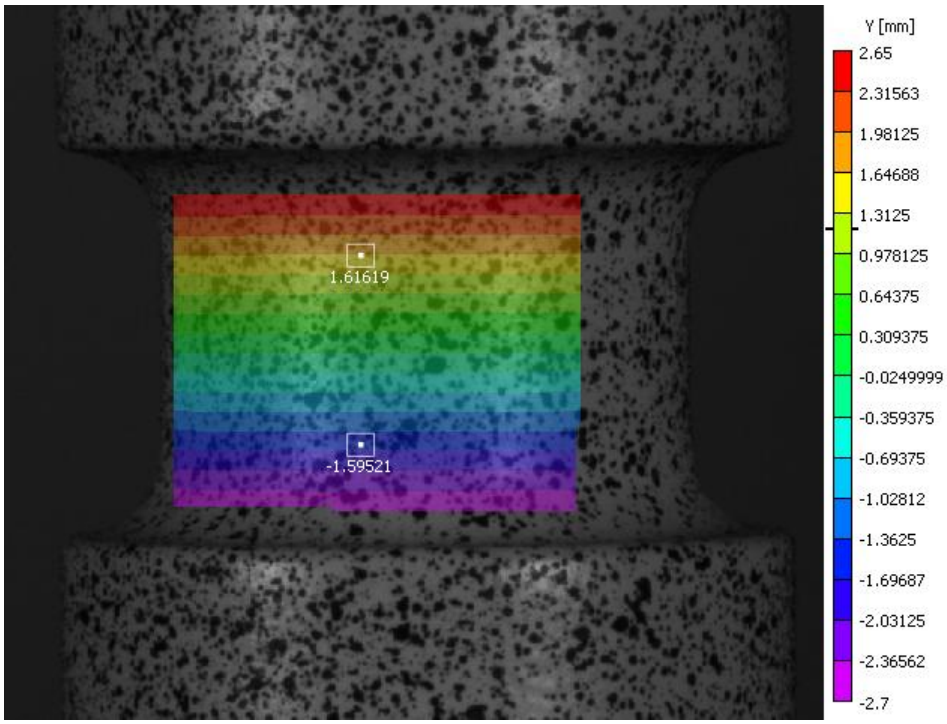

(a)

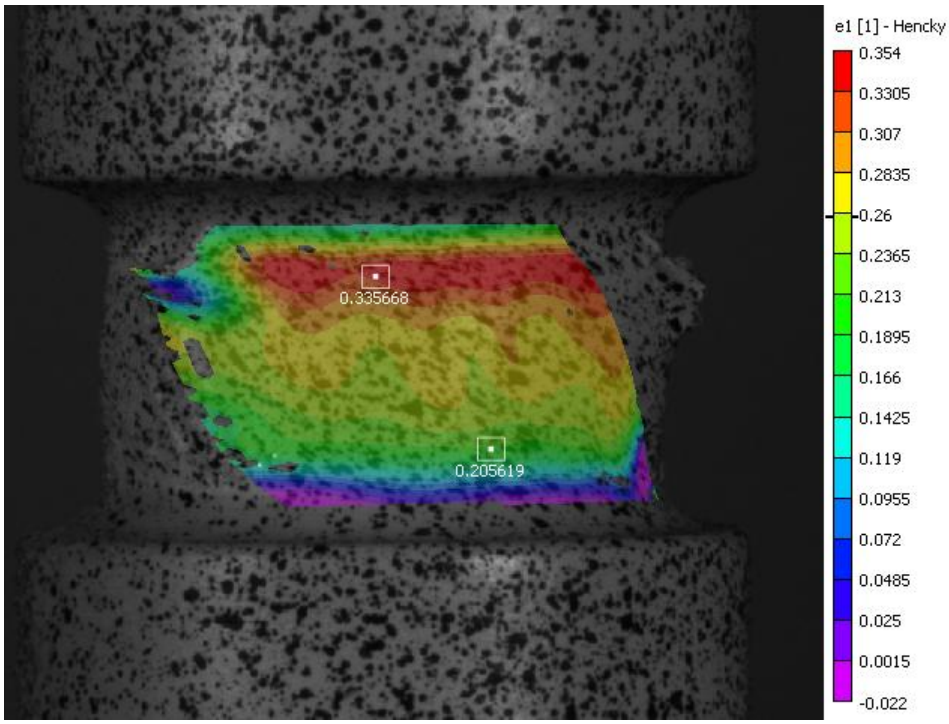

(b)

Figure E-38. The DIC Data From Test # M1-TMCL-LR4-P3-SR3-T1-N4: (a) Initial Tracking Point Positions on *y*-Coordinate Contour, (b) Tracking Point Positions Immediately Prior to Fracture on Maximum Principal Strain Contour

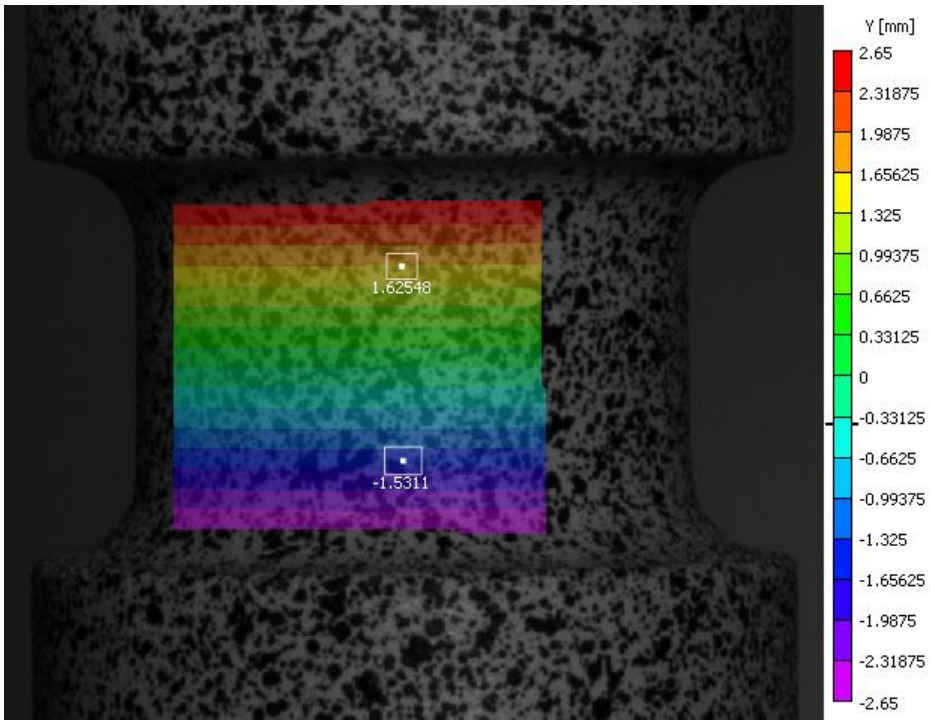

(a)

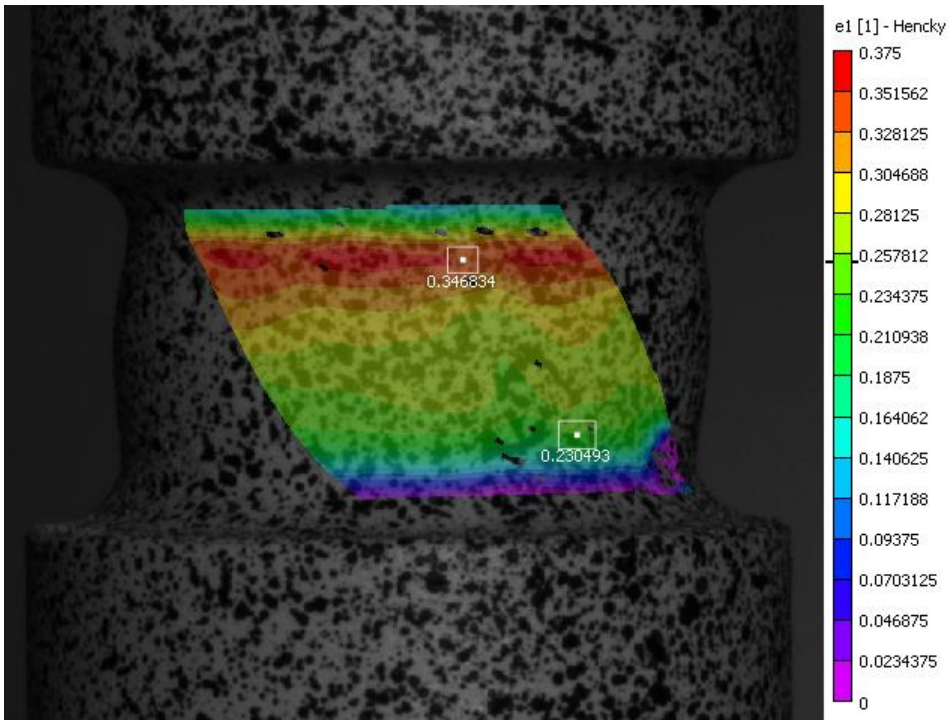

(b)

Figure E-39. The DIC Data From Test # M1-TMCL-LR4-P3-SR3-T1-N6: (a) Initial Tracking Point Positions on *y*-Coordinate Contour, (b) Tracking Point Positions Immediately Prior to Fracture on Maximum Principal Strain Contour

APPENDIX F—DATA TRANSFER PROCEDURE DOCUMENT

FAA Material Characterization Data Transfer Procedure

Presented to the Federal Aviation Administration

Jeremy D. Seidt

Amos Gilat

Dynamic Mechanics of Materials Laboratory (DMML)
http://www.mecheng.osu.edu/lab/dmm/
Department of Mechanical and Aerospace Engineering
The Ohio State University
Scott Laboratory
201 West 19th Ave.
Columbus, OH 43210

I: Introduction

This document is a data transfer procedure for the FAA Material Characterization Project. The intent is to ensure that the data from the tests conducted at OSU are transferred to the model developers at GWU in a consistent manner, eliminating confusion while developing and validating the material models. The several different types of tests conducted for this project are listed below. The tests are organized into two groups: 1) those required to characterize the constitutive behavior of the material and 2) those required to characterize the fracture behavior of the material.

Tests required to characterize the constitutive behavior include:

1) Tensile tests on thin, smooth dogbone samples:

    a. At five different strain rates: 1E-4 s^{-1}, 1E-2 s^{-1}, 1.0 s^{-1}, 500 s^{-1}, 1800 s^{-1}, at room temperature.

    b. At four different temperatures (three elevated temperatures and one low temperature) at a strain rate of 1.0 s^{-1}. The test temperatures are dependent on the material.

    c. Machined in four different orientations within the plate stock at room temperature and 1.0 s^{-1}.

2) Compression tests on cylindrical samples:

    a. At five different strain rates: 1E-4 s^{-1}, 1E-2 s^{-1}, 1.0 s^{-1}, 500 s^{-1}, 5000 s^{-1}, at room temperature.

    b. At four different temperatures (three elevated temperatures and one low temperature) at a strain rate of 1.0 s^{-1}. The test temperatures are dependent on the material.

    c. Machined in five different orientations within the plate stock at room temperature and 1.0 s^{-1}.

3) Torsion tests on thin-walled tube samples:

    a. At five different strain rates: 1E-4 s^{-1}, 1E-2 s^{-1}, 1.0 s^{-1}, 500 s^{-1}, 5000 s^{-1}, at room temperature.

    b. At four different temperatures (three elevated temperatures and one low temperature) at a strain rate of 1.0 s^{-1}. The test temperatures are dependent on the material.

Tests required to characterize the fracture behavior include:

1) Tensile tests on specimens with different geometries including:

    a. Thin, plane stress samples with three different notch radii

    b. Axisymmetric specimens with six different geometries (one with a smooth gage section and five with different notch radii)

    c. Thick, plane strain samples with three different geometries (one with a smooth gage section and two with different notch radii)

2) Combined axial-torsional tests on thin-walled tubes. Four stress states are required: two tension-torsion tests with different ratios of axial stress to shear stress, one pure shear stress state, and one compression-torsion test.

3) Punch tests on flat disk specimens.

The next section of this document identifies essential data that must be transferred for each of the tests summarized above. Finally, the Procedure section of this document briefly describes the format of the data to be transferred and the method of transfer.

<u>II: Essential Data</u>

1. Constitutive Test Series

    a. Tension Tests:

        i. Test Information:

            1. Specimen origin: specifies the stock from which the sample was cut.

            2. Specimen dimensions:

                a. Gage thickness (mm)
                b. Gage width (mm)
                c. Gage length (mm)

            3. Specimen orientation within the material stock. Both the longitudinal and width directions of the specimen will be provided.

            4. Specimen temperature at the time of test.

            5. Average strain rate during the test.

ii. Data

1. Time (s)
2. Load (N)
3. Displacement (mm)

a. Low rate tests ($\dot{\varepsilon} \leq 1.0\ s^{-1}$):

i. If digital image correlation (DIC) data is available: Relative displacement from a DIC extensometer. Initial extensometer gage length (mm) and positions (.jpg image) will also be provided.

ii. If DIC data is not available: data from a 4-mm extensometer will be provided.

iii. For elevated or low temperature tests: hydraulic load frame actuator displacement.

b. High rate tests ($\dot{\varepsilon} \geq 400\ s^{-1}$), from Hopkinson bar wave data reduction.

b. Compression Tests

i. Test information:

1. Specimen origin: specifies the stock from which the sample was cut.

2. Specimen dimensions:

a. Diameter (mm)
b. Length (mm)

3. Specimen orientation within the material stock. The orientation of the specimen's axis of symmetry will be provided.

4. Specimen temperature at the time of test.

5. Average strain rate during the test.

ii. Data:

1. Time (s)
2. Load (N)

3. Displacement (mm)

    a. Low rate tests ($\dot{\varepsilon} \leq 1.0\ s^{-1}$):

        i. If DIC data is available: relative displacement from a DIC extensometer. Initial extensometer gage length (mm) and positions (.jpg image) will also be provided.

        ii. If DIC data is not available: data from a linear variable differential transformer (LVDT) in a custom fixture designed for compression tests will be provided.

        iii. For elevated or low-temperature tests: hydraulic load frame actuator displacement.

    b. High rate tests ($\dot{\varepsilon} \geq 400\ s^{-1}$), from Hopkinson bar wave data reduction.

c. Torsion Tests

    i. Test information:

        1. Specimen origin: specifies the stock from which the sample was cut.

        2. Specimen dimensions:

            a. Inside Diameter (mm)
            b. Outside Diameter (mm)
            c. Length (mm)

        3. Specimen orientation. The orientation of the specimen's axis of symmetry will be provided.

        4. Specimen temperature at the time of test.

        5. Average strain rate during the test.

    ii. Data:

        1. Time (s)
        2. Torque (N-m)
        3. Rotation (deg)

a. Low rate tests ($\dot{\gamma} \leq 1.73\ s^{-1}$)

i. If DIC data is available: relative rotation between two points on the surface of the sample. Point positions will be provided in a .jpg image.

ii. If DIC data is not available: rotation data from a LVDT in a custom fixture designed for torsion tests will be provided.

iii. For elevated or low temperature tests: hydraulic load frame actuator rotation.

b. High rate tests ($\dot{\gamma} \geq 400\ s^{-1}$), from Hopkinson bar wave data reduction.

2. Fracture Test Series

a. Tension tests

i. Test information:

1. Specimen origin: specifies the stock from which the sample was cut.

2. Specimen Dimensions.

a. Plane stress notched samples:

i. Thickness (mm)
ii. Minimum notch width (mm)
iii. Notch radius (mm)

b. Axisymmetric smooth samples:

i. Diameter (mm)
ii. Length (mm)

c. Axisymmetric notched samples:

i. Minimum notch diameter (mm)
ii. Notch radius (mm)

d. Plane strain smooth samples:

i. Thickness (mm)
ii. Width (mm)
iii. Length (mm)

e. Plane strain notched samples:

i. Thickness (mm)
ii. Minimum notch width (mm)
iii. Notch radius (mm)

3. Specimen orientation

a. Plane stress samples: both the longitudinal and width directions of the specimen will be provided.

b. Axisymmetric samples: the orientation of the specimen's axis of symmetry will be provided.

c. Plane strain samples: both the longitudinal and width directions of the specimen will be provided.

ii. Data:

1. Time (s).

2. Load (N).

3. Displacement (mm), relative displacement from a DIC extensometer. Initial extensometer gage length (mm) and positions (.jpg image) will also be provided.

b. Combined axial-torsional tests

i. Test Information:

1. Specimen origin: specifies the stock from which the sample was cut.

2. Specimen dimensions

a. Inside diameter (mm)
b. Outside diameter (mm)
c. Length (mm)

3. Specimen orientation. The orientation of the specimen's axis of symmetry will be provided.

4. Axial stress to shear stress ratio.

ii. Data:

1. Time (s).

2. Load (N).

3. Torque (N-m).

4. Displacement (mm), relative displacement from a DIC extensometer. Initial extensometer gage length (mm) and positions (.jpg image) will also be provided.

5. Rotation (deg), relative rotation between two points on the surface of the sample. Point positions will be provided in a .jpg image.

c. Punch Tests:

i. Test Information:

1. Specimen origin.

2. Specimen Dimensions:

a. Thickness (mm)
b. Diameter (mm)

3. Specimen orientation: normal direction of the disk specimen will be provided.

4. Punch radius (mm).

5. Average relative punch velocity (m/s).

ii. Data:

1. Time (s)

2. Load (N)

3. Displacement (mm):

a. From DIC data for low rate tests
b. From Hopkinson bar wave data reduction

III: Procedure

Each experiment will have its own spreadsheet that contains both the test information and the essential data outlined above. The spreadsheet will contain two worksheets: one summarizing the test information (specimen origin and orientation, dimensions, test temperature, average strain rate, etc.) while the other contains the data (time, load, displacement, etc.). The data file will be archived in .zip files so that each test has its own directory. The directory will contain the data/test-information spreadsheet and additional test information, such as still images and movie files.

The method of data transfer is TBD. Potential data-transfer methods are listed below.

1) The data archive can be uploaded to the National Aeronautics and Space Administration (NASA) Glenn Ballistic Impact Lab Data Archive on the GRC – NASA Materials & Structure Collaboration Project (CMC Wiki). A user account is required to access the Wiki.

2) The data archive can be uploaded to the OSU Dynamic Mechanics of Materials website.

APPENDIX G—REPEATABILITY OF THE EXPERIMENTAL DATA FROM THE PLASTIC DEFORMATION TEST SERIES

The data transfer procedure (appendix C) specifies the required data to be transferred to The George Washington University (GWU) National Crash Analysis Center. For tension and compression tests from the constitutive model test series, the required test data are axial load and displacement. For torsion tests, the required data are torque and rotation. Plots of force versus displacement curves and torque versus rotation curves that were transferred to GWU are presented in this appendix. The actual specimen dimensions are also important because the specimens are so small that even small changes in the thickness from specimen to specimen can cause measureable differences in the measured forces and torques. Therefore, the actual specimen dimensions from each experiment are presented also.

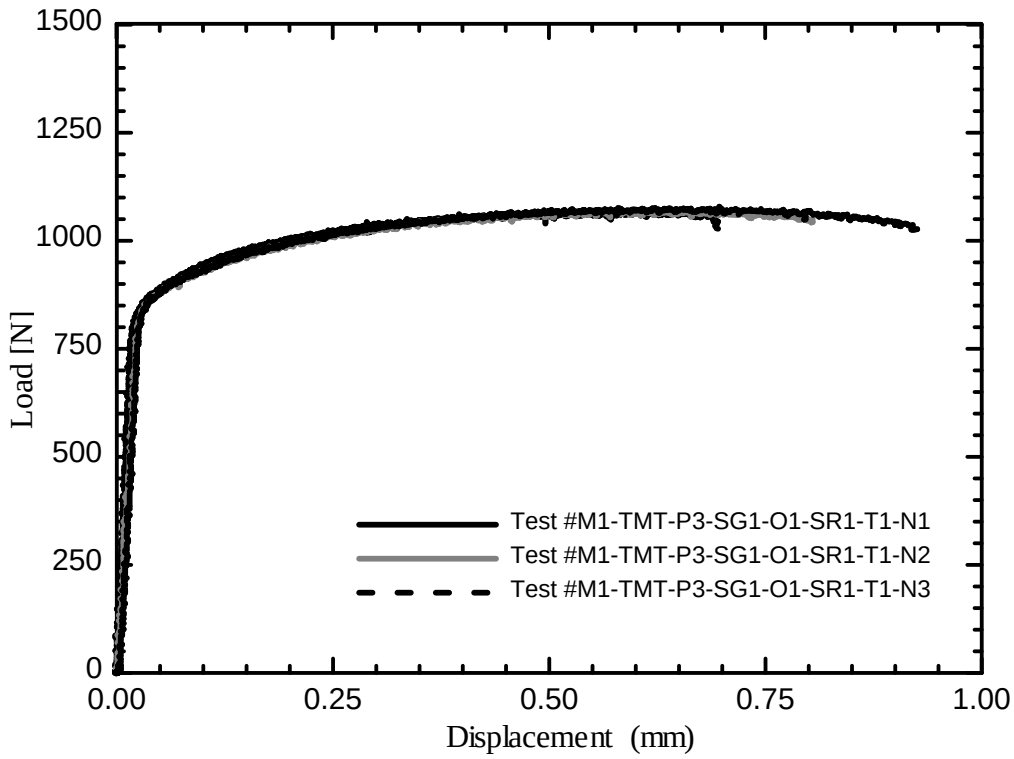

Figure G-1. Tension Data, Strain Rate: $1x10^{-4}$ s^{-1}, Room Temperature, and Rolled Direction

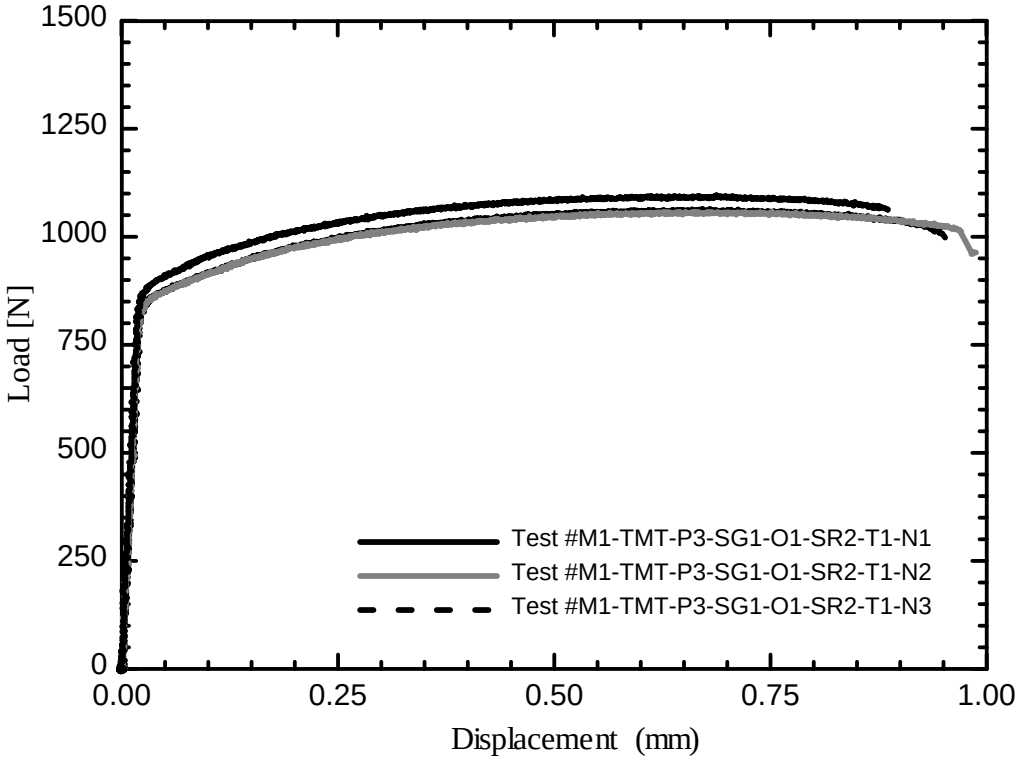

Figure G-2. Tension Data, Strain Rate $1x10^{-2}$ s^{-1}, Room Temperature, and Rolled Direction

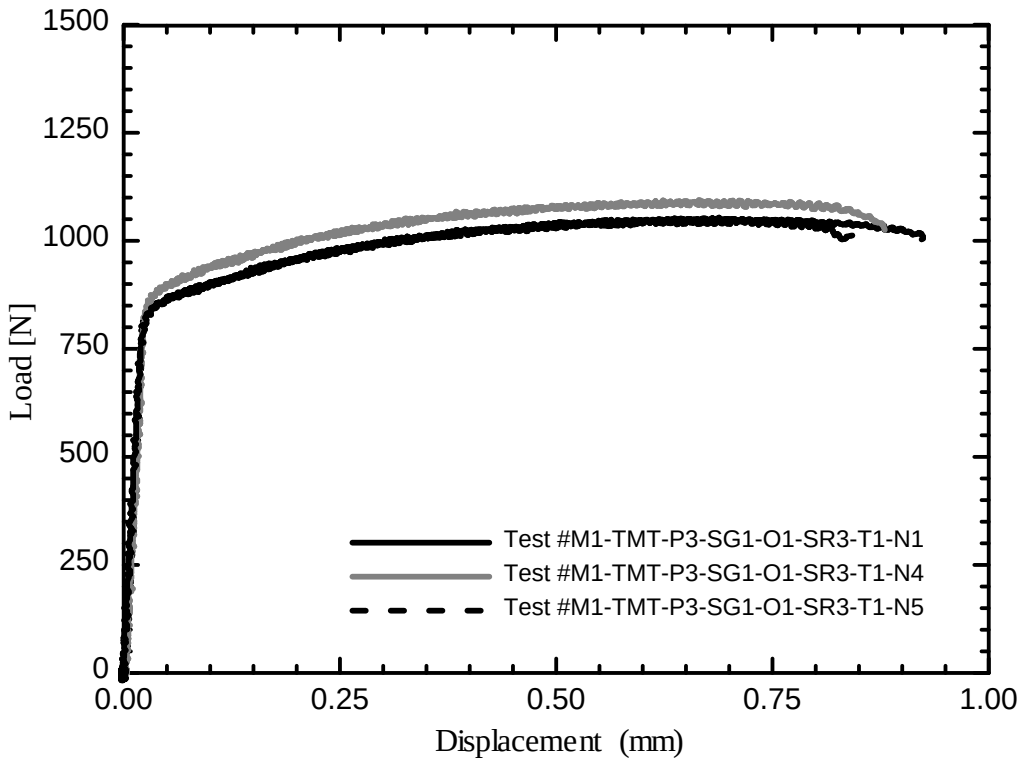

Figure G-3. Tension Data, Strain Rate 1.0 s^{-1}, Room Temperature, and Rolled Direction

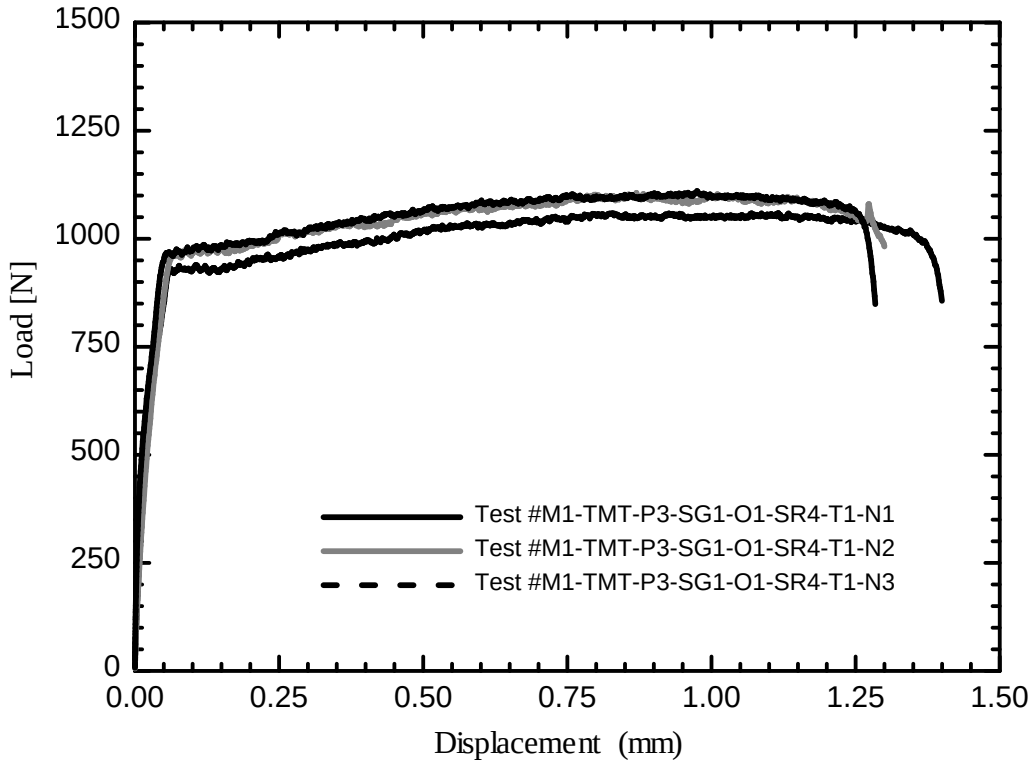

Figure G-4. Tension Data, Strain Rate 500.0 s^{-1}, Room Temperature, and Rolled Direction

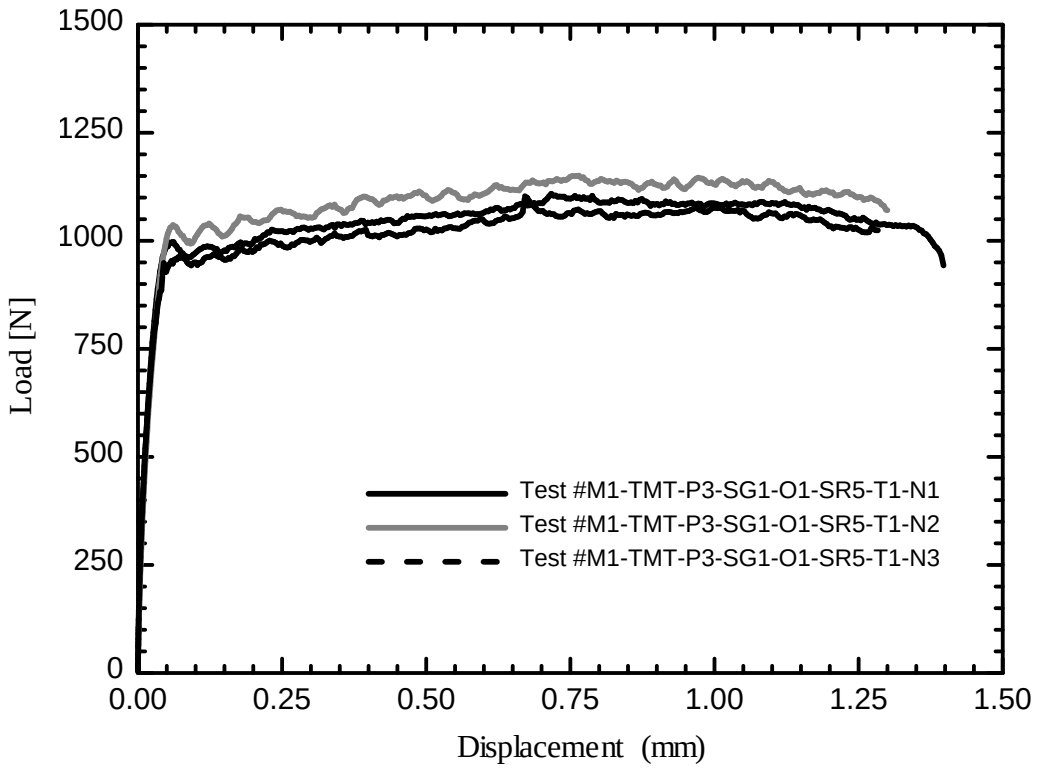

Figure G-5. Tension Data, Strain Rate 1800.0 s^{-1}, Room Temperature, and Rolled Direction

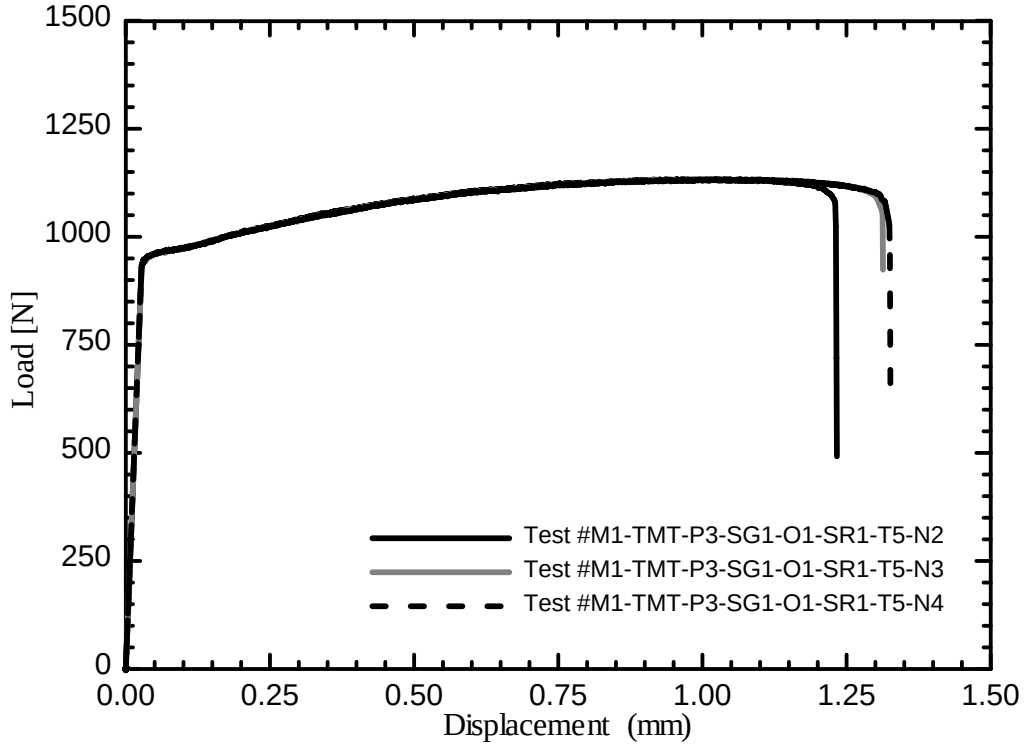

Figure G-6. Tension Data, Strain Rate 1.0 s^{-1}, -50°C, and Rolled Direction

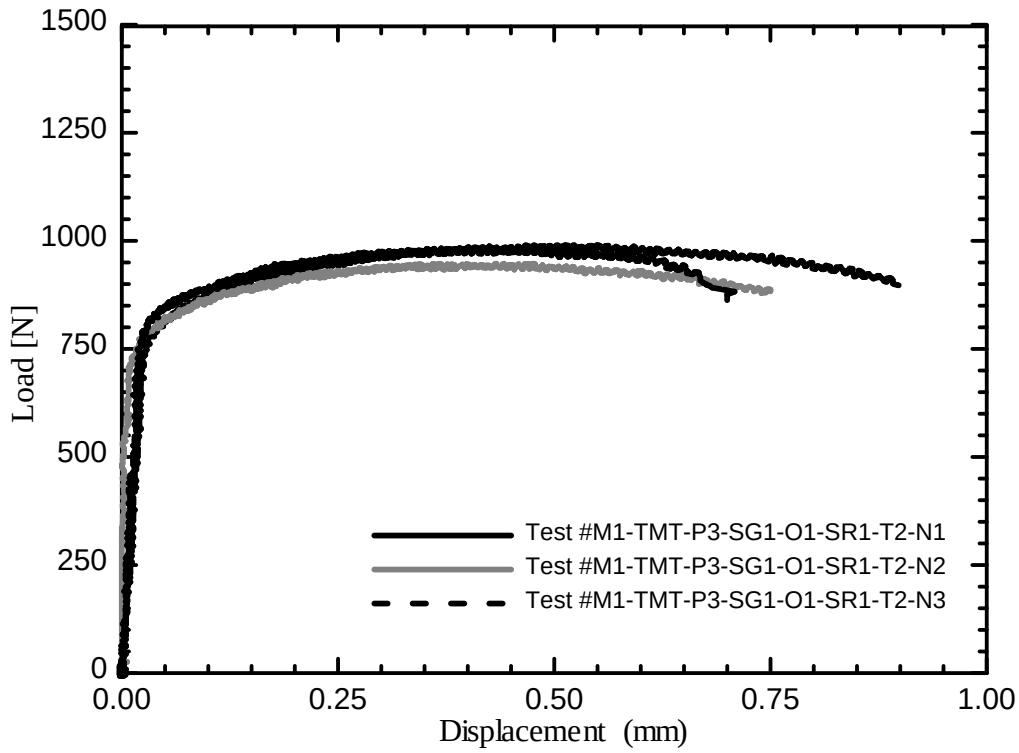

Figure G-7. Tension Data, Strain Rate 1.0 s^{-1}, 150°C, and Rolled Direction

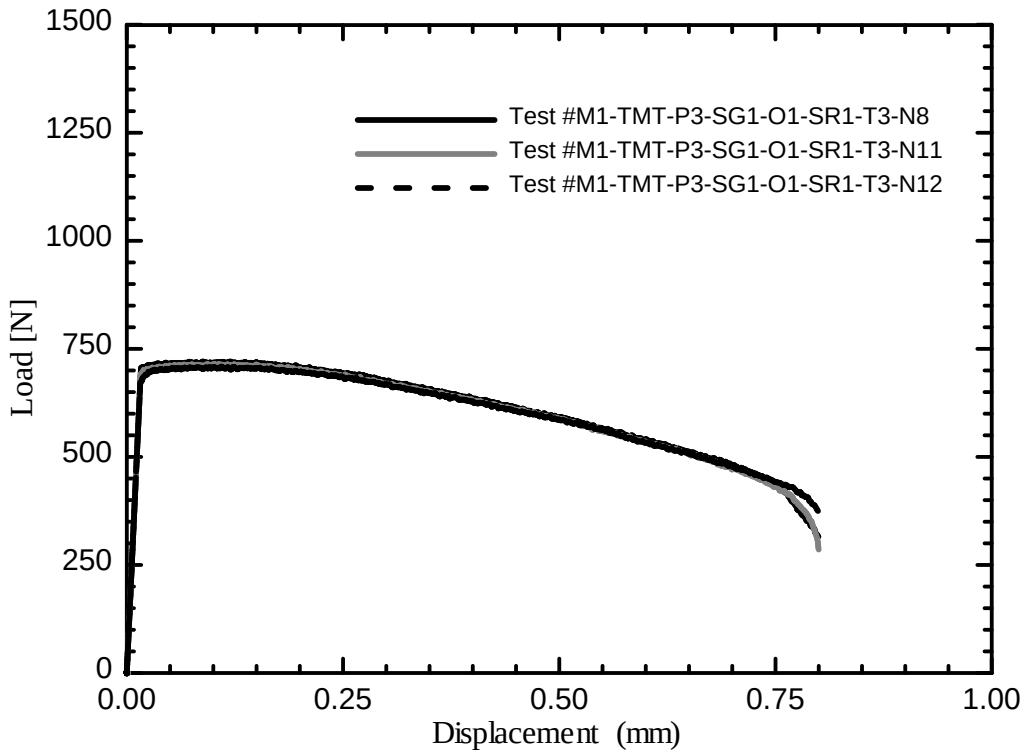

Figure G-8. Tension Data, Strain Rate 1.0 s^{-1}, 300°C, and Rolled Direction

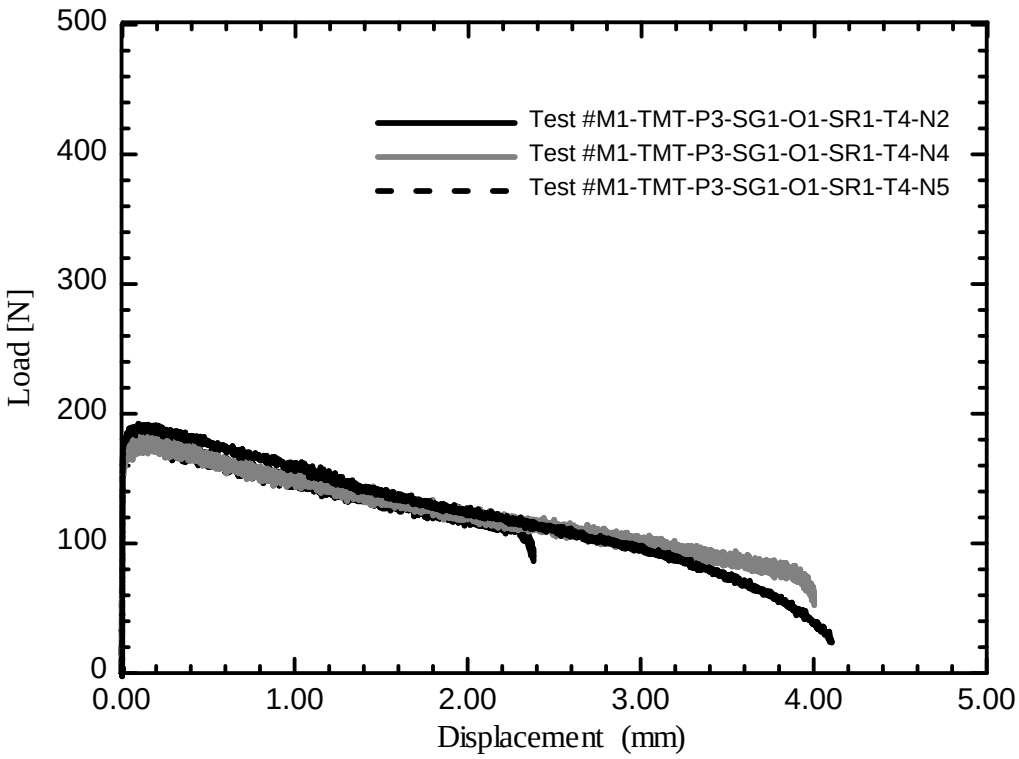

Figure G-9. Tension Data, Strain Rate 1.0 s^{-1}, 450°C, and Rolled Direction

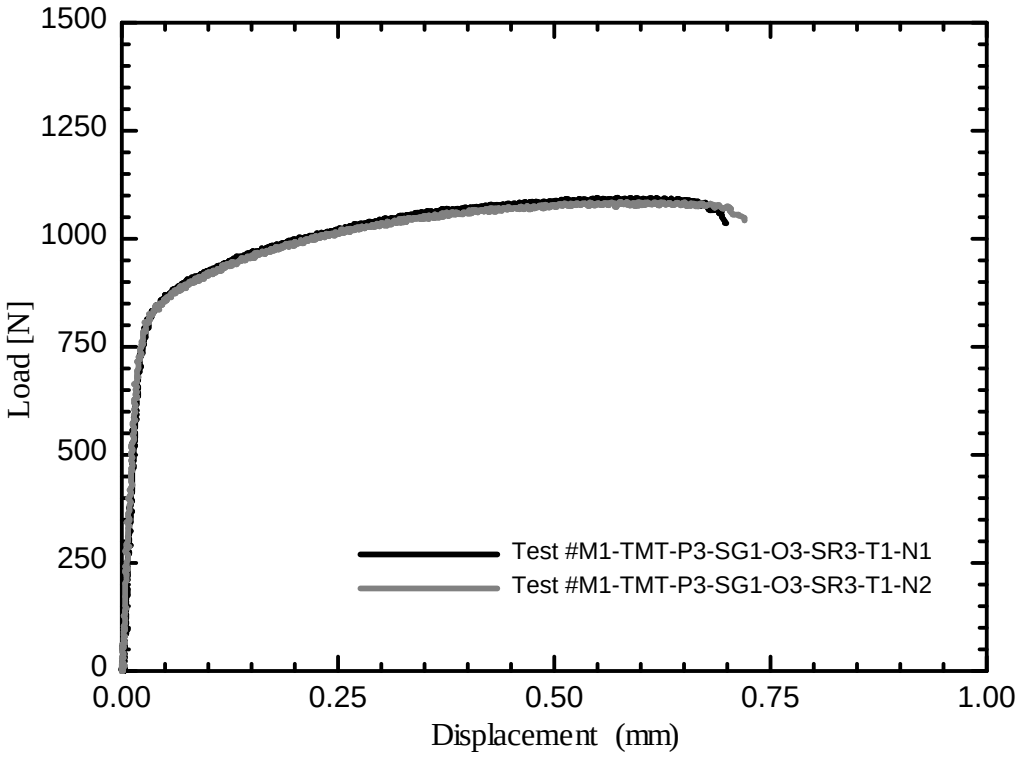

Figure G-10. Tension Data, Strain Rate 1.0 s^{-1}, Room Temperature, and Transverse Direction

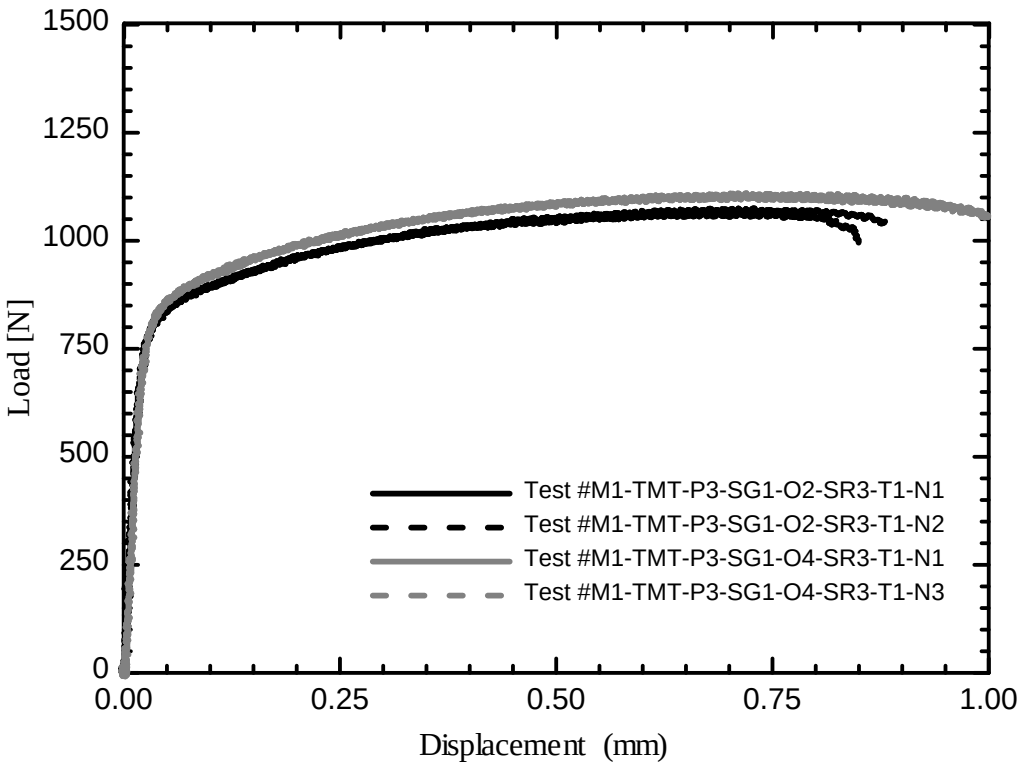

Figure G-11. Tension Data, Strain Rate: 1.0 s^{-1}, Room Temperature, and ±45° Direction

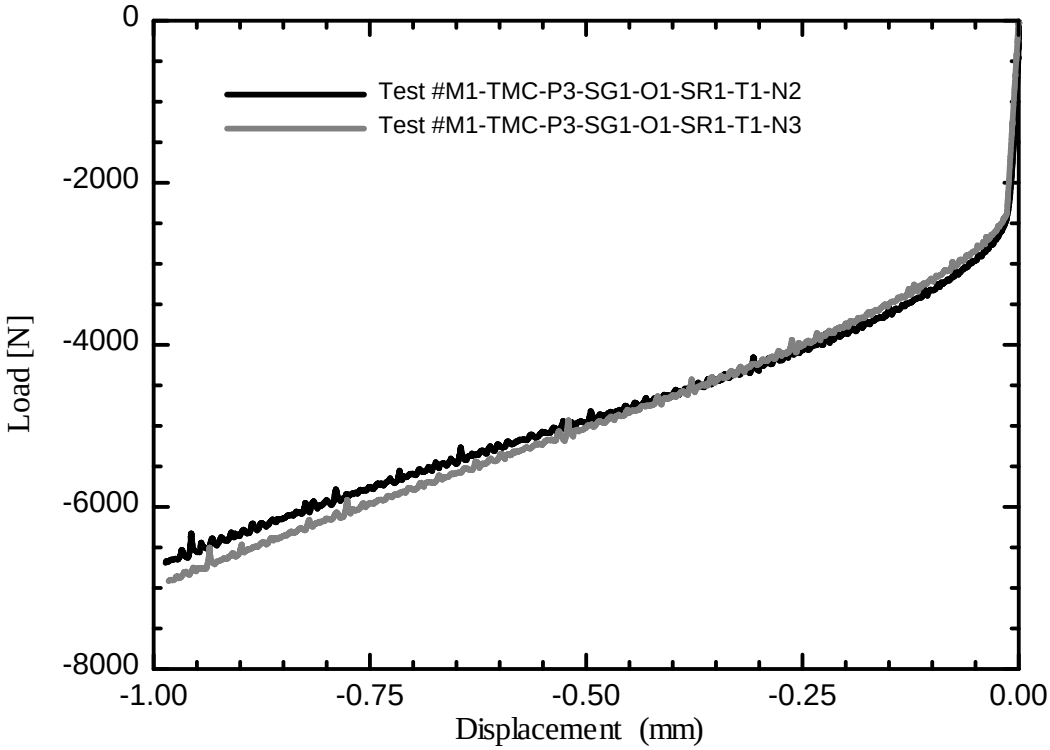

Figure G-12. Compression Data, Strain Rate $1x10^{-4}$ s^{-1}, Room Temperature, and Rolled Direction

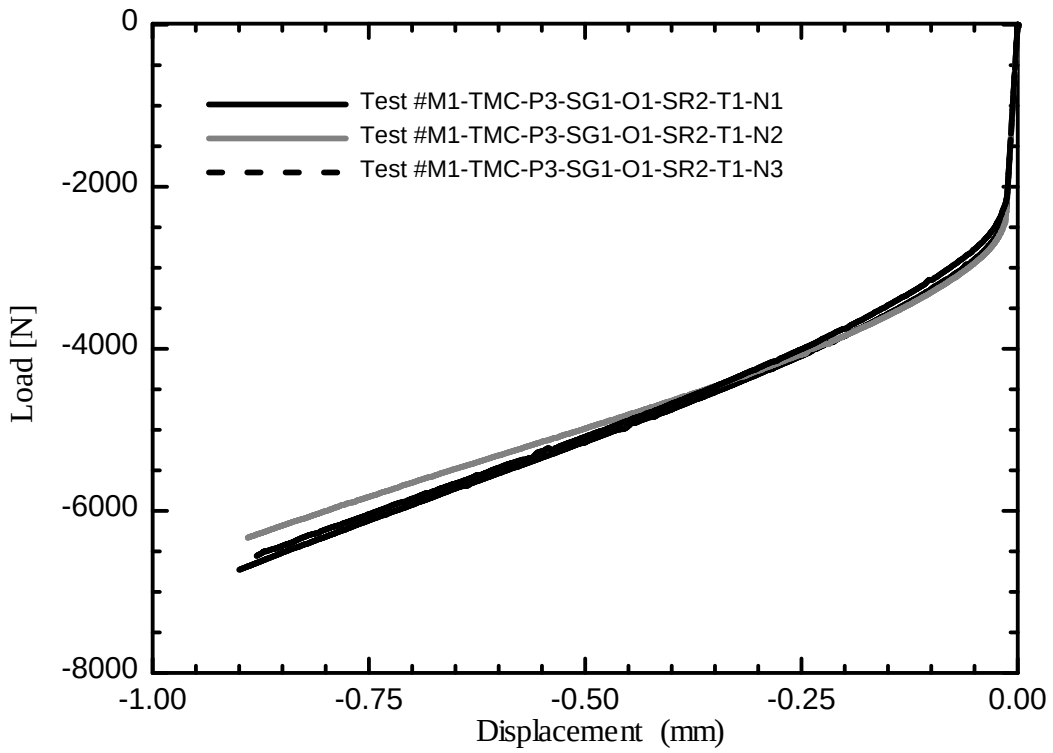

Figure G-13. Compression Data, Strain Rate $1x10^{-2}$ s^{-1}, Room Temperature, and Rolled Direction

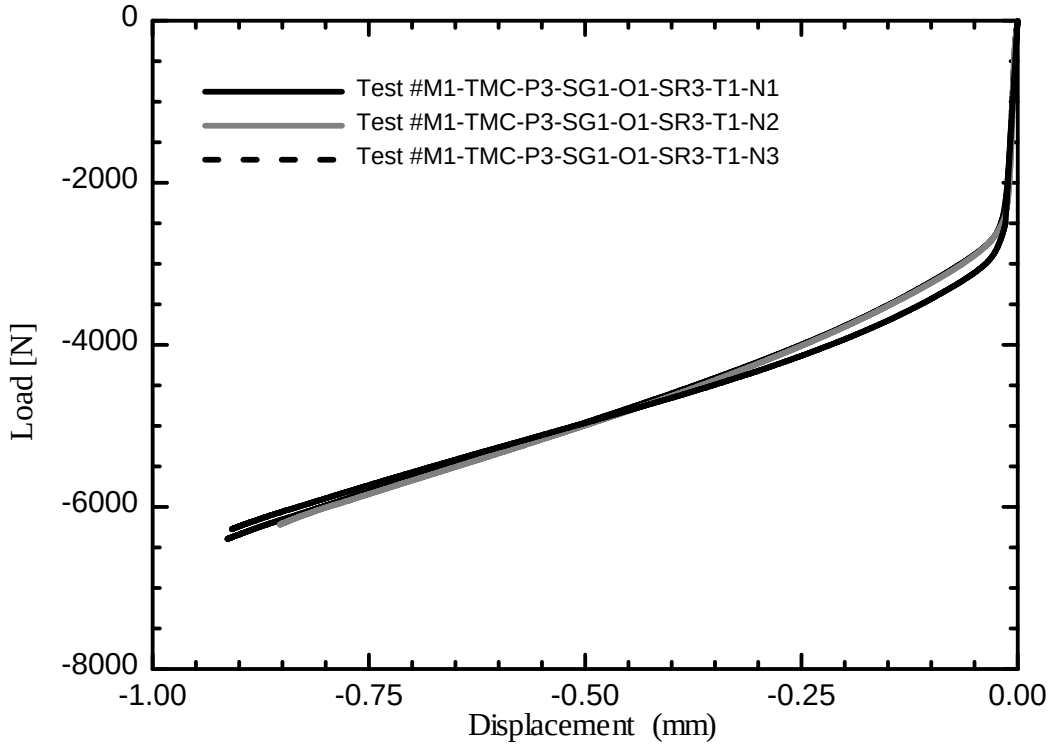

Figure G-14. Compression Data, Strain Rate 1.0 s^{-1}, Room Temperature, and Rolled Direction

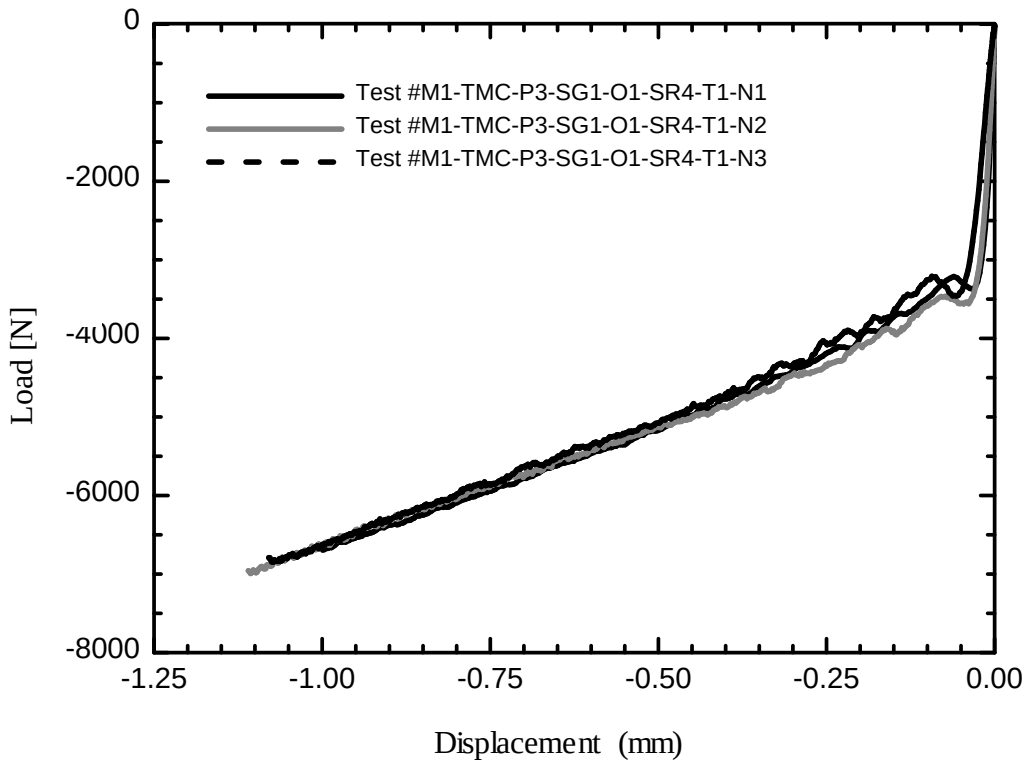

Figure G-15. Compression Data, Strain Rate 1500.0 s^{-1}, Room Temperature, and Rolled Direction

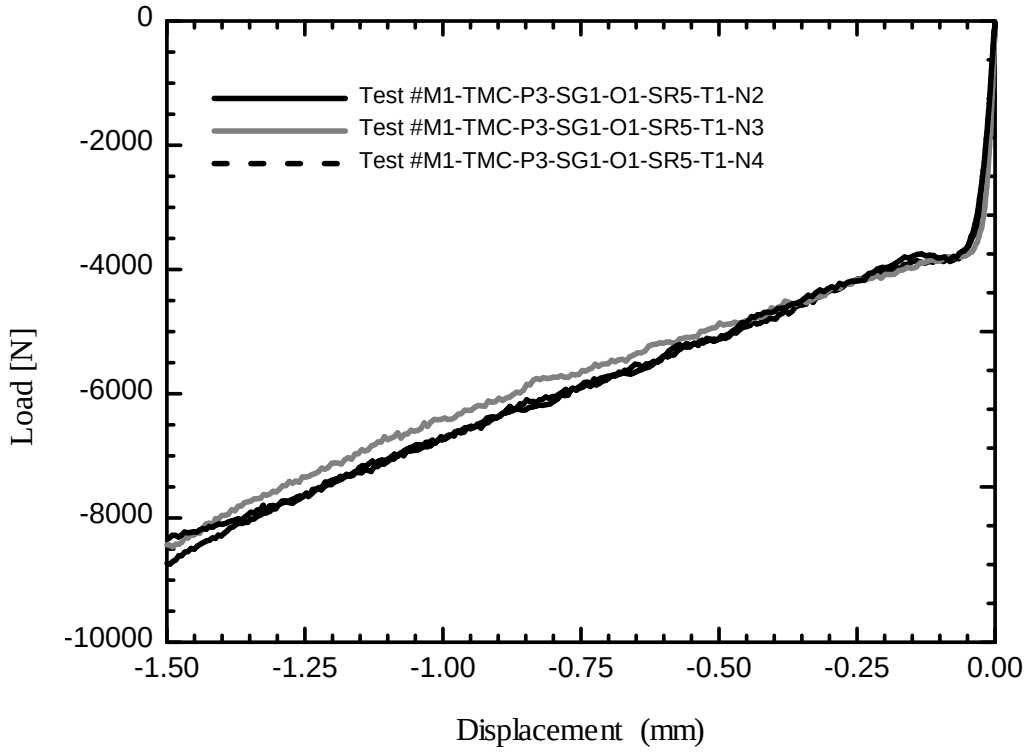

Figure G-16. Compression Data, Strain Rate 5000.0 s^{-1}, Room Temperature, and Rolled Direction

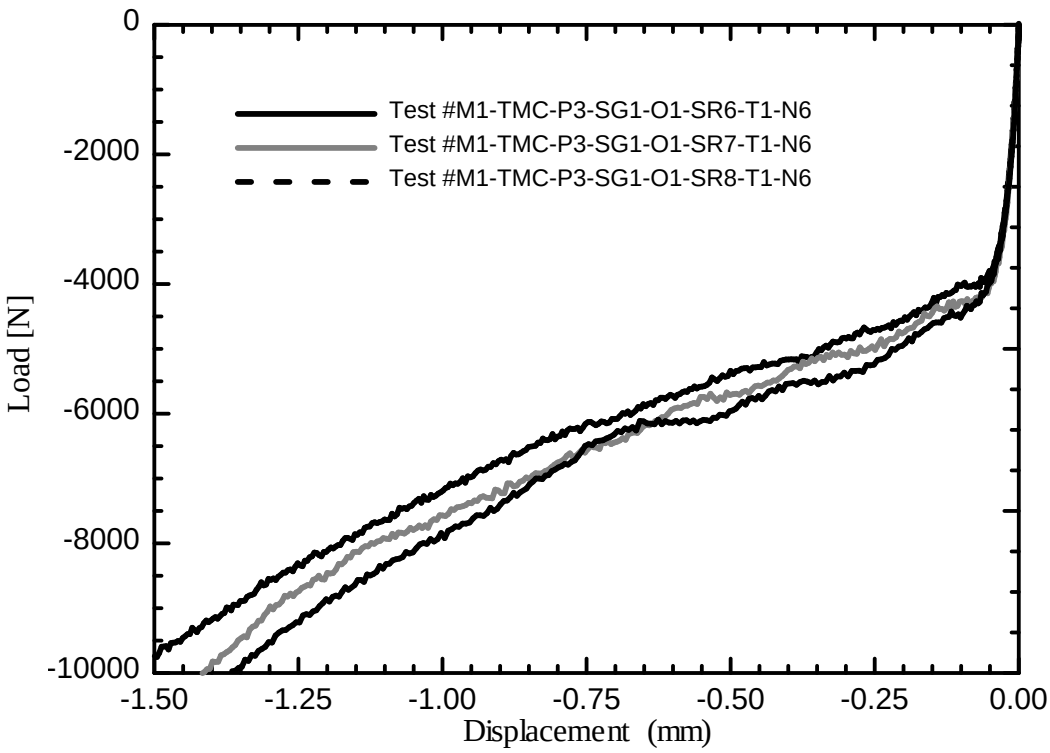

Figure G-17. Compression Data, Strain Rate 8000.0 to 11000.0 s^{-1}, Room Temperature, and Rolled Direction

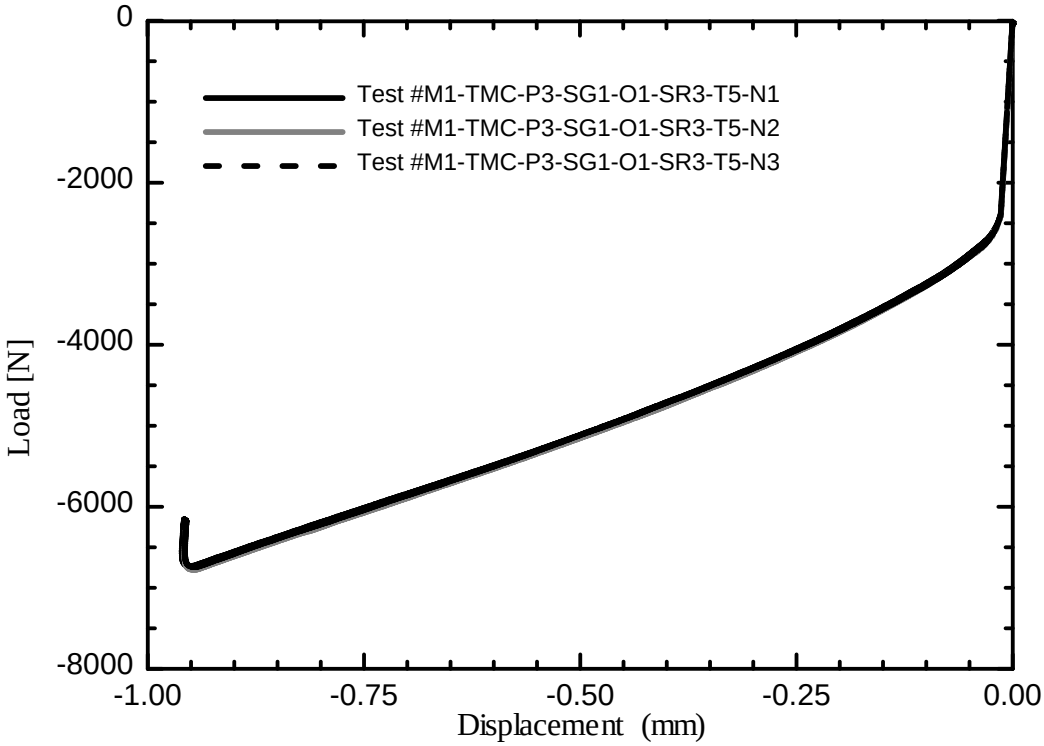

Figure G-18. Compression Data, Strain Rate 1.0 s^{-1}, -50°C, Rolled Direction

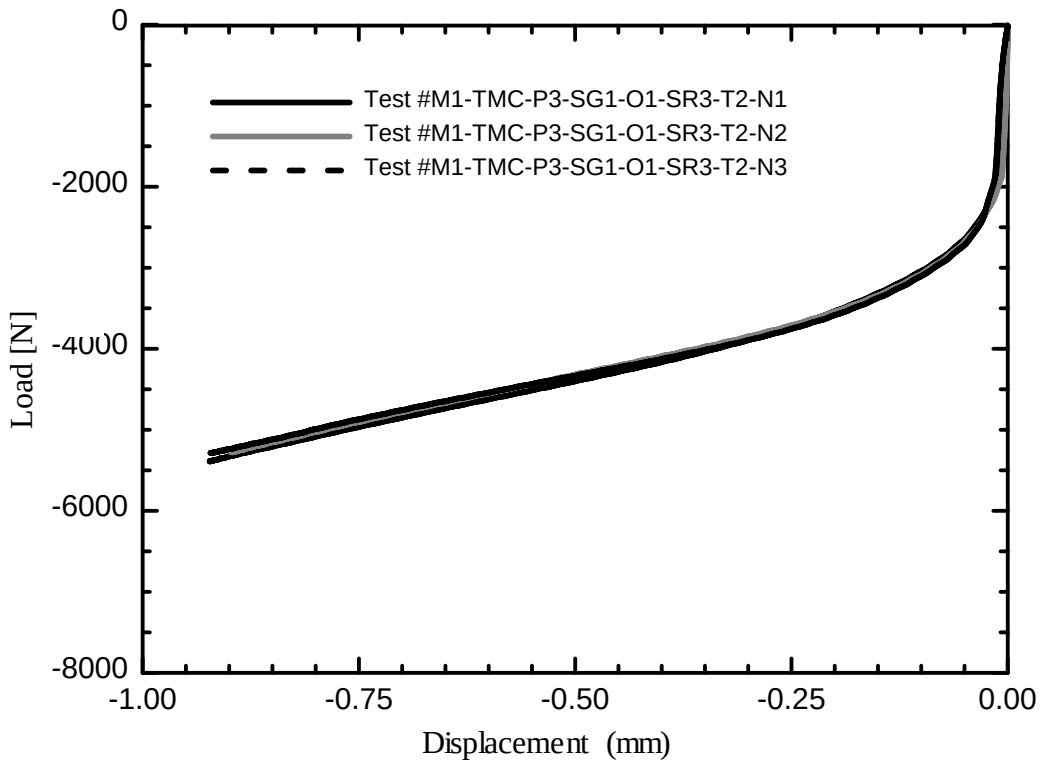

Figure G-19. Compression Data, Strain Rate 1.0 s^{-1}, 150°C, Rolled Direction

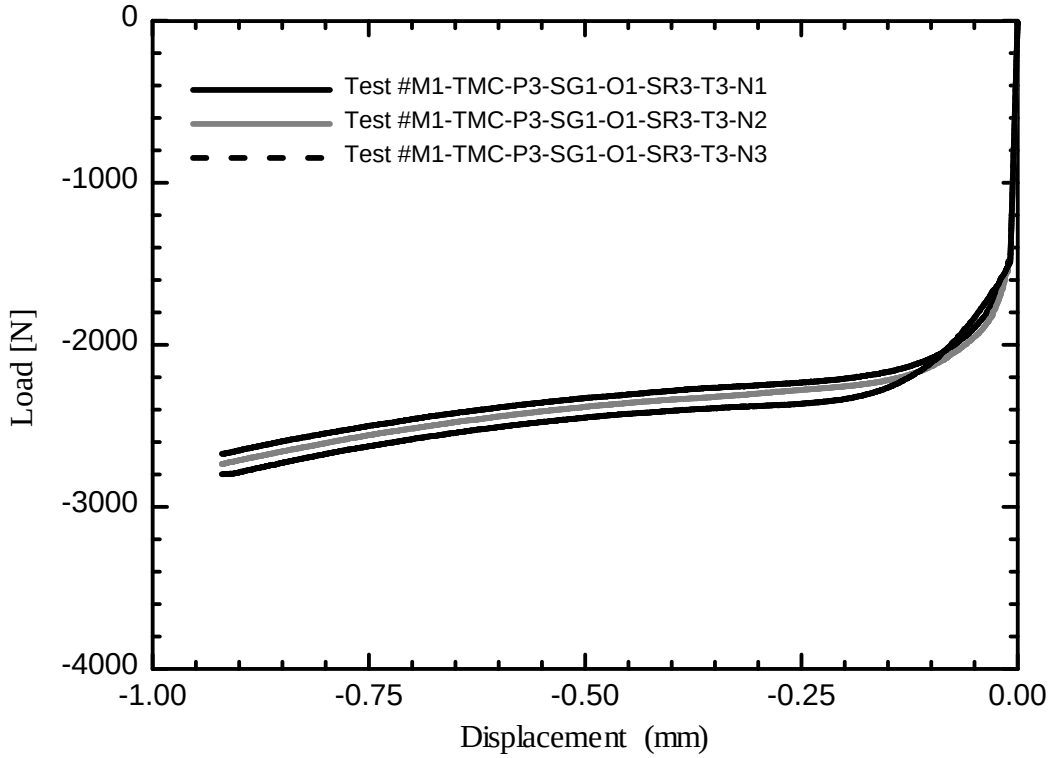

Figure G-20. Compression Data, Strain Rate 1.0 s^{-1}, 300°C, Rolled Direction

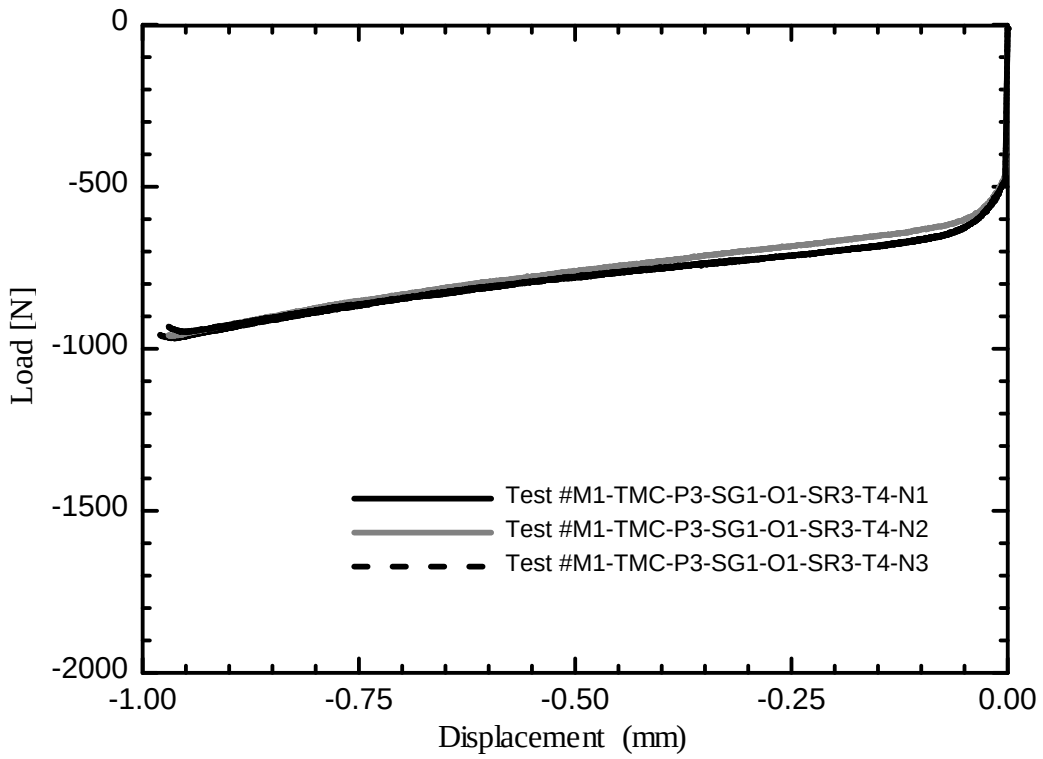

Figure G-21. Compression Data, Strain Rate 1.0 s^{-1}, 450°C, Rolled Direction

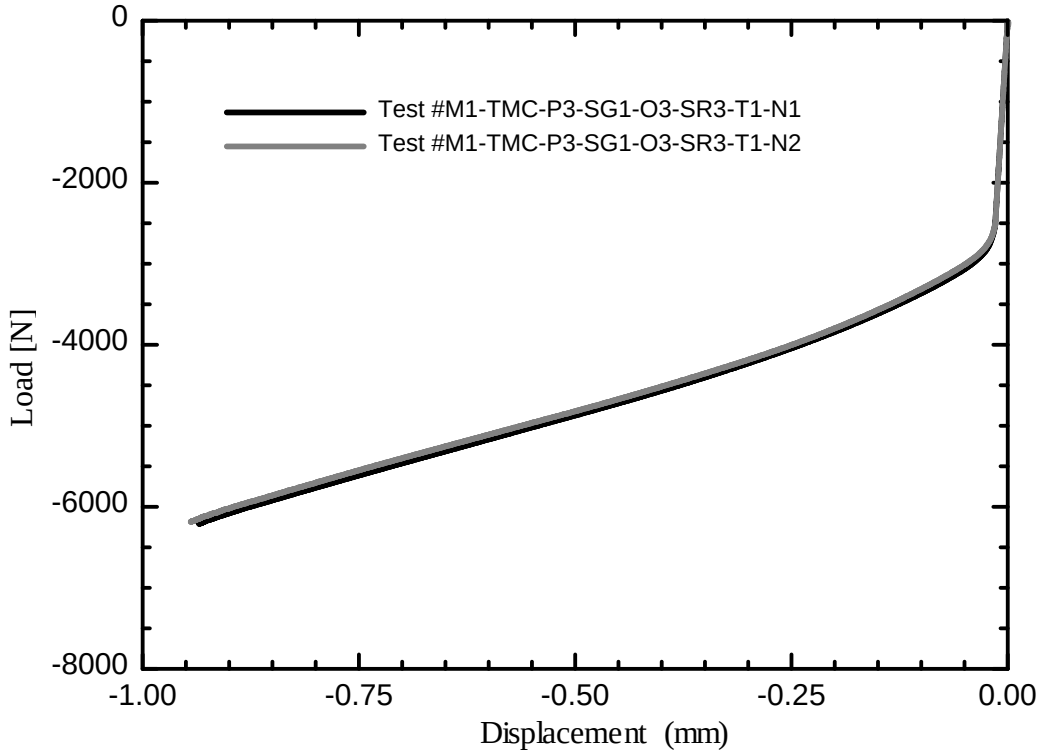

Figure G-22. Compression Data, Strain Rate 1.0 s^{-1}, Room Temperature, Transverse Direction

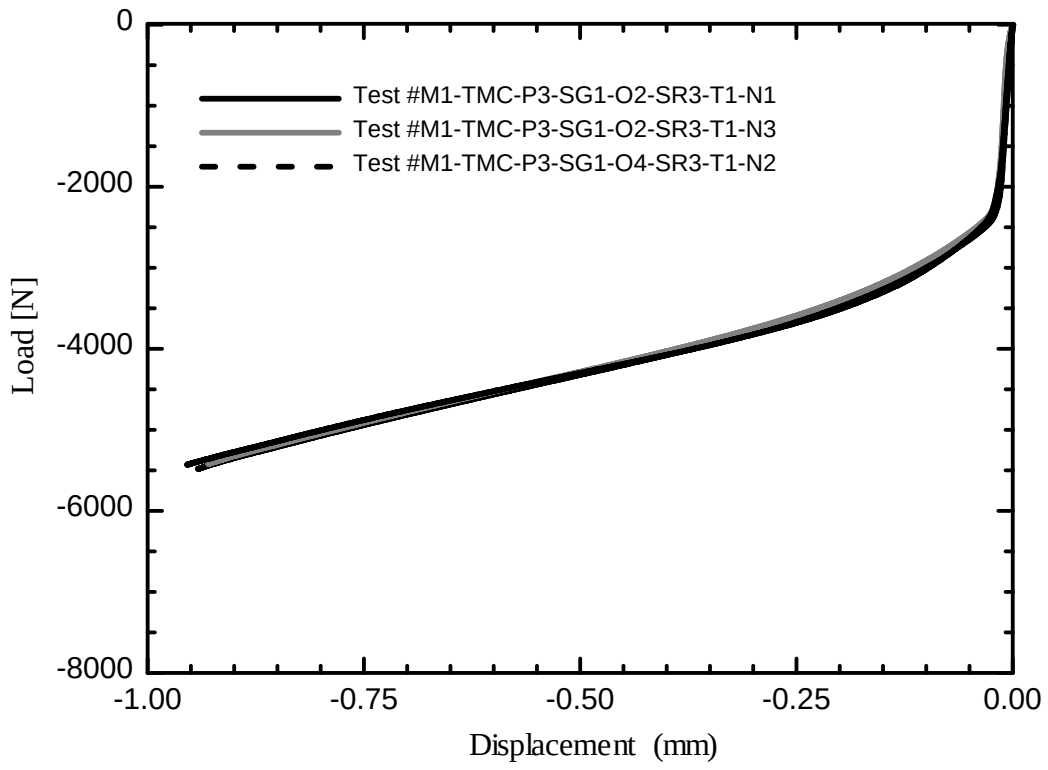

Figure G-23. Compression Data, Strain Rate 1.0 s^{-1}, Room Temperature, ±45° Direction

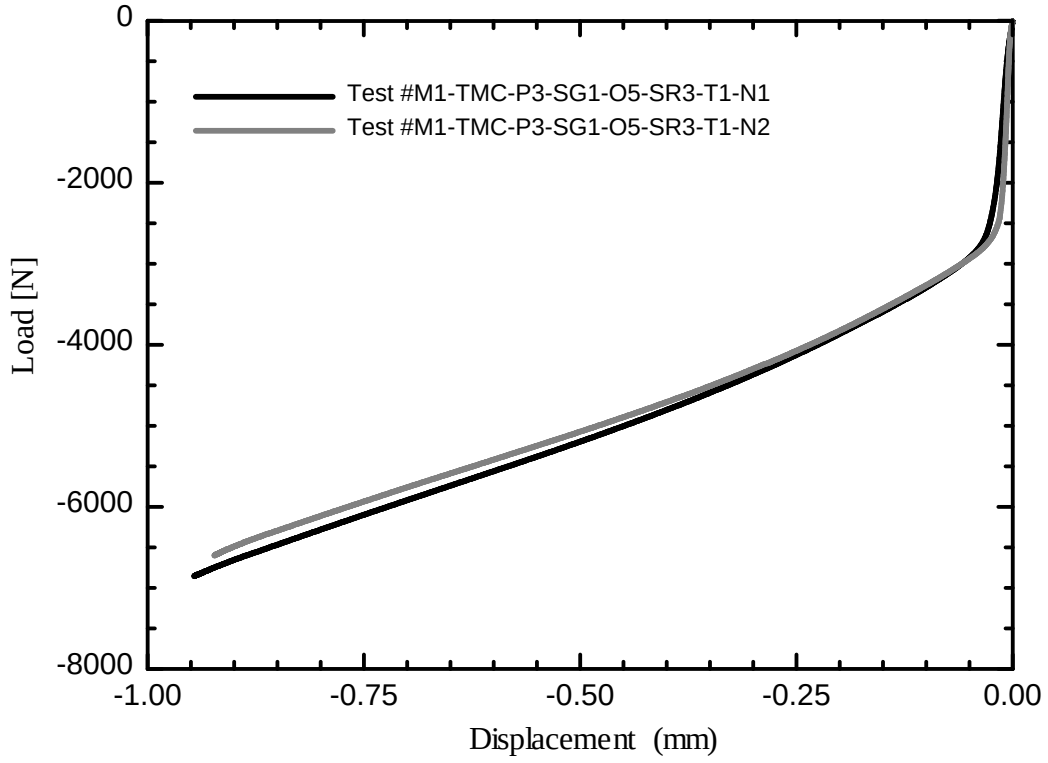

Figure G-24. Compression Data, Strain Rate 1.0 s^{-1}, Room Temperature, Thickness Direction

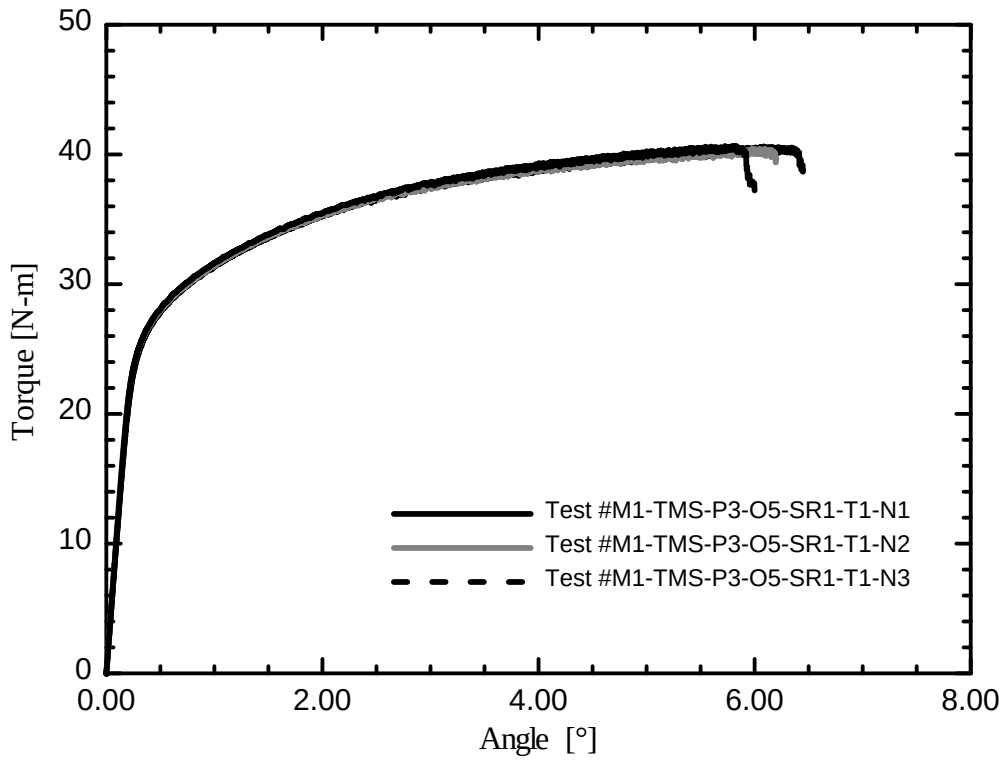

Figure G-25. Torsion Data, Strain Rate $1x10^{-4}$ s^{-1}, Room Temperature

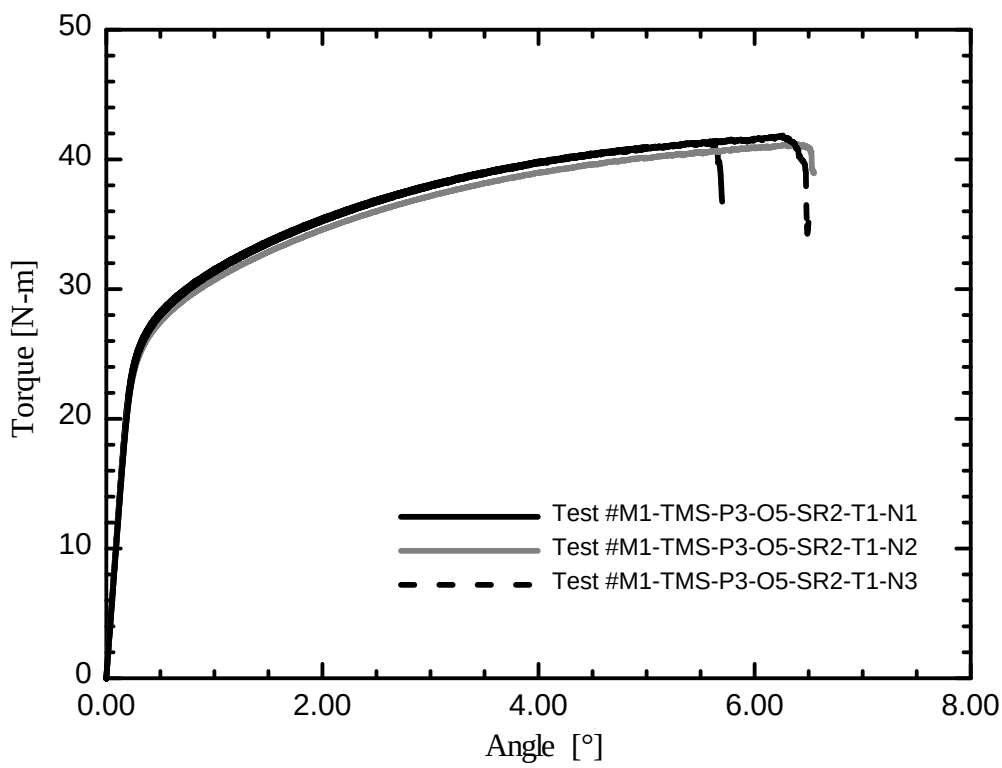

Figure G-26. Torsion Data, Strain Rate $1x10^{-2}$ s^{-1}, Room Temperature

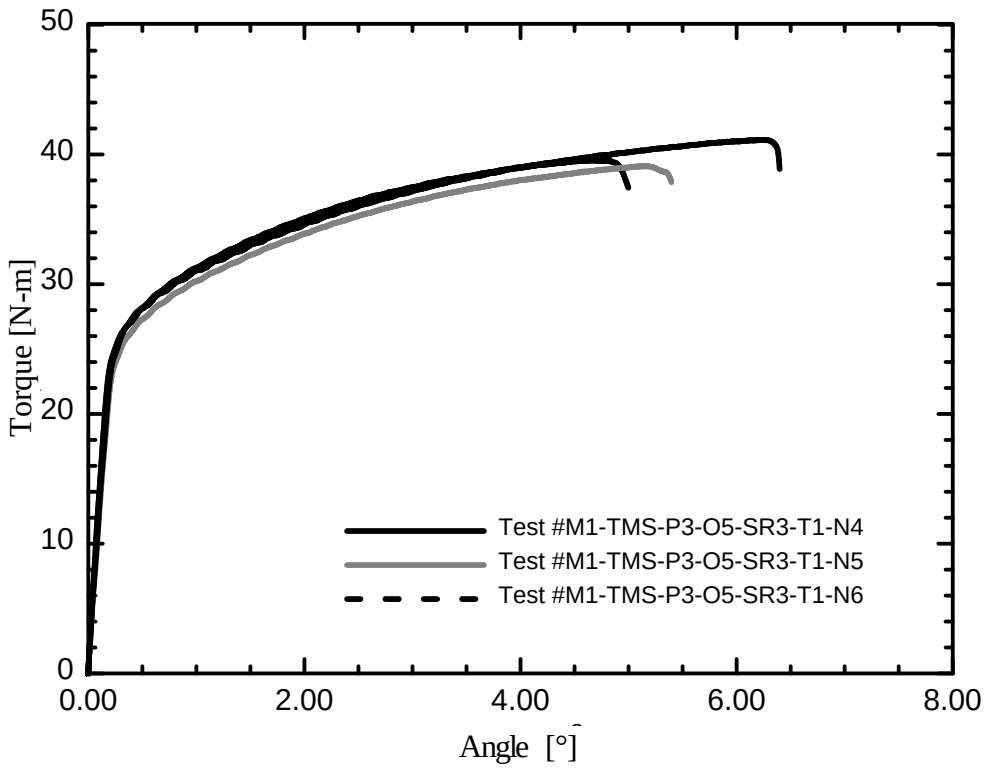

Figure G-27. Torsion Data, Strain Rate 1.0 s^{-1}, Room Temperature

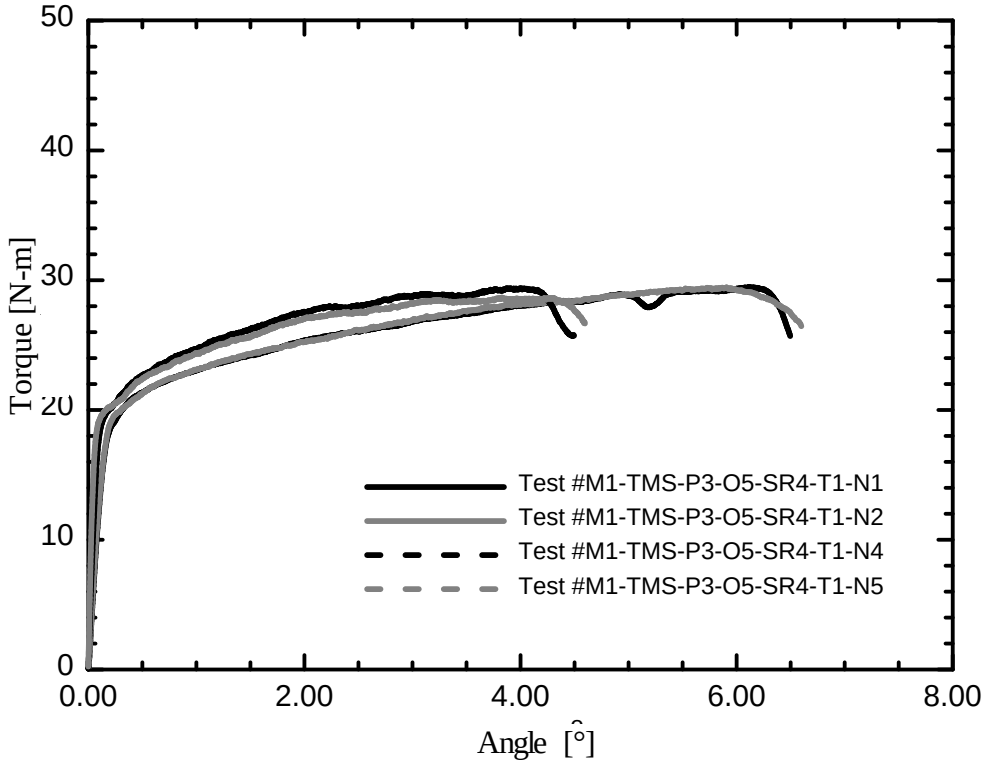

Figure G-28. Torsion Data, Strain Rate 500.0 s^{-1}, Room Temperature

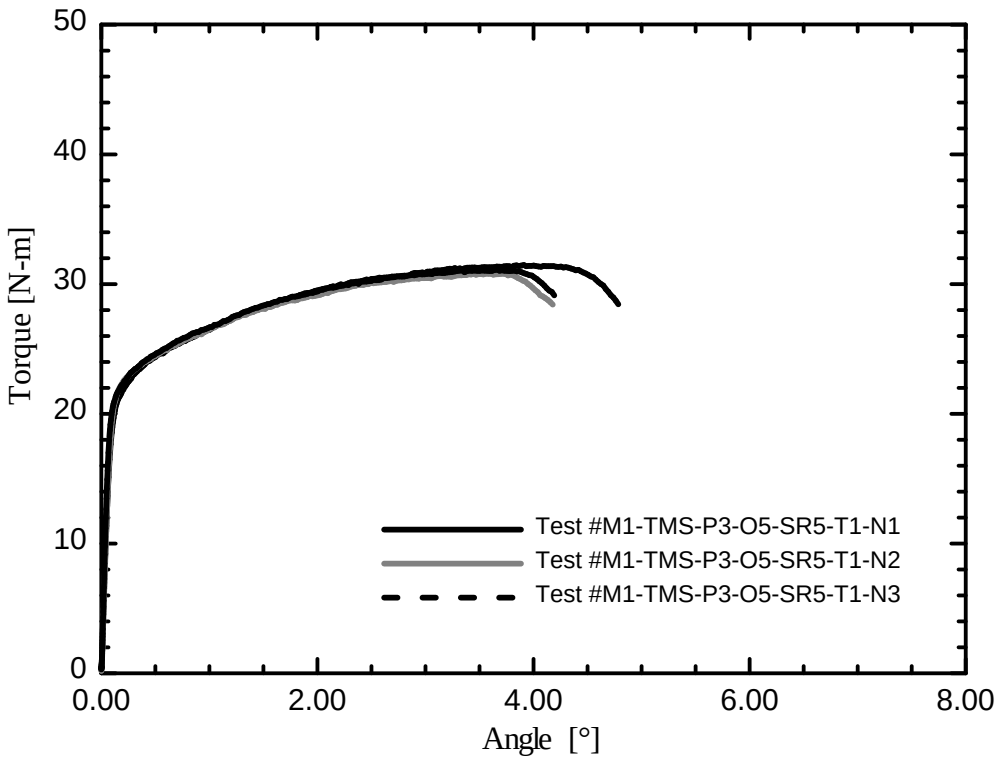

Figure G-29. Torsion Data, Strain Rate 2800.0 s^{-1}, Room Temperature

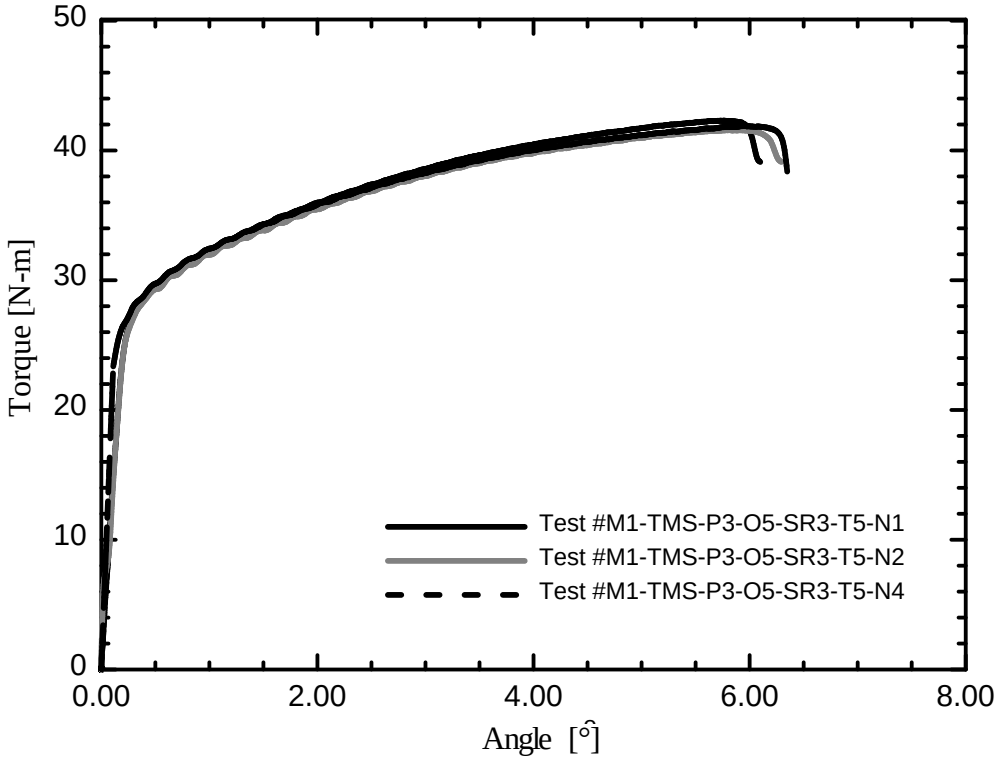

Figure G-30. Torsion Data, Strain Rate 1.0 s^{-1}, -50°C

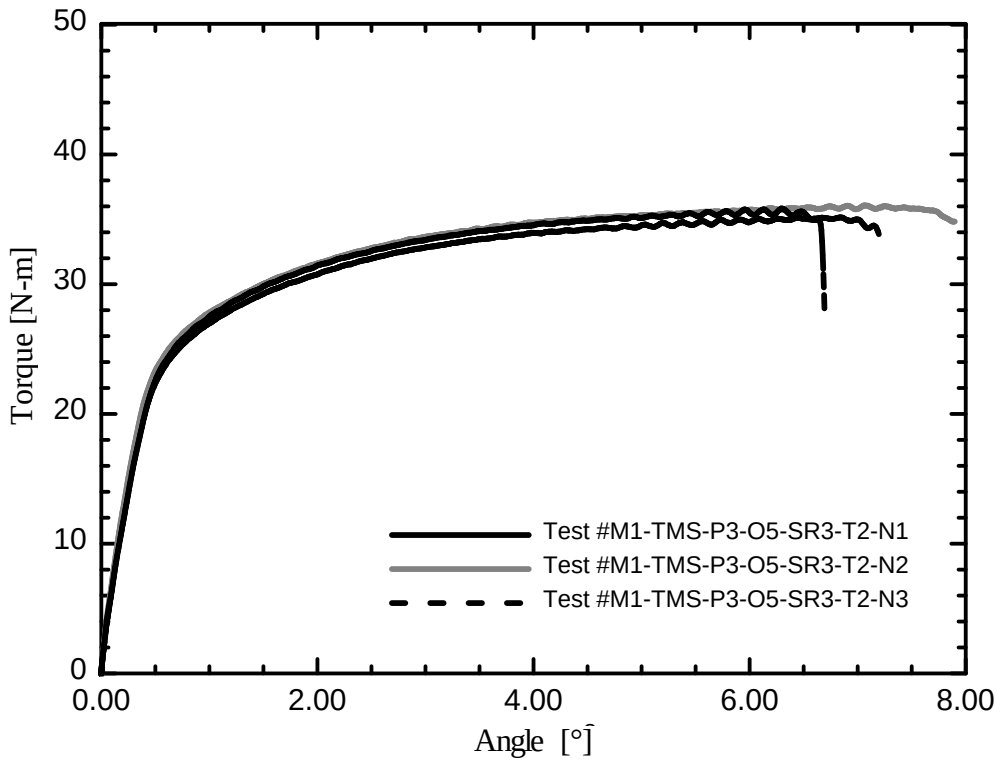

Figure G-31. Torsion Data, Strain Rate 1.0 s^{-1}, 150°C

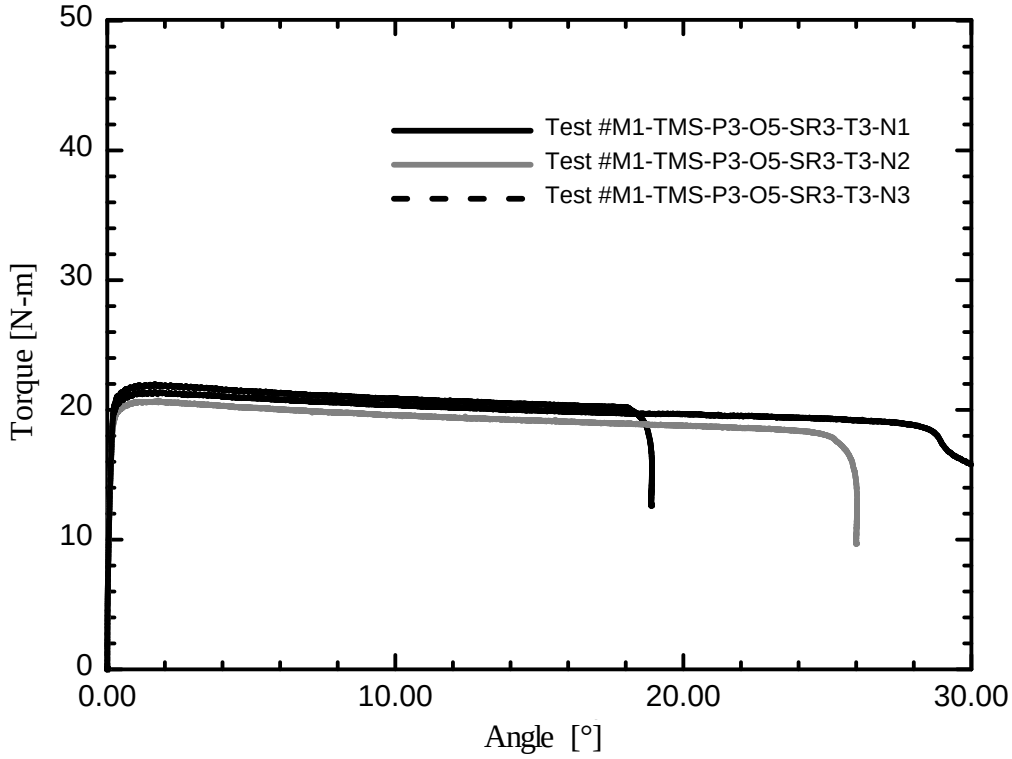

Figure G-32. Torsion Data, Strain Rate 1.0 s^{-1}, 300°C

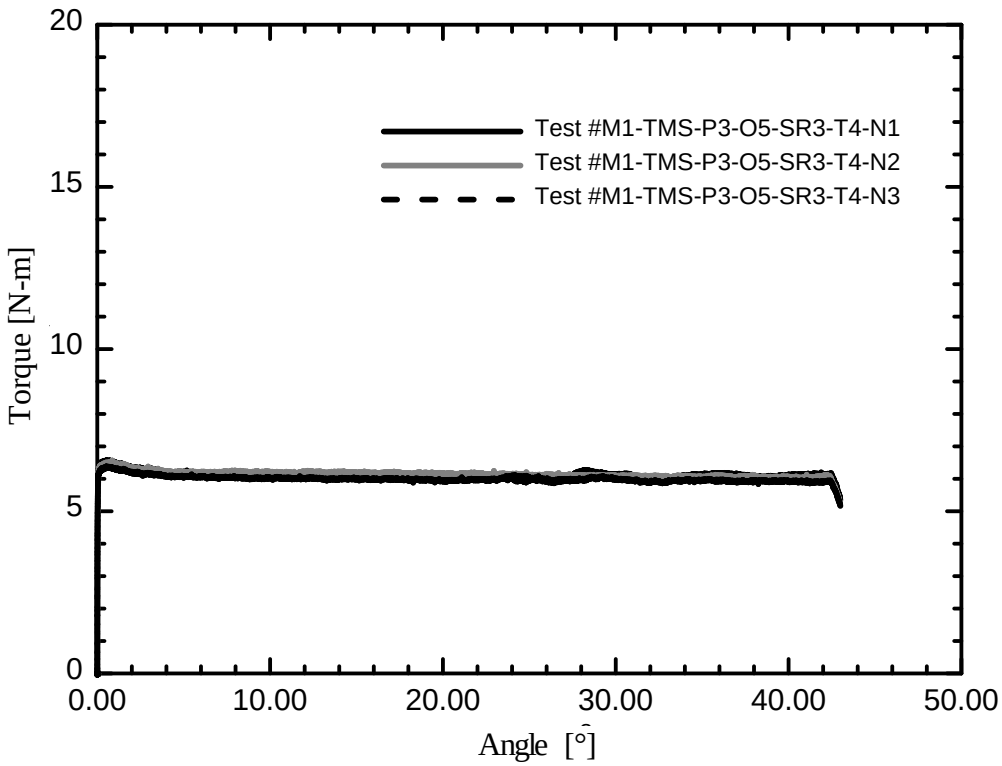

Figure G-33. Torsion Data, Strain Rate 1.0 s^{-1}, 450°C

Table G-1. Measured Dimensions of Specimens Used in the Tension Plasticity Test Series

Test #	Gage Length		Thickness		Width	
	(in)	(mm)	(in)	(mm)	(in)	(mm)
M1-TMT-P3-SG1-O1-SR1-T1-N1	0.200	5.080	0.029	0.737	0.121	3.073
M1-TMT-P3-SG1-O1-SR1-T1-N2	0.200	5.080	0.030	0.762	0.119	3.023
M1-TMT-P3-SG1-O1-SR1-T1-N3	0.200	5.080	0.030	0.762	0.120	3.048
M1-TMT-P3-SG1-O1-SR2-T1-N1	0.200	5.080	0.030	0.762	0.121	3.073
M1-TMT-P3-SG1-O1-SR2-T1-N2	0.200	5.080	0.030	0.762	0.120	3.048
M1-TMT-P3-SG1-O1-SR2-T1-N3	0.200	5.080	0.031	0.787	0.120	3.048
M1-TMT-P3-SG1-O1-SR3-T1-N1	0.200	5.080	0.030	0.762	0.120	3.048
M1-TMT-P3-SG1-O1-SR3-T1-N4	0.200	5.080	0.031	0.787	0.121	3.073
M1-TMT-P3-SG1-O1-SR3-T1-N5	0.200	5.080	0.030	0.762	0.120	3.048
M1-TMT-P3-SG1-O1-SR4-T1-N1	0.200	5.080	0.029	0.737	0.120	3.048
M1-TMT-P3-SG1-O1-SR4-T1-N2	0.200	5.080	0.031	0.787	0.119	3.023
M1-TMT-P3-SG1-O1-SR4-T1-N3	0.200	5.080	0.031	0.787	0.119	3.023
M1-TMT-P3-SG1-O1-SR5-T1-N1	0.200	5.080	0.030	0.762	0.120	3.048
M1-TMT-P3-SG1-O1-SR5-T1-N2	0.200	5.080	0.031	0.787	0.121	3.073
M1-TMT-P3-SG1-O1-SR5-T1-N3	0.200	5.080	0.030	0.762	0.120	3.048
M1-TMT-P3-SG1-O1-SR3-T2-N1	0.200	5.080	0.030	0.762	0.121	3.073
M1-TMT-P3-SG1-O1-SR3-T2-N2	0.200	5.080	0.030	0.762	0.121	3.073
M1-TMT-P3-SG1-O1-SR3-T2-N3	0.200	5.080	0.030	0.762	0.121	3.073
M1-TMT-P3-SG1-O1-SR3-T3-N8	0.200	5.080	0.031	0.787	0.120	3.048
M1-TMT-P3-SG1-O1-SR3-T3-N11	0.200	5.080	0.031	0.787	0.120	3.048
M1-TMT-P3-SG1-O1-SR3-T3-N12	0.200	5.080	0.031	0.787	0.120	3.048
M1-TMT-P3-SG1-O1-SR3-T4-N2	0.200	5.080	0.030	0.762	0.120	3.048
M1-TMT-P3-SG1-O1-SR3-T4-N4	0.200	5.080	0.030	0.762	0.120	3.048
M1-TMT-P3-SG1-O1-SR3-T4-N5	0.200	5.080	0.031	0.787	0.120	3.048
M1-TMT-P3-SG1-O1-SR3-T5-N2	0.200	5.080	0.031	0.787	0.120	3.048
M1-TMT-P3-SG1-O1-SR3-T5-N3	0.200	5.080	0.030	0.762	0.120	3.048
M1-TMT-P3-SG1-O1-SR3-T5-N4	0.200	5.080	0.031	0.787	0.120	3.048
M1-TMT-P3-SG1-O2-SR3-T1-N1	0.200	5.080	0.030	0.762	0.124	3.150
M1-TMT-P3-SG1-O2-SR3-T1-N2	0.200	5.080	0.031	0.787	0.123	3.124
M1-TMT-P3-SG1-O3-SR3-T1-N1	0.200	5.080	0.030	0.762	0.120	3.048
M1-TMT-P3-SG1-O3-SR3-T1-N2	0.200	5.080	0.030	0.762	0.120	3.048
M1-TMT-P3-SG1-O4-SR3-T1-N1	0.200	5.080	0.031	0.787	0.125	3.175
M1-TMT-P3-SG1-O4-SR3-T1-N3	0.200	5.080	0.031	0.787	0.125	3.175

Table G-2. Measured Dimensions of Specimens Used in the Compression Plasticity Test Series

Test #	Length		Diameter	
	(in)	(mm)	(in)	(mm)
M1-TMC-P3-SG1-O1-SR1-T1-N2	0.119	3.023	0.120	3.048
M1-TMC-P3-SG1-O1-SR1-T1-N3	0.120	3.048	0.120	3.048
M1-TMC-P3-SG1-O1-SR2-T1-N1	0.120	3.048	0.120	3.048
M1-TMC-P3-SG1-O1-SR2-T1-N2	0.120	3.048	0.119	3.023
M1-TMC-P3-SG1-O1-SR2-T1-N3	0.120	3.048	0.120	3.048
M1-TMC-P3-SG1-O1-SR3-T1-N1	0.120	3.048	0.120	3.048
M1-TMC-P3-SG1-O1-SR3-T1-N2	0.122	3.099	0.120	3.048
M1-TMC-P3-SG1-O1-SR3-T1-N3	0.118	2.997	0.120	3.048
M1-TMC-P3-SG1-O1-SR4-T1-N1	0.122	3.099	0.122	3.099
M1-TMC-P3-SG1-O1-SR4-T1-N2	0.121	3.073	0.121	3.073
M1-TMC-P3-SG1-O1-SR4-T1-N3	0.121	3.073	0.121	3.073
M1-TMC-P3-SG1-O1-SR5-T1-N2	0.121	3.073	0.120	3.048
M1-TMC-P3-SG1-O1-SR5-T1-N3	0.120	3.048	0.120	3.048
M1-TMC-P3-SG1-O1-SR5-T1-N4	0.121	3.073	0.120	3.048
M1-TMC-P3-SG1-O1-SR6-T1-N6	0.102	2.591	0.121	3.073
M1-TMC-P3-SG1-O1-SR7-T1-N6	0.102	2.591	0.121	3.073
M1-TMC-P3-SG1-O1-SR8-T1-N6	0.104	2.642	0.120	3.048
M1-TMC-P3-SG1-O1-SR3-T2-N1	0.120	3.048	0.120	3.048
M1-TMC-P3-SG1-O1-SR3-T2-N2	0.119	3.023	0.119	3.023
M1-TMC-P3-SG1-O1-SR3-T2-N3	0.121	3.073	0.120	3.048
M1-TMC-P3-SG1-O1-SR3-T3-N1	0.121	3.073	0.120	3.048
M1-TMC-P3-SG1-O1-SR3-T3-N2	0.121	3.073	0.120	3.048
M1-TMC-P3-SG1-O1-SR3-T3-N3	0.121	3.073	0.121	3.073
M1-TMC-P3-SG1-O1-SR3-T4-N1	0.121	3.073	0.120	3.048
M1-TMC-P3-SG1-O1-SR3-T4-N2	0.121	3.073	0.119	3.023
M1-TMC-P3-SG1-O1-SR3-T4-N3	0.123	3.124	0.120	3.048
M1-TMC-P3-SG1-O1-SR3-T5-N1	0.120	3.048	0.120	3.048
M1-TMC-P3-SG1-O1-SR3-T5-N2	0.120	3.048	0.120	3.048
M1-TMC-P3-SG1-O1-SR3-T5-N3	0.120	3.048	0.120	3.048
M1-TMC-P3-SG1-O2-SR3-T1-N1	0.121	3.073	0.120	3.048
M1-TMC-P3-SG1-O2-SR3-T1-N3	0.120	3.048	0.120	3.048
M1-TMC-P3-SG1-O3-SR3-T1-N1	0.121	3.073	0.120	3.048
M1-TMC-P3-SG1-O3-SR3-T1-N2	0.120	3.048	0.120	3.048
M1-TMC-P3-SG1-O4-SR3-T1-N2	0.121	3.073	0.120	3.048
M1-TMC-P3-SG1-O5-SR3-T1-N1	0.121	3.073	0.121	3.073
M1-TMC-P3-SG1-O5-SR3-T1-N2	0.121	3.073	0.120	3.048

Table G-3. Measured Dimensions of Specimens Used in the Torsion Plasticity Test Series

Test #	Gage Length		Gage Thickness		Inside Diameter	
	(in)	(mm)	(in)	(mm)	(in)	(mm)
M1-TMS-P3-O5-SR1-T1-N1	0.090	2.286	0.0205	0.521	0.510	12.954
M1-TMS-P3-O5-SR1-T1-N2	0.090	2.286	0.0205	0.521	0.510	12.954
M1-TMS-P3-O5-SR1-T1-N3	0.090	2.286	0.0205	0.521	0.510	12.954
M1-TMS-P3-O5-SR2-T1-N1	0.090	2.286	0.0205	0.521	0.510	12.954
M1-TMS-P3-O5-SR2-T1-N2	0.090	2.286	0.0205	0.521	0.510	12.954
M1-TMS-P3-O5-SR2-T1-N3	0.090	2.286	0.0205	0.521	0.510	12.954
M1-TMS-P3-O5-SR3-T1-N4	0.090	2.286	0.0205	0.521	0.510	12.954
M1-TMS-P3-O5-SR3-T1-N5	0.090	2.286	0.0205	0.521	0.510	12.954
M1-TMS-P3-O5-SR3-T1-N6	0.090	2.286	0.0200	0.508	0.510	12.954
M1-TMS-P3-O5-SR4-T1-N1	0.105	2.667	0.0155	0.394	0.511	12.979
M1-TMS-P3-O5-SR4-T1-N2	0.105	2.667	0.0150	0.381	0.511	12.979
M1-TMS-P3-O5-SR4-T1-N4	0.053	1.346	0.0150	0.381	0.511	12.979
M1-TMS-P3-O5-SR4-T1-N5	0.053	1.346	0.0150	0.381	0.511	12.979
M1-TMS-P3-O5-SR5-T1-N1	0.054	1.372	0.0155	0.394	0.511	12.979
M1-TMS-P3-O5-SR5-T1-N2	0.053	1.346	0.0155	0.394	0.511	12.979
M1-TMS-P3-O5-SR5-T1-N3	0.053	1.346	0.0155	0.394	0.511	12.979
M1-TMS-P3-O5-SR3-T2-N1	0.090	2.286	0.0200	0.508	0.511	12.979
M1-TMS-P3-O5-SR3-T2-N2	0.090	2.286	0.0205	0.521	0.511	12.979
M1-TMS-P3-O5-SR3-T2-N3	0.090	2.286	0.0205	0.521	0.511	12.979
M1-TMS-P3-O5-SR3-T3-N1	0.090	2.286	0.0205	0.521	0.511	12.979
M1-TMS-P3-O5-SR3-T3-N2	0.090	2.286	0.0200	0.508	0.511	12.979
M1-TMS-P3-O5-SR3-T3-N3	0.090	2.286	0.0205	0.521	0.511	12.979
M1-TMS-P3-O5-SR3-T4-N1	0.090	2.286	0.0200	0.508	0.511	12.979
M1-TMS-P3-O5-SR3-T4-N2	0.090	2.286	0.0205	0.521	0.511	12.979
M1-TMS-P3-O5-SR3-T4-N3	0.090	2.286	0.0200	0.508	0.511	12.979